

# DEVELOPMENT OF TIME-GATED LUMINESCENCE BIO-IMAGING INSTRUMENTS

By

Xianlin Zheng

Department of Physics and Astronomy

## **Supervisors:**

Prof. James A. Piper,

Prof. Dayong Jin,

Dr. Yiqing Lu



**MACQUARIE**  
University  
SYDNEY · AUSTRALIA

FACULTY OF SCIENCE AND ENGINEERING

This thesis is presented for the degree of Doctor of Philosophy

September 2016



I certify that the work in this thesis has not previously been submitted for a degree nor has it been submitted as part of requirements for a degree to any other university or institution other than Macquarie University.

I also certify that the thesis is an original piece of research and it was authored by myself. Help and assistance that I have received in the course of my research work and in the preparation of the thesis itself has, where appropriate, been acknowledged.

In addition, I certify that all information sources and literature used in the course of this research is also indicated where appropriate in this record of my thesis.



---

Xianlin Zheng 16-Sep-2016



## Acknowledgements

Firstly, I greatly appreciate the help I received from my supervisors Prof. James Piper, Prof. Dayong Jin and Dr. Yiqing Lu, who were very supportive in their guidance and who inspired me tremendously. I am also grateful for the opportunity they provided to pursue my PhD degree at Macquarie University. I would not have been able to complete this thesis and my PhD program at Macquarie University without their encouragement and support. Jim Piper is a professor of great personal charisma, always considerate, patient and encouraging. Prof. Jin is a high achieving and industrious expert in the field covered by this thesis high standards provided me with valuable training in my research and in my career development. I believe I learnt a great deal from Jin's self-motivated and optimistic attitude to life. I found Dr. Yiqing Lu to be a humble and talented supervisor and I respect very much his diligence in research and kindness. He provided great support and patient guidance for solving many of the challenges I met during the course of my experiments; he offered his constructive suggestion on the analysis of experimental data and as well his feedback of my paper and my thesis drafts for this work; and he also spent a lot of time in structuring and polishing my thesis. I appreciate this guidance, his sincere help and constructive suggestions not only with work in my PhD program, but also for his advice on the next steps to take in my research career. I feel very lucky to have such great mentors and I am very grateful to them for their enormous effort and guidance throughout my PhD study and help in reaching the completion of this work. Without their consistent guidance and inspiration, I would not have built I believe, such a solid track record of publications in top journals.

I would also like to thank Walther Adendorff, Greg Yates, Benny Wang, and Ken Yuen in Macquarie Engineering & Technical Service (METS). I appreciate as well the help I received from the METS manager Walter Adendorff and Mechanical services technician Benny Wang for their instruction in machining. I also would like to thank METS Assistant Manager (Electronic) Greg Yates and Electronic services technician Ken Yuen for their assistance in the manufacture of electric circuits. Without their consistent efforts and patience, I would not have been able to build the multi-colour time-gated luminescence microscope, time-gated animal imaging system and time-gated scanning microscope described in this work. I do appreciate their personal efforts.

Next, I would like to show my appreciations to my colleagues who contribute significantly to my PhD projects and publications, in particular, Dr. Jiangbo (Tim) Zhao, Dr. Lixin Zhang, Dr. Jie Lu and Deming Liu. Dr. Lixin Zhang helped me considerably during these years. They gave great support and patient guidance for solving the troubles I met during my experiments. I also would like to thank Dr. Wei Deng, Dr. Xiaoxue (Helen) Xu, Yujia Liu, Wei Ren, Dr Xavier Vidal Asensio, Dr. Run Zhang, Dr. Denitza Denkova and my other colleagues at the Centre for Nanoscale Biophotonics and Advanced Cytometry Labs@MQ. I had a wonderful experience working with them. I was impressed and I felt enhanced by their diverse skill sets and self-discipline. I sincerely appreciate the generous help from these nice people.

I also show my appreciations to my international collaborators: Prof. Xiaogang Liu and Yuhai Zhang from National University of Singapore who provided colour-barcoded upconversion micro-rods and plates; Prof. Fuyou Li, Prof. Wei Feng and Xingjun Zhu from Fudan University who provided data collection for my time-gated animal imaging system project; Prof. Jingli Yuan, A/Prof. Bo Song and A/Prof Zhiqiang Ye from Dalian University of Technology who provided lanthanide chelate and guided me in the preparation of the lanthanide chelate labelled bio-samples. I will continue to cherish these interactions and their great help.

Besides my team, I also received much support from colleagues at MQ Biofocus Research Centre, including Prof. Andrei Zvyagin, Dr. Ayad Anwer, Dr. Varun Sreenivasan; the people from Macquarie OptoFab Node, Australian National Fabrication Facility, including Dr Benjamin Johnston; the people from Macquarie physics department, including Prof. Judith Dawes, Prof. Michael Steel, Carol McNaught, Lisa Pesavento, Laura Yang; and High degree research manager Jane Yang. Thank you for your valuable suggestions that greatly enhanced my work.

I would like to also acknowledge the International Macquarie Research Scholarship scheme of Macquarie University for their finance supports of my PhD study. As well, I would also like to acknowledge the generous HDR budget funding support of the Department of Physics and Astronomy throughout my PhD projects; I also acknowledge the PGRF funding scheme of Macquarie University and CYTO 2015 Travel Award given by

the International Society for Advancement of Cytometry to support the conference travel where I had an opportunity to present my research to peers at international conferences.

Finally, I would like to present the special acknowledgements to my parents: Aiqiu Zheng and Bihua Chen; my parents in law: Yaneng Cai and Huimin Lin, who always support me, love me and trust me. In particular, I my love to my wife Weijia Cai who has made great sacrifice and provided great encouragement. Your love, understanding and support helped me overcome the challenges, which as the reader no doubt knows, are a part of completing a PhD.



## List of Publications

- [1]. Lixin Zhang, **Xianlin Zheng**, Wei Deng, Yiqing Lu, James A. Piper Dayong Jin et al. “Practical Implementation, Characterization and Applications of a Multi-Colour Time-Gated Luminescence Microscope”, *Scientific Reports*, 2014, 4: 6597.

*I led the design of the excitation module and the time-gated module, and contributed to system assembly and calibration, data collection and analysis, and figure illustration*

- [2]. Bo Song, Zhiqiang Ye, Yajie Yang, Hua Ma, **Xianlin Zheng**, Dayong Jin, Jingli Yuan. “Background-free *in-vivo* Imaging of Vitamin C using Time-gateable Responsive Probe”, *Scientific Reports*, 2015,5: 14194.

*I replicated the multi-colour time-gated microscope developed in [1] and trained the users for our collaborators overseas, and contributed to figure illustration.*

- [3]. **Xianlin Zheng**, Xingjun Zhu, Yiqing Lu, Jiangbo Zhao, Wei Feng, Guohua Jia, Fan Wang, Fuyou Li, Dayong Jin. “High-Contrast Visualization of Upconversion Luminescence in Mice Using Time-Gating Approach”, *Analytical Chemistry*, 2016, 88, 3449-3454.

*I designed and built the time-gated animal imaging system for our collaborators overseas and trained the users. I led experiment design, data analysis, figure illustration, and manuscript preparation, but did not participate in sample preparation and data collection.*

- [4]. **Xianlin Zheng**, Yiqing Lu, Jiangbo Zhao, Yuhai Zhang, Wei Ren, Deming Liu, Jie Lu, James A. Piper, Robert C. Lief, Xiaogang Liu and Dayong Jin. “High-Precision Pinpointing of Luminescent Targets in Encoder Assisted Scanning Microscopy Allowing High-Speed Quantitative Analysis”, *Analytical Chemistry*, 2016, 88, 1312-1319.

*On the basis of the original OSAM developed by my supervisors, I introduced the linear encoders and the autofocus unit to the platform to achieve higher spatial precision. I led the experiment design, data collection and analysis, figure illustration, and manuscript preparation. I coordinated the sample preparation with my colleagues and collaborators.*

([1] - [4] are directly related to my PhD program)

[5]. Jiangbo Zhao, **Xianlin Zheng**, Erik P. Schartner, Paul Ionescu, Run Zhang, Tich-Lam Nguyen, Dayong Jin, and Heike Ebendorff-Heidepriem. “Upconversion Nanocrystal-Doped Glass: A New Paradigms for Photonic Materials” *Advanced Optical Meterials*, 2016, DOI: 10.1002/adom.201600296.

[6]. Jiangbo Zhao, **Xianlin Zheng**, Erik P. Schartner, Paul Ionescu, Run Zhang, Tich-Lam Nguyen, Dayong Jin, and Heike Ebendorff-Heidepriem. “Upconversion Nanocrystals Doped Glass: A New Paradigm for Integrated Optical Glass” *Photonics and Fiber Technology Congress*, 2016, DOI:10.1364/ACOFT.2016.AM5C.7

[7] Yujia Liu, Yiqing Lu, Xusan Yang, Xianlin Zheng, Shihui Wen, Fan Wang, Xavier Vidal, Jiangbo Zhao, Deming Liu, Zhiguang Zhou, Chenshuo Ma, Jiajia Zhou, James A. Piper, Peng Xi and Dayong Jin. “Amplified stimulated emission in upconversion nanoparticles for super-resolution nanoscopy” *Nature*, 2017, DOI: 10.1038

([5] - [7] is from other project I involved during my PhD candidature)

## Abstract

The general goal for biosensing is to realize ultra-sensitive, high-contrast, rapid and high-throughput detection, localization and quantification of trace amounts of biomolecules and diseased cells of rare types within complex samples. Luminescent probes, such as lanthanide complexes and photon upconversion nanomaterials, hold the potential to realize this goal, due to their unique optical properties, which include long luminescence lifetimes in the microsecond region and as well sharp spectral emission spectra. Application of the time-gated and time-resolved techniques based on these probes will provide background-free detection conditions. But such a potential has been seriously limited by the availability of suitable instruments.

The focus of my PhD research program is the development and the design of new instruments to realize time-domain detection towards advanced optical characterizations of luminescent materials and their analytical applications in biosensing and bioimaging. Specifically, my research project aims to advance and translate the time-gated luminescence detection technique into three prototype instruments – the multi-colour microscope, the *in-vivo* imaging system, and the high-speed scanning cytometry.

The development of the first instrument, a multi-colour microscope, in this work had the specific aims of (a) increasing the detection efficiency, (b) improving the compatibility and stability, and (c) reducing the cost and complexity associated with time-gated luminescence microscopes. These aims were met by designing and engineering a high-efficiency excitation unit that is based on a high power and high repetition rate Xenon flash lamp, to provide broadband illumination for simultaneously exciting multiple lanthanide luminescent probes. The time-gated detection module of this apparatus is optimised by using a fast-rotating optical chopper with a pinhole on the edge of the chopper blade to realise a high switching speed. The modular design has been proved to offer high compatibility and stability when installed to a commercial inverted microscope, and high-contrast dual-colour imaging has been demonstrated in this work by imaging two types of micro-organisms stained by a red-emitting europium complex and a green-emitting terbium complex, respectively, using this setup.

The second instrument, an *in-vivo* imaging system, extended the time-gated technique used in background-free small animal imaging. In this work, the mechanics and optics of the time-gated detection unit of this instrument was re-designed so that this instrument became more suited to the visualization of upconversion nanoparticles when it was used as the optical contrast agents. Their ability to be excited at 980 nm and emit at 800 nm are advantageous for deep-tissue imaging of animal models because near-infrared light lies in the ‘biological transparent window’ where haemoglobin and proteins demonstrate a low absorption. In this work, it was shown that an excitation module housing up to eight 980 nm fibre-coupled diode lasers could be engineered, and a synchronization circuit to generate time-delayed pulses with sufficient driving capacity could be designed. Capable of significantly reducing the optical background and the thermal accumulation, the system integrating near-infrared optical imaging and time-gated technique was demonstrated that could visualise upconversion nanoparticles injected into a Kunming mouse *in vivo*.

The third instrument, a high-speed scanning cytometry, aimed to achieve high-precision pinpointing of individual luminescent targets at high sample throughput for quantitative measurements. Based on the orthogonal scanning automated microscopy (OSAM) method previously developed by members of the Author’s research group, the next-generation referenced-OSAM (R-OSAM) was further engineered by integrating two linear encoders and an autofocus unit to provide the positional reference and compensate the sample tilt in real time. It has been evaluated using micrometre-scale luminescent beads incorporating down-converting lanthanide complexes or upconversion nanoparticles, crystalline microplates, colour-barcoded microrods, and quantitative suspension array assays.

Through the course of this work, a range of device modules have been demonstrated with high detection efficiency, low cost, improved stability and compatibility to modify commercial systems. These create new opportunities for chemistry and biology laboratories to access advanced time-gated luminescence techniques for material characterisation and biosensing applications.

This work is structured as a thesis by publication. The three result chapters are presented in the form of four peer-reviewed journal papers.

**Key words:** long-lived luminescence; lanthanide; time-gated luminescence microscope; time-resolved; high throughput; high resolution; *in-vivo* imaging system

# Contents

<b>Acknowledgements</b> .....	<b>iii</b>
<b>List of Publications</b> .....	<b>vii</b>
<b>Abstract</b> .....	<b>ix</b>
<b>List of Acronyms</b> .....	<b>xv</b>
<b>Chapter 1: Introduction</b> .....	<b>1</b>
1.1    Fluorescence Biotechnology .....	2
1.1.1    A brief overview .....	2
1.1.2    The autofluorescence challenge .....	3
1.2    Time-Gated Luminescence Method .....	4
1.2.1    Fluorescence vs. Luminescence .....	4
1.2.2    Principle of time-gated luminescence detection .....	6
1.3    Long-lifetime luminescent materials .....	8
1.3.1    Lanthanide probes .....	10
1.3.2    Transition metal-ligand complexes .....	13
1.3.3    Indirect bandgap semiconductor nanoparticles .....	15
1.3.4    Non-metal probes .....	17
1.3.5    Choice of probes in the thesis .....	19
1.4    Time-Gated Luminescence Instruments .....	19
1.4.1    Time-gating devices .....	19
1.4.2    Time-gated luminescence microscopy .....	22

---

1.4.3	TGL animal imaging.....	26
1.4.4	TGL instruments for high sample throughput.....	27
1.5	Thesis Outline.....	31
1.6	Reference.....	34
<b>Chapter 2: Multi-Colour Time-Gated Luminescence Microscopy.....</b>		<b>47</b>
2.1	Optical Design.....	47
2.2	Paper 1: Practical Implementation, Characterization and Applications of a Multi-Colour Time-Gated Luminescence Microscope.....	50
2.3	Paper 2: Background-free <i>in-vivo</i> Imaging of Vitamin C using Time-gateable Responsive Probe .....	70
2.4	Remarks .....	85
<b>Chapter 3: Time-gated animal imaging system .....</b>		<b>87</b>
3.1	Optical Design.....	87
3.2	Synchronization Circuit Design.....	89
3.3	Paper 3: High-contrast visualization of upconversion luminescence in mice using time-gating approach .....	92
3.4	Remarks .....	107
<b>Chapter 4: Encoder-Assisted Scanning Microscopy.....</b>		<b>109</b>
4.1	Localization method.....	109
4.2	Paper 4: High-Precision Pinpointing of Luminescent Targets in Encoder-Assisted Scanning Microscopy Allowing High-Speed Quantitative Analysis .....	112
4.3	Remarks .....	128
<b>Chapter 5: Conclusions and Perspectives.....</b>		<b>129</b>
5.1	Summary.....	129

---

5.2	Future Scope.....	131
5.3	Reference.....	135



## List of Acronyms (in Alphabetic Order)

Ag	Argentum (Silver)
AOM	Acousto optical modulator
ARC	Arginine-rich peptide
ARC-Lum	Arginine-rich peptide Luminescence
Au	Aurum (Gold)
BHHBCB	1, 2-bis [4'-(1'', 1'', 1'', 2'', 2'', 3'', 3''-heptafluoro-4'', 6''- hexanedion-6''-yl)-benzyl]-4-chlorosulfo benzene
BHHCT	4,4'-bis(1'',1'',1'',2'',2'',3'',3''-heptafluoro-4'',6''-hexanedion-6''-yl)-chlorosulfo-o-terphenyl
BHHTEGST	1 (4, 4'-bis(1'', 1'', 1'', 2'', 2'', 3'', 3''-heptafluoro-4'', 6''- hexanedion-6''-yl) sulfonylamino-tetraethyleneglycol-succinimidyl carbonate-o-terphenyl)
BODIPY	Boron-dipyrromethene
BP	Benzophenone
BPTA	N, N, N1, N1-[2, 6-bis (3'-aminomethyl-1'-pyrzaolyl)-4-phenylpyridine ] tetrakis
CCD	Charge Coupled Device
Cd	Cadmium
Ce	Cerium
CT	Computed tomography
Cu	Cuprum (Copper)
CW	Continuous wave
DELFLIA	Dissociation Enhanced Lanthanide Fluoroimmunoassay
DNA	Deoxyribonucleic acid

---

DPA	9,10-diphenylanthracene
Dy	Dysprosium
Er	Erbium
Eu	Europium
FOV	Field of view
GALD	Gated autosynchronous luminescence detection
Ho	Holmium
IC	Internal conversion
ICCD	Intensified Charge Coupled Device
Ir	Iridium
ISC	Intersystem crossing
La	Lanthanum
LCD	Liquid crystal
LED	Light emitting diodes
Ln	Lanthanide
LPSiNPs	Luminescent porous silicon nanoparticles
Lu	Lutetium
MCP	Microchannel plate
MEMS	Microelectromechanical systems
MLC	Metal-ligand complexes
MLCT	Metal-to-ligand-charge-transfer
Mn	Manganese
MRI	Magnetic resonance imaging
Nd	Neodymium
NIR	Near infrared
Os	Osmium

---

OSAM	Orthogonal scanning automated microscopy
Pd	Palladium
PEG	Polyethylene glycol
PK	Protein Kinase
PLL	Phase-locked loop
PMT	Photomultiplier Tube
Pr	Praseodymium
Pt	Platinum
QY	Quantum yield
Re	Rhenium
Rh	Rhodium
R-OSAM	Referenced-OSAM
Ru	Ruthenium
Ru-8	$[(\text{bpy})_2\text{Ru}(3\text{-pyrenyl-1,10-phenanthroline})]^{2+}(\text{PF}_6^-)_2$
SEM	Scanning electron microscopy
Si	Silicon
Sm	Samarium
SPECT	Single-photon emission computed tomography
Tb	Terbium
TEM	Transition electron microscopy
TGL	Time-Gated Luminescence
Tm	Thulium
TRACE	Time-Resolved Amplified Cryptate Emission
TTA	Triplet-triplet annihilation
TTET	Triplet-triplet energy transfer
TTL	Transistor-Transistor Logic

UCNP	Upconversion nanoparticle
UV	Ultraviolet
VR	Vibrational Relaxation
Xe	Xenon
Yb	Ytterbium

## Chapter 1: Introduction

Time-Gated Luminescence (TGL) microscopy has been demonstrated to be a powerful tool for high-contrast imaging of rare-event cells and low-abundance biomolecules in complex biological samples using long-lifetime luminescent bioprobes [1,2]. This offers major improvements in detection limits, especially in the presence of substantial autofluorescence from the sample, and in addition, the prospect of using lifetime-coded luminescent probes for time-domain multiplexing [3-5].

This thesis reports key advances in instrumentation giving practical effect to time-gated luminescence microscopy, both for wide-field and scanning microscopes, facilitating high-throughput multiplexed detection, high-contrast *in vivo* bio-imaging of small animals, and high-speed automated scanning quantification complex samples. In particular, a new generation of time-gated wide-field microscopes has been designed which offers a compact, low cost add-on to standard inverted fluorescence microscopes which enables wide-field time-gated imaging with high autofluorescence signal rejection to deliver high contrast, while retaining a high level of flexibility in terms of spectral and temporal parameters. The efficacy of these instruments has been demonstrated in multi-colour time-gated microscopy of different microorganisms labelled with time-coded luminescent probes, and background-free (TGL) imaging *in-vivo* of specific species (Vitamin C) labelled with a long-lifetime reactive probe. Following similar design concepts a new TGL camera system has been developed for imaging whole small animals, enabling high-contrast imaging of subcutaneous organs based on TGL detection of injected up-conversion nanoparticle probes. Finally, a new generation of scanning TGL microscope has been developed and tested which enables high-speed inspection of large biological samples containing small numbers of target organisms, high-precision location of target organisms, and subsequent target intensity and lifetime measurements leading to target species identification and quantification with low levels of uncertainty. It is anticipated that these new generations of TGL instrumentation will find important applications in environmental sensing, biomedical diagnostics, and materials characterisation.

This chapter reviews the current status of instrumentation developments for the detection of long-lifetime luminescence materials and bio-analytes. It first briefly introduces the

fluorescence detection techniques and identifies the limitations; the key challenges of fluorescence techniques in practical applications; the motivation, fundamental knowledge and the major advantages of using time-gated detection technique for microscopy and imaging in related areas of the materials chemistry, instrumentation and bio-applications. A detailed thesis plan is provided at the end of this chapter.

## **1.1 Fluorescence Biotechnology**

### **1.1.1 A brief overview**

Sensitive detection of tiny and complex biomolecules and imaging of subcellular structures within cells and microorganisms are critical for understanding of biological processes [1,6-9]. Optical microscopy is widely used together with selective staining of target biomolecules and cells with fluorescent probes to provide high contrast to the non-target biological samples in different colour bands (spectra).

Over the last three decades, remarkable progress has been made in fluorescence biotechnology that drives many discoveries of biomedical research in biochemistry, biophysics, life sciences and disease diagnosis. On one hand, new classes of fluorescence probes have been designed and synthesized with unique optical properties, such as organic compounds and complexes [10-16], genetically engineered fluorescent proteins [17], semiconductor quantum dots [18-20], gold nanoparticles [20-22], silica or polymer nanoparticles [23-26], and rare earth doped nanocrystals [27-31]. On the other hand, new detection methods have been demonstrated through Instrumentation development, thanks to the rapid developments in excitation light sources, optical filters and thin-film coating technology, semiconductor detectors, as well as electronics and computing technologies. Thus detection and tracking of single molecules under fluorescence microscope or other analytical devices is already possible.

Many novel imaging techniques, including laser scanning confocal microscopy, multiphoton microscopy, and super-resolution nanoscopy, continue to extend the limit to spatial resolution from the microscopic to nanoscopic region, and many other cytometry techniques, such as polychromatic flow cytometry, laser scanning cytometry, microfluidic devices, microelectromechanical systems (MEMS), biochips, are continuing to improve the

analytical speed, throughput, sensitivity and specificity for screening multiple cellular analytes and populations of cell types.

With the interactive developments in both fluorescence probes and detection instruments, fluorescence technology has at present become a dominant methodology extensively used in a variety of fields of biotechnology and life sciences, such as biology, microbiology, cytology, molecular cytology, genetics, immunology, pathology, oncology, and medical diagnostics.

### 1.1.2 The autofluorescence challenge

A key challenge for fluorescence biotechnology, however, lies in autofluorescence, that is, the natural fluorescence emission from samples under UV-visible excitation light. Autofluorescence is commonly found in both biological and non-biological samples, including endogenous molecules, cells, tissues, microorganisms and plant debris, as well as fluids and minerals. [Figure 1-1](#) illustrates typical examples of environmental water samples excited in a fluorescence microscope without any fluorescent staining.

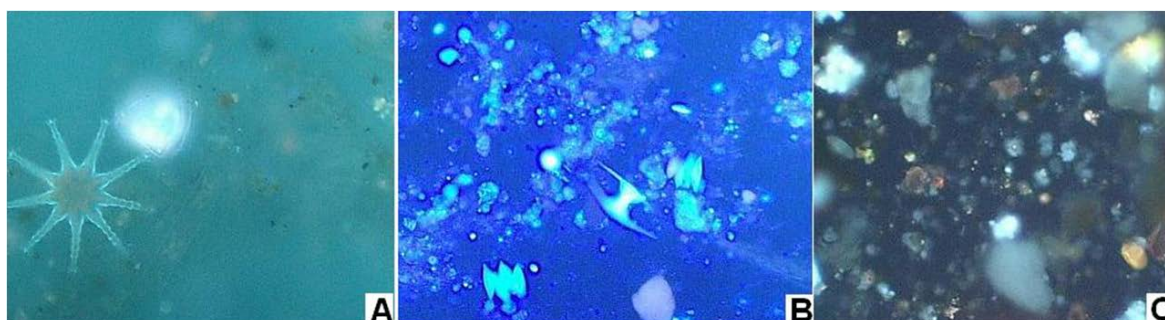


**FIGURE 1-1** Examples of autofluorescence in environmental water samples (collected from various sources in Sydney, Australia) under fluorescence microscope. Reprinted from Ref. [32].

Autofluorescence typically covers a broad range in the visible spectrum with emission lifetime of a few nanoseconds, and is often very difficult to distinguish from targets labelled with standard molecular dyes (FITC, Alexa etc.). This issue is commonly encountered in biological experiments, leading to reduced detection sensitivity and/or imaging contrast for conventional fluorescence techniques. Autofluorescence is particularly problematic in detecting trace levels of target analytes from complex samples containing a large quantity of non-target substances, since the fluorescence signals from target-of-interest are barely visible in the presence of strong autofluorescence [33]. Rare-event detection problems, such

as detection of residue cancer cells in blood at a frequency of less than one in a million and screening of rare pathogens in environmental or food samples, demand more sensitive methods to suppress the preponderant autofluorescence in most real samples.

## 1.2 Time-Gated Luminescence Method

While fluorescence detection is usually carried out in the spectral domain, the time domain offers another opportunity based on measurement of lifetimes (i.e. decay rates after pulsed excitation). Both conventional fluorophores and autofluorescence have lifetimes around a few nanoseconds, thus it is difficult to distinguish them from each other. The autofluorescence challenge, however, has been overcome by the time-gated luminescence (TGL) method proposed about 40 years ago, which takes advantage of long-lived luminescence probes.

### 1.2.1 Fluorescence vs. Luminescence

Before details of the TGL method are introduced, the concepts of fluorescence and luminescence are explained for clarity purpose.

Fluorescence is the emission of light through quantum mechanically allowed transitions by a substance that has absorbed excitation or other electromagnetic radiation. The fluorescent substance typically has multiple energy levels originating from the electron orbitals, as illustrated by the Jablonski diagram in [Figure 1-2\(a\)](#). The fluorescence process starts when a photon is absorbed by the substance in its low-energy states (the ground states), which are excited to one of the high-energy states (the excited states). Fluorescence emission occurs when an excited state relaxes to a ground state by emitting a photon.

Fluorescence is typically characterised by the emission and excitation spectra. The emission spectrum is a plot of the fluorescence intensity as a function of emission wavelength (or wavenumber), measured at a single constant excitation wavelength. The excitation spectrum is the dependence of emission intensity, measured at a single emission wavelength, upon scanning the excitation wavelength. In most cases, the emission light has a longer wavelength, and therefore lower energy, than the absorbed light. Thus, colour filters with different transmission bands can be used to separate the excitation and emission in the

spectral domain. This renders labelled targets distinguishable from non-targets in fluorescence detection.

In comparison, luminescence is a process superficially similar to fluorescence but with fundamental difference in terms of transitions between energy states. In luminescent materials, radiative relaxation from excited states back to the ground states is typically forbidden quantum mechanically due to spectroscopic selection rules, including the spin rule and the Laporte rule. The former states that electrons can only transit between energy levels with identical spin quantum number, while other transitions, e.g. transitions between singlet states to triplet states, are spin forbidden. The latter states that electronic transitions must invert parity for centrosymmetric molecules and atoms. Because different electron configurations on the same orbits share the same parity, electrons must transit to different orbits next to their original ones, such as d-f, while d-d and f-f transitions are Laporte forbidden. Nevertheless, in reality these forbidden transitions still happen, but at much lower probabilities (rates). The average time spent in the excited state, which is the emission lifetime, is thus much longer compared to allowed transitions in the case of fluorescence.

Since the forbidden nature not only influences emission but excitation as well, instead of direct pumping onto the excited states for emission, luminescent probes usually employ other excited states of higher energy for efficient energy sensitizing. For example, in the Jablonski diagram in [Figure 1-2\(d\)](#), the substance exhibits two excited states – a higher singlet excited state that facilitates transition to the singlet ground state, and a lower triplet excited state where the forbidden transition from/to the ground state occurs at very slow rates. To enable efficient luminescence, it is required that the singlet excited state is capable of rapid, nonradiative relaxation to the triplet state compared to radiative relaxation to the ground state, so that most of the excitation energy is stored for subsequent slow release. This is typically realised by attaching a ligand as the light antenna, to emitters such as lanthanide and transition metal ions. A brief summary of existing long lifetime luminescent materials will be given in Section 1.3.

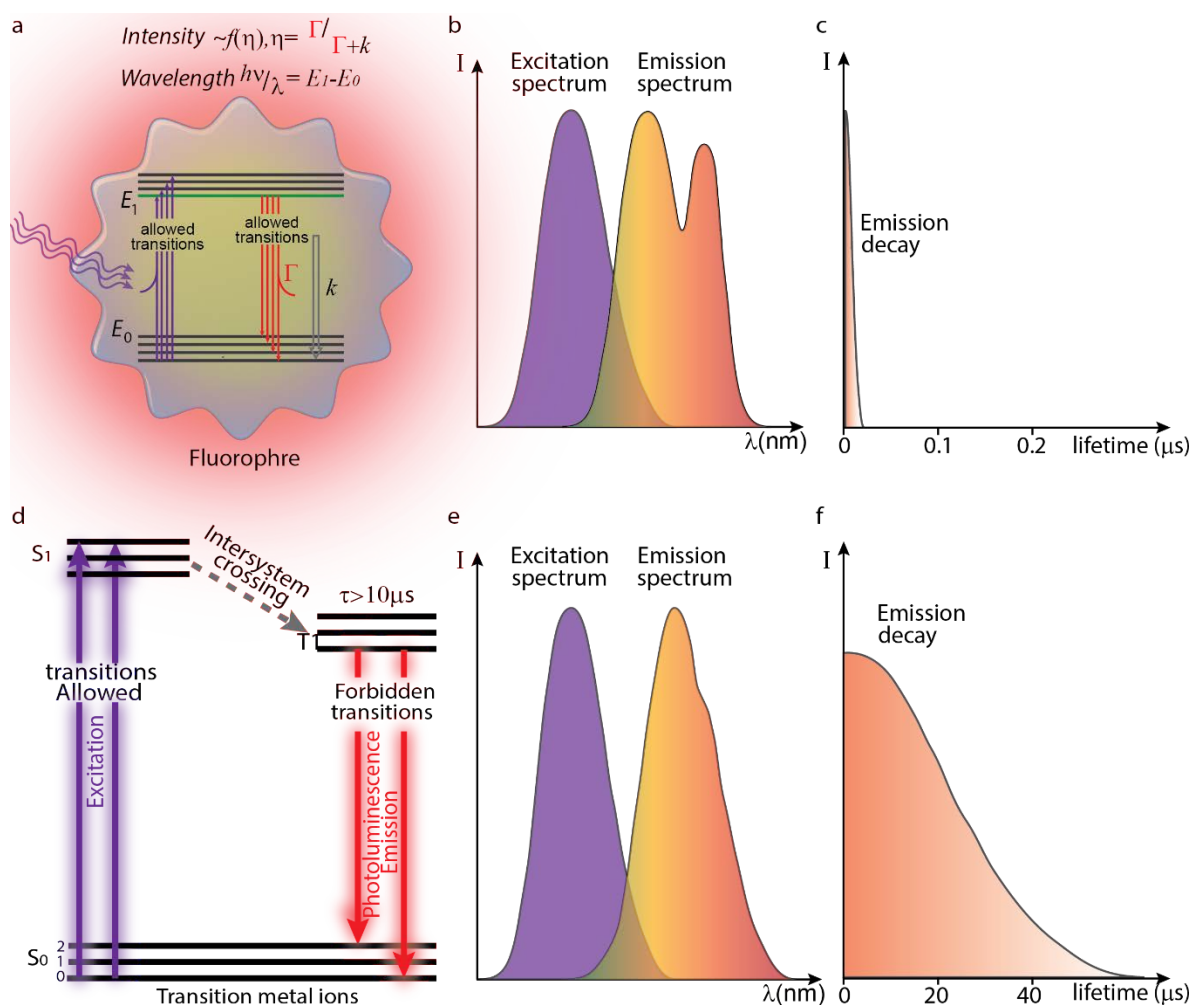


**Figure 1-2.** The Jablonski diagram illustrates the process of fluorophore (a) and photoluminescence in a singlet and triplet system (d). (b) and (e) show the excitation and emission spectrum of fluorophore and long-lived luminescence complexes. (c) and (f) show the emission decay of fluorophore and emission decay of long-lived luminescence complexes.

## 1.2.2 Principle of time-gated luminescence detection

To overcome the autofluorescence problem for enhanced detection sensitivity in immunoassays, the time-gated luminescence (TGL) method was proposed in the 1970s as a solution [34,35]. Based on the outstanding difference in decay lifetimes between luminescent probes and autofluorescence, the TGL method employs periodical pulsed excitation and time-delayed detection to differentiate signal from background. As shown in Figure 1-3(a), a typical detection cycle consists of an excitation pulse, an appropriate period of time delay, and a gated detection window. Following the pulsed excitation, the signal luminescence decays much slower than the short-lived autofluorescence background, so that after the time delay, autofluorescence as well as residual scatterings of the excitation light vanishes, and

only long-lived signal luminescence from labelled analytes will be detected. As shown in Figure 1-3(b and c), this significantly enhances the signal-to-background ratio [3,36-40]. Long integration time consisting of multiple TGL cycles is often used to accumulate the luminescence signal and average out the random electronic noise to further improve the contrast.

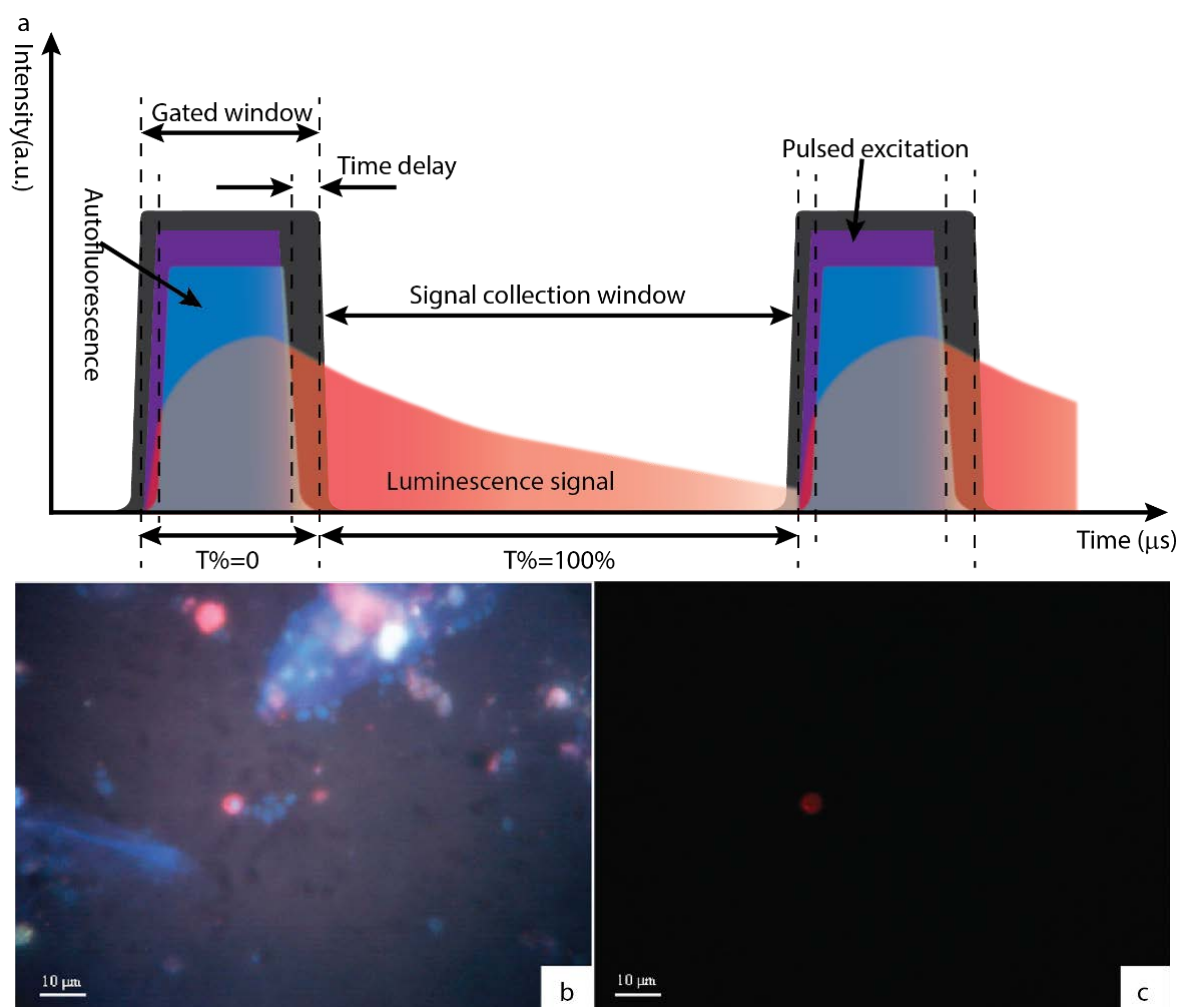


**FIGURE 1-3** (a) Schematic diagram illustrating the principle of time-gated luminescence detection for long-lived luminescence materials. During the gated window, only the pulsed excitation is switched on. After the excitation pulse, the short-lived autofluorescence background is eliminated by a suitable time delay before the signal collection window. During the signal collection window, only long-lived luminescence signal is detected by the detector. True-colour images of a BHHCT-europium complex labelled *Cryptosporidium parvum* oocyst within fruit juice concentrate are shown: (b) a conventional fluorescence microscope image; (c) a time-gated luminescence microscope image of the same sample. Reproduced from Ref. [3,39,41]

### 1.3 Long-lifetime luminescent materials

Time-gated luminescence techniques rely on the unique property of long lifetime luminescence materials. Ideally, the emission lifetimes of these materials should be in the microseconds range. On one side, measuring lifetimes shorter than a microsecond requires sophisticated and expensive equipment; on the other side, when the lifetime of luminescent probes is longer than 1 ms, the luminescent intensity becomes relatively weak, which needs to be compensated by extended detection time. Existing luminescence materials with lifetimes in the above range, as summarised in [Figure 1-4](#) and [Table 1-1](#), are briefly introduced in this section.

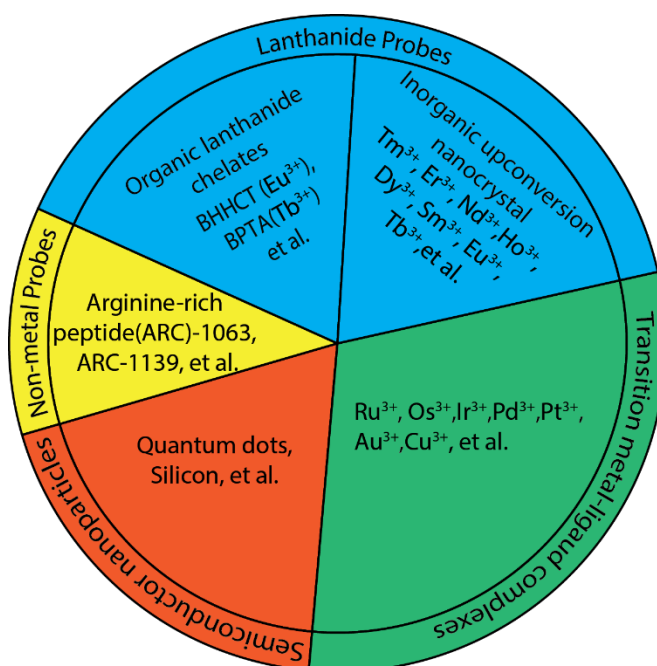


**Figure 1-4** A classification of the long-lifetime luminescence materials is shown. These include organic lanthanide luminescence complexes, inorganic upconversion nanocrystals, transition metal-ligand complexes, doped semiconductor quantum dots, and non-metal probes.

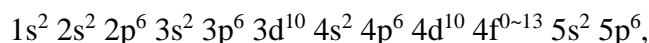
**TABLE 1-1** Long-lived Luminescence probes.

Element	Mechanism	Example Form	Typical Peak Excitation (nm)	Typical Peak Emission (nm)	Typical Lifetime ( $\mu$ s)	Quantum Efficiency	Ref.
Ru*	T $\rightarrow$ S	bipyridine complex	350	600	148	0.071	[54]
Rh*	T $\rightarrow$ S	dimine complex	310	505	162-176	0.008-0.017	[52,53]
Pd*	T $\rightarrow$ S	porphyrin complex	380	660	1100	0.17	[51]
Ir*	T $\rightarrow$ S	polypyridine complex	280	560	11.38	0.0792	[49,50]
Pt*	T $\rightarrow$ S	porphyrin complex	400	680	45.8	0.05	[38]
Eu $\dagger$	4f $\rightarrow$ 4f	$\beta$ -diketone complex	325	610	384	0.506	[13,48]
Tb $\dagger$	4f $\rightarrow$ 4f	phenylpyridine complex	325	545	2700	0.58	[14]
Sm $\dagger$	4f $\rightarrow$ 4f	trifluoroacetone complex	360	650	96	--	[11]
Dy $\dagger$	4f $\rightarrow$ 4f	trifluoroacetone complex	315	575	27	--	[10]
Er $\dagger$	4f $\rightarrow$ 4f	upconversion nanocrystal	980	540,	20~550	0.00005-0.003	[27,47]
Tm $\dagger$	4f $\rightarrow$ 4f	upconversion nanocrystal	980	455,475,650,800	25~670	0.0045-0.012	[45,46]
Au*	T $\rightarrow$ S	Cyclometalated complex	UV/Vis	530	5~270	0.101	[44]
Re*	T $\rightarrow$ S	Proteinbound luminophore	290	550	2.7	0.05-0.12	[12]
Ag*	T $\rightarrow$ S	Supramolecular complex	355	412	3.9, 4.9	--	[43]
Cd*	T $\rightarrow$ S	Coordination polymers	340	510	120 and 1200	--	[42]
Mn*	3d $\rightarrow$ 3d	Doped Semiconductor	365	570	50~1000	0.7	[18]
Si	T $\rightarrow$ S	Silica nanoparticle	365	460	60	0.1	[24]
PK $\ddagger$	T $\rightarrow$ S	Protein Kinase ARC-Lum probes	337	675	19~266	0.7	[17]

**Note: (\*) indicates transition metal probes and ( $\dagger$ ) lanthanide probes. ( $\ddagger$ ) protein. T: triplet state; S: singlet state.**

### 1.3.1 Lanthanide probes

Lanthanides comprise 15 chemical elements with atomic number from 57 to 71. Excepting Lanthanum (La) and Lutetium (Lu), the remaining 13 elements are inclined to form trivalent ions  $\text{Ln}^{3+}$  with the similar electron configuration of



often represented in short as  $[\text{Xe}] 4f^{0-13}$ . The partially-filled 4f orbitals shielded by 5s and 5p electrons provide with well-defined energy levels hardly influenced by physical and/or chemical surroundings, as depicted by the well-known Dieke Diagram that has been discussed by Dieke and Crosswhite in 1963 for depicting energy levels of  $\text{Ln}^{3+}$  in  $\text{LaCl}_3$ . Consequently, the emission peaks of lanthanide (III) 4f-4f transitions are characteristic of the elements, and have much narrower spectral bandwidth compared to other luminescent materials.

A variety of organic ligands/chelates have been designed to form luminescent complexes with  $\text{Ln}^{3+}$  ions, so that they can absorb excitation light more efficiently and transfer the sensitized energy to  $\text{Ln}^{3+}$  for luminescence emission. These ligands also function as a scaffold for biomolecular conjugation and cell staining. Developing long-lifetime lanthanide bioprobes started in the late 1970s coincident with the conception of the TGL method, leading to development and implementation of four lanthanide probes (Eu, Tb, Sm, Dy) in the 1980s [55-58]. In 1998, Yuan, Matsumoto and Kimura developed a new Tetradentate  $\beta$ -diketonate-europium chelate (BHHCT, [Figure 1-5 \(a\)](#)) with long lifetime around 500  $\mu\text{s}$  and high quantum yield of 20%, and successfully bound it to proteins for time-resolved fluoroimmunoassay [13]. In 2001, Yuan et al. reported a new nonadentate ligand (BPTA) to chelate  $\text{Tb}^{3+}$ , with a luminescence quantum yield of 1.00 and lifetime of 2.681 ms [14]. In 2012, Zhang et al. developed new class of Tetradentate  $\beta$ -Diketonate-Europium Complexes (BHHBCB with 40% quantum efficiency and lifetime of 0.52 ms, [Figure 1-5 \(a\)](#)) that could be covalently bound to proteins as biolabels for highly sensitive time-gated luminescence bioassay in clinical diagnostic and biotechnology discoveries [15]. Recently, Sayyadi et al. developed a novel biocompatible europium ligand BHHTEGST, which is shown in [Figure 1-5 \(a\)](#), and which displayed superior synthesis yield, stability, binding and emission characteristics (40% quantum efficiency) [16]. These major advances in materials have

enabled lanthanide complexes to be applied for a variety of biosensing and bioimaging applications [59-63].

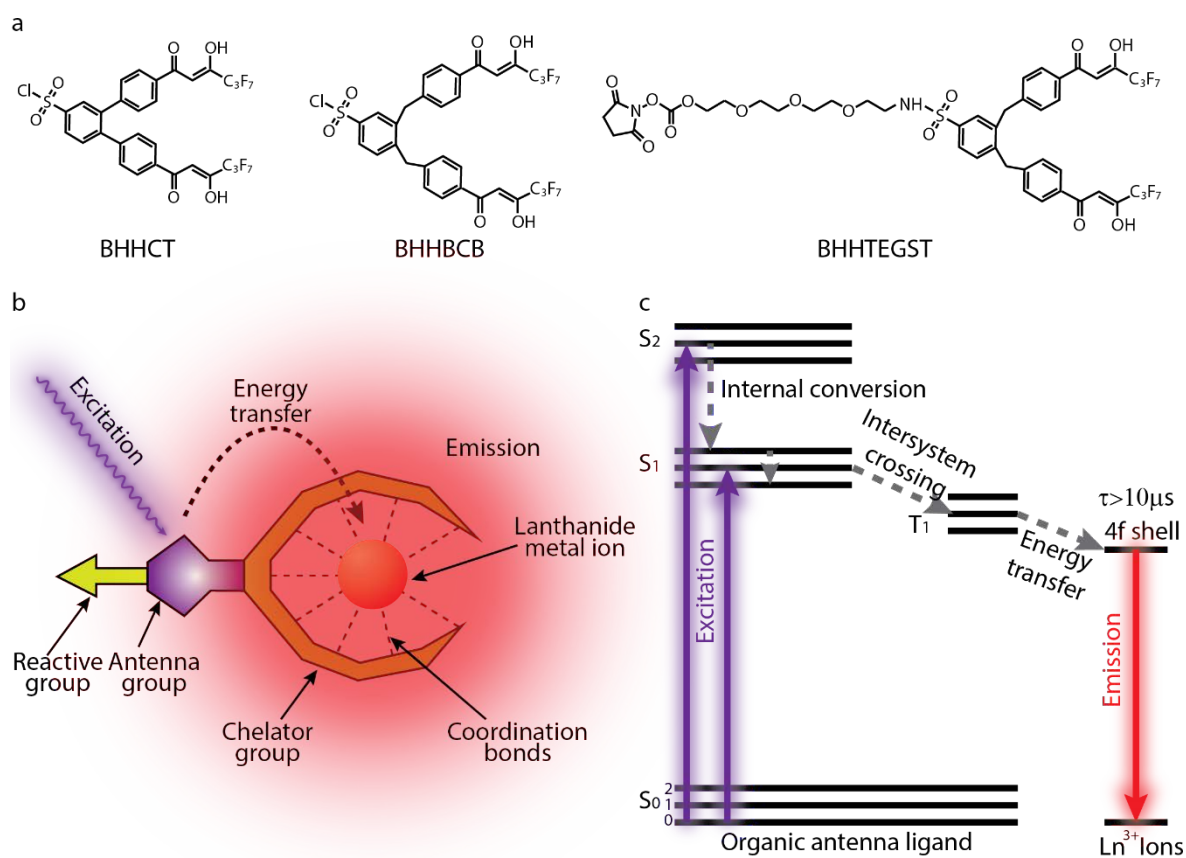


**Figure 1-5.** (a) Three advanced europium chelates for luminescence bioprobes: BHHCT, BHHBCB and BHHTEGST are given [13,15,16]. (b) The schematic diagram illustrates luminescence from a lanthanide complex (lanthanide ion chelated by an organic antenna ligand). The antenna ligand absorbs the excitation photons then transfers the energy non-radiatively to the lanthanide ion that emits long-lived luminescence. (c) A Jablonski diagram illustrates this process of lanthanide ion chelated by an organic antenna ligand [1].

Another promising development in lanthanide probes has happened in the area of inorganic upconversion nanocrystals. Because lanthanides have multiple excited-state energy levels with similar intervals, some systems can convert two or more low-energy near-infrared photons into one photon of higher energy and shorter wavelength. For example, in Yb-Tm or Yb-Er co-doped nanocrystals (Figure 1-6), the Yb<sup>3+</sup> sensitizers absorb excitation at 980 nm and transfer the sensitized energy to Tm<sup>3+</sup> or Er<sup>3+</sup> acceptors, which subsequently emit upconversion luminescence in blue or green colours. This is advantageous in bioimaging applications as near-infrared (NIR) has less photo-toxicity, produces negligible

autofluorescence, and penetrates deeper into the tissue samples through the so-called “biological transparent window” (650 nm - 900 nm)[64,65].

In 2006 Wang et al. used green upconversion nanocrystals as probes for DNA detection. In 2008, Prasad et al. used fluoride nanophosphors doped with  $\text{Tm}^{3+}$  and  $\text{Yb}^{3+}$  for high contrast *in vitro* and *in vivo* photoluminescence bioimaging. The rapid developments in nanoscience and nanotechnology have made robust synthesis protocols available to produce monodisperse nanocrystal hosts, including fluorides ( $\text{NaYF}_4$ ,  $\text{NaGdF}_4$ ,  $\text{NaYbF}_4$ ,  $\text{NaLuF}_4$ ), and oxides ( $\text{Y}_2\text{O}_3$ ,  $\text{Gd}_2\text{O}_3$ ). Generally speaking, rare earth doped fluoride nanocrystals are the best due to their low phonon energy, good thermal stability, optical stability, high transparency, high refractive index and high capacity for doping lanthanide ions. By doping the trivalent Ln ions ( $\text{Er}^{3+}$ ,  $\text{Tm}^{3+}$ ,  $\text{Ho}^{3+}$ ,  $\text{Pr}^{3+}$ ,  $\text{Ce}^{3+}$ ,  $\text{Nd}^{3+}$ ,  $\text{Tb}^{3+}$ ,  $\text{Dy}^{3+}$ ,  $\text{Sm}^{3+}$  and  $\text{Eu}^{3+}$ ) as emitters, multi-colour emissions from UV to visible to near infrared have been demonstrated, as shown in Figure 1-6; and only  $\text{Yb}^{3+}$ ,  $\text{Nd}^{3+}$  ions have been demonstrated as efficient sensitizers to absorb 980 nm and 808 nm excitations. Recently, core-shell structured nanoparticles composing of an upconversion emission core and a photosensitizer-embodied shell arrangement, whose structure indicated that the upconversion emission core can be passivated efficiently to reduce the core surface defects and insulated from the environmental effects, have also been extensively exploited to display dramatically improved upconversion efficiency [66,67]. The surface of nanoparticles can be deliberately modified by ligand attraction, self-assembly, surface polymerization or ligand engineering, and then covalently conjugated to functional biomolecules [68-74]. These strategies render inorganic nanocrystals biocompatible as luminescent tags to target biomolecules for bio-detection and bio-imaging applications.

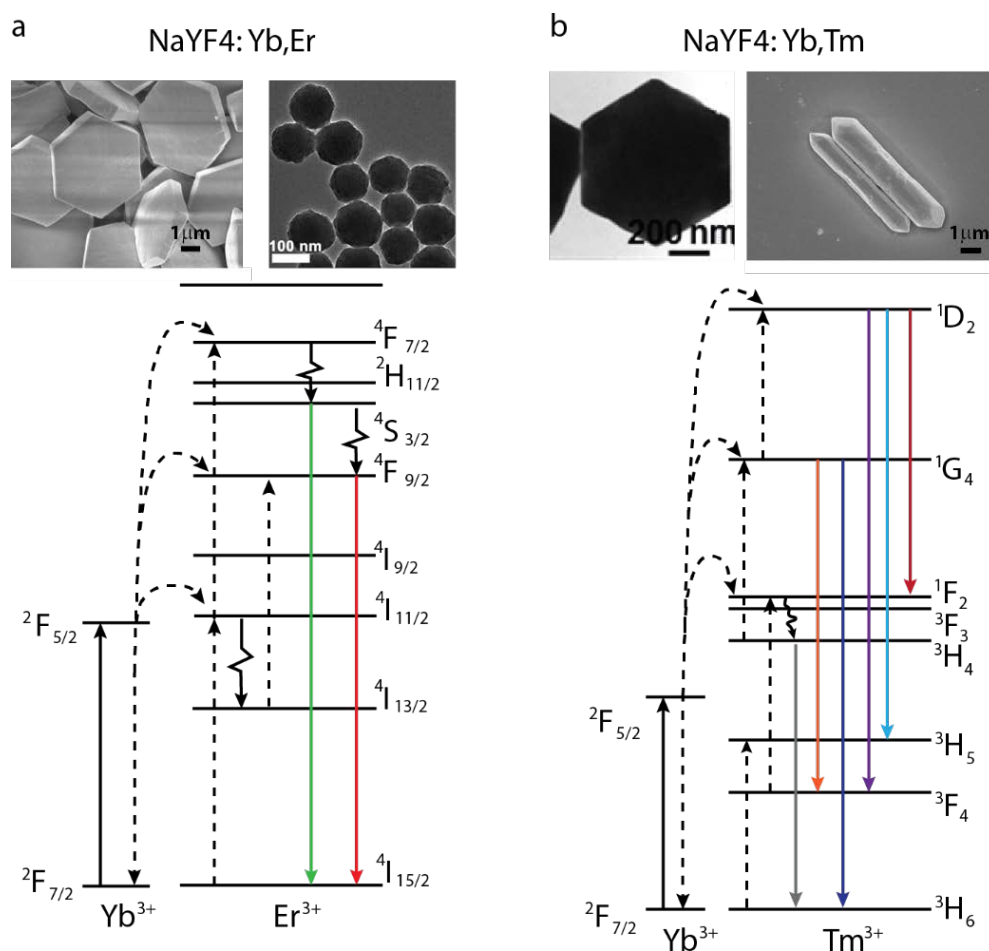


**Figure 1-6.** (a) The TEM and the SEM image of NaYF<sub>4</sub>:Yb/Er plate and nanocrystals, and the simplified energy-level scheme of NaYF<sub>4</sub>:Yb/Er nanocrystals indicating major energy levels. (b) The TEM and the SEM image of NaYF<sub>4</sub>:Yb/Tm nanocrystals and microrods, and the simplified energy-level scheme of NaYF<sub>4</sub>:Yb/Tm nanocrystals are also given indicating major energy levels. Reprinted from Ref. [4,75-79].

### 1.3.2 Transition metal-ligand complexes

Transition metal-ligand complexes (MLC) consist of a transition metal ion in the central position chelated by several ligands. They exhibit complex excited states, typically resulting from charge transfer between the molecular entities. With ions that possess d<sup>6</sup>, d<sup>8</sup> or sometimes d<sup>10</sup> electron configurations, including Ru(II), Os(II), Ir(III), Pd(II), Pt(II), Au(I), Cu(I) etc., MLC typically show strong spin-orbit coupling, allowing efficient intersystem crossing from singlet excited states to triplet states. A variety of MLC have been developed as photo-luminescent probes and sensors at room temperature.

In 1996, E.J. Hennink et al. used long-lived luminescent Pt-Porphine beads to evaluate time-resolved fluorescent microscopy [38]. In 2013, Buddha et al. reported that gold clusters in traditional fluorescence probes emit bright luminescence with short (up to 100 ns) and long lifetimes (up to 280  $\mu$ s), and good photo-stability [80]. Wang et al. synthesised three novel 3D Cd(II) coordination polymers and demonstrated luminescence with emission maxima in the deep blue, blue and green, respectively, with luminescent lifetime around 10  $\mu$ s [81]. Morris et al. studied the photo-physical properties of a Ruthenium (II) tris (2, 2'-bipyridine)-doped Zirconium UiO-67 metal-organic framework, with the emission decaying exponentially for low concentration Ruthenium (II) tris (5, 5'-dicarboxy-2, 2'-bipyridine) (Ru-DCBPY) (at doping concentration of 3 mmolar), but with non-exponential decay under high doping conditions [82].

Similar to lanthanides, MLC have also been utilized to generate upconversion luminescence based on triplet-triplet annihilation (TTA). TTA upconversion employs two triplet compounds with matching energy levels of their excited states as the sensitizer and emitter (also called annihilator). The excitation energy is harvested by the sensitizer, followed by triplet-triplet energy transfer (TTET) to the emitter. When two emitters in the triplet excited state collide with each other, one of them will pass on the energy to pump the other into a higher singlet excited level, which results in emission at shorter wavelength than the excitation light, as shown in [Figure 1-7](#). A variety of MLC, such as Ru(II), Pt(II), Pd(II) and Ir(III) complexes, have been demonstrated to be efficient triplet sensitizers, while anthracene, perylene, DPA (9,10-diphenylanthracene) and BODIPY (boron-dipyrromethene) have been the common triplet emitters.

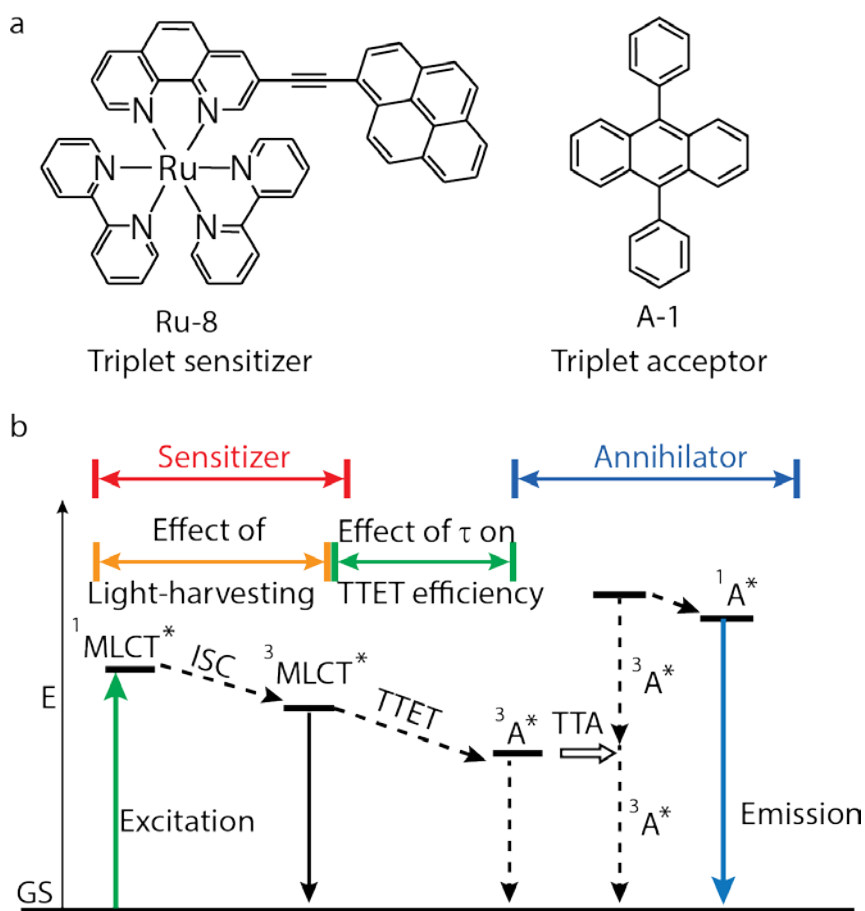


**FIGURE 1-7** (a) A triplet sensitizer  $[(\text{bpy})_2\text{Ru}(3\text{-pyrenyl-1,10-phenanthroline})]^{2+}(\text{PF}_6)_2$  (Ru-8) and the triplet sensitizer 9,10-diphenylanthracene (DPA, A-1) for triplet–triplet annihilation based upconversion is shown. (b) A qualitative Jablonski Diagram illustrating the sensitized TTA upconversion process between triplet sensitizer and acceptor (annihilator/emitter) is given. The effect of the light-harvesting ability and the excited state lifetime of the sensitizer on the efficiency of the TTA upconversion is also shown. E is energy. GS is ground state ( $S_0$ ).  $^3\text{MLCT}^*$  is the metal-to-ligand-charge-transfer triplet excited state. TTET is triplet–triplet energy transfer.  $^3\text{A}^*$  is the triplet excited state of annihilator. TTA is triplet–triplet annihilation.  $^1\text{A}^*$  is the singlet excited state of annihilator. The emission band observed for the sensitizers alone is the  $^3\text{MLCT}$  emissive excited state. The emission bands observed in the TTA experiment are the simultaneous  $^3\text{MLCT}^*$  emission (phosphorescence) and the  $^1\text{A}^*$  emission (fluorescence). Reprinted from Ref. [83,84].

### 1.3.3 Indirect bandgap semiconductor nanoparticles

Semiconductor materials can absorb light to generate electrons in the conduction band and holes in the valence bands, followed by radiative recombination to emit light. For indirect bandgap semiconductors, such as silicon, their minimum-energy state in the conduction band and the maximum-energy state in the valence band have different

wavevectors, so that extra phonons are required for momentum conservation in radiative recombination, as shown in Figure 1-8. This effectively means the luminescence in silicon is of low probability and thus has long lifetimes, on the order of milliseconds for pure silicon and tens of microseconds for nanoparticles.

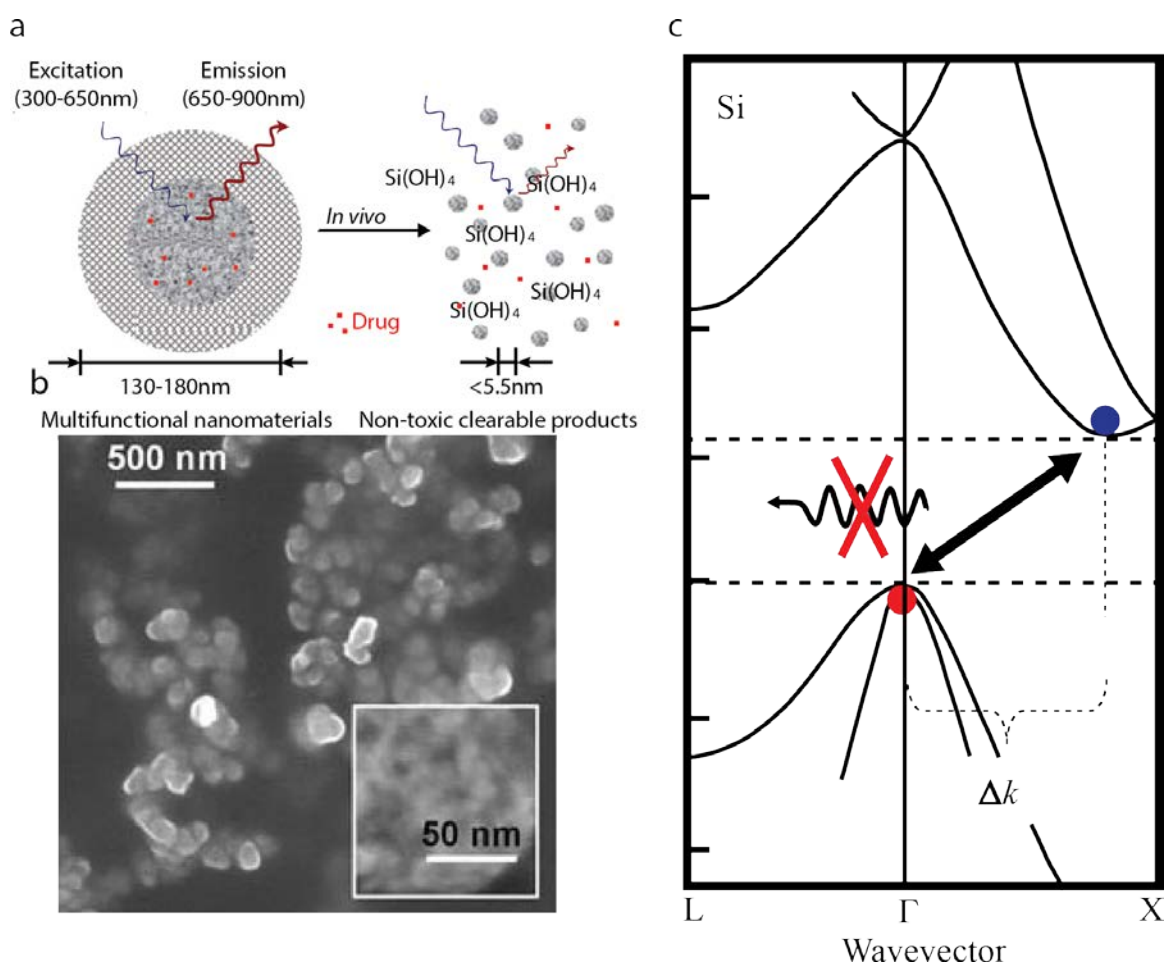


**FIGURE 1-8** (a) the Schematic diagram depicting the structure and *in vivo* degradation process for (biopolymer-coated) nanoparticles is given [85]. (b) the SEM image of luminescent porous silicon nanoparticles (LPSiNPs) (the inset shows the porous nanostructure of one of the nanoparticles) is illustrated [85]. (c) The energy-band diagram for silicon where the dispersion curves are along the [100] direction (X-point) and the [111] direction (L-point) is shown. Conduction electrons (blue circles) and valence holes (red circles) occupy the band's minima with  $\Delta k$  (momentum/ $\hbar$ ) being the wavevector's difference for silicon [23]. Photon emission is not allowed for silicon [23].

In 2013, Gu et al. first demonstrated time-gated imaging of porous silicon nanoparticles in a live mouse, which were spontaneously accumulated in a tumour xenograft following polyethylene glycol (PEG) coating and intravenous injection [86]. These nanoparticles have broad absorption band in the UV-blue region with peak around 370 nm, and emit broadly in

the red-NIR region with peak around 790 nm and lifetime 5-13  $\mu$ s. The quantum yield has also been reported as high as 10% [86]. Offering high biodegradability, low toxicity, large free volume and high flexibility for biofunctionalization, the porous silicon nanoparticles represent promising new luminescent probes for various multi-functional diagnostic and therapeutic applications [85-87].

### **1.3.4 Non-metal probes**

It is known that some pure organic compounds, such as tryptophan residues and benzophenone (BP) derivatives, are capable of long-lived luminescence when crystallized or embedded into solids. However, they generally become non-emissive when dissolved in solvents, due to nonradiative decays of their long-lived triplet excited states caused by intramolecular motions and intermolecular collisions at room temperature. To reactivate the emission, a novel strategy has emerged using a fluorescent dye as the acceptor, so that the energy is transferred from the triplet excited states of the luminophore to the singlet excited states of the dyes for efficient photon emission, as shown in [Figure 1-9](#). The emission lifetime of the dye thus follows that of the luminophore, presenting a new strategy to develop long-lifetime luminescent probes.

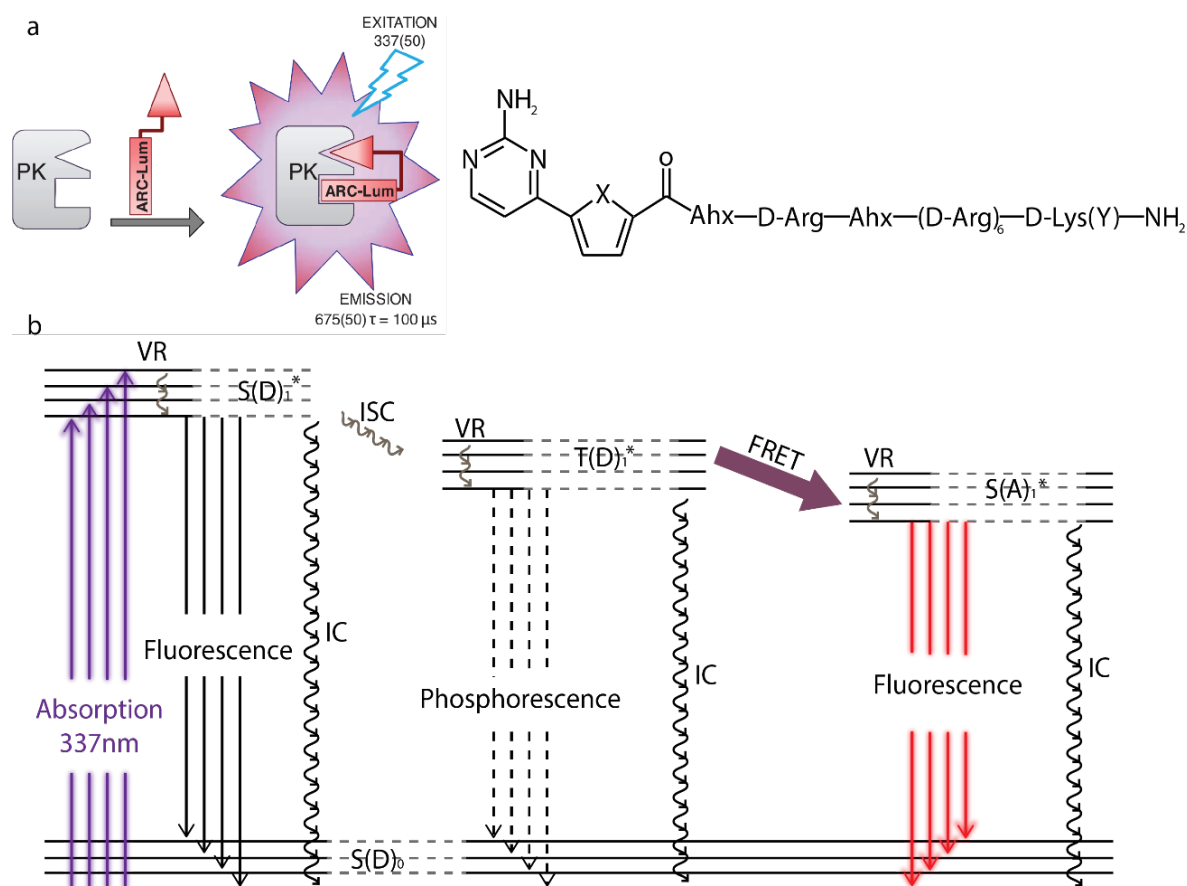


**FIGURE 1-9** (a) Structures and Arginine-rich peptide (ARC) codes of Arginine-rich peptide Luminescence (ARC-Lum) probes and Scheme of the protein-induced long lifetime luminescence is shown [17]. (b) The Jablonski diagram of long lifetime luminescence of labelled thiophene- and selenophene-containing ARC-Lum probes in the complex with protein kinases is given. The thiophene- or selenophene-containing fragment (donor, D) is flash-excited at 337 nm to singlet excited state  $S(D)_1^*$ , followed by intersystem crossing (ISC) to the triplet state of the fragment ( $T(D)_1^*$ ). Thereafter the energy is passed to the conjugated dye (acceptor, A) that is excited (singlet excited state of the conjugated dye,  $S(A)_1^*$ ), followed by the radiation at the emission wavelength of the acceptor dye that is measured. IC, internal conversion; VR vibrational relaxation. Reprinted from Ref. [17]. Theoretical explanations and mathematical equations of this type of optical transitions have been discussed by Engvall et al[88] and Lakowicz et al[89,90].

Several non-metal long-lifetime probes have been reported employing the energy transfer scheme. For example, Enkvist et al. developed protein-induced non-metal luminescent probes using arginine-rich peptides as the triplet donor, showing lifetimes from 19  $\mu\text{s}$  to 266  $\mu\text{s}$  associated with 675 nm emission under 300-360 nm UV excitation when attached to target protein kinases [17]. Recently, Xiong et al. reported a pure organic compound displaying long luminescent lifetime of 22.11  $\mu\text{s}$  in deaerated ethanol with quantum

efficiency around 84%, based on a similar scheme in which the energy gap between the singlet and triplet states was small enough to allow efficient reverse intersystem crossing from the triplet excited state back to the singlet excited state [91]. This effect is often called delayed fluorescence[92].

### 1.3.5 Choice of probes in the thesis

While all the probes above are compatible with time-gated luminescence detection, in this thesis work, we mainly employed lanthanide complexes and upconversion nanoparticles. The complexes behave similarly to conventional fluorescent dyes, which is convenient for biosensing and bioimaging applications to adopt. The nanoparticles provide brighter signal due to multiple emitters in a single unit. They are also more flexible in engineering the luminescence properties through different doping elements and concentrations. Although extra efforts are needed to achieve robust and reliable functionalization of lanthanide upconversion nanoparticles to reduce aggregation and non-specific binding issues, they are ready to be used directly in experiments studying cell uptake [93,94], *in vivo* injection [31,95,96] and as encoding substrates for suspension arrays [4,97,98].

## 1.4 Time-Gated Luminescence Instruments

Since the concept of time-gated luminescence detection was proposed in the 1970s to improve the detection sensitivity of immunoassays [34,35], early TGL instruments were mainly variants of fluorometers, with a number of commercial platforms eventually becoming available. TGL imaging was not possible until the 1990s, when digital camera technology had been significantly advanced. Since then, a range of techniques have been implemented to realise time-gated luminescence instruments, which in return has stimulated remarkable progress in luminescent material synthesis and applications.

### 1.4.1 Time-gating devices

The TGL method requires rapid switching for both the light source and the photo-detector, as well as precise time-synchronisation to ensure the excitation pulses and the detection windows are clearly separated. Depending on the actual components, some light sources (e.g. Light-emitting diodes, laser diode etc.) and detectors (e.g. Intensified Charge Coupled Device (ICCD), Single-photon avalanche diode etc.) can be modulated directly,

while others require external gating devices for switching. This leads to three major designs for TGL instruments as illustrated in Figure 1-10. And Table 1-2 illustrates the key challenges of different types of time-gated instruments.

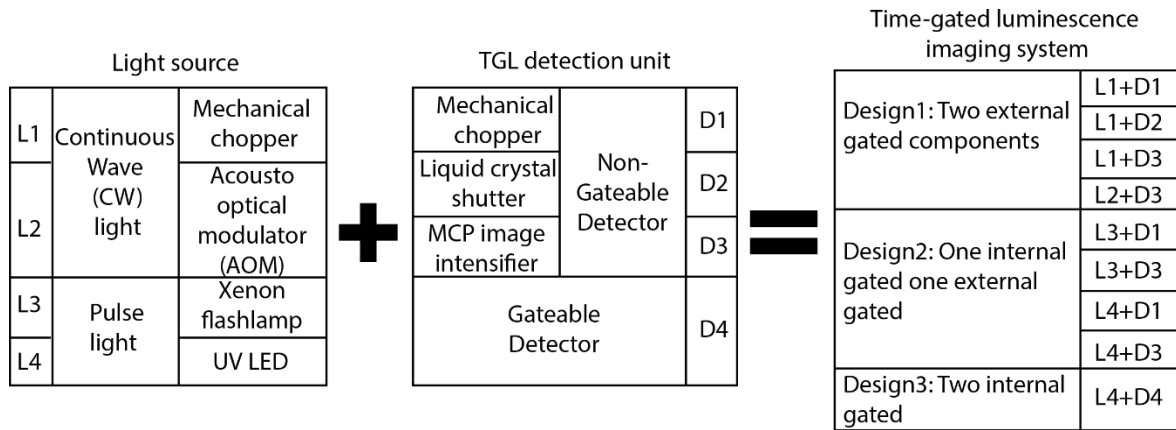


**Figure 1-10** the three major designs of Time-gated luminescent instruments

**Table 1-2** the key challenges of different types of TGL instrument

Design method		Challenges	Ref
Design 1: Two external gated components	L1+D1	(1) Difficult to accurately synchronise two mechanical choppers (2) Low frequency	[36,37]
	L1+D2	(1) Low switching efficiency (2) Low switching speed (3) Need Polarized light (4) Low contrast	[41,51,99,100]
	L1+D3	(1) High noise from the intensifier itself (2) Low quantum efficiency	[101]
	L2+D3	(3) High cost	[38,102]
Design 2: One internal gated one external gated	L3+D1	(1) Low repetition rate of xenon flash lamp (2) Variability in pulse to pulse energy (3) Limited lamp lifetime	[103-105]
	L3+D3	(4) Long tails of flash lamp (5) Low frequency of chopper (6) High noise from the intensifier itself (7) High cost of intensifier	[39,106,107]
	L4+D1	(1) Sophisticated assembly (2) Low compatibility	[3,108,109]
	L4+D3	(1) High noise from the intensifier itself (2) High cost of intensifier	[2,24,86,110]
Design 3: Two internal gated	L4+D4	(1) Cannot image (2) Only collect signal from one time-gated cycle	[40,111,112]

External gating devices have been widely employed, especially in the early development of TGL instruments when accessibility was limited for light sources and detectors capable of electronic gating. [Table 1-3](#) summarises the performance characteristics of typical gating devices used previously for time-gated luminescence detection. Among them, mechanical choppers offer highest flexibility, due to 100% switching efficiency with no restriction on the wavelength or polarisation of the light [3,108,109]. Liquid crystal shutters have been used to achieve more accurate control of synchronization and time delay [5,99,100], but were found not very efficient mainly because of incomplete shut off. Acousto-optical modulators (AOM) provide high switching speed and efficiency, yet requiring rigorous optical alignment that is difficult to implement for wide-field imaging. Image intensifiers, which are now available as an integrated part of ICCD cameras, provide excellent overall gating performance in conjunction with image sensors, yet at relatively high cost.

**Table 1-3** the performances of different types of optical chopper

	Mechanical chopper	Liquid crystal shutter (LCD)	MCP image intensifier	Acousto-optical modulator (AOM)
Switch ON/OFF time	23 $\mu$ s	>50 $\mu$ s	>1 $\mu$ s	>150 ns
Maximum Frequency	Up to 5 KHz	Up to 1 KHz	500 KHz	<40 MHz
Switching efficiency	100%	<90%	>99%	Depend on refractive index
Wavelength	All wave band	300 nm-1800 nm	180 nm-1100 nm	250 nm-1600 nm
Requirement for incident light	None	Polarized light	None	None
Gain	No	No	$10^6$	No
Dark noise	None	None	>200 cps/cm <sup>2</sup>	None
Cost	Around \$1000	Several hundreds	Several thousands	Several thousands

### 1.4.2 Time-gated luminescence microscopy

Early designs of time-gated luminescence microscopes are typically based on externally gated devices. In 1991, Marriott et al. employed two mechanical choppers to create pulsed excitation from an argon ion laser and time-gated imaging using a CCD camera [36] as shown in [Figure 1-11\(a\)](#). Although phase lock was implemented, it remains challenging to realise precise and stable synchronization between excitation and detection. This is because the fast-spinning blades of mechanical choppers vibrate, affecting the accurate positions of gating in different detection cycles. The fluctuation in delay time, therefore, reduced the efficiency in blocking the autofluorescence background. In 1992, an alternative development was reported by two groups independently using xenon flash lamps as the light source [104,105], as shown in [Figure 1-11\(b\)](#). The synchronisation pulses from the built-in sensor of the detection chopper were used to trigger the excitation pulses. This improved the accuracy of time delay; however, the xenon lamps available then were only capable of operating at 50~70 Hz, trading off the excitation efficiency. In 1994, Verwoerd et al. used a ferro-electric liquid crystal shutter to replace the chopper in the detection path [41], as shown in [Figure 1-11\(c\)](#). Synchronization signals were sent from the excitation chopper to the shutter for time delay. But the switching speed of the ferro-electric liquid crystal shutter was

relatively slow (typically takes longer than 60  $\mu\text{s}$  to switch off up to 90%), resulting in incomplete rejection of the autofluorescence background.

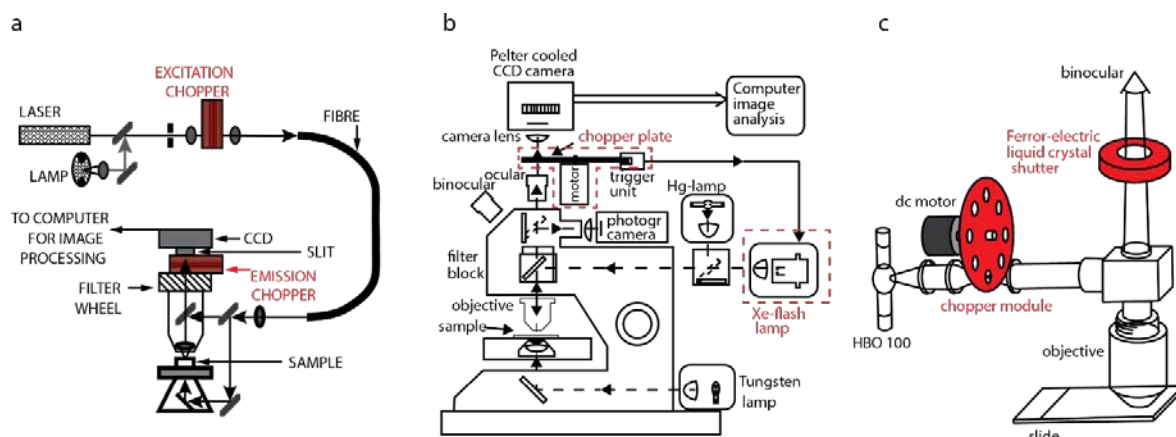


**Figure 1-11** The schematic of three types of TGL microscope is shown: (a) Time-gated microscope based on two mechanical choppers, (b) Time-gated microscope using xenon flash lamp and mechanical chopper, and (c) Time-gated microscope based on one ferro-electric liquid crystal shutter to replace the chopper in the detection path. Reprinted from Ref. [36,41,105]

The second generation design for time-gated luminescence microscope employs image intensifiers consisting of micro-channel plates (MCP) and phosphor screens. As illustrated in [Figure 1-12\(a\)](#), the MCP is equivalently a compact grid of microscopic photomultiplier tubes, which convert the photons arriving at the photocathodes to generate electrons pulses for each channel of MCP. The phosphor screen then converts the electrons back to an optical image. Capable of time gating electronically at high speed in nanosecond range, MCP image intensifiers were implemented by a few groups to realise time-gated luminescence imaging. In 1996, Hennink et al. demonstrated a time-gated microscope using an acousto-optical modular (AOM) in the excitation path and a MCP image intensifier to gate the detection path for imaging of Pt-porphine [38]. In 1998, Vereb et al. reported a similar design with additional applications with lanthanide chelates [101]. Due to high flexibility in time-gating and high gain for low light sensing, the use of MCP image intensifiers became widely adopted in 2000s for a range of analytical chemistry and microbiology applications, especially as companies started to provide intensifier CCD (ICCD) cameras that integrate MCP image intensifiers with CCD sensors [24,39,86,106]. The major challenges with ICCD, however, are their limited pixel numbers (typically 256x256, way below high-definition digital cameras), noticeable electronic noise level, and high cost[113].

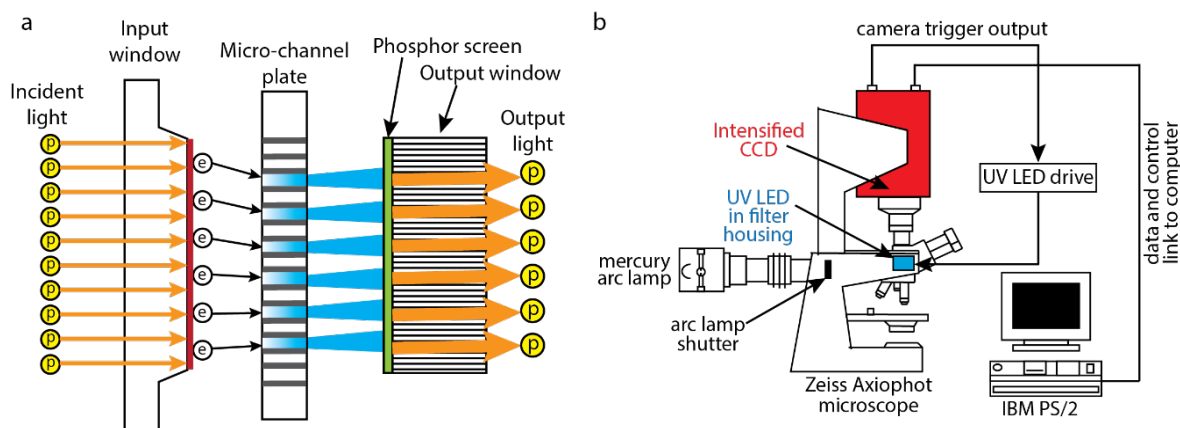


**Figure 1-12** (a) A schematic of image intensifiers consisting of micro-channel plates (MCP) and phosphor screens. (b) The layout of the time-gated fluorescence microscope based on intensified CCD and high power UV LED. Reprinted from Ref. [110]

The recent development of high-power, solid-state light emitting diodes (LEDs) have greatly promoted the development of time-gated luminescence detection techniques, because these light sources can be easily switched by the power supply current. The first generation time-gated luminescence microscopy using a high power (100mW) UV LED and image-intensified CCD camera is developed by Connally, Jin and Piper in 2006 for the detection of immunofluorescently labelled *Giardia cysts* [110], as shown in Figure 1-12(b). After that, in 2011, Jin and Piper demonstrated a simple low-cost modification of time-gated luminescence microscope approach using UV LED as excitation source and a mechanical chopper behind the microscopy eyepiece to allow time-gated detection of target pathogenic microorganisms among spectrally contaminated samples (juice or water concentrate) by naked eye [3], as shown in Figure 1-13(a). This work achieved real-time and high-contrast true colour imaging of pathogenic microorganisms, with an 18-fold improvement of signal-to-noise ratio compared to the conventional fluorescence mode. But this prototype requires customized mechanical parts to be mounted upon an upright microscope to hold the chopper, which is difficult to precisely align the optics and causes vibration during operation, consequently affecting the imaging quality and contrast. Besides, as the spectra of UV LEDs are relatively narrow, the light source needs to be switched for efficient excitation of a single colour probe, either europium complex probes in red [3] or terbium complex probe in green [108]. In parallel, a new compact design of gated autosynchronous luminescence detection (GALD) was realized using a rotor of mirrors placed at  $45^\circ$  to the rotation axis. As shown in Figure 1-13(b), the rotor serves as a chopper for both the excitation and emission beams in

anti-phase as well as the function of dichroic mirror to separate the beams. Time-gated luminescence images with signal-to-noise ratio of 114:1 were captured using 100 ms exposure time. The GALD represents a novel design in concept; however, since all the components are pre-selected and fixed, little flexibility is left in changing the excitation wavelength and the time sequences to suit luminescent probes with different spectra and lifetimes.

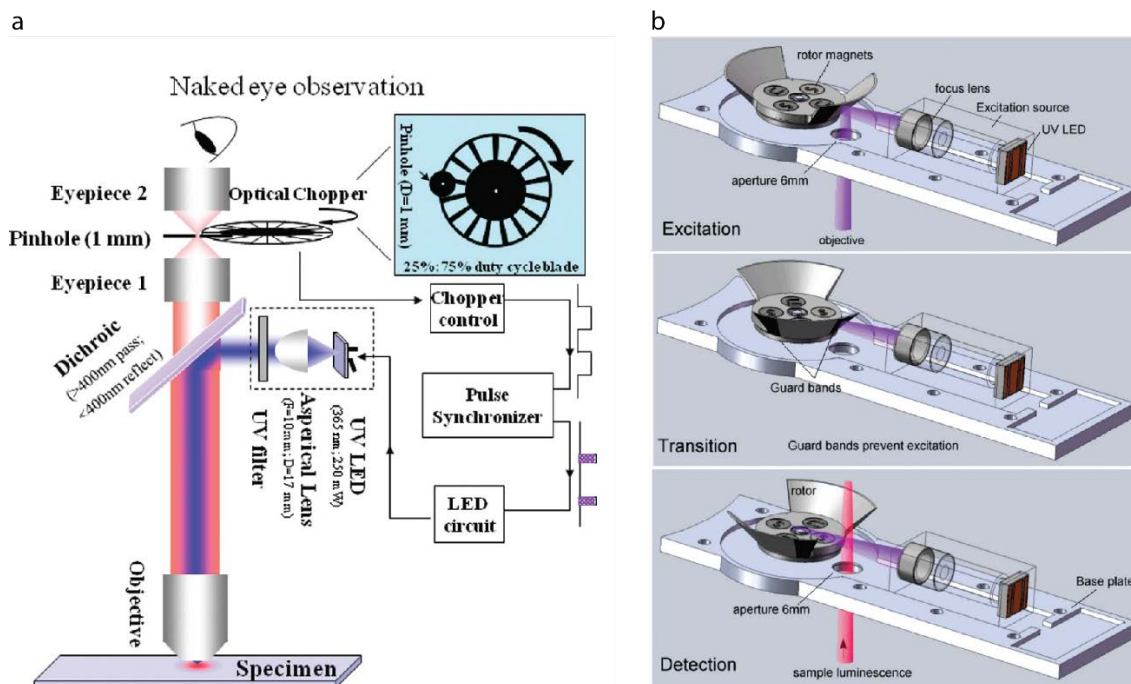


**Figure 1-13** (a) The schematic layout of the time-gate luminescence microscope using UV LED as excitation source and a mechanical chopper behind the microscopy eyepiece. (b) The component parts of the GALD are illustrated here, with the exception of the electromagnetic drive coils that sit above the rotor in the upper housing and which are hidden for the sake of clarity. Reprinted from Ref. [3,114].

The research project which is the subject of this thesis has aimed at overcoming the problem of current technology through comprehensive development of a low-cost multi-colour time-gated luminescence detection unit engineered for commercial inverted microscopes. Availability of practical time-gated fluorescence (luminescence) microscopes is expected to stimulate broad adoption of time-gated luminescence microscopy by biological and pathology labs and other end-users.

### 1.4.3 TGL animal imaging

While major efforts have been made on TGL microscopy, opportunities lie in extending the TGL method to the area of small animal imaging, which suffers not only from tissue autofluorescence but also strong scattering of the excitation light. In 2013, Gu et al. reported the first *in vivo* TGL imaging setup modified from a commercial animal imaging system [86]. This employs a 470 nm pulsed laser with 40 MHz repetition rate and an ICCD camera. Observation of porous silicon nanoparticles was realized with improved signal-to-background ratio by >20-fold *in vivo* comparing with steady-state imaging. The imaging contrast was further improved to >100-fold by the same group in 2015 when they changed the light source to a 365-nm UV LED with optimized time sequence [24], as shown in [Figure 1-14](#).

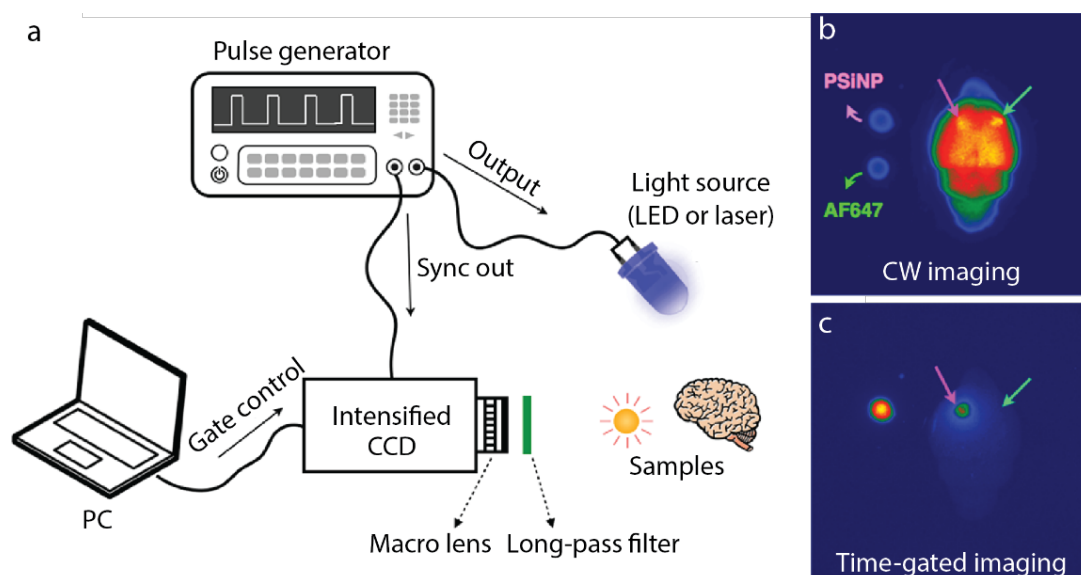


**Figure 1-14.** TGL techniques are applied in animal imaging. (a) is the schematic of TGL animal imaging system. (b) and (c) are non-time-gated and time-gated image of the mice brain. Reprinted from Ref. [24].

The key challenge, however, has been the lack of luminescent probes observable under deep tissue. Because biological tissues have strong absorption and scattering of the UV and visible light, the ideal probes should be capable of excitation and emission in the infrared region to allow deep optical penetration through the tissue environment. This critical requirement excludes most of the available luminescent probes. In fact, for porous silicon nanoparticles, UV excitation is still required, which does not allow deep penetration so that the luminescence signal was quite low.

Over the last ten years, there are major developments in design and synthesis of a new generation of photon upconversion nanocrystals as robust and multifunctional luminescent probes for deep tissue optical imaging. The Yb-Tm codoped NaYF<sub>4</sub> nanocrystals, for example, absorb at 980 nm and emit strongly at 800 nm, both are near-infrared wavelengths with penetration depth ~3 cm into biological tissues. Nevertheless, as high-power lasers are typically used as the excitation source, substantial scattering from skin and fur is often encountered and cannot be sufficiently suppressed using spectral filtering, resulting in significant background that lowers the imaging contrast and blurs the targeted area.

To overcome this challenge, I have undertaken development of a time-gated luminescence imaging system capable of excitation and detection in the near infrared wavelengths, which will take advantage of the long lived emission of upconversion nanocrystals for high-contrast, *in vivo* imaging under deep tissue.

#### **1.4.4 TGL instruments for high sample throughput**

Thanks to the high signal-to-background ratios that TGL detection offers, opportunity arises for automating the detection process at high speed and accuracy. The early TGL fluorimeters were later equipped with motorised stage to form automated plate readers, so that TGL assays can be carried out automatically on multi-microwell plates. Several platforms became commercially available, including DELFIA (Dissociation Enhanced Lanthanide Fluoroimmunoassay) [115], CyberFluor (or FIAgen) [116], Enzyme-Amplified Time-Resolved Fluorometric system [117], and TRACE (Time-Resolved Amplified Cryptate Emission) system [118].

To further improve the analytical throughput at the single cell level, time-gated luminescence detection has been combined with flow cytometry, which is extensively used for biological and biomedical applications. The rapid movement of the cells allows time gating to be realised through spatial arrangement of the excitation area and the detection area. In 1994, Condrau et al. reported a first TGL flow cytometer employing a HeCd laser and a single photon counting photomultiplier tube (PMT) detector [119,120]. In 2007, Jin et al. reported a TGL flow cytometry using a pulsed UV LED as excitation and a gated PMT as detection for rare-event applications [32,121].

For solid-phase samples that are difficult to analyse by flow cytometry, a TGL scanning microscope has been developed in 2011 [109], which employed a single-element detector instead of a camera to monitor the TGL signal in the entire detection field-of-view (FOV) scanned over the sample in a grid pattern. This dramatically reduces the requirements for data storage, scene segmentation and analytical time compared to conventional image analysis. However, the scanning speed was too low and the resulting scan times for a standard sample too long to meet the requirements for quantitative assays. To further improve the throughput, the orthogonal scanning automated microscopy (OSAM) technique was demonstrated in 2012 [111], employing continuous scanning rather than steps of defined intervals. As illustrated in [Figure 1-15](#), a sample slide is first examined in a serpentine pattern, with continuous movement along X axis. When one target is scanned over the field-of-view (FOV), a train of time-gated luminescence signal is detected, from which the position of the target on the sample can be obtained with a precise X coordinate and a rough Y coordinate. All detected targets are then scanned sequentially at respective X coordinates along Y-axis to obtain precise Y coordinates. This allows a  $15 \times 15 \text{ mm}^2$  slide area to be scanned in about 3 minutes with extremely low level of background. Detection of rare-event *Giardia cysts* labelled by europium complex and cancer cells expressing low-level of surface antigens was successfully demonstrated using the OSAM [111].

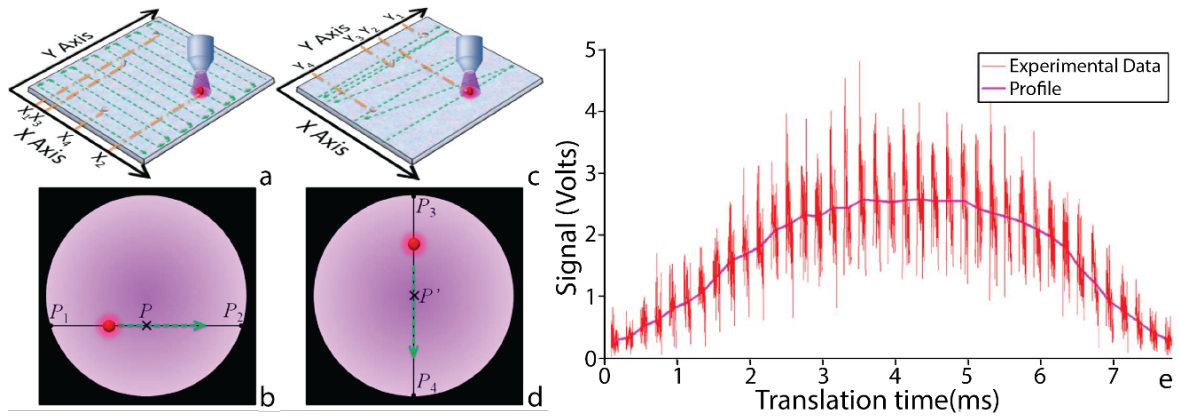


**Figure 1-15.** A schematic diagram showing the two-step orthogonal scanning method to discover and localise targets of interest. (a) The sample is first examined in a serpentine pattern, with continuous movement along X axis to obtain precise X coordinates and rough Y coordinates for each target. (b) the one target moves into the field of view (FOV), on-the-fly TGL scanning gives the X coordinates of P1 and P2, so that the precise X coordinate of the particles at (P) is obtained; (c) the targets are then scanned sequentially at precision X coordinates along Y-axis to obtain precise Y coordinates. (d) The precise X coordinate obtained in the first step scanning ensures that each target translates in the exact middle of the FOV. Since on-the-fly TGL scanning provides the Y coordinates of P3 and P4, the precise Y coordinate of the particle (at P') is determined. (e) shows a real signal when the TGL cycle duration is 0.2ms, along with its profile of average intensity. Reprinted from Ref. [111].

The key to accurate quantification is that every individual target is measured under identical illumination and detection conditions, which can be achieved if the measurements occur at the same position inside the FOV, ideally at the centre. However, we found that the first generation OSAM can only offer positional accuracy around 30  $\mu\text{m}$  along X-axis and Y-axis, with targets sometimes located at the periphery of the field-of-view, as shown in [Figure 1-16](#). This has been caused by electronic jitter and mechanical lag of the scanning stage, as well as the optical defocusing of the often tilted slide. As cells and microorganisms are typically of 5~20  $\mu\text{m}$  in size, the large variance in space when individual targets are measured leads to inaccuracy in the quantification.

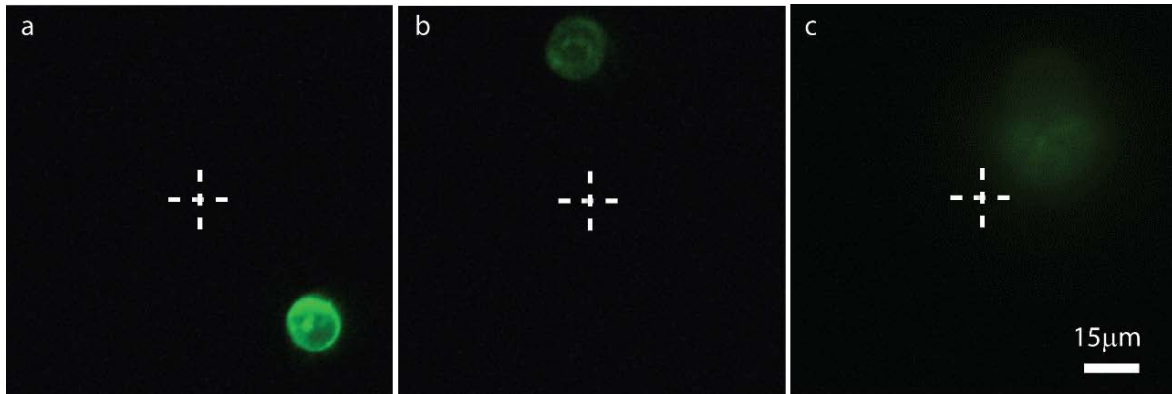


**Figure 1-16.** The location of the upconversion nanoparticle-impregnated microspheres obtained by OSAM. Most time, the targets are located at the centre of the field-of-view with positional accuracy around  $30\mu\text{m}$  along X-axis and Y-axis.

In a major development of TG OSAM, I have used linear encoders to give positional reference, and an autofocus unit for compensation of sample tilt, to achieve accurate positioning of every target in 3 dimensions during high-speed scanning. With the improved engineering, individual targets can be located precisely at high throughput to ensure their luminescence intensities are quantified with little variation in excitation and detection efficiencies.

## 1.5 Thesis Outline

Motivated by the above identified opportunities, my PhD program has been aligned to establishment of a new generation of TGL luminescence detection instruments for automated, high speed, sensitive, quantitative and multiplexing bio-detection. [Table 1-4](#) summarizes the challenges and proposed solutions to realize three types of time-gated luminescence instruments as the core of my thesis. The key result chapters of this thesis are presented in the format of four published journal papers, describing the key experimental results and prototype devices as a result of my PhD candidature.

**Table 1-4** the challenges and proposed solutions of time-gated luminescence microscope, small animal imaging system and scanning microscopy system

TGL instrument	Challenges	Solutions	Expected outcomes
TGL microscope	1) only single-colour image at a time 2) compatibility limited by gating schemes 3) costly components and sophisticated assembly	1) high frequency, high power ceramic xenon flash lamp as excitation source 2) modularise excitation unit and time-gated detection unit	Multi-Colour Time-Gated Luminescence Microscope ref. [122] described in chapter 2.
TGL animal imaging system	1) limited by the fluorescence probe 2) cannot achieve whole body imaging by time-gated techniques 3) restricted by the penetration of the excitation source	1) use upconversion nanocrystals emit NIR emission 2) redesign optical system 3) use NIR diode laser to increase penetration depth	TGL <i>in-vivo</i> animal imaging system ref. [123] described in chapter 3.
TGL scanning microscope	1) limitation of the location precision	1) integrate X- and Y-axis linear encoders, and autofocus unit	referenced-OSAM ref. [124] described in chapter 4

**Chapter 2** reports successful construction and applications of a low-cost multi-colour time-gated luminescent microscope. This chapter combines the key results from two co-authored papers with my role in leading the design and engineering of the microscope as well as participating characterization and data analysis. The first work, published in

*Scientific Reports* in 2014, reports a stand-alone excitation unit using high-power flash lamp that can be externally triggered at high repetition rate (up to 1 kHz) to simultaneously excite multiple fluorescence probes from its broad-band excitation. To make a better adoption of the time-gated luminescence technique, we also demonstrated a modularised time-gated detection unit to be inserted between any commercial microscope and the camera to perform time-gated luminescence detection. We demonstrated that simultaneous multi-colour background free imaging of two kinds of microorganisms using the parallel labelling by a europium complex in red and terbium complex in green. We further showed a high detection sensitivity by imaging single europium-doped nanocrystals. The second work, published in *Scientific Reports* in 2015, extends the multi-colour time-gated luminescence microscope for *in-vivo* animal imaging of *Daphnia magna*. My purpose is to design and build a microscope for my international collaborators to demonstrate the background-free *in-vivo* Imaging of Vitamin C based on a new responsive time-gateable probe. Both projects reported in Chapter 2 overcome the previous impediments of high cost, low throughput, and poor compatibility to commercial systems, opening the past to practical time-gated luminescence microscopes to the end-users and applications.

**Chapter 3** further demonstrates our successful adoption of time-gated luminescence detection for *in-vivo* animal imaging of upconversion nanoparticles as the novel optical contrast agents in mice. This chapter is in the format of a first-authored paper published in the journal of *Analytical Chemistry* in 2016. In this work, I engineered a time-gated unit inside the animal imaging house and an illumination unit by a near infrared excitation laser diode to produce pulsed excitation. Optical imaging through the near-infrared window provides deep penetration of light up to several centimetres into biological tissues. Capable of emitting 800 nm luminescence under 980 nm illumination, the recently developed upconversion nanoparticles may become a promising optical contrast agent for *in vivo* bio-imaging. However, there remains significant amount of scattering and autofluorescence backgrounds from the skin and tissues. I demonstrated that the time-gated imaging approach delivers high contrast to detect upconversion nanoparticles free of autofluorescence and scatterings. The system also helps to reduce the thermal accumulation from the excitation source, which alleviates a critical issue associated with the high power excitation that results in thermal damage to the tissue in small animals. We also showed the time-gating unit is compatible with any camera.

**Chapter 4** further extends the time-gated luminescence detection for high speed scanning and automated microscopy imaging system. This chapter is also in the format of another first-authored paper published in *Analytical Chemistry* in 2016. In this work, I engineered two virtual grids set by a pair of encoders along x-axis and y-axis respectively and an autofocus unit for z-axis. The encoder-assisted scanning microscopy allows high-speed quantitative analysis. Compared with routine microscopy imaging of a few analytes at a time, rapid scanning through the whole sample area of a microscope slide to locate every single target object offers many advantages in terms of simplicity, speed, throughput, and potential for robust quantitative analysis. We demonstrate that our new system is capable of target pinpointing in three dimensions during rapid scanning over a whole microscopic slide, enabling accurate quantification of the luminescence intensities, ratios and lifetimes of each individual targets. This work addresses the key challenge in rapid scanning and high-precision pinpointing of luminescent targets allowing high-speed quantitative analysis. This robust system also supports quantitative measurement of lifetime values and luminescence intensities for high-throughput analysis. Moreover, we demonstrated the upconversion nanoparticles as background-free reporter probes suitable for quantitative biomolecular assays based on the suspension arrays, opening new opportunities in high-throughput multiplexed screening for analytical chemistry, micro- and molecular biology, pharmaceutical discoveries, and clinical diagnostics.

**Chapter 5** summarises the key research outcomes of this thesis, and discusses the future prospects of our time-gated detection technology for developing advanced optical systems for both materials characterizations and bio-applications of the long-lifetime luminescence materials.

## 1. 6 Reference

- [1] Soini, E., Lövgren, T. & Reimer, C. B. Time-resolved fluorescence of lanthanide probes and applications in biotechnology. *CRC Critical Reviews in Analytical Chemistry* **18**, 105-154 (1987).
- [2] Gahlaut, N. & Miller, L. W. Time - resolved microscopy for imaging lanthanide luminescence in living cells. *Cytometry Part A* **77**, 1113-1125 (2010).
- [3] Jin, D. & Piper, J. A. Time-gated luminescence microscopy allowing direct visual inspection of lanthanide-stained microorganisms in background-free condition. *Analytical Chemistry* **83**, 2294-2300 (2011).
- [4] Lu, Y., Zhao, J., Zhang, R., Liu, Y., Liu, D., Goldys, E. M., Yang, X., Xi, P., Sunna, A. & Lu, J. Tunable lifetime multiplexing using luminescent nanocrystals. *Nature Photonics* **8**, 32-36 (2014).
- [5] Connally, R. E. & Piper, J. A. Time - Gated Luminescence Microscopy. *Annals of the New York Academy of Sciences* **1130**, 106-116 (2008).
- [6] D'Hallewin, M.-A., Bezdetnaya, L. & Guillemin, F. Fluorescence detection of bladder cancer: a review. *European Urology* **42**, 417-425 (2002).
- [7] Weiss, S. Fluorescence spectroscopy of single biomolecules. *Science* **283**, 1676-1683 (1999).
- [8] Goldys, E. M. *Fluorescence applications in biotechnology and life sciences*. (John Wiley & Sons, 2009).
- [9] Rigler, R. Fluorescence correlations, single molecule detection and large number screening applications in biotechnology. *Journal of Biotechnology* **41**, 177-186 (1995).
- [10] Xu, Y.-Y. & Hemmilä, I. A. Co-fluorescence enhancement system based on pivaloyltrifluoroacetone and yttrium for the simultaneous detection of europium, terbium, samarium and dysprosium. *Analytica Chimica Acta* **256**, 9-16 (1992).
- [11] Xu, Y.-Y., Hemmilä, I., Mikkala, V.-M., Holttinen, S. & Lövgren, T. Co-fluorescence of europium and samarium in time-resolved fluorimetric immunoassays. *Analyst* **116**, 1155-1158 (1991).
- [12] Guo, X.-Q., Castellano, F. N., Li, L. & Lakowicz, J. R. Use of a long-lifetime Re (I) complex in fluorescence polarization immunoassays of high-molecular-weight analytes. *Analytical Chemistry* **70**, 632-637 (1998).

- [13] Yuan, J., Matsumoto, K. & Kimura, H. A new tetradentate  $\beta$ -diketonate-europium chelate that can be covalently bound to proteins for time-resolved fluoroimmunoassay. *Analytical Chemistry* **70**, 596-601 (1998).
- [14] Yuan, J., Wang, G., Majima, K. & Matsumoto, K. Synthesis of a terbium fluorescent chelate and its application to time-resolved fluoroimmunoassay. *Analytical Chemistry* **73**, 1869-1876 (2001).
- [15] Zhang, L., Wang, Y., Ye, Z., Jin, D. & Yuan, J. New class of tetradentate  $\beta$ -diketonate-europium complexes that can be covalently bound to proteins for time-gated fluorometric application. *Bioconjugate Chemistry* **23**, 1244-1251 (2012).
- [16] Sayyadi, N., Connally, R. E. & Try, A. A novel biocompatible europium ligand for sensitive time-gated immunodetection. *Chemical Communications* **52**, 1154-1157 (2016).
- [17] Enkvist, E., Vaasa, A., Kasari, M., Kriisa, M., Ivan, T., Ligi, K., Raidaru, G. & Uri, A. Protein-induced long lifetime luminescence of nonmetal probes. *ACS Chemical Biology* **6**, 1052-1062 (2011).
- [18] Pu, C., Ma, J., Qin, H., Yan, M., Fu, T., Niu, Y., Yang, X., Huang, Y., Zhao, F. & Peng, X. Doped Semiconductor-Nanocrystal Emitters with Optimal Photoluminescence Decay Dynamics in Microsecond to Millisecond Range: Synthesis and Applications. *ACS Central Science* (2015).
- [19] Nirmal, M., Murray, C. & Bawendi, M. Fluorescence-line narrowing in CdSe quantum dots: Surface localization of the photogenerated exciton. *Physical Review B* **50**, 2293 (1994).
- [20] Huang, D., Niu, C., Ruan, M., Wang, X., Zeng, G. & Deng, C. Highly sensitive strategy for Hg<sup>2+</sup> detection in environmental water samples using long lifetime fluorescence quantum dots and gold nanoparticles. *Environmental Science & Technology* **47**, 4392-4398 (2013).
- [21] Chhabra, R., Sharma, J., Wang, H., Zou, S., Lin, S., Yan, H., Lindsay, S. & Liu, Y. Distance-dependent interactions between gold nanoparticles and fluorescent molecules with DNA as tunable spacers. *Nanotechnology* **20**, 485201 (2009).
- [22] Wu, Z. & Jin, R. On the ligand's role in the fluorescence of gold nanoclusters. *Nano Letters* **10**, 2568-2573 (2010).
- [23] Saar, A. Photoluminescence from silicon nanostructures: the mutual role of quantum confinement and surface chemistry. *Journal of Nanophotonics* **3**, 032501-032501-032542 (2009).

- [24] Joo, J., Liu, X., Kotamraju, V. R., Ruoslahti, E., Nam, Y. & Sailor, M. J. Gated Luminescence Imaging of Silicon Nanoparticles. *ACS Nano* **9**, 6233-6241 (2015).
- [25] Ow, H., Larson, D. R., Srivastava, M., Baird, B. A., Webb, W. W. & Wiesner, U. Bright and stable core-shell fluorescent silica nanoparticles. *Nano Letters* **5**, 113-117 (2005).
- [26] Sun, W., Yu, J., Deng, R., Rong, Y., Fujimoto, B., Wu, C., Zhang, H. & Chiu, D. T. Semiconducting Polymer Dots Doped with Europium Complexes Showing Ultranarrow Emission and Long Luminescence Lifetime for Time - Gated Cellular Imaging. *Angewandte Chemie International Edition* **52**, 11294-11297 (2013).
- [27] Zhao, J., Lu, Z., Yin, Y., McRae, C., Piper, J. A., Dawes, J. M., Jin, D. & Goldys, E. M. Upconversion luminescence with tunable lifetime in NaYF<sub>4</sub>: Yb, Er nanocrystals: role of nanocrystal size. *Nanoscale* **5**, 944-952 (2013).
- [28] Bünzli, J.-C. G. Lanthanide luminescence for biomedical analyses and imaging. *Chemical Reviews* **110**, 2729-2755 (2010).
- [29] Wang, F., Banerjee, D., Liu, Y., Chen, X. & Liu, X. Upconversion nanoparticles in biological labeling, imaging, and therapy. *Analyst* **135**, 1839-1854 (2010).
- [30] Zhou, J., Sun, Y., Du, X., Xiong, L., Hu, H. & Li, F. Dual-modality in vivo imaging using rare-earth nanocrystals with near-infrared to near-infrared (NIR-to-NIR) upconversion luminescence and magnetic resonance properties. *Biomaterials* **31**, 3287-3295 (2010).
- [31] Liu, Q., Feng, W., Yang, T., Yi, T. & Li, F. Upconversion luminescence imaging of cells and small animals. *Nature Protocols* **8**, 2033-2044 (2013).
- [32] Jin, D., Connally, R. & Piper, J. Practical time - gated luminescence flow cytometry. II: Experimental evaluation using UV LED excitation. *Cytometry Part A* **71**, 797-808 (2007).
- [33] Aubin, J. Autofluorescence of viable cultured mammalian cells. *Journal of Histochemistry & Cytochemistry* **27**, 36-43 (1979).
- [34] Leif, R., Clay, S., Gratzner, H., Haines, H. & Vallarino, L. in *Tutorials of Cytology* 313 (1976).
- [35] Soini, E. & Hemmilä, I. Fluoroimmunoassay: present status and key problems. *Clinical Chemistry* **25**, 353-361 (1979).
- [36] Marriott, G., Clegg, R. M., Arndt-Jovin, D. J. & Jovin, T. M. Time resolved imaging microscopy. Phosphorescence and delayed fluorescence imaging. *Biophysical Journal* **60**, 1374 (1991).

- [37] Marriott, G., Heidecker, M., Diamandis, E. P. & Yan-Marriott, Y. Time-resolved delayed luminescence image microscopy using an europium ion chelate complex. *Biophysical Journal* **67**, 957-965 (1994).
- [38] Hennink, E., De Haas, R., Verwoerd, N. & Tanke, H. Evaluation of a time-resolved fluorescence microscope using a phosphorescent Pt-porphine model system. *Cytometry* **24**, 312-320 (1996).
- [39] Connally, R., Veal, D. & Piper, J. Flash lamp-excited time-resolved fluorescence microscope suppresses autofluorescence in water concentrates to deliver an 11-fold increase in signal-to-noise ratio. *Journal of Biomedical Optics* **9**, 725-734 (2004).
- [40] Connally, R. & Piper, J. Solid-state time-gated luminescence microscope with ultraviolet light-emitting diode excitation and electron-multiplying charge-coupled device detection. *Journal of Biomedical Optics* **13**, 034022-034022-034026 (2008).
- [41] Verwoerd, N., Hennink, E., Bonnet, J., Van der Geest, C. & Tanke, H. Use of ferro - electric liquid crystal shutters for time - resolved fluorescence microscopy. *Cytometry* **16**, 113-117 (1994).
- [42] Salinas-Castillo, A., Calahorra, A., Choquesillo-Lazarte, D., Seco, J. M. & Rodríguez-Diéguez, A. A new 2D cadmium chloride network with 2-aminopyrimidine displaying long lifetime photoluminescence emission. *Polyhedron* **30**, 1295-1298 (2011).
- [43] Ahern, J. C., Shilabin, A., Henline, K. M., Pike, R. D. & Patterson, H. H. Photophysical properties of {[Ag (CN) 2]-} 2 complexes trapped in a supramolecular electron-acceptor organic framework. *Dalton Transactions* **43**, 12044-12049 (2014).
- [44] Hung, F. F., To, W. P., Zhang, J. J., Ma, C., Wong, W. Y. & Che, C. M. Water - Soluble Luminescent Cyclometalated Gold (III) Complexes with cis - Chelating Bis (N - Heterocyclic Carbene) Ligands: Synthesis and Photophysical Properties. *Chemistry–A European Journal* **20**, 8604-8614 (2014).
- [45] Lu, Y., Lu, J., Zhao, J., Cusido, J., Raymo, F. M., Yuan, J., Yang, S., Leif, R. C., Huo, Y. & Piper, J. A. On-the-fly decoding luminescence lifetimes in the microsecond region for lanthanide-encoded suspension arrays. *Nature Communications* **5** (2014).
- [46] Liu, H., Xu, C. T., Lindgren, D., Xie, H., Thomas, D., Gundlach, C. & Andersson-Engels, S. Balancing power density based quantum yield characterization of upconverting nanoparticles for arbitrary excitation intensities. *Nanoscale* **5**, 4770-4775 (2013).

- [47] Boyer, J.-C. & Van Veggel, F. C. Absolute quantum yield measurements of colloidal NaYF<sub>4</sub>: Er<sup>3+</sup>, Yb<sup>3+</sup> upconverting nanoparticles. *Nanoscale* **2**, 1417-1419 (2010).
- [48] Tan, M., Wang, G., Hai, X., Ye, Z. & Yuan, J. Development of functionalized fluorescent europium nanoparticles for biolabeling and time-resolved fluorometric applications. *Journal of Materials Chemistry* **14**, 2896-2901 (2004).
- [49] Lo, K. K.-W., Ng, D. C.-M. & Chung, C.-K. First examples of luminescent cyclometalated iridium (III) complexes as labeling reagents for biological substrates. *Organometallics* **20**, 4999-5001 (2001).
- [50] Lo, K. K. W., Lau, J. S. Y., Lo, D. K. K. & Lo, L. T. L. Luminescent Cyclometalated Iridium (III) Polypyridine Complexes Containing a Thiourea Moiety: Synthesis, Characterization, Photophysics, Electrochemistry and Anion - Binding Properties. *European Journal of Inorganic Chemistry* **2006**, 4054-4062 (2006).
- [51] de Haas, R. R., van Gijlswijk, R. P., van der Tol, E. B., Veuskens, J., van Gijssel, H. E., Tijdens, R. B., Bonnet, J., Verwoerd, N. P. & Tanke, H. J. Phosphorescent platinum/palladium coproporphyrins for time-resolved luminescence microscopy. *Journal of Histochemistry & Cytochemistry* **47**, 183-196 (1999).
- [52] Lo, K. K.-W., Li, C.-K., Lau, K.-W. & Zhu, N. Luminescent cyclometalated rhodium (III) bis (pyridylbenzaldehyde) complexes with long-lived excited states. *Dalton Transactions*, 4682-4689 (2003).
- [53] Leung, S.-K., Kwok, K. Y., Zhang, K. Y. & Lo, K. K.-W. Design of luminescent biotinylation reagents derived from cyclometalated iridium (III) and rhodium (III) bis (pyridylbenzaldehyde) complexes. *Inorganic Chemistry* **49**, 4984-4995 (2010).
- [54] Tyson, D. S., Bialecki, J. & Castellano, F. N. Ruthenium (II) complex with a notably longexcited state lifetime. *Chemical Communications*, 2355-2356 (2000).
- [55] Meurman, O., Hemmilä, I., Lövgren, T. & Halonen, P. Time-resolved fluoroimmunoassay: a new test for rubella antibodies. *Journal of Clinical Microbiology* **16**, 920-925 (1982).
- [56] Siitari, H., Hemmilä, I., Soini, E., Lövgren, T. & Koistinen, V. Detection of hepatitis B surface antigen using time-resolved fluoroimmunoassay. *Nature* **301**, 258-260 (1983).
- [57] Leif, R. & Vallarino, L. Rare-earth chelates as fluorescent markers in cell separation and analysis. *ACS Symposium Series* **464**, 41-58 (1991).

- [58] Selvin, P. R. & Hearst, J. E. Luminescence energy transfer using a terbium chelate: improvements on fluorescence energy transfer. *Proceedings of the National Academy of Sciences* **91**, 10024-10028 (1994).
- [59] Selvin, P. R. Principles and biophysical applications of lanthanide-based probes. *Annual Review of Biophysics and Biomolecular Structure* **31**, 275-302 (2002).
- [60] Ma, Y. & Wang, Y. Recent advances in the sensitized luminescence of organic europium complexes. *Coordination Chemistry Reviews* **254**, 972-990 (2010).
- [61] Carlos, L. D., Ferreira, R. A., de Zea Bermudez, V., Julian-Lopez, B. & Escribano, P. Progress on lanthanide-based organic-inorganic hybrid phosphors. *Chemical Society Reviews* **40**, 536-549 (2011).
- [62] Pandya, S., Yu, J. & Parker, D. Engineering emissive europium and terbium complexes for molecular imaging and sensing. *Dalton Transactions*, 2757-2766 (2006).
- [63] Butler, S. J., Delbianco, M., Lamarque, L., McMahan, B. K., Neil, E. R., Pal, R., Parker, D., Walton, J. W. & Zwier, J. M. EuroTracker® dyes: design, synthesis, structure and photophysical properties of very bright europium complexes and their use in bioassays and cellular optical imaging. *Dalton Transactions* **44**, 4791-4803 (2015).
- [64] Weissleder, R. A clearer vision for in vivo imaging. *Nature biotechnology* **19**, 316-316 (2001).
- [65] Smith, A. M., Mancini, M. C. & Nie, S. Second window for in vivo imaging. *Nature nanotechnology* **4**, 710 (2009).
- [66] Li, X., Shen, D., Yang, J., Yao, C., Che, R., Zhang, F. & Zhao, D. Successive layer-by-layer strategy for multi-shell epitaxial growth: shell thickness and doping position dependence in upconverting optical properties. *Chemistry of Materials* **25**, 106-112 (2012).
- [67] Chen, G., Qiu, H., Prasad, P. N. & Chen, X. Upconversion nanoparticles: design, nanochemistry, and applications in theranostics. *Chemical Reviews* **114**, 5161-5214 (2014).
- [68] Lu, J., Chen, Y., Liu, D., Ren, W., Lu, Y., Shi, Y., Piper, J., Paulsen, I. & Jin, D. One-step protein conjugation to upconversion nanoparticles. *Analytical Chemistry* **87**, 10406-10413 (2015).
- [69] Lin, M., Zhao, Y., Wang, S., Liu, M., Duan, Z., Chen, Y., Li, F., Xu, F. & Lu, T. Recent advances in synthesis and surface modification of lanthanide-doped upconversion nanoparticles for biomedical applications. *Biotechnology Advances* **30**, 1551-1561 (2012).

- [70] Wang, M., Abbineni, G., Clevenger, A., Mao, C. & Xu, S. Upconversion nanoparticles: synthesis, surface modification and biological applications. *Nanomedicine: Nanotechnology, Biology and Medicine* **7**, 710-729 (2011).
- [71] Li, L.-L., Wu, P., Hwang, K. & Lu, Y. An exceptionally simple strategy for DNA-functionalized up-conversion nanoparticles as biocompatible agents for nanoassembly, DNA delivery, and imaging. *Journal of the American Chemical Society* **135**, 2411-2414 (2013).
- [72] Liu, Q., Chen, M., Sun, Y., Chen, G., Yang, T., Gao, Y., Zhang, X. & Li, F. Multifunctional rare-earth self-assembled nanosystem for tri-modal upconversion luminescence/fluorescence/positron emission tomography imaging. *Biomaterials* **32**, 8243-8253 (2011).
- [73] Boyer, J.-C., Manseau, M.-P., Murray, J. I. & van Veggel, F. C. Surface modification of upconverting NaYF<sub>4</sub> nanoparticles with PEG– phosphate ligands for NIR (800 nm) biolabeling within the biological window. *Langmuir* **26**, 1157-1164 (2009).
- [74] Yi, G.-S. & Chow, G.-M. Water-soluble NaYF<sub>4</sub>: Yb, Er (Tm)/NaYF<sub>4</sub>/polymer core/shell/shell nanoparticles with significant enhancement of upconversion fluorescence. *Chemistry of Materials* **19**, 341-343 (2007).
- [75] Wang, F., Deng, R., Wang, J., Wang, Q., Han, Y., Zhu, H., Chen, X. & Liu, X. Tuning upconversion through energy migration in core–shell nanoparticles. *Nature Materials* **10**, 968-973 (2011).
- [76] Zhang, F., Shi, Q., Zhang, Y., Shi, Y., Ding, K., Zhao, D. & Stucky, G. D. Fluorescence upconversion microbarcodes for multiplexed biological detection: nucleic acid encoding. *Advanced Materials* **23**, 3775-3779 (2011).
- [77] Zhang, Y., Zhang, L., Deng, R., Tian, J., Zong, Y., Jin, D. & Liu, X. Multicolor barcoding in a single upconversion crystal. *Journal of the American Chemical Society* **136**, 4893-4896 (2014).
- [78] Wang, J., Wang, F., Wang, C., Liu, Z. & Liu, X. Single - band upconversion emission in lanthanide - doped KMnF<sub>3</sub> nanocrystals. *Angewandte Chemie International Edition* **50**, 10369-10372 (2011).
- [79] Wang, Y.-F., Liu, G.-Y., Sun, L.-D., Xiao, J.-W., Zhou, J.-C. & Yan, C.-H. Nd<sup>3+</sup>-sensitized upconversion nanophosphors: efficient in vivo bioimaging probes with minimized heating effect. *ACS Nano* **7**, 7200-7206 (2013).

- [80] Mali, B., Dragan, A. I., Karolin, J. & Geddes, C. D. Photophysical characterization and  $\alpha$ -type delayed luminescence of rapidly prepared Au clusters. *The Journal of Physical Chemistry C* **117**, 16650-16657 (2013).
- [81] Gao, S., Fan, R.-Q., Qiang, L.-S., Wang, P., Chen, S., Wang, X.-M. & Yang, Y.-L. Effects of solvents and temperature on the luminescence properties of Cd-isonicotinic acid frameworks based on mono-, bi-, and trinuclear cluster units. *CrystEngComm* **16**, 1113-1125 (2014).
- [82] Maza, W. A. & Morris, A. J. Photophysical Characterization of a Ruthenium (II) Tris (2, 2' -bipyridine)-Doped Zirconium UiO-67 Metal – Organic Framework. *The Journal of Physical Chemistry C* **118**, 8803-8817 (2014).
- [83] Zhao, J., Ji, S. & Guo, H. Triplet–triplet annihilation based upconversion: from triplet sensitizers and triplet acceptors to upconversion quantum yields. *Rsc Advances* **1**, 937-950 (2011).
- [84] Ji, S., Wu, W., Wu, W., Song, P., Han, K., Wang, Z., Liu, S., Guo, H. & Zhao, J. Tuning the luminescence lifetimes of ruthenium (II) polypyridine complexes and its application in luminescent oxygen sensing. *Journal of Materials Chemistry* **20**, 1953-1963 (2010).
- [85] Park, J.-H., Gu, L., Von Maltzahn, G., Ruoslahti, E., Bhatia, S. N. & Sailor, M. J. Biodegradable luminescent porous silicon nanoparticles for in vivo applications. *Nature Materials* **8**, 331-336 (2009).
- [86] Gu, L., Hall, D. J., Qin, Z., Anglin, E., Joo, J., Mooney, D. J., Howell, S. B. & Sailor, M. J. In vivo time-gated fluorescence imaging with biodegradable luminescent porous silicon nanoparticles. *Nature Communications* **4** (2013).
- [87] Tasciotti, E., Liu, X., Bhavane, R., Plant, K., Leonard, A. D., Price, B. K., Cheng, M. M.-C., Decuzzi, P., Tour, J. M. & Robertson, F. Mesoporous silicon particles as a multistage delivery system for imaging and therapeutic applications. *Nature Nanotechnology* **3**, 151-157 (2008).
- [88] Engvall, E. & Perlmann, P. Enzyme-linked immunosorbent assay (ELISA) quantitative assay of immunoglobulin G. *Immunochemistry* **8**, 871-874 (1971).
- [89] Maliwal, B. P., Gryczynski, Z. & Lakowicz, J. R. Long-wavelength long-lifetime luminophores. *Analytical Chemistry* **73**, 4277-4285 (2001).
- [90] Kang, J. S., Piszczek, G. & Lakowicz, J. R. Enhanced emission induced by FRET from a long-lifetime, low quantum yield donor to a long-wavelength, high quantum yield acceptor. *Journal of Fluorescence* **12**, 97-103 (2002).

- [91] Xiong, X. Q., Zheng, L. J., Yan, J., Ye, F., Qian, Y. F. & Song, F. L. A turn-on and colorimetric metal-free long lifetime fluorescent probe and its application for time-resolved luminescent detection and bioimaging of cysteine. *Rsc Advances* **5**, 53660-53664, doi:10.1039/c5ra08539j (2015).
- [92] Parker, C. A. *Photoluminescence of solutions*. (Elsevier Publishing Company, 1968).
- [93] Yang, D., Kang, X., Dai, Y., Hou, Z., Cheng, Z., Li, C. & Lin, J. Hollow structured upconversion luminescent NaYF<sub>4</sub>: Yb<sup>3+</sup>, Er<sup>3+</sup> nanospheres for cell imaging and targeted anti-cancer drug delivery. *Biomaterials* **34**, 1601-1612 (2013).
- [94] Shan, J., Chen, J., Meng, J., Collins, J., Soboyejo, W., Friedberg, J. S. & Ju, Y. Biofunctionalization, cytotoxicity, and cell uptake of lanthanide doped hydrophobically ligated NaYF<sub>4</sub> upconversion nanophosphors. *Journal of Applied Physics* **104**, 094308 (2008).
- [95] Xiong, L., Chen, Z., Tian, Q., Cao, T., Xu, C. & Li, F. High contrast upconversion luminescence targeted imaging in vivo using peptide-labeled nanophosphors. *Analytical Chemistry* **81**, 8687-8694 (2009).
- [96] Nyk, M., Kumar, R., Ohulchanskyy, T. Y., Bergey, E. J. & Prasad, P. N. High contrast in vitro and in vivo photoluminescence bioimaging using near infrared to near infrared up-conversion in Tm<sup>3+</sup> and Yb<sup>3+</sup> doped fluoride nanophosphors. *Nano Letters* **8**, 3834-3838 (2008).
- [97] Leng, Y., Sun, K., Chen, X. & Li, W. Suspension arrays based on nanoparticle-encoded microspheres for high-throughput multiplexed detection. *Chemical Society Reviews* **44**, 5552-5595 (2015).
- [98] Pääkkilä, H., Ylihärsilä, M., Lahtinen, S., Hattara, L., Salminen, N., Arppe, R., Lastusaari, M., Saviranta, P. & Soukka, T. Quantitative multianalyte microarray immunoassay utilizing upconverting phosphor technology. *Analytical Chemistry* **84**, 8628-8634 (2012).
- [99] Phimphivong, S., Kölchens, S., Edmiston, P. L. & Saavedra, S. S. Time-resolved total internal reflection fluorescence microscopy of cultured cells using a Tb chelate label. *Analytica Chimica Acta* **307**, 403-417 (1995).
- [100] de Haas, R. R., Verwoerd, N. P., Van der Corput, M., Van Gijlswijk, R., Siitari, H. & Tanke, H. J. The use of peroxidase-mediated deposition of biotin-tyramide in combination with time-resolved fluorescence imaging of europium chelate label in

immunohistochemistry and in situ hybridization. *Journal of Histochemistry & Cytochemistry* **44**, 1091-1099 (1996).

[101] Vereb, G., Jares-Erijman, E., Selvin, P. R. & Jovin, T. M. Temporally and spectrally resolved imaging microscopy of lanthanide chelates. *Biophysical Journal* **74**, 2210-2222 (1998).

[102] de Haas, R. R., van Gijlswijk, R. P., van der Tol, E. B., Zijlmans, H. J., Bakker-Schut, T., Bonnet, J., Verwoerd, N. P. & Tanke, H. J. Platinum porphyrins as phosphorescent label for time-resolved microscopy. *Journal of Histochemistry & Cytochemistry* **45**, 1279-1292 (1997).

[103] Beverloo, H., Van Schadewijk, A., van Gelderen - Boele, S. & Tanke, H. Inorganic phosphors as new luminescent labels for immunocytochemistry and time - resolved microscopy. *Cytometry* **11**, 784-792 (1990).

[104] Beverloo, H., Van Schadewijk, A., Bonnet, J., Van der Geest, R., Runia, R., Verwoerd, N., Vrolijk, J., Ploem, J. & Tanke, H. Preparation and microscopic visualization of multicolor luminescent immunophosphors. *Cytometry* **13**, 561-570 (1992).

[105] Seveus, L., Väisälä, M., Syrjänen, S., Sandberg, M., Kuusisto, A., Harju, R., Salo, J., Hemmilä, I., Kojola, H. & Soini, E. Time - resolved fluorescence imaging of europium chelate label in immunohistochemistry and in situ hybridization. *Cytometry* **13**, 329-338 (1992).

[106] Connally, R., Veal, D. & Piper, J. High resolution detection of fluorescently labeled microorganisms in environmental samples using time-resolved fluorescence microscopy. *FEMS Microbiology Ecology* **41**, 239-245 (2002).

[107] Hanaoka, K., Kikuchi, K., Kobayashi, S. & Nagano, T. Time-resolved long-lived luminescence imaging method employing luminescent lanthanide probes with a new microscopy system. *Journal of the American Chemical Society* **129**, 13502-13509 (2007).

[108] Jin, D. Demonstration of true - color high - contrast microorganism imaging for terbium bioprobes. *Cytometry Part A* **79**, 392-397 (2011).

[109] Lu, Y., Jin, D., Leif, R. C., Deng, W., Piper, J. A., Yuan, J., Duan, Y. & Huo, Y. Automated detection of rare - event pathogens through time - gated luminescence scanning microscopy. *Cytometry Part A* **79**, 349-355 (2011).

[110] Connally, R., Jin, D. & Piper, J. High intensity solid - state UV source for time - gated luminescence microscopy. *Cytometry Part A* **69**, 1020-1027 (2006).

- [111] Lu, Y., Xi, P., Piper, J. A., Huo, Y. & Jin, D. Time-gated orthogonal scanning automated microscopy (OSAM) for high-speed cell detection and analysis. *Scientific Reports* **2:837**, doi: 10.1038 (2012).
- [112] Razali, W. A., Sreenivasan, V. K., Bradac, C., Connor, M., Goldys, E. M. & Zvyagin, A. V. Wide - field time - gated photoluminescence microscopy for fast ultrahigh - sensitivity imaging of photoluminescent probes. *Journal of biophotonics Biophotonics* **1-11**, doi: 10.1002 (2016).
- [113] Hirvonen, L. M., Kilfeather, T. & Suhling, K. Single-molecule localization software applied to photon counting imaging. *Applied Optics* **54**, 5074-5082 (2015).
- [114] Connally, R. A device for gated autosynchronous luminescence detection. *Analytical Chemistry* **83**, 4782-4787 (2011).
- [115] Ogata, A., Tagoh, H., Lee, T., Kuritani, T., Takahara, Y., Shimamura, T., Ikegami, H., Kurimoto, M., Yoshizaki, K. & Kishimoto, T. A new highly sensitive immunoassay for cytokines by dissociation-enhanced lanthanide fluoroimmunoassay (DELFI). *Journal of Immunological Methods* **148**, 15-22 (1992).
- [116] Morton, R. C. & Diamandis, E. P. Streptavidin-based macromolecular complex labeled with a europium chelator suitable for time-resolved fluorescence immunoassay applications. *Analytical Chemistry* **62**, 1841-1845 (1990).
- [117] Templeton, E., Wong, H. E., Evangelista, R. A., Granger, T. & Pollak, A. Time-resolved fluorescence detection of enzyme-amplified lanthanide luminescence for nucleic acid hybridization assays. *Clinical Chemistry* **37**, 1506-1512 (1991).
- [118] Bazin, H., Trinquet, E. & Mathis, G. Time resolved amplification of cryptate emission: a versatile technology to trace biomolecular interactions. *Reviews in Molecular Biotechnology* **82**, 233-250 (2002).
- [119] Condrau, M. A., Schwendener, R. A., Niederer, P. & Anliker, M. Time - resolved flow cytometry for the measurement of lanthanide chelate fluorescence: I. Concept and theoretical evaluation. *Cytometry* **16**, 187-194 (1994).
- [120] Condrau, M. A., Schwendener, R. A., Zimmermann, M., Muser, M. H., Graf, U., Niederer, P. & Anliker, M. Time - resolved flow cytometry for the measurement of lanthanide chelate fluorescence: II. Instrument design and experimental results. *Cytometry* **16**, 195-205 (1994).

- [121] Jin, D., Connally, R. & Piper, J. Practical time - gated luminescence flow cytometry. I: Concepts. *Cytometry Part A* **71**, 783-796 (2007).
- [122] Zhang, L., Zheng, X., Deng, W., Lu, Y., Lechevallier, S., Ye, Z., Goldys, E. M., Dawes, J. M., Piper, J. A. & Yuan, J. Practical implementation, characterization and applications of a multi-colour time-gated luminescence microscope. *Scientific Reports* **4**, 6597, doi: 10.1038 (2014).
- [123] Zheng, X., Zhu, X., Lu, Y., Zhao, J., Feng, W., Jia, G., Wang, F., Li, F. & Jin, D. High-contrast visualization of upconversion luminescence in mice using time-gating approach. *Analytical Chemistry* **88**, 3449-3454 (2016).
- [124] Zheng, X., Lu, Y., Zhao, J., Zhang, Y., Ren, W., Liu, D., Lu, J., Piper, J. A., Leif, R. C. & Liu, X. High-Precision Pinpointing of Luminescent Targets in Encoder-Assisted Scanning Microscopy Allowing High-Speed Quantitative Analysis. *Analytical Chemistry* **88**, 1312-1319 (2015).



## Chapter 2: Multi-Colour Time-Gated Luminescence Microscopy

This chapter explores the design and evaluation of a low-cost and easy-to-assemble multi-colour time-gated luminescence microscope. This work was carried out during the first year of my PhD candidature. An excitation module and a time-gated detection module with precise synchronization control were engineered, providing a reproducible solution to convert a commercial epi-fluorescence microscope into a multi-colour time-gated system. Simultaneous background-free imaging was demonstrated using two pathogenic microorganisms – *Giardia lamblia* stained with a red europium probe and *Cryptosporidium parvum* with a green terbium probe. After this, I built an identical system at Dalian University of Technology in China, which was employed to image Vitamin C in live *Daphnia magna*. These works are reported in the form of two published journal papers.

### 2.1 Optical Design

As discussed in 1.4.2, the previous time-gated luminescence microscope developed by Jin and Piper in 2011 has two major limitations: 1) vibration associated with the upright setup, and 2) narrow-band light source incapable of exciting multiple luminescent probes simultaneously. To overcome these issues, I engineered an excitation module featuring a high-repetition rate (up to 1 kHz) ceramic xenon flash lamp, whose output was precisely synchronised using Transistor-Transistor Logic (TTL) signals with the chopper-based time-gated detection module. The xenon flash lamp offers a broad emission spectrum from 250nm to 2000nm, covering the UV wavelengths (320-400 nm) required for different lanthanide probes when a suitable band-pass excitation filter is used to remove the unwanted wavelengths (Figure 2-1). The optics was carefully designed to minimize image aberration (scheme shown in Figure 2-2). The excitation module is coupled to the back port of an Olympus IX71 inverted microscope, replacing the original mercury lamp and connecting to the collimator through a homemade adaptor. The mechanics of the time-gated detection module was also re-configured, allowing easy assembly and alignment via the side port of

the IX71 microscope. Mounting of the time-gated detection module on the base of the microscope substantially reduced vibration originating from the high-speed chopper.

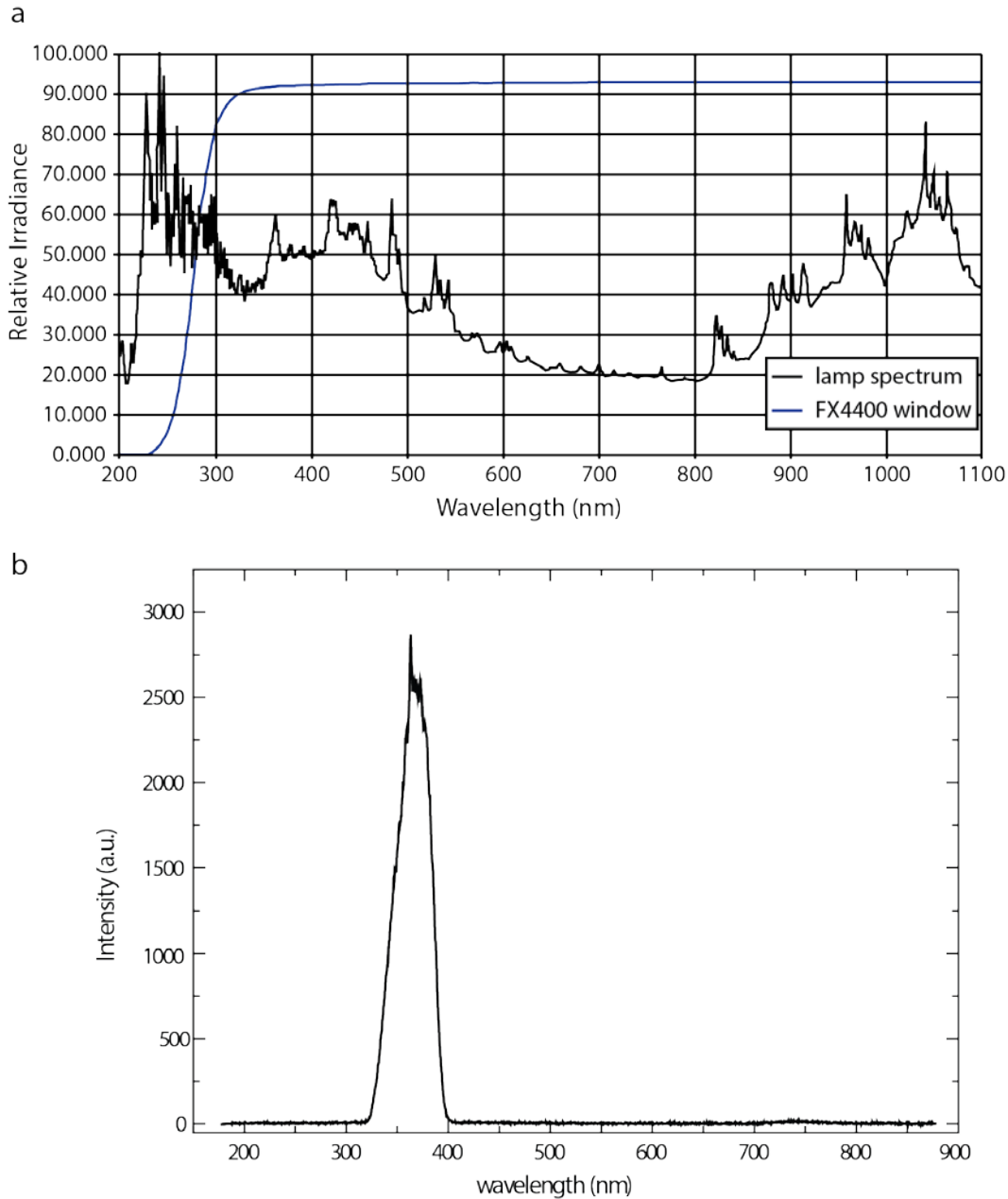


**FIGURE 2-1** (a) shows the original spectral distribution of ceramic xenon flash lamp. (b) shows the excitation spectrum selected by band-pass UV excitation filter.

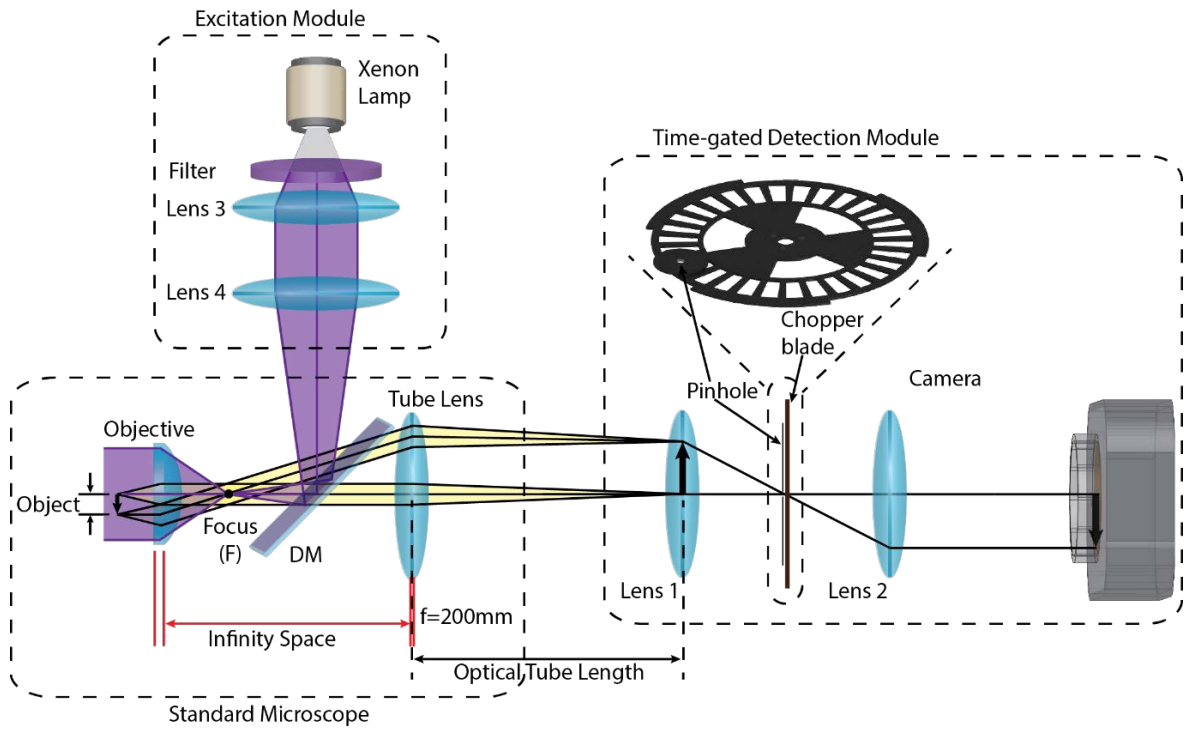


**FIGURE 2-2** The optical schematic of this multi-colour TGL microscope.

## 2.2 Paper 1

Lixin Zhang, **Xianlin Zheng**, Wei Deng, Yiqing Lu, Severine Lechevallier, Zhiqiang Ye, Ewa M. Goldys, Judith M.Dawes, James A. Piper, Jingli Yuan, Marc Verelst and Dayong Jin, "Practical Implementation, Characterization and Applications of a Multi-Colour Time-Gated Luminescence Microscope" *Scientific Reports*, 2014, DOI:10.1038/srep06597.

I did this work with my peer Lixin Zhang under the supervision of Prof. Dayong Jin and Dr. Yiqing Lu. I led the design of the excitation module and the time-gated module using SolidWorks software. The hardware module was fabricated with the assistance of Macquarie Engineering & Technical Services workshop. Zhang and I set up the system and collected the experimental data. I assisted Zhang in preparing the biological samples, and contributed to data analysis and figure illustrations. Author contributions to this paper are summarised in [Table 2-1](#).

**TABLE 2-1** Summary of author contributions to paper 1 following the order of authors.

	L. Z	X. Z	W. D	Y .L	S. L	Z. Y	E. G	J. D	J. P	J. Y	M. V	D .J
Project Design	•			•								•
System Design		•										
System Setup	•	•										
Sample Preparation	•	•	•		•					•	•	
Data Collection	•	•										
Analysis	•	•		•								
Figures	•	•		•								
Manuscript	•			•		•	•	•	•			•



OPEN

SUBJECT AREAS:  
IMAGING TECHNIQUES  
OPTICS AND PHOTONICSReceived  
10 March 2014Accepted  
17 September 2014Published  
13 October 2014Correspondence and  
requests for materials  
should be addressed to  
Y.L. (yiqing.lu@mq.  
edu.au) or D.J.  
(dayong.jin@mq.edu.  
au)

## Practical Implementation, Characterization and Applications of a Multi-Colour Time-Gated Luminescence Microscope

Lixin Zhang<sup>1</sup>, Xianlin Zheng<sup>1</sup>, Wei Deng<sup>1</sup>, Yiqing Lu<sup>1</sup>, Severine Lechevallier<sup>2</sup>, Zhiqiang Ye<sup>3</sup>,  
Ewa M. Goldys<sup>1</sup>, Judith M. Dawes<sup>1</sup>, James A. Piper<sup>1</sup>, Jingli Yuan<sup>3</sup>, Marc Verelst<sup>2</sup> & Dayong Jin<sup>1</sup><sup>1</sup>Advanced Cytometry Labs, ARC Centre of Excellence for Nanoscale BioPhotonics (CNBP), Macquarie University, Sydney, NSW 2109, Australia, <sup>2</sup>Centre d'Élaboration de Matériaux et d'Études Structurales (CERMES - CNRS), Paul Sabatier University, France, <sup>3</sup>State Key Laboratory of Fine Chemicals, School of Chemistry, Dalian University of Technology, Dalian 116024, China.

**Time-gated luminescence microscopy using long-lifetime molecular probes can effectively eliminate autofluorescence to enable high contrast imaging. Here we investigate a new strategy of time-gated imaging for simultaneous visualisation of multiple species of microorganisms stained with long-lived complexes under low-background conditions. This is realized by imaging two pathogenic organisms (*Giardia lamblia* stained with a red europium probe and *Cryptosporidium parvum* with a green terbium probe) at UV wavelengths (320–400 nm) through synchronization of a flash lamp with high repetition rate (1 kHz) to a robust time-gating detection unit. This approach provides four times enhancement in signal-to-background ratio over non-time-gated imaging, while the average signal intensity also increases six-fold compared with that under UV LED excitation. The high sensitivity is further confirmed by imaging the single europium-doped Y<sub>2</sub>O<sub>3</sub>S nanocrystals (150 nm). We report technical details regarding the time-gating detection unit and demonstrate its compatibility with commercial epi-fluorescence microscopes, providing a valuable and convenient addition to standard laboratory equipment.**

**A**utofluorescence in biological samples presents a universal challenge for conventional fluorescence techniques to detect or visualize target species<sup>1–6</sup>. The time-gated luminescence (TGL) technique, which takes advantages of long-lived luminescent probes (e.g. lanthanide complexes) and time-delayed detection, substantially enhances the signal-to-noise ratio and contrast by suppressing the autofluorescence contribution<sup>7–12</sup>. However, the presently reported TGL microscopes can only image one colour at a time, due to the gating schemes and/or imaging devices that only allow monochromatic visualization<sup>8,13–17</sup>. Though multiple colours can be superimposed via image processing<sup>18,19</sup>, it requires frequent changing of filters and reduces the efficiency when examining different species, as well as limits the opportunity to investigate their interactions. Meanwhile, the previous TGL microscopes required costly components and sophisticated assembly, which are often inaccessible in most chemical and biological laboratories<sup>20–24</sup>. These issues have been hindering broad implementation of the time-gated imaging technique.

In our previous work, we demonstrated a low-cost true-colour TGL microscope, featuring an ultraviolet light-emitting diode (UV LED) for excitation and a mechanical chopper for time-gating<sup>13,25,26</sup>. In order to simultaneously excite multiple long-lived probes, especially terbium with sensitizing moiety complex that needs a triplet energy around 30,000 cm<sup>-1</sup> to pump Tb<sup>3+</sup> to its excited state (<sup>5</sup>D<sub>3</sub>; 20,400 cm<sup>-1</sup>)<sup>25</sup>, efficient excitation at 300–340 nm is required; however, the power of currently available UV LEDs at this wavelength range is not strong enough. On the other hand, flash lamps emitting deep UV with high power but low repetition rate (less than 100 Hz) have been used for TGL microscopy<sup>27,28</sup>, but the long detection windows prevent efficient collection of lanthanide luminescence typically with decay lifetimes of ~1 ms or less, as well as having stability issues when synchronized to mechanical choppers.

In this work, we report a highly efficient TGL microscopy system for dual-colour low-background imaging. It uses a high-power flash lamp that can be externally triggered at high repetition rate (up to 1 kHz). This system also comprises a purpose designed and optimized time-gating unit that can be simply inserted into a commercial



epi-fluorescence microscope. We apply the new imaging system for simultaneous detection of both *Giardia lamblia* stained with a red-emitting europium complex probe and *Cryptosporidium parvum* stained with a green-emitting terbium complex probe against strong autofluorescent background. Sufficient sensitivity of this combined system is demonstrated by imaging single nanoparticles.

## Results

To set up the multi-colour TGL microscope, we built an illuminator featuring a new-generation ceramic xenon flash lamp (FX-4400, Excelitas Technologies) capable of delivering high-power light pulses to excite the sample, and a time-gating unit incorporating a modified mechanical chopper to discriminate long-lived luminescence against rapidly decaying autofluorescence. Both modules were designed and engineered in such a way that they can be directly coupled onto commercial microscopes, for example the Olympus IX71 epi-fluorescence microscope used in our study, to perform TGL imaging with minimum effort required for configuration and alignment.

**Optical layout.** The schematic diagram of this multi-colour TGL microscope is shown in Figure 1a and 1b. In the excitation phase (Figure 1a), the beam from the xenon lamp passes through a UV band-pass filter (U-360, Edmund), and is reflected by a dichroic mirror (DC shown in Figure 1; 400DCLP, Chroma). Then, it is focused through an objective lens (60 $\times$ , NA 0.75, Edmund), onto a microscopic slide to excite the specimen. The generated luminescence is collected by the same objective. It is separated from the excitation path by the dichroic mirror, and coupled to the time-gating unit consisting of the chopper, two eyepieces and a

digital colour camera (DP71, Olympus). Two eyepieces (Eyepiece 1:  $\times 10$ , Olympus; Eyepiece 2: RKE 32 mm, wide angle, Edmund) are used to bring down the size of the emission beam, so that the chopper can be placed at the focal spot to block the emission with minimised dead time during the periods of pulsed excitation<sup>13</sup>. When the excitation is off, a short time delay is applied to allow the prompt fading of the autofluorescence background. Therefore, in the detection phase, only the luminescence from the long lifetime lanthanide probes is captured by the camera (Figure 1b). The synchronisation between excitation phase and detection phase should be carefully and accurately carried out. The time sequence used is given in Figure 1c, and the details of synchronisation are described below.

**Excitation source.** In this system, the ceramic xenon flash lamp used outputs an average power of 60 W over its full spectrum (from 160 nm to 2000+ nm), and more importantly, a high repetition rate up to 1 kHz. It was coupled into the back port of the IX71 microscope, replacing the original mercury lamp and connecting the collimator using a customized adaptor. In order to minimise the optical background and photo-bleaching of the sample, a UV band-pass filter was used to only select the spectral region which contributed to the excitation of lanthanide probes (320–400 nm; see Supplementary Figure S1). The average excitation power entering the rear aperture of the objective lens was measured to be 2.7 mW. It had a reasonably uniform distribution over a sample area of 200  $\mu\text{m}$  in diameter, leading to an excitation intensity of 8.6 W/cm<sup>2</sup>.

For comparison, our previously reported system using a UV LED (UVTOP310, 315  $\pm$  15 nm; Sensor Electronic Technology) for

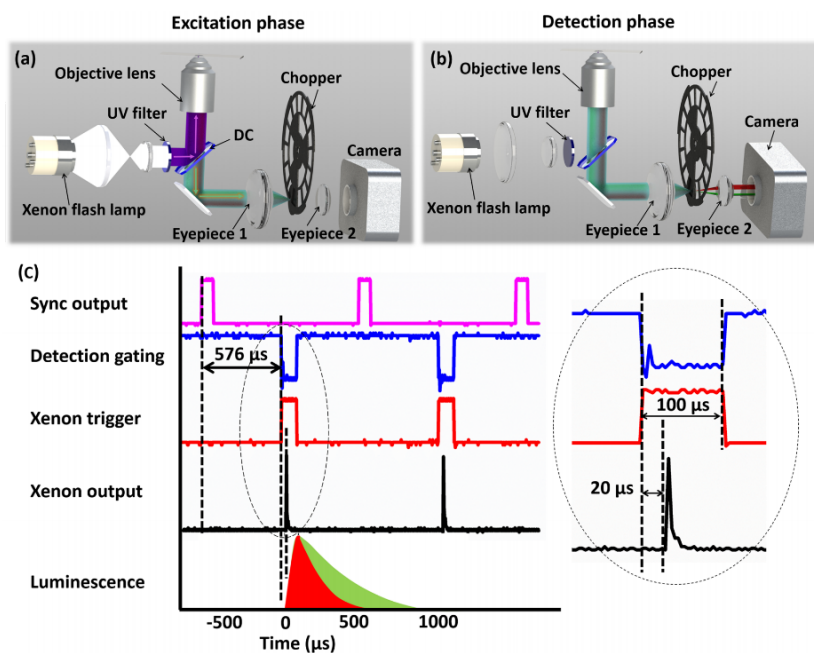


**Figure 1** | Schematic diagrams of the multi-colour TGL microscope. (a) In the excitation phase, a pulsed excitation light illuminates the sample, while the chopper stops the luminescence/autofluorescence being captured by camera. (b) In the detection phase, the excitation is turned off, and the chopper allows the luminescence to reach the camera. (c) The time sequence of the system is shown, with every repetition cycle containing a gating window of 88  $\mu\text{s}$  and a detection window of 968  $\mu\text{s}$ . Each flash pulse is released 20  $\mu\text{s}$  after the trigger and last around 17  $\mu\text{s}$ .



excitation<sup>23</sup> was also investigated for multi-colour TGL imaging. Its average excitation power at the rear aperture of the objective lens was measured to be 0.5 mW, hence an excitation intensity of 1.6 W/cm<sup>2</sup>.

**Chopper modification.** In order to achieve optimum performance and compatibility with the xenon flash lamp, we modified a high-speed mechanical chopper (C995, Terahertz Technologies Inc). Originally, this device had 30 blades with a fixed duty cycle of 1:1, and it was able to run at a frequency up to 5 kHz. Considering that the highest frequency of the xenon lamp was 1 kHz and the lifetimes of lanthanide probes were in the range of tens to hundreds of  $\mu$ s, we removed 25 blades using ultrafast laser micromachining and only kept one blade out of every six, so that the duty cycle became 1:11 (see Supplementary Figure S2). It is worth mentioning that the reduced weight of the chopper blades also helped reduce the vibration of the time-gating unit to some degree.

A plate with a 1-mm-diameter pinhole was attached to the chopper enclosure to increase the chopping efficiency by removing stray light, as well as protecting the device from dust. The highest chopping frequency after modification was measured to be 947 Hz, which yielded 88  $\mu$ s for gating and 968  $\mu$ s for detection.

**Time-gating unit.** Incorporating the modified chopper, a time-gating unit was designed and built, as shown in Figure 2. An aluminium frame was machined to mount the eyepieces, the chopper and the camera, alongside an adaptor for the camera port of a standard microscope, in our case the Olympus IX71. Fine alignment of the components was conducted in the bright-field mode illuminated by a halogen lamp. In the first step, the pair of eyepieces was adjusted to make their focuses completely overlap. Since the eyepieces had the same magnification, this was verified by measuring the beam size at a long distance (e.g. 1 m) away along the optical path, which should remain identical regardless of the presence/absence of the two eyepieces. In the second step, the modified chopper was inserted between the eyepieces, so that its pinhole plate was located exactly at the common focus of the two eyepieces. In the third step, the camera was mounted after the second

eyepiece. The imaging quality of the system was examined using a microscopic reticle (grid distortion targets, Thorlabs). The most common optical aberration encountered during the alignment was the “barrel distortion” (see Supplementary Figure S3); however, this could be effectively overcome once all optical components were adjusted to be exactly coaxial. After proper alignment, the obtained field-of-view was 150  $\times$  150  $\mu$ m<sup>2</sup>.

**Synchronisation.** After all the components were properly aligned, synchronisation between the excitation and the time-gated detection was elaborately carried out to ensure maximum contrast enhancement for TGL imaging. As shown in Figure 1c, we first measured the time delay between the *Sync Output* from the chopper controller (which was generated by a built-in sensor in the chopper head for monitoring the rotation of the blades) and the physical opening/blockage of the detection path. The latter was recorded by a photodiode placed after the second eyepiece when the bright-field illumination was switched on. With the modified chopper blades, this delay from the rising edge of *Sync Output* to the blockage of the detection path was determined as 576  $\mu$ s, which was essentially caused by the different positions of the sensor and the pinhole. Then, we fed the *Sync Output* from the chopper controller to a digital delay generator (DG535, Stanford Research Systems), which sent TTL pulses of 100  $\mu$ s duration to trigger the xenon lamp. Because of the gas discharge process, there was another time delay from the rising edge of the trigger signal to the time of flashing, which was measured as 20  $\mu$ s. Finally, we adjusted the delay value between the *Sync Output* channel and the xenon trigger channel while monitoring the level of autofluorescence leakage using a piece of paper as the reference sample. It was found that a delay value of 576  $\mu$ s (same as the delay between *Sync Output* and chopper blockage) rendered the autofluorescence invisible and allowed the maximum luminescence signal to be captured.

**Dual-colour imaging.** Two waterborne pathogens, *Giardia lamblia* and *Cryptosporidium parvum*, were labelled with Eu and Tb luminescent complexes, respectively (see Methods for details). The mixed samples were imaged under xenon flash lamp excitation, with the non-time-gated result shown in Figure 3a and the time-gated result shown in Figure 3b for one typical sample area. To evaluate the signal-to-background ratios in an accurate and objective way, the intensity levels of targets as well as the rest areas were carefully analysed in the separate red and green channels (detailed procedures see Supplementary Information S4). As shown in Figure 3c and 3d, the part of signals that were once submerged under the background clearly stood out after the time-gated mode was applied. The average values given in Figure 3e, after statistically measuring 10 pairs of non-time-gated and time-gated images (complete data see Supplementary Table S1 and S2), indicate the signal-to-background ratio is enhanced by 4.3-folds (from 126:44 to 137:11) for the red channel, as well as 3.3-folds (from 91:45 to 74:11) for the green channel, with camera exposure time of 5 seconds. By contrast, previously it took 15 seconds (repetition rate 2.5 kHz, excitation pulse 100  $\mu$ s, detection window 300  $\mu$ s) to accumulate enough luminescent signals (average 70 for red and 37 for green) under 315 nm UV LED excitation (see Supplementary Information S5). Therefore, it is calculated that the excitation efficiency of the xenon lamp is 5.9 times in red and 6.0 times in green higher than that of the UV LED, thus more suitable for multi-colour TGL microscopy.

**Crosstalk between red (Eu) and green (Tb) channels.** We proposed a calibration method to calculate the crosstalk from the emission spectra of lanthanide chelates and the responsivity curves of the true-colour DP71 camera (detailed procedures see Supplementary Information S6). Briefly, 78.6% of the total emission from the Eu complexes is collected into the red channel of the camera, along with

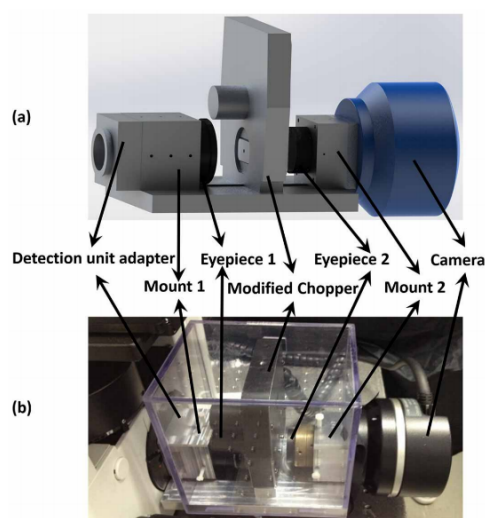


**Figure 2** | The time-gating unit consists of two eyepieces, one chopper and one camera, all of which are mounted on a common frame. Top: the schematics; Bottom: a photo of the real system.

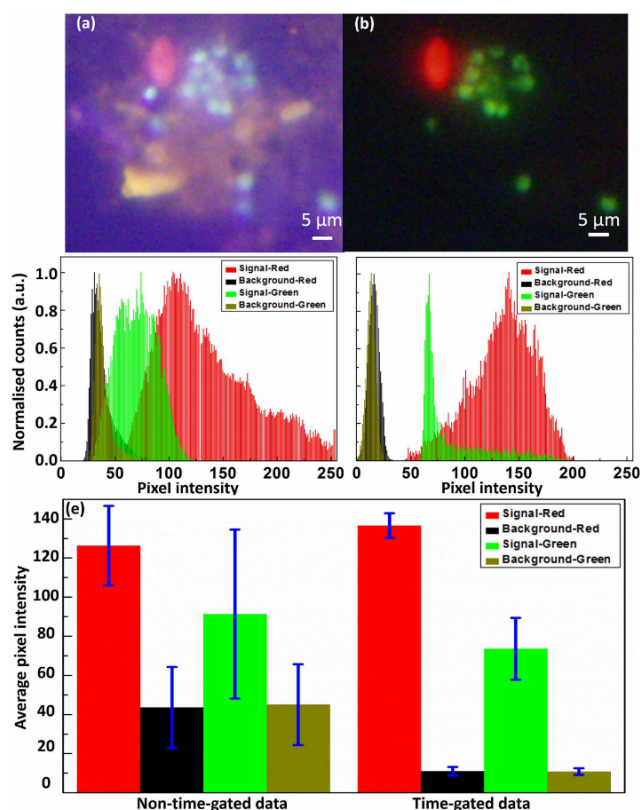


**Figure 3 | Two-colour imaging under xenon lamp excitation.** (a) and (b) are non-time-gated and time-gated images of *Giardia lamblia* cysts labelled with a red europium probe and *Cryptosporidium parvum* oocysts labelled with a green terbium probe (exposure time: 5 seconds). (c) and (d) show the pixel intensity histograms for the signal area (target cells) and the background area in separate red and green channels for (a) and (b), respectively. (e) is a bar chart showing the average signal and background levels summarised from 10 pairs of non-time-gated and time-gated dual-colour images. Error bars represent  $\pm 1$  s.e.m.

13.6% and 7.8% into green and blue channels, respectively. Meanwhile, for the Tb complexes, since its emission spectrum has satellite peaks in the blue and red range, 59.9% of the total emission is collected into the green channel, 19.2% into the red channel, and 20.9% into the blue channel. These values can be applied to compensate the original imaging results to achieve more precise quantitative measurement. However, for applications that aim to detect target cells or analytes only, the crosstalk issue may be ignored if the contrast in time-gated images is sufficiently high, as was the case in this study.

**Single nanoparticle sensitivity.** We further evaluated the sensitivity of the new time-gated luminescence microscope by imaging single nanoparticles. Figure 4 presents a typical result of 150 nm  $Y_2O_3:Eu^{3+}$  nanoparticles under xenon lamp excitation with an exposure time of 30 seconds. While the non-time-gated mode failed to provide enough contrast (Figure not shown), the time-gated mode offered sufficient sensitivity to observe these nanoparticles down to a single one (Figure 4a). Figure 4b enlarges images of the luminescent spots which potentially contain single nanoparticles (others were easily to be identified as aggregation of nanoparticles). Following a literature

method<sup>14,29</sup>, they were eventually confirmed in the corresponding transmission electron microscopy (TEM) image (Figure 4c), which showed perfect correlation with the luminescence image (Figure 4d; detailed procedures see Supplementary Information S7).

## Discussion and Conclusion

In this study, we demonstrate for the first time that simultaneous dual-colour visualisation can be realised in TGL imaging for two species of microorganisms stained with different lanthanide probes. We show that outstanding sensitivity and contrast can be achieved with a new-generation xenon flash lamp that is capable of pulsed excitation at high repetition rate. Our compact time-gating unit provides an easy-to-use and low-cost option to chemists developing lanthanide materials and biologists who wish to eliminate autofluorescence background. Furthermore, the system is also compatible to the automated scanning and lifetime measurement techniques<sup>30,31</sup>, to enable high-throughput detection and analysis of multiple target microorganisms. With the rapid progress in lanthanide chemistry, especially the new development of lifetime-tunable lanthanide probes<sup>32</sup>, we believe such multi-colour TGL

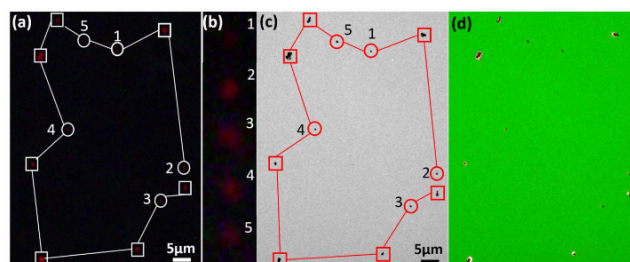


**Figure 4** | Imaging results of the  $Y_2O_2S:Eu$  nanoparticles. (a) A time-gated image shows a pattern of luminescence spots. The spots marked with circles (numbered as 1 to 5) contain single Eu nanoparticles, while the others marked with squares contain aggregation of nanoparticles. (b) The enlarged images are given for spots 1–5. (c) The TEM image shows the same pattern for the spots of nanoparticles. (d) Co-localisation analysis confirms the perfect match between the time-gated image and the TEM image.

technique will have a broad range of impact on analytical and bio-sensing applications.

## Methods

**Immunoluminescent staining of *Giardia lamblia*.** Immunofluorescence staining of *Giardia lamblia* was carried out based on the published method<sup>24</sup> with slight modifications. 30  $\mu$ L of mouse monoclonal anti-*Giardia* antibody G203 (IgG, cyst-wall specific, 0.44 mg/mL, BTF-bioMérieux), 100  $\mu$ L of biotinylated goat anti-mouse IgG antibody (1:10 dilution; Catalogue Number AP200B, ChemiCon International, Millipore Bioscience Division), and 100  $\mu$ L of SA-BSA-BHHCT-Eu<sup>3+</sup> conjugate (50  $\mu$ g/mL) (the synthesis method was reported in literature<sup>13</sup>) were mixed with 10  $\mu$ L suspension of *Giardia lamblia* (containing ~2,500 *Giardia lamblia* cysts, BTF-bioMérieux), and incubated at room temperature for 12 hours. In order to separate the Eu-labelled cysts, the FACSAria flow cytometer (Becton Dickinson) was used to sort out the sample prepared above, which yielded ~2,000 stained cysts in 400  $\mu$ L 1.25% PBS solution.

**Immunoluminescent staining of *Cryptosporidium parvum*.** For staining of *Cryptosporidium parvum*, a method similar to that reported in literature<sup>25</sup> was used. In a typical procedure, 10  $\mu$ L suspension of *Cryptosporidium parvum* oocysts (~ $10^6$  oocysts/mL in PBS, BTF-bioMérieux) was mixed with 20  $\mu$ L of mouse monoclonal anti-*Cryptosporidium* antibody C104 (IgG, 0.44 mg/mL; BTF-bioMérieux) and incubated for 24 hours at room temperature. The mixture was then centrifuged (at 12,000 rpm, 5 minutes) and washed with PBS (pH 7.2) three times. After removing the supernatant, 20  $\mu$ L of 10-fold diluted biotinylated goat anti-mouse IgG antibody was added and incubated for another 24 hours at room temperature, followed by washing and centrifugation. Subsequently, 20  $\mu$ L of the Tb-labelled streptavidin (1:20 dilution of 1 mg/mL kit, LanthaScreen® Tb-Streptavidin, Invitrogen) was added and the suspension was incubated for another 48 hours. Finally, the stained *Cryptosporidium* oocysts were washed three times with PBS.

**Preparation of mixed pathogen samples.** In order to demonstrate the background suppression feature of our system, a sample exhibiting strong autofluorescence was prepared. Flower petals with different colours of native chromophores were pulverized and mixed with fruit juice, which is also known to be autofluorescent. They were filtered through a centrifugal filter device (UFC30GV00, Millipore) to remove large fragments.

The two stained microorganisms and artificial background samples were mixed and sandwiched between a glass slide and a coverslip. 5  $\mu$ L of background solution was dropped onto a glass slide. After it dried, 2  $\mu$ L of the Eu-probe-labelled *Giardia lamblia* cysts was added. 10 minutes later, 2  $\mu$ L of the Tb-probe-labelled *Cryptosporidium parvum* was dropped on top of the sample, and the whole preparation was covered with a coverslip.

**Preparation of single nanoparticle samples.** 10  $\mu$ L of an ethanol solution containing 0.25 mg/mL Eu-doped nanoparticles  $Y_2O_2S:Eu^{3+}$  (5% dopants, average size 150 nm)<sup>26</sup> was dropped on the copper grids coated by amorphous carbon. The nanoparticles on the grid were imaged by a transmission electron microscope (TEM, Philips CM10).

- Gahlaut, N. & Miller, L. W. Time-resolved microscopy for imaging lanthanide luminescence in living cells. *Cytom Part A* **77A**, 1113–1125, doi:10.1002/Cyto.A.20964 (2010).
- Tian, L. *et al.* Preparation and time-gated luminescence bioimaging applications of long wavelength-excited silica-encapsulated europium nanoparticles. *Nanoscale* **4**, 3551–3557, doi:10.1039/C2nr30233k (2012).

- Rich, R. M. *et al.* Elimination of autofluorescence background from fluorescence tissue images by use of time-gated detection and the AzaDiOxaTriAngulanium (ADOTA) fluorophore. *Anal Bioanal Chem* **405**, 2065–2075, doi:10.1007/s00216-012-6623-1 (2013).
- Bunzli, J. C. G. & Eliseeva, S. V. Intriguing aspects of lanthanide luminescence. *Chem Sci* **4**, 1939–1949, doi:10.1039/C3sc22126a (2013).
- Shinoda, S. Dynamic cyclen-metal complexes for molecular sensing and chirality signaling. *Chemical Society reviews* **42**, 1825–1835, doi:10.1039/C2cs35295h (2013).
- Cheng, L., Wang, C. & Liu, Z. Upconversion nanoparticles and their composite nanostructures for biomedical imaging and cancer therapy. *Nanoscale* **5**, 23–37, doi:10.1039/c2nr32311g (2013).
- Lichtman, J. W. & Conchello, J. A. Fluorescence microscopy. *Nature methods* **2**, 910–919, doi:10.1038/nmeth817 (2005).
- Sagolla, K., Lohmannsroben, H. G. & Hille, C. Time-resolved fluorescence microscopy for quantitative Ca<sup>2+</sup> imaging in living cells. *Anal Bioanal Chem* **405**, 8525–8537, doi:10.1007/s00216-013-7290-6 (2013).
- Vaasa, A. *et al.* Time-gated luminescence microscopy with responsive nonmetal probes for mapping activity of protein kinases in living cells. *Chemical communications* **48**, 8595–8597, doi:10.1039/c2cc33565d (2012).
- Moore, J. D., Lord, R. L., Cisneros, G. A. & Allen, M. J. Concentration-independent pH detection with a luminescent dimetallic Eu(III)-based probe. *Journal of the American Chemical Society* **134**, 17372–17375, doi:10.1021/ja307098z (2012).
- Lechevallier, S. *et al.* Luminescence properties of mesoporous silica nanoparticles encapsulating different europium complexes: application for biolabelling. *J Nanomater*, doi:10.1155/2013/918369 (2013).
- Rich, R. M. *et al.* Multiple-pulse pumping for enhanced fluorescence detection and molecular imaging in tissue. *Methods*, doi:10.1016/j.jymeth.2013.08.026 (2013).
- Jin, D. & Piper, J. A. Time-gated luminescence microscopy allowing direct visual inspection of lanthanide-stained microorganisms in background-free condition. *Analytical chemistry* **83**, 2294–2300, doi:10.1021/ac103207r (2011).
- Deng, W. *et al.* Ultrabright Eu-doped plasmonic Ag@SiO<sub>2</sub> nanostructures: time-gated bioprobes with single particle sensitivity and negligible background. *Advanced materials* **23**, 4649–4654, doi:10.1002/adma.201102027 (2011).
- Wu, J. *et al.* Visible-light-sensitized highly luminescent europium nanoparticles: preparation and application for time-gated luminescence bioimaging. *J Mater Chem* **19**, 1258–1264, doi:10.1039/B815999h (2009).
- Duncan, M. D., Mahon, R., Tankersley, L. L. & Reintjes, J. Time-gated imaging through scattering media using stimulated raman amplification. *Opt Lett* **16**, 1868–1870, doi:10.1364/OL.16.001868 (1991).
- Requejo-Isidro, J. *et al.* High-speed wide-field time-gated endoscopic fluorescence-lifetime imaging. *Opt Lett* **29**, 2249–2251, doi:10.1364/OL.29.002249 (2004).
- Soini, A. E., Kuusisto, A., Meltola, N. J., Soini, E. & Seveus, L. A new technique for multiparameter imaging microscopy: use of long decay time photoluminescent labels enables multiple color immunocytochemistry with low channel-to-channel crosstalk. *Microscopy research and technique* **62**, 396–407, doi:10.1002/jemt.10389 (2003).
- Hanaoka, K., Kikuchi, K., Kobayashi, S. & Nagano, T. Time-resolved long-lived luminescence imaging method employing luminescent lanthanide probes with a new microscopy system. *Journal of the American Chemical Society* **129**, 13502–13509, doi:10.1021/ja073392j (2007).
- Connally, R., Jin, D. & Piper, J. High intensity solid-state UV source for time-gated luminescence microscopy. *Cytometry. Part A: the journal of the International Society for Analytical Cytology* **69**, 1020–1027, doi:10.1002/cyto.a.20326 (2006).
- Connally, R. E. & Piper, J. A. Time-gated luminescence microscopy. *Annals of the New York Academy of Sciences* **1130**, 106–116, doi:10.1196/annals.1430.032 (2008).



22. Hu, B. L., He, Y. H. & Liu, Z. Y. NIR area array CCD-based singlet oxygen luminescence imaging for photodynamic therapy. *J Phys Conf Ser* **277**, doi:10.1088/1742-6596/277/1/012011 (2011).
23. Ibanez, G., McBean, J. L., Astudillo, Y. M. & Luo, M. K. An enzyme-coupled ultrasensitive luminescence assay for protein methyltransferases. *Analytical biochemistry* **401**, 203–210, doi:10.1016/j.ab.2010.03.010 (2010).
24. Lu, Y. *et al.* Automated detection of rare-event pathogens through time-gated luminescence scanning microscopy. in *Cytometry A* Vol. 79, 349–355, doi: 10.1002/Cyto.A.21045 (2011).
25. Jin, D. Y. Demonstration of true-color high-contrast microorganism imaging for terbium bioprobes. *Cytom Part A* **79A**, 392–397, doi:10.1002/Cyto.A.21052 (2011).
26. Jin, D. Y., Li, Y. Q., Leif, R. C., Yang, S., Rajendran, M. & Miller, L. W. in *Current Protocols in Cytometry How to build a time-gated luminescence microscope* 67: 62.22:62.22.61–62.22.36. (2014).
27. Beverloo, H. B., Vanschadewijk, A., Vangelderboele, S. & Tanke, H. J. Inorganic phosphors as new luminescent labels for immunocytochemistry and time-resolved microscopy. *Cytometry* **11**, 784–792, doi:10.1002/cyto.990110704 (1990).
28. Vereb, G., Jares-Erijman, E., Selvin, P. R. & Jovin, T. M. Temporally and spectrally resolved imaging microscopy of lanthanide chelates. *Biophysical journal* **74**, 2210–2222, doi:10.1016/S0006-3495(98)77930-5 (1998).
29. Wu, S. *et al.* Non-blinking and photostable unconverted luminescence from single lanthanide-doped nanocrystals. *Proceedings of the National Academy of Sciences of the United States of America* **106**, 10917–10921, doi:10.1073/pnas.0904792106 (2009).
30. Lu, Y., Xi, P., Piper, J. A., Huo, Y. & Jin, D. Time-gated orthogonal scanning automated microscopy (OSAM) for high-speed cell detection and analysis. *Sci. Rep.* **2**, 837, doi:10.1038/srep00837 (2012).
31. Lu, Y. *et al.* On-the-fly decoding luminescence lifetimes in the microsecond region for lanthanide-encoded suspension arrays. *Nature Communications*, doi:10.1038/ncomms4741 (2014).
32. Lu, Y. *et al.* Tunable lifetime multiplexing using luminescent nanocrystals. *Nature Photonics* **8**, 33–37, doi:10.1038/nphoton.2013.322 (2014).
33. Yuan, J. L., Wang, G. L., Kimura, H. & Matsumoto, K. Highly sensitive time-resolved fluoroimmunoassay of human immunoglobulin E by using a new europium fluorescent chelate as a label. *Analytical biochemistry* **254**, 283–287, doi:10.1006/abio.1997.2444 (1997).
34. Osseni, S. A. *et al.* Gadolinium oxysulfide nanoparticles as multimodal imaging agents for T2-weighted MR, X-ray tomography and photoluminescence. *Nanoscale* **6**, 555–564, doi:10.1039/c3nr03982j (2013).

### Acknowledgments

The authors acknowledge Dr. Benjamin Johnston (Macquarie OptoFab Node, Australian National Fabrication Facility) for laser micromachining to modify the optical chopper blades, the financial support from Australian Research Council (DP1095465, LP130100517, and FT130100517), Macquarie University Research Fellowship (Y.L.), and International Macquarie University Research Excellence Scholarships (L.Z. and X.Z.). Y.L. and D.J. acknowledge the International Society for Advancement of Cytometry for support as ISAC Scholars.

### Author contributions

Y.L. and D.J. conceived the project, designed the experiments and supervised the research. L.Z., X.Z. and D.J. were primarily responsible for microscopy setups, evaluation, data collection and analysis. L.Z., X.Z., Y.L. and D.J. prepared figures and wrote the main manuscript text. W.D., S.L., J.Y., Z.Y. and M.V. provided the samples and conducted image data analysis. J.M.D., E.M.G. and J.A.P. contributed to data analysis and manuscript preparation.

### Additional information

**Supplementary information** accompanies this paper at <http://www.nature.com/scientificreports>

**Competing financial interests:** The authors declare no competing financial interests.

**How to cite this article:** Zhang, L. *et al.* Practical Implementation, Characterization and Applications of a Multi-Colour Time-Gated Luminescence Microscope. *Sci. Rep.* **4**, 6597; DOI:10.1038/srep06597 (2014).



This work is licensed under a Creative Commons Attribution 4.0 International License. The images or other third party material in this article are included in the article's Creative Commons license, unless indicated otherwise in the credit line; if the material is not included under the Creative Commons license, users will need to obtain permission from the license holder in order to reproduce the material. To view a copy of this license, visit <http://creativecommons.org/licenses/by/4.0/>

## Practical Implementation, Characterization and Applications of a Multi-Colour Time-Gated Luminescence Microscope

Lixin Zhang<sup>1</sup>, Xianlin Zheng<sup>1</sup>, Wei Deng<sup>1</sup>, Yiqing Lu<sup>1\*</sup>, Severine Lechevallier<sup>2</sup>, Zhiqiang Ye<sup>3</sup>, Ewa Goldys<sup>1</sup>, Judith M. Dawes<sup>1</sup>, James A Piper<sup>1</sup>, Jingli Yuan<sup>3</sup>, Marc Verelst<sup>2</sup>, Dayong Jin<sup>1\*</sup>

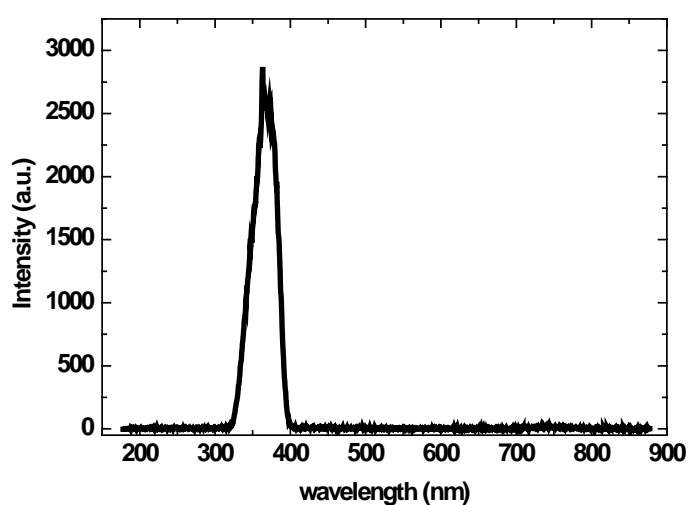
<sup>1</sup>Advanced Cytometry Labs, ARC Centre of Excellence for Nanoscale BioPhotonics (CNBP), Macquarie University, Sydney, NSW 2109, Australia

<sup>2</sup>Centre d'Élaboration de Matériaux et d'Études Structurales (CERMES - CNRS), Paul Sabatier University, France

<sup>3</sup>State Key Laboratory of Fine Chemicals, School of Chemistry, Dalian University of Technology, Dalian 116024, China

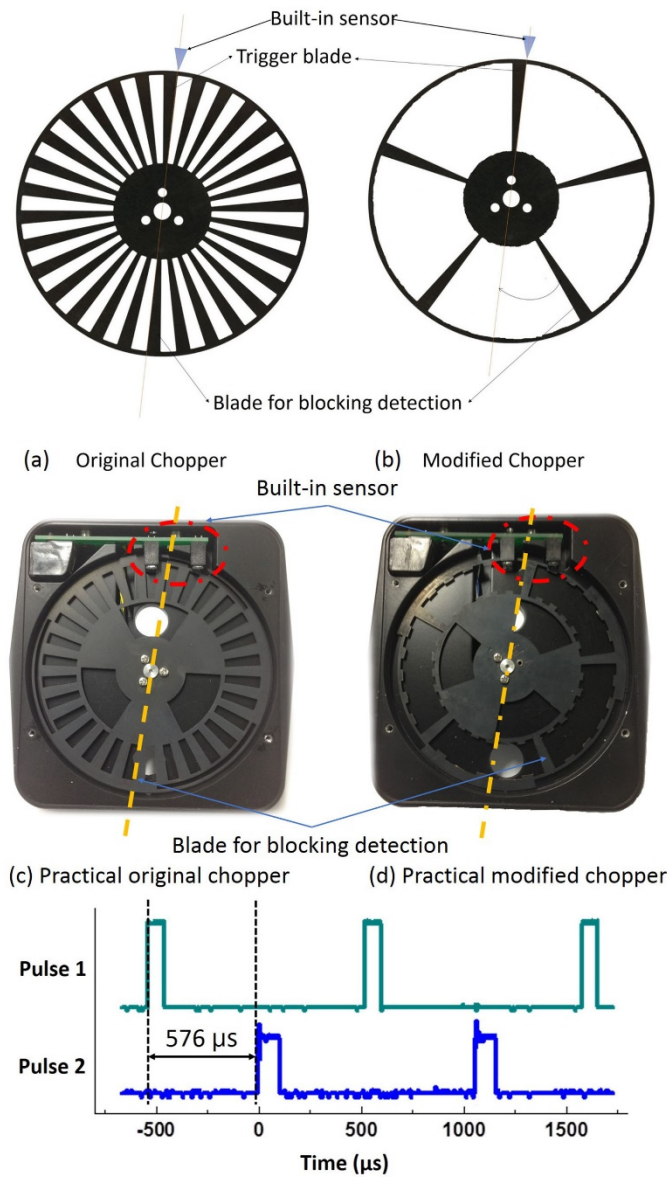
\*Email: [yiqing.lu@mq.edu.au](mailto:yiqing.lu@mq.edu.au); or: [dayong.jin@mq.edu.au](mailto:dayong.jin@mq.edu.au)

### S1. Xenon lamp excitation spectrum

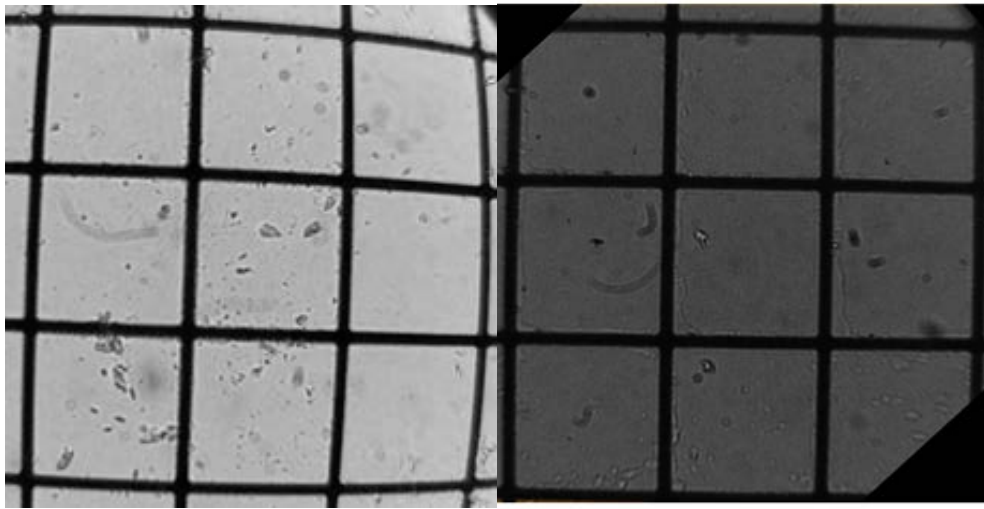


**Figure S1.** The excitation light from the xenon flash lamp has a spectral region from 320 nm to 400 nm, after passing through a UV band-pass filter (U-360, Edmund)

## S2. Modification of chopper blades



**Figure S2.** The induced time delay between the sensor trigger blade and the detection blocking blade in the modified chopper

**S3. Correction of optical distortion**

**Figure S3.** A wide-field image with barrel distortion (left), and its improved image without barrel distortion (right), after all optical components are aligned to be exactly coaxial. Each grid represents  $50 \times 50 \mu\text{m}^2$ .

#### S4. Image analysis to determine the signal-to-background ratio

The average signal and background levels for the red and the green channels of the images captured under the non-time-gated mode and the time-gated mode were analysed based on the procedures illustrated below, with the two images in Figure S4 as the example. Matlab was used in this study, but other image processing software, such as ImageJ, can also be used.

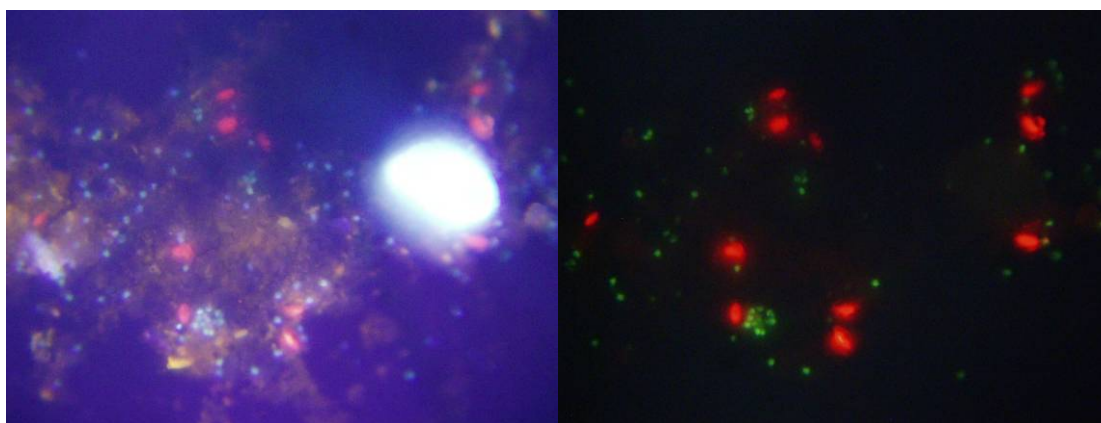


**Figure S4.** The non-time-gated (left) and time-gated (right) dual-colour images to be referred to in the image analysis demonstration. Each image represents  $225 \times 300 \mu\text{m}^2$ .

##### S4.1 Analysing signal levels in time-gated images

The time-gated colour image was split into the red, green and blue channels. Figure S4.1-1 shows the monocolour images of the red and green channels, while the blue channel was not considered in the following analysis.

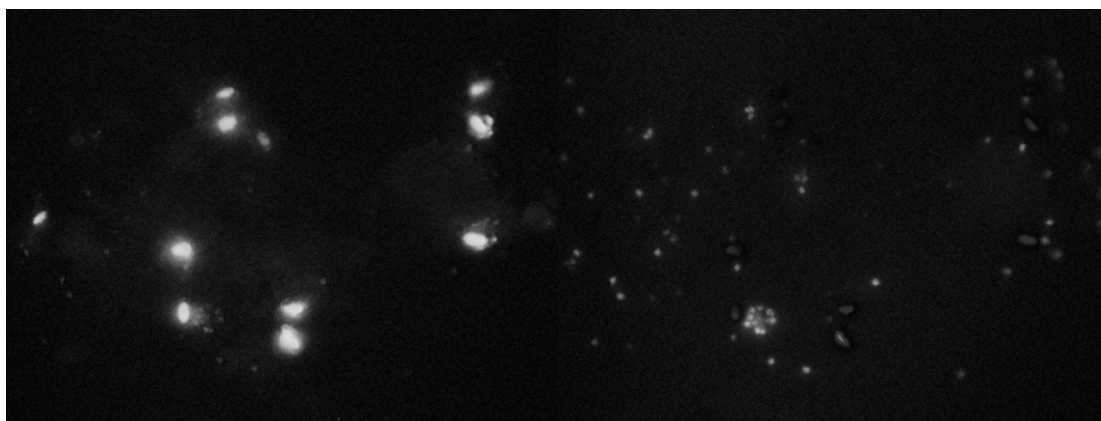


**Figure S4.1-1** The red (left) and green (right) channels of the time-gated image.

Image masks with thresholds equal to 0.3 times the maximum intensities in respective channels were applied on these monocolour images to effectively select target cells, as shown in Figure S4.1-2.

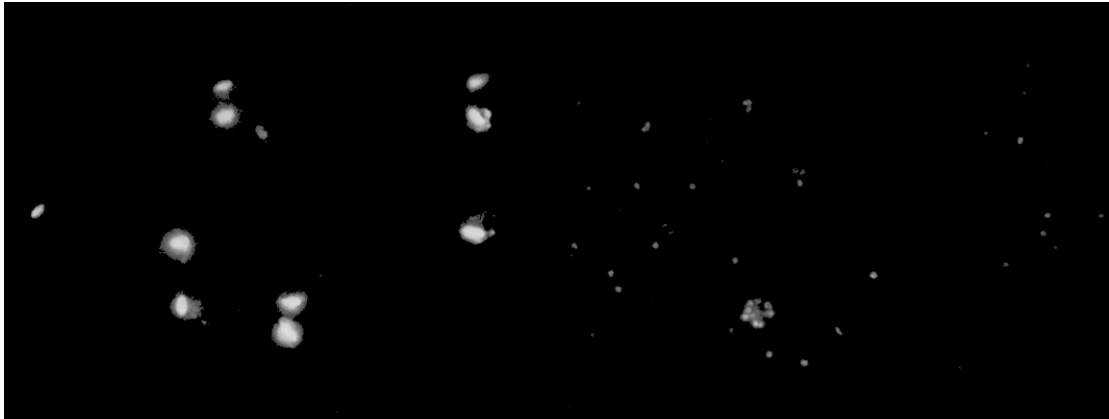


**Figure S4.1-2** The time-gated monocolour images with masks to select target cells, for the red channel (left) and the green channel (right).

The maximum, minimum and average signal intensities were obtained for the masked areas.

#### **S4.2 analysing background levels in time-gated images**

The above masks were reversed and then applied to the images in Figure S4.1-1 again, to select the non-target areas, as shown in Figure S4.2, before the maximum, minimum and average background intensities were calculated.

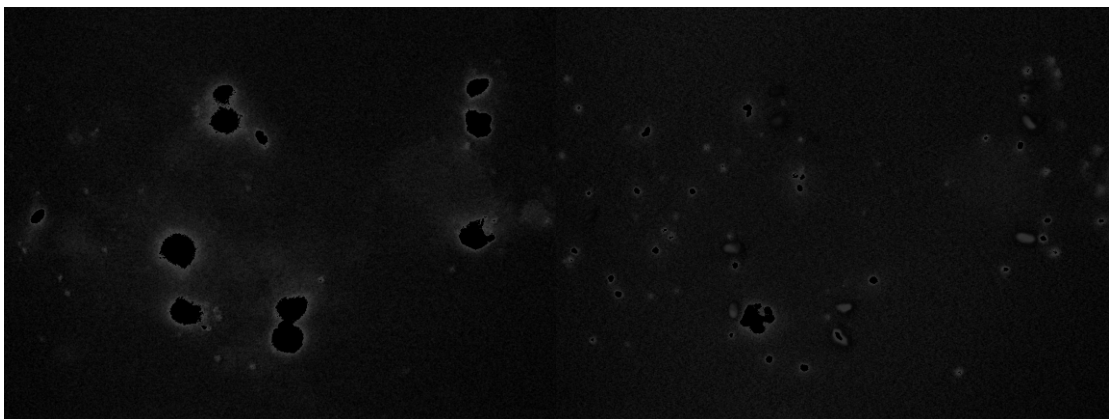


**Figure S4.2** The time-gated monocolour images with background areas masked for the red channel (left) and the green channel (right).

### S4.3 Analysing signal levels in non-time-gated images

The non-time-gated colour image was split into the red, green and blue channels, as shown in Figure S4.3-1 (again, the blue channel was ignored).

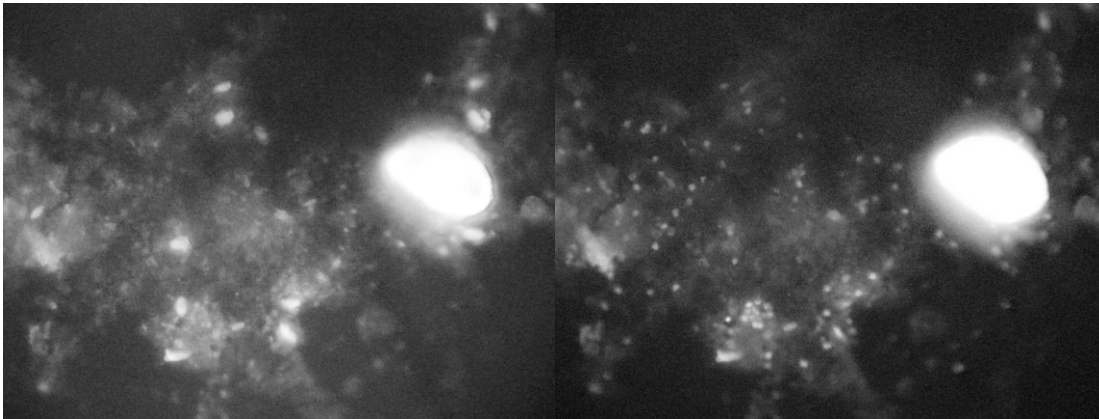


**Figure S4.3-1** The red (left) and green (right) channels of the non-time-gated image.

The same masks used in S4.1 were applied to select the areas that contained target cells, and the maximum, minimum and average signal intensities were calculated.



**Figure S4.3-2.** The non-time-gated monocolour images with masks selecting target cells, for the red channel (left) and the green channel (right).

### S4.4 Analysing background levels in non-time-gated images

The same masks used in S4.2 were applied to the images in Figure S4.3-1, to select the non-target areas, as shown in Figure S4.4, before the maximum, minimum and average background intensities were calculated.

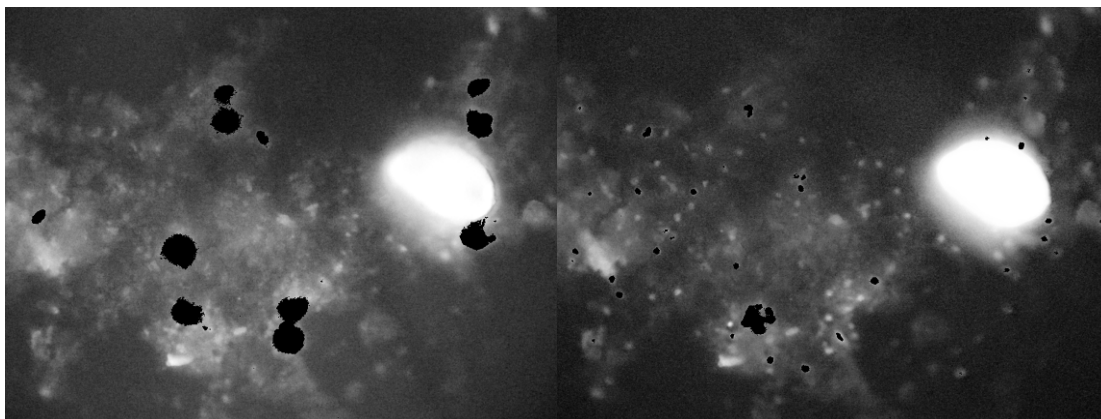


**Figure S4.4.** The non-time-gated monochrome images with background areas masked for the red channel (left) and the green channel (right).

**Table S1.** Signal and background levels of the red channel for ten pairs of images under non-time-gated and time-gated modes.

Luminescence from Eu complexes measured in the red channel							
	Image No.	S_max	S_min	S_avg	B_max	B_min	B_avg
Non-time-gated mode	1	252	75	167	255	11	82
	2	221	74	147	183	14	51
	3	168	42	105	126	0	29
	4	239	63	150	254	20	81
	5	219	37	112	107	0	26
	6	217	31	112	182	0	42
	7	219	34	122	109	0	23
	8	219	38	114	118	0	28
	9	226	34	129	173	3	42
	10	208	35	105	128	2	33
Time-gated mode	1	228	69	133	68	0	15
	2	220	67	130	66	0	10
	3	205	62	133	61	0	8
	4	222	67	144	66	0	12
	5	220	67	137	66	0	11
	6	221	67	141	66	0	9
	7	220	67	147	66	0	8
	8	222	67	142	66	0	12
	9	222	67	132	66	0	14
	10	222	67	127	66	0	11

**Table S2.** Signal and background levels of the green channel for ten pairs of images under non-time-gated and time-gated modes.

Luminescence from Tb complexes measured in the green channel							
	Image No.	S_max	S_min	S_avg	B_max	B_min	B_avg
Non-time-gated mode	1	252	46	144	255	11	84
	2	221	38	101	213	14	52
	3	108	23	71	168	0	29
	4	241	57	190	254	20	82
	5	102	23	58	219	0	27
	6	217	18	79	217	0	43
	7	131	17	41	219	0	24
	8	219	19	64	219	0	30
	9	226	16	107	226	3	44
	10	103	18	58	208	2	34
Time-gated mode	1	194	59	91	58	0	15
	2	111	34	45	33	0	11
	3	178	54	80	53	0	9
	4	114	35	47	34	0	11
	5	206	62	91	61	0	10
	6	184	56	74	55	0	9
	7	181	55	66	54	0	11
	8	188	57	78	56	0	11
	9	179	54	73	53	0	11
	10	189	57	89	56	0	10

### S5. Imaging results under UV LED excitation

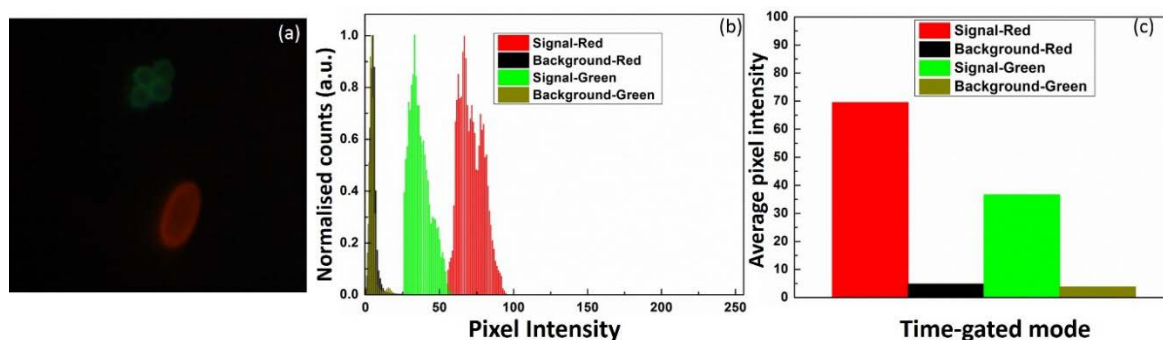


**Figure S5.** Imaging results under UV LED excitation. (a) Dual-colour time-gated image of Eu-labelled *Giardia* and Tb-labelled *Cryptosporidium*, with an exposure time of 15 seconds. (b) Pixel intensity histograms of the signal and background levels in the red and green channels. (c) Bar chart showing the average signal and background levels. The signal-to-background ratios are 70:5.6 for the red channel and 37:4.2 for the green channel.

### S6. Calculation of the crosstalk

In addition to time gating, accurate quantification of the luminescence intensities for the two pathogens requires calibration of the crosstalk between the red and green channels, which is caused by the satellite emission peaks of the Eu and Tb complexes.

The relative responsivity curves for the red, green and blue channels of the Olympus DP71 camera can be found in its user manual available online, as shown in Figure S6.1. The curves were digitized using the GetData Graph Digitizer software.

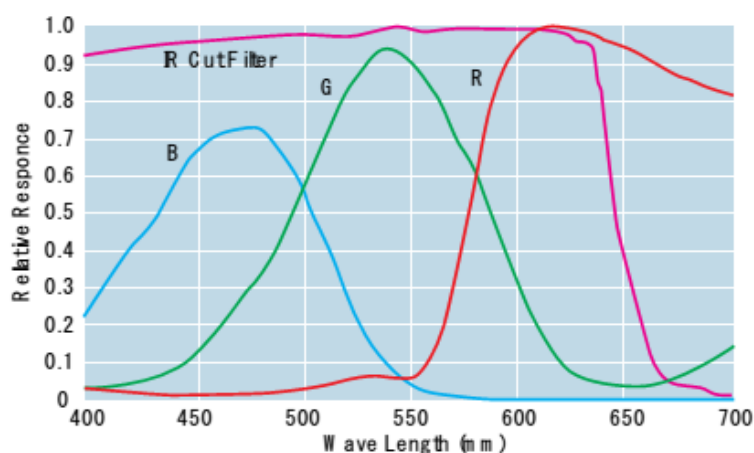


**Figure S6.1** Relative responsivity curves for the Olympus DP71 camera.

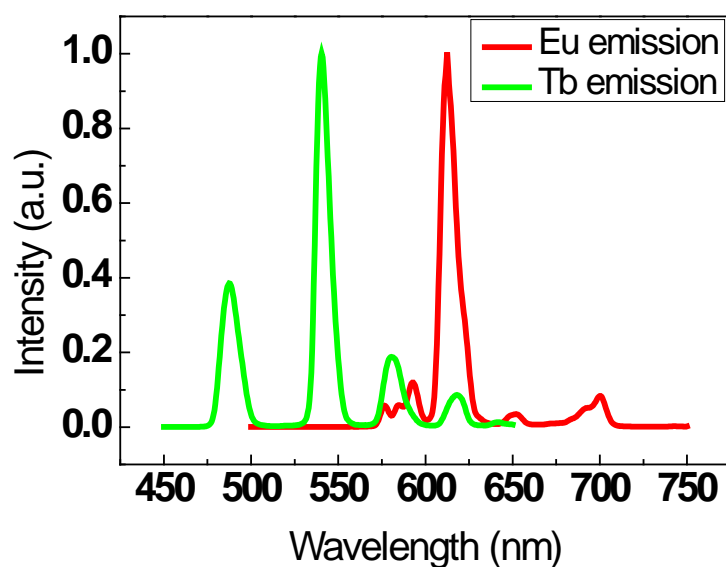


**Figure S6.2** Emission spectra of the Eu and Tb complexes.

The emission spectra of the Eu and Tb complexes, as shown in Figure S11, were multiplied by the three responsivity curves, respectively, followed by normalisation, to calculate their contribution proportions to the three colour channels. The results are given in Table S3.

**Table S3.** The contributions of the Eu and Tb emission to the colour channels of the camera.

	Red Channel	Green Channel	Blue Channel
Eu emission	78.6%	13.6%	7.8%
Tb emission	19.2%	59.9%	20.9%

### S7. Co-localization analysis of the nanoparticle images

The time-gated luminescence image of the Eu nanoparticles and its corresponding TEM image were compared using the colocalization function in the ImageJ software. The images were first resized to ensure they covered the identical area, before transformed into 8-bit grey-scale, as shown in Figure S7.

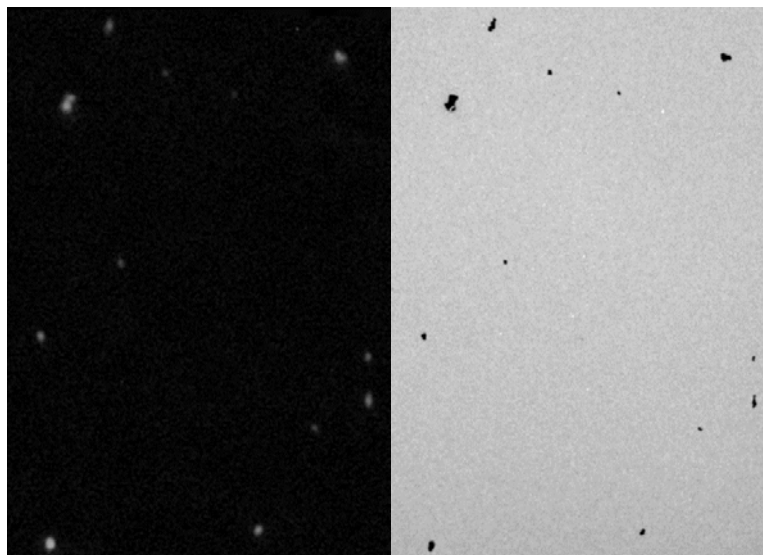


**Figure S7.** Grey-scale images of the original time-gated luminescence image (left) and the TEM image (right) of the Eu nanoparticles.

They were imported into the colocalization plugin to generate the co-localisation image, as shown in Figure 4d in the main text.

## 2.3 Paper 2

Bo Song, Zhiqing Ye, Yajie Yang, Hua Ma, **Xianlin Zheng**, Dayong Jin and Jingli Yuan, "Background-free in-vivo Imaging of Vitamin C using Time-gateable Responsive Probe" *Scientific Reports*, 2015, DOI:10.1038/srep14194.

In this published work, I replicated the multi-colour time-gated microscope and trained the users for our collaborators at Dalian University of Technology in China. *In-vivo* imaging of Vitamin C in live *Daphnia magna* was successfully demonstrated, providing an evident outcome of my first project. This paper is thus appended to this chapter. Author contributions to this paper are summarised in [Table 2-2](#).

**TABLE 2-2** Summary of author contributions to paper 1 following the order of authors.

	B.S	Z.Y	Y.Y	H.M	X.Z	D.J	J.Y
Experiment Design	●						●
System Setup					●		
Sample Preparation	●		●	●			
Data Collection	●	●	●	●			
Analysis	●	●					
Figures	●				●		
Manuscript	●					●	●

# SCIENTIFIC REPORTS

## OPEN Background-free *in-vivo* Imaging of Vitamin C using Time-gateable Responsive Probe

Received: 16 April 2015  
Accepted: 17 August 2015  
Published: 16 September 2015

Bo Song<sup>1</sup>, Zhiqing Ye<sup>2</sup>, Yajie Yang<sup>2</sup>, Hua Ma<sup>3</sup>, Xianlin Zheng<sup>2</sup>, Dayong Jin<sup>2</sup> & Jingli Yuan<sup>1</sup>

Sensitive optical imaging of active biomolecules in the living organism requires both a molecular probe specifically responsive to the target and a high-contrast approach to remove the background interference from autofluorescence and light scatterings. Here, a responsive probe for ascorbic acid (vitamin C) has been developed by conjugating two nitroxide radicals with a long-lived luminescent europium complex. The nitroxide radical withholds the probe on its "off" state (barely luminescent), until the presence of vitamin C will switch on the probe by forming its hydroxylamine derivative. The probe showed a linear response to vitamin C concentration with a detection limit of 9.1 nM, two orders of magnitude lower than that achieved using electrochemical methods. Time-gated luminescence microscopy (TGLM) method has further enabled real-time, specific and background-free monitoring of cellular uptake or endogenous production of vitamin C, and mapping of vitamin C in living *Daphnia magna*. This work suggests a rational design of lanthanide complexes for background-free small animal imaging of biologically functional molecules.

Ascorbic acid (vitamin C), an essential nutrient for humans, has been well known for a long time because of its essential role in the prevention of deficiency diseases, for example, scurvy<sup>1</sup>. It helps also in healthy cell development, calcium absorption, the healing of injuries and burns, and the synthesis of collagen, blood vessels, cartilage, bone and tendons<sup>2-4</sup>. In recent years vitamin C has attracted considerable attentions for its role in the promotion of healthy brain aging and potential in cancer treatment<sup>5,6</sup>. An increasing number of studies have been focused on clarifying the biological roles of vitamin C, but one of the most important difficulties preventing these studies attributes to the lacking of a robust method to monitor vitamin C in living systems.

The most commonly reported analytical methods for vitamin C are based on electrochemical approaches<sup>7,8</sup>, but the interference from other non-specific molecules, such as uric acid and dopamine, can seriously disturb the results in real-time monitoring of vitamin C in living samples. The fluorescent microscopy using a responsive fluorescent probe could provide superior advantages in high sensitivity and selectivity to investigate vitamin-induced inhibition of cancer cell growth, but developing such functional probes is still in its early stage<sup>9</sup>. A vitamin C-responsive fluorescence probe can be designed by linking a nitroxide radical to a fluorophores<sup>9-11</sup>, in which design the nitroxide radical moiety not only quenches the fluorescence of the probe by intramolecular electron exchange interaction but also specifically reacts with vitamin C to switch on the fluorescence of the probe<sup>9-11</sup>. But due to their insufficient sensitivity, this kind probe can only provide quantification of vitamin C in aqueous media at relatively high concentration range (>μM)<sup>10,11</sup>, and also requires long incubation time and high concentration of extracellular vitamin C for the intracellular imaging demonstration<sup>9</sup>.

On the other hand, time-gated detection technique using lanthanide complexes as luminescence probes has been widely used to achieve highly sensitive luminescence immunoassay<sup>12</sup>, DNA hybridization

<sup>1</sup>State Key Laboratory of Fine Chemicals, School of Chemistry, Dalian University of Technology, Dalian 116024, P. R. China. <sup>2</sup>Advanced Cytometry Labs, ARC Centre of Excellence for Nanoscale BioPhotonics (CNBP), Macquarie University, NSW 2109, Sydney, Australia. Correspondence and requests for materials should be addressed to J.Y. (email: jlyuan@dlut.edu.cn)

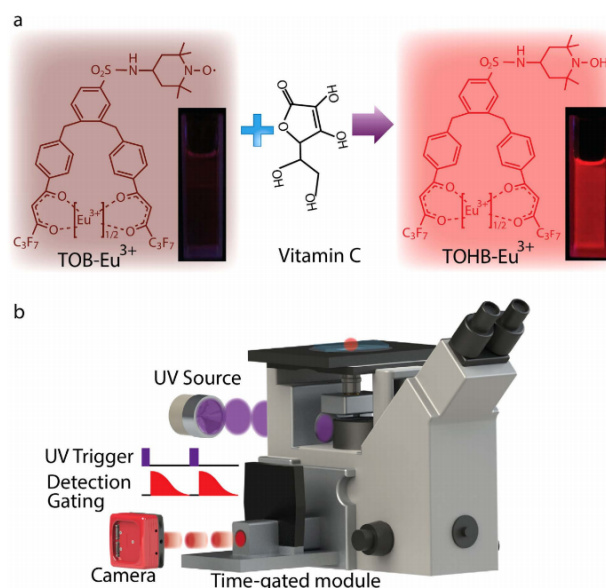


**Figure 1.** Schematic diagram illustrates the design of a “turn-on” molecular probe specific to vitamin C with long-lived luminescence suitable for time-gated luminescence microscopy (TGLM) system. (a) The luminescence probe TOB-Eu<sup>3+</sup> turns on in its hydroxylamine derivative form of TOHB-Eu<sup>3+</sup> in the presence of vitamin C (photographs show luminescence colours of the complex solutions under a 365 nm UV lamp). (b) The TGLM system employs a rapid-switching flash lamp synchronized to a time-gated optical chopper in front of the camera. The camera is externally shut off during the excitation pulse period, and a short time delay is given to allow the short-lived autofluorescence to vanish before the chopper opens for long-lived luminescence detection in absence of optical backgrounds.

assay<sup>13</sup>, evaluation of enzyme activities<sup>14</sup> and detection of various intracellular analytes<sup>15–20</sup>. Compared to the conventional organic fluorescence probes, lanthanide-based probes exhibit several unique features including large Stokes shifts, sharp emission profiles and long emission lifetimes. The exceptionally long luminescence lifetime (>10 μs) enables time-gated luminescence microscopy (TGLM) imaging of rare cell types<sup>21</sup> and trace amount of molecules<sup>22</sup> with high signal-to-noise contrast ratio and therefore ultra-high sensitivity, since all the short-lived autofluorescence from biological components and excitation scatterings by the optics can be efficiently eliminated (time-gated). Thus, once a lanthanide complex-based responsive probe can be developed specific for vitamin C TGLM imaging, it will be applied to monitor vitamin C's distribution and dynamic activities in living cells and laboratory animals.

In this work, by linking a stable free radical of 2,2,6,6-tetramethyl-1-oxy-4-aminopiperidine (4-amino-TEMPO) to a highly luminescent Eu<sup>3+</sup> complex, 1,2-bis[4'-(1'',1'',1'',2'',2'',3'',3''-heptafluoro-4'',6''-hexanedion-6''-yl)-benzyl]-4-chlorosulfobenzene-Eu<sup>3+</sup> (BHHBCB-Eu<sup>3+</sup>), we designed and synthesized a time-gated luminescence probe for detecting vitamin C. The designed Eu<sup>3+</sup> complex probe, TOB-Eu<sup>3+</sup> (Fig. 1), is weakly luminescent due to the strong luminescence quenching effect of two TEMPO radicals. It can specifically react with vitamin C to afford its hydroxylamine derivative, TOHB-Eu<sup>3+</sup>, accompanied by a remarkable luminescence enhancement, which allows the probe to be favorably used for the *in vivo* time-gated luminescence detection of vitamin C in aqueous media, living cell samples and laboratory animals.

## Results

**The synthesis.** The new ligand TOB was synthesized by covalently conjugating 4-amino-TEMPO to BHHBCB through the formation of sulfonamide. The corresponding complex, TOB-Eu<sup>3+</sup>, was synthesized by mixing double molar of TOB with europium(III) triflate in acetonitrile, and the reduced product, TOHB-Eu<sup>3+</sup>, was obtained by reacting TOB-Eu<sup>3+</sup> with vitamin C in acetonitrile. All the above compounds were well characterized by HPLC, ESI-MS, and CHN elementary analyses (Figure S1–S2).

Complex	$\lambda_{em,max}$ (nm)	$\epsilon_{339nm}$ ( $cm^{-1}M^{-1}$ )	$\lambda_{ex,max}$ (nm)	$\Phi$ (%) <sup>1</sup>	$\tau$ (ms)
TOB-Eu <sup>3+</sup>	329	$4.13 \times 10^4$	608	7.5	0.18
TOHB-Eu <sup>3+</sup>	332	$6.53 \times 10^4$	608	73.7	0.38

**Table 1. Luminescence properties of TOB-Eu<sup>3+</sup> and TOHB-Eu<sup>3+</sup> in 1:1 ethanol-0.05 M Tris-HCl buffer of pH 7.5.** <sup>1</sup>Quantum yields were measured in 3:1 ethanol-0.05 M Tris-HCl buffer of pH 7.5.

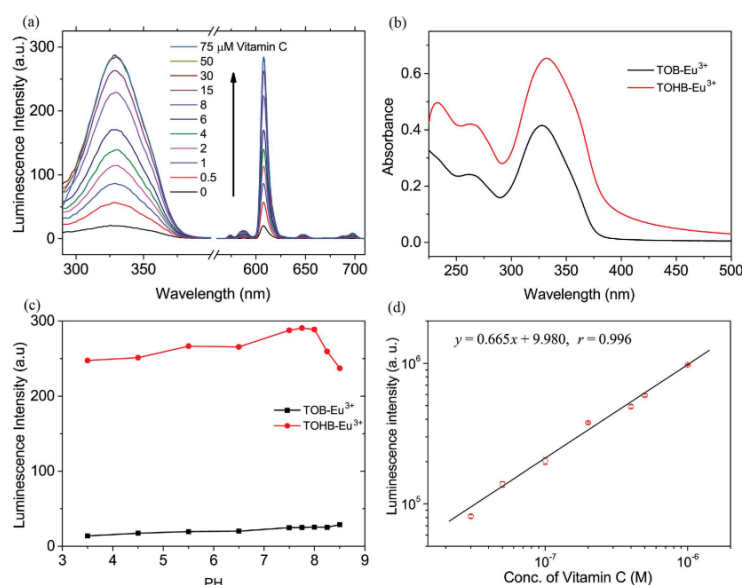


**Figure 2. Basic characterizations of the responsive probe TOB-Eu<sup>3+</sup> and its on-state compound TOHB-Eu<sup>3+</sup>.** (a) Time-gated excitation ( $\lambda_{em} = 608$  nm) and emission ( $\lambda_{ex} = 330$  nm) spectra of TOB-Eu<sup>3+</sup> (0.5  $\mu$ M) in the presence of different concentrations of vitamin C in 1:1 ethanol-0.05 M Tris-HCl buffer of pH 7.5. (b) UV-vis absorption spectra of TOB-Eu<sup>3+</sup> (10  $\mu$ M, black) and TOHB-Eu<sup>3+</sup> (10  $\mu$ M, red) in 1:1 ethanol-0.05 M Tris-HCl buffer of pH 7.5. (c) Effects of pH on the luminescence intensities of TOB-Eu<sup>3+</sup> (0.5  $\mu$ M, black) and TOHB-Eu<sup>3+</sup> (0.5  $\mu$ M, red) in solutions of 0.05 M Tris-HCl/ethanol (v/v = 1:1) with different pH values. (d) Calibration curve for vitamin C measured on Perkin Elmer Victor 1420 multilabel counter.

**Luminescence properties.** The luminescence properties of TOB-Eu<sup>3+</sup> and TOHB-Eu<sup>3+</sup> were determined in 1:1 ethanol-0.05 M Tris-HCl buffer of pH 7.5, and the results were summarized in Table 1. Both TOB-Eu<sup>3+</sup> and TOHB-Eu<sup>3+</sup> showed almost the same maximum excitation and emission wavelengths at  $\sim 330$  nm and 608 nm, respectively, and exhibited a typical Eu<sup>3+</sup> emission pattern (Fig. 2a) consisting of several discrete bands between 580 and 710 nm corresponding to the  $^5D_0 \rightarrow ^7F_1$  ( $J = 0-4$ ) transitions of Eu<sup>3+</sup>. There is no remarkable differences in the UV spectrum profiles between TOB-Eu<sup>3+</sup> and TOHB-Eu<sup>3+</sup>, but the molar absorption coefficient of TOHB-Eu<sup>3+</sup> increased by 0.5 times than that of TOB-Eu<sup>3+</sup> (Fig. 2b). After the vitamin C reduction, the luminescence quantum yield and lifetime of TOB-Eu<sup>3+</sup> were 10-fold and 2-fold increased, respectively. These results suggest that TOB-Eu<sup>3+</sup> can act as a turn-on luminescence probe for the time-gated luminescence detection of vitamin C.

**pH stability.** Furthermore, the effects of pH on the luminescence intensities of TOB-Eu<sup>3+</sup> and TOHB-Eu<sup>3+</sup> were examined. As shown in Fig. 2c, the luminescence intensity of TOB-Eu<sup>3+</sup> is stable in the range of pH 3.5–8.5, while that of TOHB-Eu<sup>3+</sup> shows slight increases when pH is increased from 3.5 to 8.0. At pH > 8.0, luminescence intensity of TOHB-Eu<sup>3+</sup> shows distinct decreases, which might be due to the deprotonation of HO-TEMPO moiety in TOHB-Eu<sup>3+</sup>.

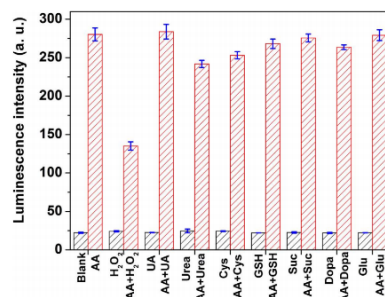


**Figure 3. Specificity evaluations.** Luminescence intensities of the products of TOB-Eu<sup>3+</sup> (5.0 μM) reacted with 200 μM different biological reductants and 400 μM H<sub>2</sub>O<sub>2</sub> in 1:1 ethanol-0.05 M Tris-HCl buffer of pH 7.5 (black shade bars). The red shade bars show the luminescence intensities of the products of TOB-Eu<sup>3+</sup> (5.0 μM) reacted with 200 μM different biological reductants and 400 μM H<sub>2</sub>O<sub>2</sub> in the presence of ascorbic acid (AA) (100 μM) in the buffer.

**Quantitative detection.** To evaluate the applicability of TOB-Eu<sup>3+</sup> as a time-gated luminescence probe for the quantitative detection of vitamin C, the time-gated emission spectra of TOB-Eu<sup>3+</sup> in the presence of different concentrations of vitamin C were recorded in 1:1 ethanol-0.05 M Tris-HCl buffer of pH 7.5. As shown in Fig. 2a, upon reaction with different concentrations of vitamin C, the luminescence intensity of the probe gradually increased with up to 14.5-fold enhancement, which indicates the formation of TOHB-Eu<sup>3+</sup> as the turned-on state of the probe with strong luminescence. This exhibits much higher contrast ratio than that achieved by the reported phthalocyaninatosilicon probe<sup>9</sup>. When the measurements were carried out on a more sensitive Perkin Elmer Victor 1420 multilabel counter (96-well microtiter plates as cuvettes) in time-gated detection mode, the dose-dependent luminescence enhancement showed a good linearity between the luminescence intensity and the vitamin C concentration (Fig. 2d). The detection limit for vitamin C, calculated as the concentration corresponding to triple standard deviations of the background signal, is 9.1 nM, achieving two orders of magnitude lower than that of the electrochemical methods<sup>23</sup>.

**Specificity.** To evaluate the response specificity of TOB-Eu<sup>3+</sup> to vitamin C, the reactions of TOB-Eu<sup>3+</sup> with different biological reductants were examined under the same conditions. As shown in Fig. 3, the luminescence intensity of TOB-Eu<sup>3+</sup> did not respond to reduced glutathione (GSH), dopamine (Dopa), cysteine (Cys), succinimide (Suc), uric acid (UA), urea, glucose (Glu) and H<sub>2</sub>O<sub>2</sub>, whereas a remarkable increase was observed after the probe reacted with vitamin C (ascorbic acid, simplified as AA in Fig. 3). Furthermore, the competition experiments were carried out to evaluate the luminescence response of TOB-Eu<sup>3+</sup> to vitamin C in the presence of coexisting biological reductants. The results indicate that, except for H<sub>2</sub>O<sub>2</sub>, the chosen biological reductants have no significant influences on the luminescence response of TOB-Eu<sup>3+</sup> to vitamin C (Fig. 3, red shade bars). The effect of H<sub>2</sub>O<sub>2</sub> can be attributed to the oxidation of vitamin C by H<sub>2</sub>O<sub>2</sub>, which forms dehydroascorbic acid (DHA) to block the reaction of TOB-Eu<sup>3+</sup> with vitamin C, and thus the luminescence response of TOB-Eu<sup>3+</sup> to vitamin C is obviously reduced. It was reported that vitamin C at high levels can act as prodrug to deliver a significant flux of H<sub>2</sub>O<sub>2</sub> to tumors<sup>24</sup>, so the mentioned finding could be useful for detection of vitamin C-mediated H<sub>2</sub>O<sub>2</sub> generation. In summary the luminescence probe TOB-Eu<sup>3+</sup> is highly specific for detecting the presence of vitamin C.

**Time-gated luminescence imaging and quantification of extracellular vitamin C uptake in living cells.** Before describing luminescence imaging experiments, the influence of TOB-Eu<sup>3+</sup> on cell proliferation and viability was examined by the MTT assay. As shown in Figure S3, the cell viabilities remained still at above 90% after incubation with up to 100 μM of TOB-Eu<sup>3+</sup> for 24 h, which indicates that the new probe is biocompatible with low cytotoxicity for the sensing of vitamin C in living cells.

It is well-known that human body cannot synthesize vitamin C because the gene encoding L-gulonolactoneoxidase (GLO), the enzyme required for the last step in ascorbate synthesis, is not functional<sup>25</sup>. Thus, dietary intake of vitamin C becomes vital. The typical human diet contains both vitamin C and DHA, while vitamin C is accumulated in cells by Na<sup>+</sup>-dependent vitamin C transporters (SVCTs), and DHA is absorbed via a Na<sup>+</sup>-independent facilitative glucose transporters (GLUTs) followed by intracellular reduction<sup>26–28</sup>.

To evaluate the feasibility of TOB-Eu<sup>3+</sup> for the luminescent imaging of vitamin C in living cells, the cellular uptake of vitamin C and the endogenous production of vitamin C by intracellular reduction of

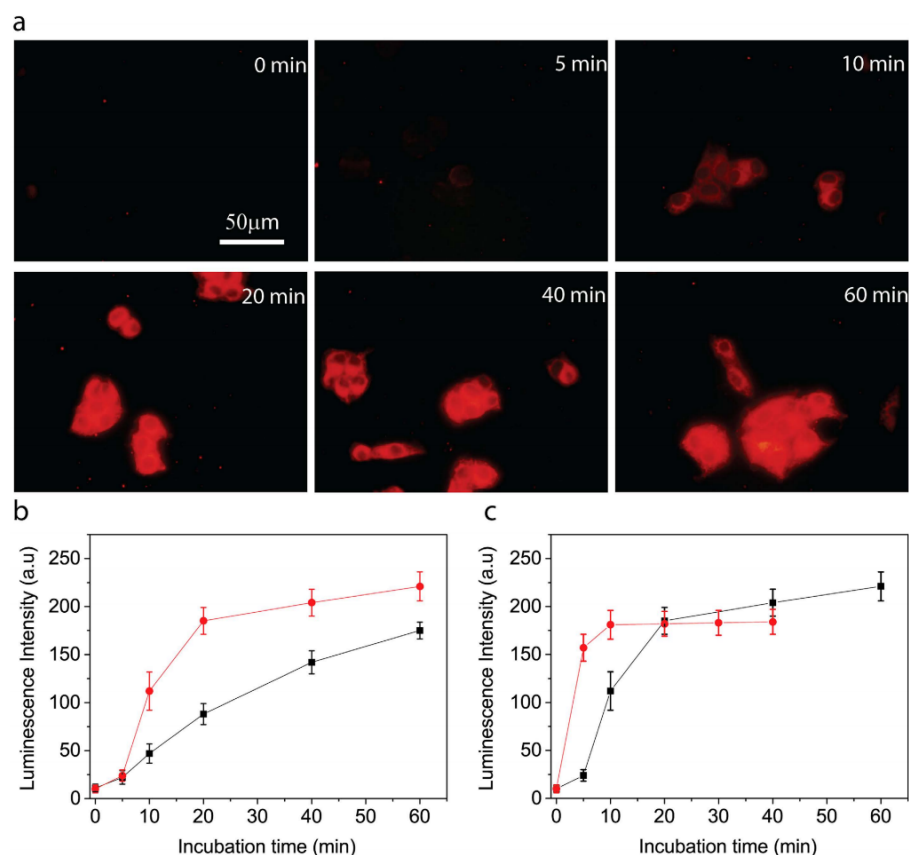


**Figure 4. Time-gated luminescence imaging and real-time quantifications of the extracellular vitamin C uptake and intracellular production of vitamin C in living cells.** (a) Time-gated luminescence microscopy images of HepG2 cells loaded with 1.0 mM vitamin C at different loading times and followed by incubation with 20  $\mu$ M TOB-Eu<sup>3+</sup> for 1 h. Scale bar: 50  $\mu$ m. (b) Time-gated luminescence intensities of HepG2 (●) and HeLa (●) cells loaded with 1.0 mM vitamin C for various incubation times and followed by incubation with 20  $\mu$ M TOB-Eu<sup>3+</sup> for 1 h. (c) Time-gated luminescence intensity of HepG2 cells loaded with 1.0 mM AA (●) or 1.0 mM DHA (●) for various incubation times and followed by incubation with 20  $\mu$ M TOB-Eu<sup>3+</sup>.

DHA were monitored using TOB-Eu<sup>3+</sup> as a probe. For investigating cellular uptake of vitamin C, human HepG2 cells were incubated with an isotonic saline solution containing 1.0 mM vitamin C for various incubation times. Then the vitamin C-loaded cells were incubated with 20  $\mu$ M TOB-Eu<sup>3+</sup> probes in the isotonic saline solution containing 0.5 mg/mL solubilizer, cremophor C040 for 1 h under the same condition. The luminescence images of the cells were recorded on a true-colour time-gated luminescence microscope<sup>29</sup>. As shown in Fig. 4, in the beginning of the loading process, cells without internalized vitamin C displayed negligibly weak luminescence. After vitamin C incubation for 10 minutes, the cells showed clearly observable luminescence, and luminescence intensities of cells were gradually increased with the increase of vitamin C loading time. These results demonstrate that the uptake process of vitamin C by HepG2 cells is successfully monitored by using our TOB-Eu<sup>3+</sup> probe. The amount of the probe per cell as measured by inductively coupled plasma-optical emission spectroscopy (ICP-OES) was  $\sim 1.5 \times 10^{-15}$  mol. Taking into account a cell volume of  $\sim 4.2 \times 10^3 \mu\text{m}^3$ , the intracellular concentration of

the probe can be estimated at  $\sim 0.36$  mM. Compared to the steady-state luminescence image, the background interference from blue autofluorescence of the cells and light scatterings were completely suppressed under time-gated mode, so that a high-contrast and background-free cell image with strongly red luminescence signals was recorded (Figure S4). It is notable that the luminescence signals originated from the reacted probes with the intracellular vitamin C were distributed over the whole cell except the nucleus, which is consistent with the reported fluorescence cell images of vitamin C using hydrophobic phthalocyaninatasilicon fluorophore as a probe<sup>9</sup>. Furthermore even incubated with TOB-Eu<sup>3+</sup> for 4 h, the HepG2 cells did not show obvious red luminescence in the cells (Figure S5). This result implied that the TOB-Eu<sup>3+</sup> probe could be stable in the cell and would not be reduced by other naturally existing intracellular reductants.

The TOB-Eu<sup>3+</sup> probe has been found to be sensitive in quantifying the time-dependent cellular uptake rate of vitamin C by different cell types. Using TOB-Eu<sup>3+</sup> probe, the cellular uptake of vitamin C by HeLa cells was also monitored (shown in the supplementary Figure S6), and the uptake rate of vitamin C by HeLa cells is slower than that by HepG2 cells (Fig. 4b), which could be due to the higher level express of SVCTs proteins in HepG2 cells<sup>30</sup>.

**Time-gated luminescence imaging and quantification of intracellular production of vitamin C in living cells.** Since DHA can be transported into cells and then reduced to vitamin C by intracellular reductants and enzyme systems, our TOB-Eu<sup>3+</sup> probe has been further verified to monitor the time-dependent production of vitamin C during the cellular uptake process of DHA. In buffer, DHA could not turn on the TOB-Eu<sup>3+</sup> probes, but HepG2 cells loaded by DHA for 5 minutes and incubated with TOB-Eu<sup>3+</sup> displayed bright red luminescence, and the luminescence intensity increased with the increase of the DHA-loading time (Fig. 4c and supplementary Figure S7). These results illuminate that, after transported into the cells, DHA could be reduced to vitamin C by intracellular reductants and enzyme systems, so that the probes were turned on by the intracellularly produced vitamin C and became strongly luminescent.

The quantification capability and rapid response of the TOB-Eu<sup>3+</sup> probe enable real-time monitoring of the transportation process of DHA into HepG2 cells or/and the intracellular reduction process of DHA. It is notable that DHA can be rapidly transported into HepG2 cells by GLUTs systems within 10 minutes, while extracellular vitamin C uptake requires approximately 20 minutes by SVCTs system to reach the same intracellular concentration of vitamin C (Fig. 4c). This finding confirms a recent report that the uptake of extracellular vitamin C lasted much longer than the uptake of DHA and its intracellular conversion to vitamin C in EA.hy926 cells (several hours vs. 15 minutes)<sup>31</sup>.

**In vivo imaging of vitamin C in laboratory animal.** A further exploratory effort has been made to evaluate TOB-Eu<sup>3+</sup> for imaging vitamin C in living *Daphnia magna*, a widely used laboratory animal as an indicator of aquatic ecosystem health and as a model organism in ecotoxicology<sup>32,33</sup>. While vitamin C plays an important role in protecting bioorganism against chemical pollutions such as ozone<sup>34</sup> and organochlorine<sup>35</sup>, it also shows considerable toxicity in the FETAX testing (Frog Embryo Teratogenesis Assay-Xenopus)<sup>36</sup>. Largely used in foods, animal feed, pharmaceutical formulations and cosmetic applications, the release of vitamin C into the aquatic environment and its effects on ecotoxicity remain largely unknown. The quantitative *in vivo* imaging of vitamin C in *Daphnia magna* could provide useful insights for understanding its bioaccumulation and effect on aquatic organisms. As shown in Fig. 5, *Daphnia magna*, treated by TOB-Eu<sup>3+</sup>, displayed only weak luminescence, but with vitamin C-loading and TOB-Eu<sup>3+</sup> incubation, showed strong and clear red luminescence. The head part, midgut and thoracic appendages of *Daphnia magna* exhibited stronger luminescence signals, which might be ascribed to the convenient contact of the probe with vitamin C in these parts. In the absence of time-gated detection as shown in Fig. 5d, *Daphnia magna* emit strongly blue autofluorescence under UV excitation. The red luminescence signals of probes overlapped with the blue autofluorescence of *Daphnia magna* (only a purple color was observed in Fig. 5d), which makes it difficult to unambiguously identify the target. Applying time-gated detection as shown in Fig. 5c, the background autofluorescence is substantially suppressed, so that a highly specific and background-free image of *Daphnia magna* with strong red luminescence signals was recorded.

It should be noted that no immobilization of *Daphnia magna* treated by TOB-Eu<sup>3+</sup> was observed, and the TOB-Eu<sup>3+</sup> treatment did not induce a significant change on the heart rate of *Daphnia magna* ( $\sim 200$  beats per minute) during the incubation<sup>37</sup>, which suggests that the probe is biocompatible and low-toxic for *in vivo* imaging of vitamin C in living bodies.

## Discussion

We have successfully developed a responsive luminescence probe, TOB-Eu<sup>3+</sup>, for specific recognition and background-free quantification of vitamin C in living cells and lab animals. Its potential has been comprehensively evaluated by the imaging and quantification of extracellular uptake and intracellular production of vitamin C in cancerous cells and laboratory animals *in vivo*. We presents a useful tool for visualizing the temporal and spatial distribution of vitamin C in cells, biological tissues and living organisms to facilitate the understanding of the roles of vitamin C and DHA in physiological, disease states and ecotoxicology. The rational design of lanthanide-based responsive probes suggests several additional

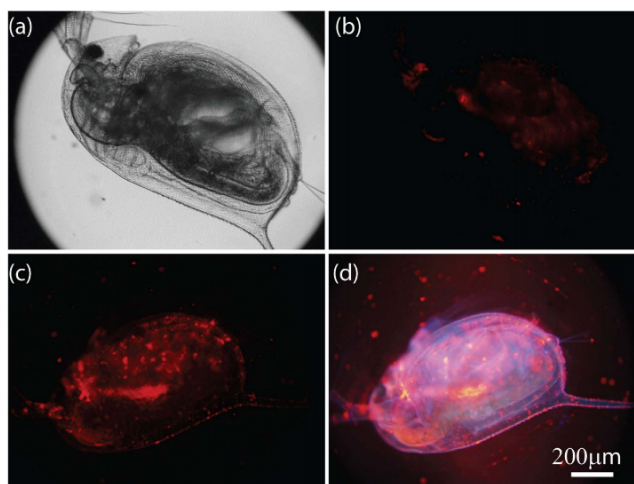


**Figure 5.** Time-gated *in vivo* imaging of vitamin C in living *Daphnia magna*. Bright-field (a) and time-gated luminescence images (b) of *Daphnia magna* incubated with 5.0  $\mu\text{M}$  TOB-Eu<sup>3+</sup> for 1 h. Time-gated (c) and steady-state (d) luminescence images of *Daphnia magna* loaded with 1.0 mM vitamin C for 40 min and followed by incubation with 5.0  $\mu\text{M}$  TOB-Eu<sup>3+</sup> for 1 h. Scale bar: 200  $\mu\text{m}$ .

favorable features including high specificity and sensitivity for functional biomolecules, pH-independent luminescence response over the physiological range, and long luminescence lifetime. These features are further enhanced by the high-contrast time-gated luminescence detection of analytes in complex biochemical environments. Therefore, this work further suggests that a library of responsive probes could be designed and synthesized for real-time quantitative imaging of active biomolecules in the living organisms with high specificity and high contrast, immunizing to the background interference from autofluorescence and light scatterings.

## Methods

**Materials and Physical Measurements.** BHHBCB was synthesized using previous method<sup>38</sup>. 4-Amino-TEMPO was purchased from TCI. Ascorbic acid, dehydroascorbic acid, dopamine, reduced glutathione, cysteine, succinimide, uric acid and dimethylaminopyridine were purchased from Sigma-Aldrich. Cultured HepG2 cells and HeLa cells were obtained from Dalian Medical University. Cultured *Daphnia magna* were obtained from Professor Jingwen Chen's group at School of Environmental Science and Technology, Dalian University of Technology. Unless otherwise stated, all chemical materials were purchased from commercial sources and used without further purification.

<sup>1</sup>H NMR spectra were measured on a Bruker Avance spectrometer (400 MHz). Mass spectra were measured on a HP1100 LC/MSD MS spectrometer. Elemental analysis was carried out on a Vario-EL analyser. Time-gated luminescence spectra were measured on a Perkin-Elmer LS 50B luminescence spectrometer with the settings of delay time, 0.2 ms; gate time, 0.4 ms; cycle time, 20 ms; excitation slit, 10 nm; and emission slit, 5 nm. Time-gated luminescence measurements using 96-well microtiter plates as cuvettes were carried out on a Perkin-Elmer Victor 1420 multilabel counter with the settings of delay time, 0.2 ms; window time (counting time), 0.4 ms; cycling time, 1.0 ms; excitation wavelength, 340 nm; and emission wavelengths, 615 nm. All bright-field and luminescence imaging measurements were carried out on a laboratory-use true colour time-gated luminescence microscope<sup>29</sup>. The luminescence quantum yields of TOB-Eu<sup>3+</sup> and TOHB-Eu<sup>3+</sup> were measured by an absolute method using an integration sphere on an Edinburgh FLS920 fluorimeter.

**Synthesis of TOB.** 4-Amino-TEMPO (0.48 mmol, 82.2 mg) was dissolved in anhydrous CH<sub>2</sub>Cl<sub>2</sub> (5 mL), and then NEt<sub>3</sub> (0.72 mmol, 0.10 mL), BHHBCB (0.24 mmol, 200 mg) and DMAP (dimethylaminopyridine) (0.024 mmol, 2.9 mg) were added with stirring. The reaction mixture was stirred for 7 days at room temperature in the dark. After solvent was removed, the residue was washed with 50 mL diluted hydrochloric acid (1.0 M), and then dissolved in 150 mL CH<sub>2</sub>Cl<sub>2</sub>. The CH<sub>2</sub>Cl<sub>2</sub> solution was washed three times with 100 mL water, dried with Na<sub>2</sub>SO<sub>4</sub> and evaporated to dryness. The desired ligand TOB was obtained as brick-red solid (202.7 mg, 87% yield). <sup>1</sup>H NMR (400 MHz, DMSO-d<sub>6</sub>):  $\delta$  (ppm) = 0.95–1.42 (m, br,

16H), 4.20 (s, br, 4H), 6.87–7.91 (m, br, 13H). ES-API MS (m/z): 966.2 ( $[M-H]^-$ , 100%). Elemental analysis calcd.(%) for  $C_{41}H_{37}F_{14}N_2O_7S \cdot 1.5H_2O$  (TOB-1.5H<sub>2</sub>O): C, 49.50; H, 4.05; N, 2.82. Found (%): C, 49.64; H, 4.29; N, 2.78. HPLC analysis: retention time, 8.01 min (purity, 95.3% integrated intensity); Sinochrom ODS-BP (5 μm) 250 mm × 4.6 mm C18 reverse-phase column; eluent, acetonitrile/H<sub>2</sub>O = 90/10 containing 0.1% trifluoroacetic acid; flow rate, 1.0 mL/min. The elution was monitored at 330 nm.

**Synthesis of TOB-Eu<sup>3+</sup>.** TOB (49.7 mg, 0.05 mmol) and europium(III) triflate (16.5 mg, 0.0275 mmol) were dissolved in 5.0 mL CH<sub>3</sub>CN, followed by adding 0.5 mL NaOH (8 mg/mL) dropwise. The reaction mixture was stirred at room temperature for 12 hours. After evaporation, the residue was washed with water and Et<sub>2</sub>O to give the target complex as pale powder. ES-API MS (m/z): 2083.4 ( $[M-Na]^-$ , 100%). Elemental analysis calcd.(%) for  $C_{82}H_{70}F_{28}N_4O_{14}S_2NaEu \cdot CH_3CN \cdot 2H_2O$  (TOB-Eu<sup>3+</sup>·CH<sub>3</sub>CN·2H<sub>2</sub>O): C, 46.20; H, 3.55; N, 3.21. Found (%): C, 46.23; H, 3.66; N, 3.27. HPLC analysis: retention time, 9.93 min (purity, 95.6% integrated intensity); Sinochrom ODS-BP (5 μm) 250 mm × 4.6 mm C18 reverse-phase column; eluent, acetonitrile/H<sub>2</sub>O = 90/10 containing 0.1% trifluoroacetic acid; flow rate, 1.0 mL/min. The elution was monitored at 330 nm.

**Synthesis of TOHB-Eu<sup>3+</sup>.** TOB-Eu<sup>3+</sup> (43.6 mg, 0.02 mmol) and ascorbic acid (70 mg, 0.4 mmol) were dissolved in 5.0 mL CH<sub>3</sub>CN, and the reaction mixture was stirred at room temperature for 3 hours. After evaporation, the residue was washed with water and CH<sub>3</sub>CN to give the target complex as pale powder. ES-API MS (m/z): 2085.3 ( $[M-Na]^-$ , 100%). Elemental analysis calcd.(%) for  $C_{82}H_{72}F_{28}N_4O_{14}S_2NaEu \cdot CH_3CN \cdot 3H_2O$  (TOHB-Eu<sup>3+</sup>·CH<sub>3</sub>CN·3H<sub>2</sub>O): C, 45.78; H, 3.70; N, 3.18. Found (%): C, 45.87; H, 3.58; N, 2.91. HPLC analysis: retention time, 6.71 min (purity, 97.2% integrated intensity); Sinochrom ODS-BP (5 μm) 250 mm × 4.6 mm C18 reverse-phase column; eluent, acetonitrile/H<sub>2</sub>O = 90/10 containing 0.1% trifluoroacetic acid; flow rate, 1.0 mL/min. The elution was monitored at 330 nm.

**Reaction of TOB-Eu<sup>3+</sup> with vitamin C.** The reaction of TOB-Eu<sup>3+</sup> with vitamin C was performed in 1:1 ethanol-0.05 M Tris-HCl buffer of pH 7.5. After 5.0 μM TOB-Eu<sup>3+</sup> was reacted with different concentrations of vitamin C, respectively, the solutions were 10-fold diluted (final probe concentration, 0.5 μM) with the buffer, and then the excitation and emission spectra of the solutions were measured with time-gated mode.

**Reactions of TOB-Eu<sup>3+</sup> with different biological reductants.** All the reactions were carried out in 1:1 ethanol-0.05 M Tris-HCl buffer of pH 7.5 with the same concentration of TOB-Eu<sup>3+</sup> (5.0 μM) for 1.5 h at 37 °C. After the reaction, the solutions were 10-fold diluted (final probe concentration, 0.5 μM) with the buffer, and then the luminescence intensities of the solutions were measured with time-gated mode.

**MTT Assay.** The cytotoxicity of TOB-Eu<sup>3+</sup> to HepG2 cells was measured by the MTT assay using the previously reported method<sup>39</sup>. HepG2 cells, cultured in RPMI-1640 medium, supplemented with 10% fetal bovine serum, 1% penicillin and 1% streptomycin, were washed with fresh culture medium, and then incubated with the different concentrations of TOB-Eu<sup>3+</sup> (0, 25, 50, 75 and 100 μM) for 24 h at 37 °C in a 5% CO<sub>2</sub>/95% air incubator. After the culture medium was removed, the cells were further incubated with the PBS buffer containing 0.5 mg/mL of MTT for 4 h in the incubator. After the supernatants were removed, the cells were dissolved in DMSO, and then the absorbance at 490 nm was measured.

**Luminescence imaging of vitamin C in living Cells.** HepG2 cells (or HeLa cells), cultured on a 35 mm glass-bottom culture dish (φ20 mm) in RPMI-1640 medium, supplemented with 10% fetal bovine serum, 1% penicillin, and 1% streptomycin, were washed three times with an isotonic saline solution (140 mM NaCl, 10 mM glucose and 3.5 mM KCl), and then incubated in the isotonic saline solution containing 1.0 mM vitamin C (or DHA) for various incubation times at 37 °C in a 5% CO<sub>2</sub>/95% air incubator. The vitamin C-loaded cells at different incubation times were washed three times with the isotonic saline solution, and then incubated in the isotonic saline solution containing 20 μM TOB-Eu<sup>3+</sup> and 0.5 mg/mL cremophor C040 for 1 h under the same condition. The cells were washed five times with the isotonic saline solution, and then subjected to the luminescence imaging measurements on the microscope (excitation filter, 330–380 nm; dichroic mirror, 400 nm; emission filter, >590 nm, no emission filter was used for luminescence imaging in Figure S4). The time-gated luminescence imaging measurements were carried out with the conditions of delay time, 33 μs; gate time, 1.0 ms; lamp pulse width, 80 μs; and exposure time, 2 s. The steady-state luminescence imaging measurements were carried out with exposure time of 4 s.

**Quantifying the intracellular concentration of the probe.** The intracellular concentration of the probe was measured by the inductively coupled plasma-optical emission spectrometer (ICP-EOS) assay using the previously reported method<sup>40</sup>. HepG2 cells cultured in a 75 cm<sup>2</sup> culture flask were washed three times with an isotonic saline solution and then incubated in the isotonic saline solution containing 1.0 mM vitamin C for 1 h at 37 °C in a 5% CO<sub>2</sub>/95% air incubator. The vitamin C-loaded cells washed

three times with the isotonic saline solution, and then incubated in the isotonic saline solution containing 20  $\mu\text{M}$  TOB-Eu<sup>3+</sup> and 0.5 mg/mL cremophor C040 for 1 h under the same condition. The cells were washed three times with PBS and harvested by trypsin treatment. The cell density was determined with a Neubauer improved hemacytometer. The numbered Eu<sup>3+</sup> complex-deposited cells were suspended in the acidic solution containing 3.7% HCl and 6.5% HNO<sub>3</sub>, and then subjected to the ICP-EOS measurement.

**Luminescence imaging of vitamin C in *Daphnia magna*.** *Daphnia magna* were cultured in non-chlorinated tap water that was aerated for 3 days and saturated in dissolved oxygen at 20 °C under cool-white fluorescent light with a 14:10 h light:dark photoperiod. Culture medium was renewed three times a week. *Scenedesmus obliquus* were fed to *Daphnia magna* daily. The new born *Daphnia magna* (age < 48 h) were first exposed to 1.0 mM vitamin C solution in the culture medium for 40 min at 25 °C. After washing three times with culture medium, the vitamin C-loaded *Daphnia magna* were incubated with 5.0  $\mu\text{M}$  TOB-Eu<sup>3+</sup> in the culture medium containing 1% ethanol for 1 h at 25 °C. The *Daphnia magna* were washed four times with culture medium, and then subjected to the luminescence imaging measurements on the microscope (excitation filter, 330–380 nm; dichroic mirror, 400 nm; no emission filter was used). The time-gated luminescence imaging measurements were carried out with the conditions of delay time, 33  $\mu\text{s}$ ; gate time, 1.0 ms; lamp pulse width, 80  $\mu\text{s}$ ; and exposure time, 0.5 s. The steady-state luminescence imaging measurements were carried out with exposure time of 1 s.

## References

- Kondo, Y. *et al.* Senescence marker protein 30 functions as gluconolactonase in L-ascorbic acid biosynthesis, and its knockout mice are prone to scurvy. *Proceedings of the National Academy of Sciences* **103**, 5723–5728 (2006).
- Davies, M. B., Austin, J. & Partridge, D. A. *Vitamin C: its chemistry and biochemistry*. (royal society of chemistry, 1991).
- Eipper, B. A., Mains, R. E. & Glembotski, C. C. Identification in pituitary tissue of a peptide alpha-amidation activity that acts on glycine-extended peptides and requires molecular oxygen, copper, and ascorbic acid. *Proceedings of the National Academy of Sciences* **80**, 5144–5148 (1983).
- Klebanoff, S., Dziewiatkowski, D. & Okinaka, G. The effect of ascorbic acid oxidation on the incorporation of sulfate by slices of calf costal cartilage. *The Journal of general physiology* **42**, 303–318 (1958).
- Harrison, F. E., Bowman, G. L. & Polidori, M. C. Ascorbic acid and the brain: Rationale for the use against cognitive decline. *Nutrients* **6**, 1752–1781 (2014).
- Du, J., Cullen, J. J. & Buettner, G. R. Ascorbic acid: chemistry, biology and the treatment of cancer. *Biochimica et Biophysica Acta (BBA)-Reviews on Cancer* **1826**, 443–457 (2012).
- Wu, G.-h. *et al.* An electrochemical ascorbic acid sensor based on palladium nanoparticles supported on graphene oxide. *Analytica chimica acta* **745**, 33–37 (2012).
- Zhang, X., Cao, Y., Yu, S., Yang, F. & Xi, P. An electrochemical biosensor for ascorbic acid based on carbon-supported PdNanoparticles. *Biosensors and Bioelectronics* **44**, 183–190 (2013).
- Ishii, K., Kubo, K., Sakurada, T., Komori, K. & Sakai, Y. Phthalocyanine-based fluorescence probes for detecting ascorbic acid: phthalocyaninatosilicon covalently linked to TEMPO radicals. *Chemical Communications* **47**, 4932–4934 (2011).
- Matsuoka, Y., Yamato, M., Yamasaki, T., Mito, F. & Yamada, K.-i. Rapid and convenient detection of ascorbic acid using a fluorescent nitroxide switch. *Free Radical Biology and Medicine* **53**, 2112–2118 (2012).
- Lozinsky, E. *et al.* Dual fluorophore-nitroxide probes for analysis of vitamin C in biological liquids. *Journal of biochemical and biophysical methods* **38**, 29–42 (1999).
- Hemmilä, I. & Mukkala, V.-M. Time-resolution in fluorometry technologies, labels, and applications in bioanalytical assays. *Critical reviews in clinical laboratory sciences* **38**, 441–519 (2001).
- Selvin, P. R. Principles and biophysical applications of lanthanide-based probes. *Annual review of biophysics and biomolecular structure* **31**, 275–302 (2002).
- Terai, T. *et al.* Modulation of luminescence intensity of lanthanide complexes by photoinduced electron transfer and its application to a long-lived protease probe. *Journal of the American Chemical Society* **128**, 6938–6946 (2006).
- Heffern, M. C., Matosziuk, L. M. & Meade, T. J. Lanthanide probes for bioresponsive imaging. *Chemical reviews* **114**, 4496–4539 (2013).
- Bünzli, J.-C. G. Lanthanide luminescence for biomedical analyses and imaging. *Chemical reviews* **110**, 2729–2755 (2010).
- Delbianco, M. *et al.* Bright, highly water-soluble triazaacyclononane europium complexes to detect ligand binding with time-resolved FRET microscopy. *Angewandte Chemie-International Edition* **53**, 10718–10722 (2014).
- McMahon B.K., Pala R. & Parker, D. A bright and responsive europium probe for determination of pH change within the endoplasmic reticulum of living cells. *Chemical Communications* **49**, 1127–1129 (2013).
- Shao, N. *et al.* Europium(III) complex-based luminescent sensing probes for multi-phosphate anions: Modulating selectivity by ligand choice. *Chemical Communications* 1127–1129 (2008).
- Hanaoka, K., Kikuchi, K., Kojima, H., Urano, Y. & Nagano, T. Development of a zinc ion-selective luminescent lanthanide chemosensor for biological applications. *Journal of the American Chemical Society* **126**, 12470–12476 (2004).
- Jin, D. & Piper, J. A. Time-gated luminescence microscopy allowing direct visual inspection of lanthanide-stained microorganisms in background-free condition. *Analytical chemistry* **83**, 2294–2300 (2011).
- Lu, J. *et al.* Resolving low-expression cell surface antigens by time-gated orthogonal scanning automated microscopy. *Analytical chemistry* **84**, 9674–9678 (2012).
- Shi, W. *et al.* An ascorbic acid amperometric sensor using over-oxidized polypyrrole and palladium nanoparticles composites. *Biosensors and Bioelectronics* **38**, 100–106 (2012).
- Chen, Q. *et al.* Ascorbate in pharmacologic concentrations selectively generates ascorbate radical and hydrogen peroxide in extracellular fluid *in vivo*. *Proceedings of the National Academy of Sciences* **104**, 8749–8754 (2007).
- Nishikimi, M., Fukuyama, R., Minoshima, S., Shimizu, N. & Yagi, K. Cloning and chromosomal mapping of the human nonfunctional gene for L-gulonolactone oxidase, the enzyme for L-ascorbic acid biosynthesis missing in man. *Journal of Biological Chemistry* **269**, 13685–13688 (1994).
- Vera, J. C. *et al.* Resolution of the facilitated transport of dehydroascorbic acid from its intracellular accumulation as ascorbic acid. *Journal of Biological Chemistry* **270**, 23706–23712 (1995).
- Savini, I., Rossi, A., Pierro, C., Avigliano, L. & Catani, M. SVCT1 and SVCT2: key proteins for vitamin C uptake. *Amino acids* **34**, 347–355 (2008).

28. Welch, R. W. *et al.* Accumulation of vitamin C (ascorbate) and its oxidized metabolite dehydroascorbic acid occurs by separate mechanisms. *Journal of Biological Chemistry* **270**, 12584–12592 (1995).
29. Zhang, L. *et al.* Practical implementation, characterization and applications of a multi-colour time-gated luminescence microscope. *Scientific reports* **4** (2014) DOI: 10.1038/srep06597.
30. Reidling, J. C., Subramanian, V. S., Dahhan, T., Sadat, M. & Said, H. M. Mechanisms and regulation of vitamin C uptake: studies of the hSVCT systems in human liver epithelial cells. *American Journal of Physiology-Gastrointestinal and Liver Physiology* **295**, G1217–G1227 (2008).
31. May, J. M., Qu, Z.-C. & Li, X. Ascorbic acid blunts oxidant stress due to menadione in endothelial cells. *Archives of biochemistry and biophysics* **411**, 136–144 (2003).
32. Heinlaan, M., Ivask, A., Blinova, I., Dubourguier, H.-C. & Kahru, A. Toxicity of nanosized and bulk ZnO, CuO and TiO<sub>2</sub> to bacteria *Vibrio fischeri* and crustaceans *Daphnia magna* and *Thamnocephalus platyurus*. *Chemosphere* **71**, 1308–1316 (2008).
33. Lovren, S. B. & Klaper, R. *Daphnia magna* mortality when exposed to titanium dioxide and fullerene (C60) nanoparticles. *Environmental Toxicology and Chemistry* **25**, 1132–1137 (2006).
34. Sandermann, H. Ecotoxicology of ozone: bioactivation of extracellular ascorbate. *Biochemical and biophysical research communications* **366**, 271–274 (2008).
35. Agrawal, N., Juneja, C. & Mahajan, C. Protective role of ascorbic acid in fishes exposed to organochlorine pollution. *Toxicology* **11**, 369–375 (1978).
36. Bantle, J. A. *et al.* FETAX interlaboratory validation study: Phase III-Part 1 testing. *Journal of Applied Toxicology* **16**, 517–528 (1996).
37. Penalva-Arana, D., Forshay, K., Johnson, P. T., Strickler, J. & Dodson, S. I. Chytrid infection reduces thoracic beat and heart rate of *Daphnia pulicaria*. *Hydrobiologia* **668**, 147–154 (2011).
38. Zhang, L., Wang, Y., Ye, Z., Jin, D. & Yuan, J. New class of tetradentate  $\beta$ -diketonate-europium complexes that can be covalently bound to proteins for time-gated fluorometric application. *Bioconjugate chemistry* **23**, 1244–1251 (2012).
39. Schatzschneider, U. *et al.* Cellular uptake, cytotoxicity, and metabolic profiling of human cancer cells treated with ruthenium(II) polypyridyl complexes [Ru(bpy)<sub>2</sub>(N[BOND]N)Cl<sub>2</sub>] with N[BOND]N=bpy, phen, dpq, dppz, and dppn. *ChemMedChem* **3**, 1104–1109 (2008).
40. Song, B. *et al.* A europium(III)-based PARACEST agent for sensing singlet oxygen by MRI. *Dalton Transactions* **42**, 8066–8069 (2013).

### Acknowledgements

Financial supports from the National Natural Science Foundation of China (Grant No. 21275025; J. Yuan), the Specialized Research Fund for the Doctoral Program of Higher Education of China (Grant No. 20130041130003; J. Yuan), the Fundamental Research Funds for the Central Universities (Grant No. DUT12RC(3)83), the ARC Future FellowshipScheme (FT 130100517; D. Jin), and the ARC Centre of Excellence for Nanoscale BioPhotonics (CE140100003; D. Jin), are gratefully acknowledged.

### Author Contributions

J.Y. and B.S. conceived the project and designed the experiments. B.S., Y.Y. and H.M. performed the synthesis and characterization of the probe. B.S. and Z.Y. performed the imaging experiments and all data analysis. X.Z. and D.J. built the time-gated luminescence microscope. B.S. and X.Z. illustrated the figures. B.S., D.J. and J.Y. wrote the main manuscript text. All authors participated in discussion and editing of the manuscript.

### Additional Information

**Supplementary information** accompanies this paper at <http://www.nature.com/srep>

**Competing financial interests:** The authors declare no competing financial interests.

**How to cite this article:** Song, B. *et al.* Background-free *in-vivo* Imaging of Vitamin C using Time-gateable Responsive Probe. *Sci. Rep.* **5**, 14194; doi: 10.1038/srep14194 (2015).



This work is licensed under a Creative Commons Attribution 4.0 International License. The images or other third party material in this article are included in the article's Creative Commons license, unless indicated otherwise in the credit line; if the material is not included under the Creative Commons license, users will need to obtain permission from the license holder to reproduce the material. To view a copy of this license, visit <http://creativecommons.org/licenses/by/4.0/>

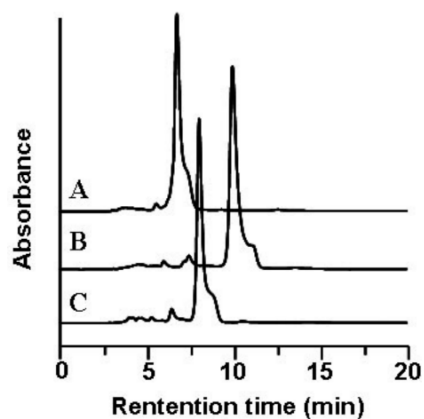
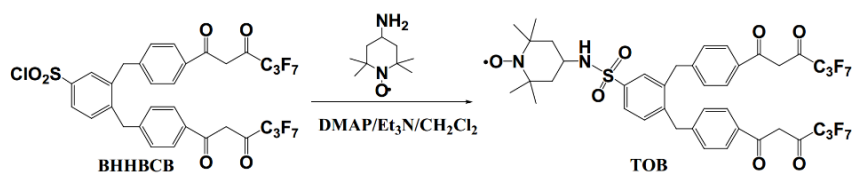
Supporting information for:

**Background-free *in-vivo* Imaging of Vitamin C using Time-gateable  
Responsive Probe**

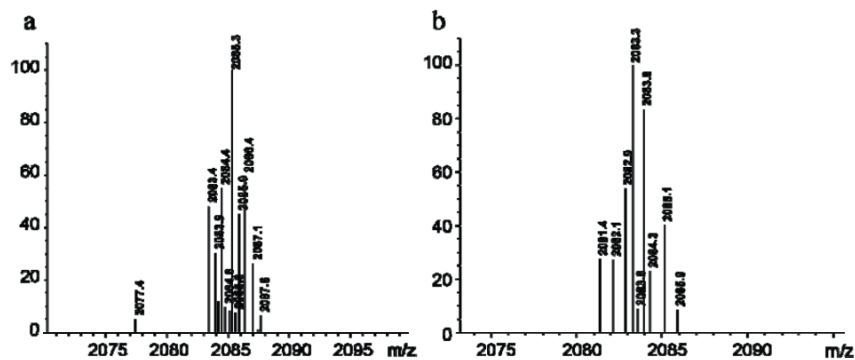
Bo Song,<sup>[1]</sup>Zhiqiang Ye,<sup>[1]</sup> Yajie Yang,<sup>[1]</sup> Hua Ma,<sup>[1]</sup> Xianlin Zheng,<sup>[2]</sup> Dayong Jin,<sup>[2]</sup> and Jingli  
Yuan<sup>\*[1]</sup>

<sup>[1]</sup>State Key Laboratory of Fine Chemicals, School of Chemistry, Dalian University of Technology,  
Dalian 116024, P. R. China.

<sup>[2]</sup>Advanced Cytometry Labs, ARC Centre of Excellence for Nanoscale BioPhotonics (CNBP),  
Macquarie University, NSW 2109, Sydney, Australia.



**Figure S1.** HPLC chromatograms of TOHB-Eu<sup>3+</sup> (A), TOB-Eu<sup>3+</sup> (B) and TOB (C).



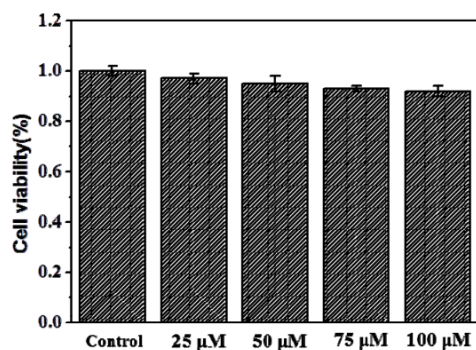


**Figure S3.** Viabilities of the HepG2 cells after incubated with different concentrations of TOB-Eu<sup>3+</sup> for 24 h.

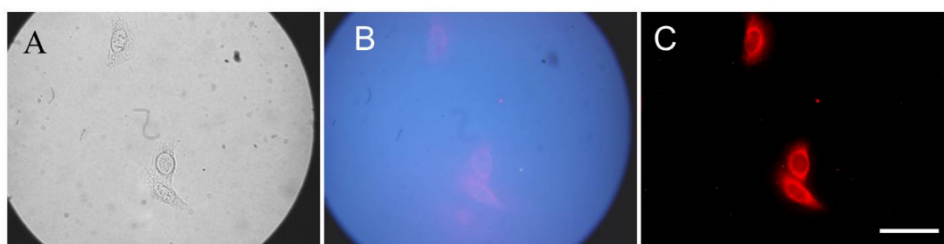


**Figure S4.** Bright-field (A), steady-state (B) and time-gated luminescence images (C) of HepG2 cells loaded with 1.0 mM vitamin C for 40 min and followed by incubation with 20  $\mu\text{M}$  TOB-Eu<sup>3+</sup> for 1 h. Scale bar: 50  $\mu\text{m}$ .

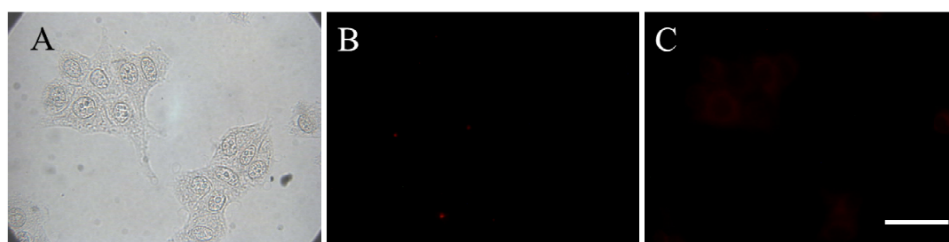


**Figure S5.** Bright-field (A) and time-gated luminescence images of HepG2 cells incubated with 20  $\mu\text{M}$  TOB-Eu<sup>3+</sup> for 1 h (B) or 4 h (C). Scale bar: 50  $\mu\text{m}$ .

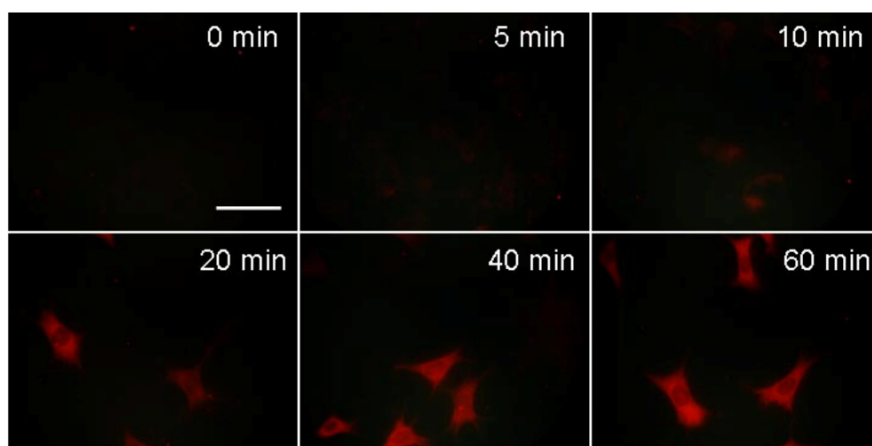


**Figure S6.** Time-gated luminescence microscopy images of HeLa cells loaded with 1.0 mM AA for various incubation times and followed by incubation with 20  $\mu\text{M}$  TOB-Eu<sup>3+</sup> for 1 h. Scale bar: 50  $\mu\text{m}$ .

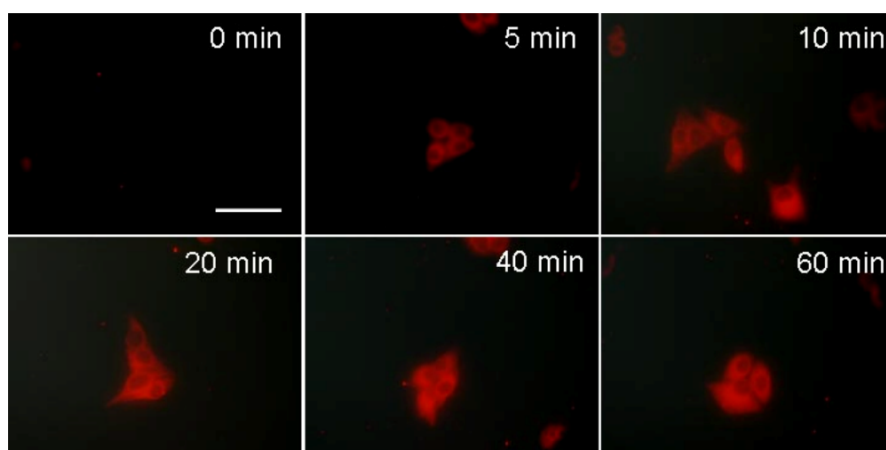


**Figure S7.** Time-gated luminescence microscopy images of HepG2 cells loaded with 1.0 mM DHA for various incubation times and followed by incubation with 20  $\mu\text{M}$  TOB-Eu<sup>3+</sup> for 1 h. Scale bar: 50  $\mu\text{m}$ .

## 2.4 Remarks

The modular design applied in this chapter presents a practical method to modify a commercial inverted microscope into a multi-colour time-gated microscope. The use of broadband xenon flash lamp enables multiple lanthanide probes to be visualized at the same time, with high sensitivity down to a single nanoparticle, and high signal-to-background ratio demonstrated by detecting pathogens from complex, autofluorescent samples. The system engineered here is expected to provide a robust and low-cost solution to broad biological and analytical applications using luminescent probes and time-gated imaging.

Although this system allows high-contrast imaging of live *Daphnia magna*, it is not possible to image animals of larger size, such as mice, based on the microscope platform. Addressing this challenge will be discussed in the next chapter. On the other hand, while engineering the time-gating module to fit an inverted microscopy substantially reduce the vibration issue to a point that it no longer affects the imaging quality, the acoustic noise generated by the high-speed optical chopper remains an unpleasant experience for end-users, especially if they work for a long period of time. Successful translation of this method will require the acoustic noise to be overcome in future.



## Chapter 3: Time-gated animal imaging system

This chapter extends time-gated luminescence microscopy into *in-vivo* animal imaging. Taking advantage of upconversion nanoparticles (UCNPs) that are excited and emit at near-infrared wavelengths with long luminescence lifetime, a prototype system comprising a modified time-gated imaging module and an illumination module employing 980-nm diode lasers was designed and constructed. Compared to conventional methods, high-contrast imaging was realised using Kunming mice injected with these UCNPs, which also significantly lowered thermal accumulation of the whole animal. This work is reported in the form of a published journal paper.

### 3.1 Optical Design

As discussed in 1.4.1, the critical requirement to achieve efficient time gating lies in fast switching of the detector/camera. For the chopper-based time-gated microscope, this is achieved by focusing the emission light out of the side port of the microscope, which is almost collimated, through a small pinhole placed very close to the chopper blade, so that the switching time is effectively the size of the pinhole divided by the linear velocity of the blade.

For macroscopic imaging (photography), a camera lens is typically used to project a large object onto the film/sensor of the camera as a demagnified real image. However, the light output by the camera lens has a large variety of angles, which cannot be focused into a small spot completely using a simple lens. In this case, the addition of pinhole will result in either decreased field-of-view or impaired light collection, or a combination of both.

To balance such trade-off, I followed two principles in my design: 1) reduced FOV is acceptable as long as the entire small animal (Kunming mice) can be imaged; and 2) reduced light collection is acceptable provided the attenuation is uniform over the FOV. Illustrated in [Figure 3-1](#), the camera lens (SIGMA 50MM F1.4 EX DG HSM; 50 mm focus, full-frame) has a magnification  $\times 10$  when positioned  $D_1 = 500$  mm above the object. A Kunming mouse, which is typically  $O_1 \approx 80$  mm in length, is therefore projected as an 8 mm image on the



the shade of one laser to be illuminated by other lasers, so that the object receives uniform irradiation, as shown in [Figure 3-2](#).

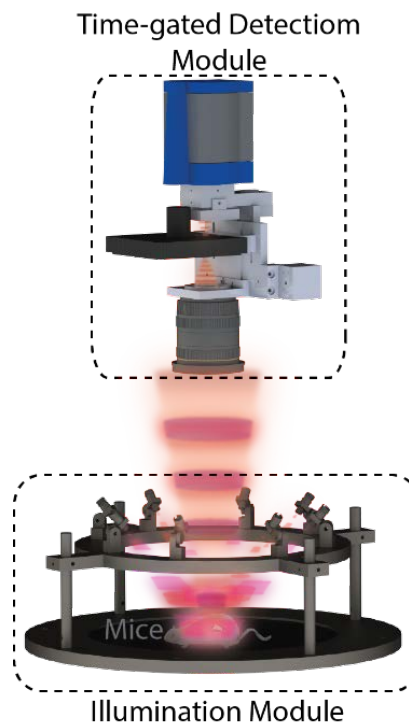


**Figure 3-2** shows the illuminator module as well as the time-gated detection module for the whole time-gated animal imaging system.

## 3.2 Synchronization Circuit Design

Synchronisation between the lasers and the chopper was carried out by time-delay electronic I designed based on dual-precision monostable multivibrators (MC74HC4538A; Motorola Semiconductor). As shown in [Figure 3-3](#), the time-delay electronic first shapes the TTL pulses output from the chopper to provide sharp rise and fall edges with transition time shorter than 500 ns. Then, a delay time in the range of 5 $\mu$ s to 1000 $\mu$ s is induced by adjusting a 100 K $\Omega$  adjustable resistor (RV2). After that, the duration of the delayed pulses is altered via a 20K $\Omega$  adjustable resistor (RV3). Finally, the delayed pulses are isolated through buffer amplifiers (M74HC405 HEX Buffer/converter) to generate eight outputs with sufficient power capacity to drive the excitation lasers individually. [Figure 3-4](#) shows the top overlay (a) and bottom overlay (b) circuit diagram of the synchronization delay electronic.

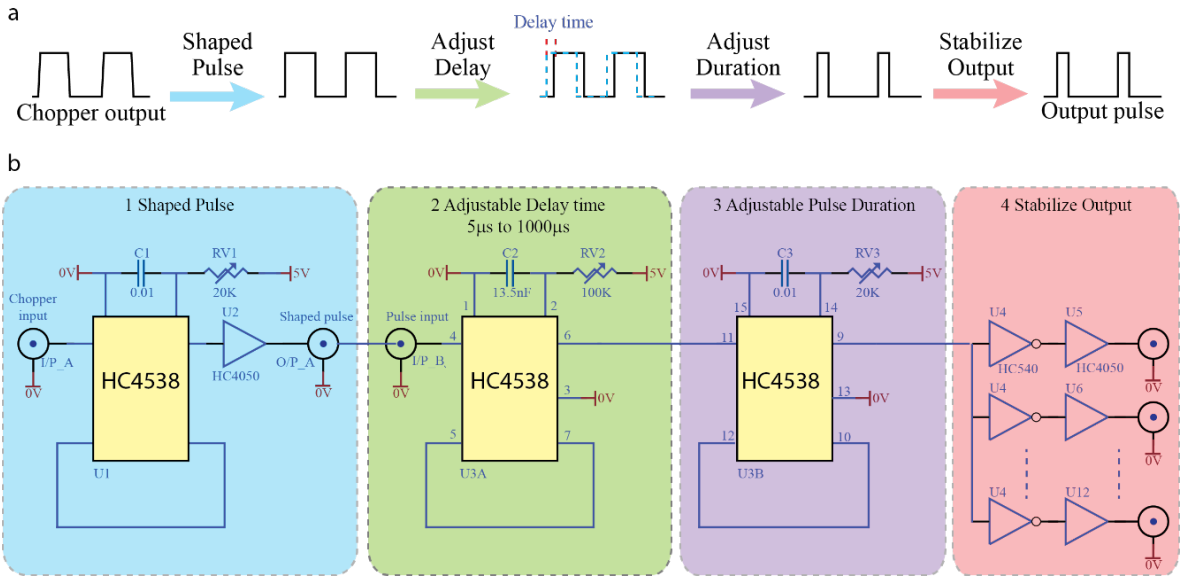


**FIGURE 3-3** (a) shows schematic of the synchronization delay electronic. (b) shows the circuit diagram of the delay electronic.



### 3.3 Paper 3

**Xianlin Zheng**, Xingjun Zhu, Yiqing Lu, Jiangbo Zhao, Wei Feng, Guohua Jia, Fan Wang, Fuyou Li and Dayong Jin, "High-Contrast Visualization of Upconversion Luminescence in Mice Using Time-Gating Approach" *Analytical Chemistry*, 2016, DOI: 10.1021/acs.analchem.5b04626.

I completed the entire instrumentation part of this work, including mechanical design, optical design, electronic design, system assembly, alignment, and software programming. For preliminary evaluation, I used a silica gel mat, which has substantial scattering and autofluorescence at a level similar to that of the skin and fur of mice. The optics and electronics were fine tuned to minimise such background in the system. After evaluation in our lab, I transferred all the components and rebuilt the system for our collaborators at Fudan University, who did the animal experiment after receiving operation training from me. During the entire study, the mice were treated with compliance of standards established in the Guide for the Care and Use of Laboratory Animals, with ethics approval obtained from Fudan University.

I led the experiment design, data analysis, and preparation of the manuscript and the figures. Our Fudan collaborators prepared the sample and collected all the data. I analyzed the data to validate the system performance. Author contributions to this paper are summarised in [Table 3-1](#).

**TABLE 3-1** Summary of author contribution to paper 3 following the order of authors.

	<b>X.Zheng</b>	X.Zhu	Y.L	J.Z	W.F	G.J	F.W	F.L	D.J
Project Design	●		●						●
System Design	●								
System Setup	●								
Sample Preparation		●							
Data Collection		●							
Analysis	●		●						
Figures	●	●	●						
Manuscript	●		●	●	●	●	●	●	●

## High-Contrast Visualization of Upconversion Luminescence in Mice Using Time-Gating Approach

Xianlin Zheng,<sup>†</sup> Xingjun Zhu,<sup>‡</sup> Yiqing Lu,<sup>†</sup> Jiangbo Zhao,<sup>†,§</sup> Wei Feng,<sup>‡</sup> Guohua Jia,<sup>||,⊥</sup> Fan Wang,<sup>†,⊥</sup> Fuyou Li,<sup>\*,‡</sup> and Dayong Jin<sup>\*,†,⊥</sup>

<sup>†</sup>Advanced Cytometry Laboratories, ARC Centre of Excellence for Nanoscale BioPhotonics (CNBP), Macquarie University, Sydney, New South Wales 2109, Australia

<sup>‡</sup>Department of Chemistry & Institutes of Biomedical Sciences & State Key Laboratory of Molecular Engineering of Polymers, Fudan University, Shanghai, 200433, PR China

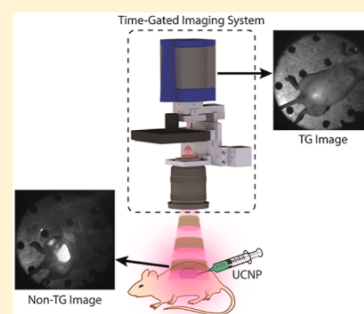
<sup>§</sup>Institute for Photonics and Advanced Sensing and School of Physical Sciences, University of Adelaide, Adelaide, South Australia 5005, Australia

<sup>||</sup>Nanochemistry Research Institute, Department of Chemistry, Curtin University, Perth, Western Australia 6102, Australia

<sup>⊥</sup>Institute for Biomedical Materials and Devices, Faculty of Science, University of Technology Sydney, Sydney, New South Wales 2007, Australia

### Supporting Information

**ABSTRACT:** Optical imaging through the near-infrared (NIR) window provides deep penetration of light up to several centimeters into biological tissues. Capable of emitting 800 nm luminescence under 980 nm illumination, the recently developed upconversion nanoparticles (UCNPs) suggest a promising optical contrast agent for *in vivo* bioimaging. However, presently they require high-power lasers to excite when applied to small animals, leading to significant scattering background that limits the detection sensitivity as well as a detrimental thermal effect. In this work, we show that the time-gating approach implementing pulsed illumination from a NIR diode laser and time-delayed imaging synchronized via an optical chopper offers detection sensitivity more than 1 order of magnitude higher than the conventional approach using optical band-pass filters (S/N, 47321/6353 vs 5339/58), when imaging UCNPs injected into Kunming mice. The pulsed laser illumination (70  $\mu$ s ON in 200  $\mu$ s period) also reduces the overall thermal accumulation to 35% of that under the continuous-wave mode. Technical details are given on setting up the time-gating unit comprising an optical chopper, a pinhole, and a microscopy eyepiece. Being generally compatible with any camera, this provides a convenient and low cost solution to NIR animal imaging using UCNPs as well as other luminescent probes.



Near-infrared (NIR) optical imaging has drawn increasing attention due to the desire for whole animal and deep tissue imaging at high resolution.<sup>1,2</sup> This is because (1) NIR light of 700–1100 nm is capable of penetrating several centimeters into tissues with much lower scattering compared to visible wavelengths<sup>3–5</sup> and (2) much lower autofluorescence background exists in the NIR range, facilitating sensitive fluorescence detection.<sup>6,7</sup> Thanks to the availability of NIR fluorescent dyes such as indocyanine green, *in vivo* NIR imaging has been adopted preclinically and clinically for identifying disease biomarkers,<sup>8,9</sup> monitoring disease progression,<sup>10,11</sup> determining the pharmaceutical effects of new drugs,<sup>12–14</sup> and fluorescence image-guided surgery.<sup>15–17</sup> Other nanoprobes, such as dye-encapsulated silica nanoparticles and semiconductor quantum dots, have also been proposed and demonstrated for quality NIR imaging under preclinical settings.<sup>18–22</sup>

Compared to these down-conversion materials, lanthanide-based upconversion nanoparticles (UCNPs) offers a promising

alternative with their unique anti-Stokes-shifted and long-lived luminescence.<sup>23–25</sup> The past decade has witnessed rapid progress in material science to develop highly controlled UCNPs as a new type of high-sensitive, photostable, low-toxic, and multifunctional optical contrast agent for broad biological and biomedical applications.<sup>26–31</sup> In particular, UCNPs codoped with Yb<sup>3+</sup> and Tm<sup>3+</sup> ions are capable of stepwise absorbing 980 nm low-energy photons and emitting strong 800 nm luminescence, thus suitable for deep-tissue imaging in the NIR window.<sup>14,32–39</sup> However, when whole animals are interrogated in practice, substantial scattering from skin and fur is often encountered for the excitation light as well as the emission luminescence, dramatically reducing the imaging contrast and blurring the targeted area.<sup>4,40,41</sup> Additionally, high excitation power under the continuous-wave mode is

Received: December 6, 2015

Accepted: February 25, 2016

Published: February 25, 2016

typically used, resulting in accumulated absorption and thermal effect that adversely affects or even damages the samples.<sup>42</sup>

To overcome these challenges, one opportunity arises from the long luminescence lifetimes of UCNP (tens to hundreds of microseconds) that allows the time-gated luminescence (TGL) technique to be applied. We have previously demonstrated TGL microscopes employing pulsed excitation and time-delayed detection to eliminate short-lived background from autofluorescence (with lifetimes typically of ~nanoseconds), achieving high detection sensitivity and imaging contrast using long-lived luminescent probes.<sup>43–45</sup> In this paper, we explore the time-gating approach for NIR imaging of UCNP in small animals. We demonstrate a system consisting of a fast-switchable 980 nm diode laser and a high-speed optical chopper, which is precisely synchronized for high-contrast time-gated imaging without posing any restrictions on the camera. The performance is evaluated in comparison to the conventional filter-based imaging approach, using Kunming mice injected with hydrophilic Yb<sup>3+</sup>/Tm<sup>3+</sup> codoped UCNP as the model.

## EXPERIMENTAL SECTION

**TGL Imaging System.** The schematic diagram of the TGL system for *in vivo* animal imaging is given in Figure 1. Briefly, a time-gating unit comprising a high-speed optical chopper and a microscope eyepiece (Olympus WHN10X) was inserted between a camera lens (Nikon SIGMA 50MM F1.4 EX DG HSM) and an EMCCD camera (Andor iXon Ultra 897). TGL imaging was realized by synchronizing the chopper with a

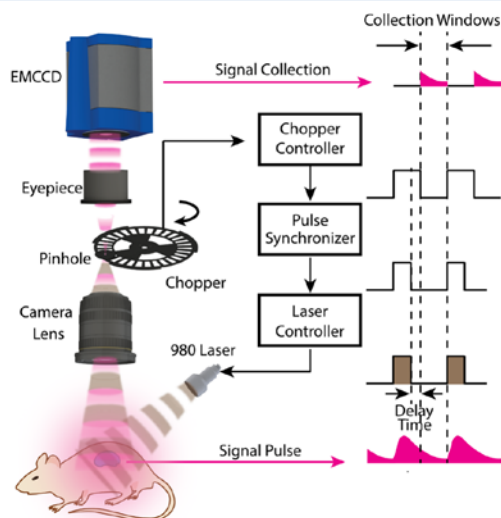


**Figure 1.** Schematics illustrating the TGL system for *in vivo* NIR imaging. The optical chopper (5 kHz, 1:1 duty ratio) generates a TTL pulse from its reference output to trigger an in-house pulse synchronizer, which times a fixed 70  $\mu$ s pulse (with 5  $\mu$ s delay from the chopper output) to enable the 980 nm NIR laser. The pulsed 980 nm light illuminates the mouse to excite the UCNP. The luminescence signal is collected by a camera lens, passes through a 1 mm pinhole attached to the optical chopper, relayed by a microscope eyepiece, and recorded by an EMCCD camera for *in vivo* imaging. The delay time between the switching-off of the 980 nm pulse and the switching-on of the EMCCD via chopping is 25  $\mu$ s, followed by a collection window of 100  $\mu$ s.

pulsed 980 nm fiber-coupled diode laser (LE-LS-980-10000T FC, LEO Photonics; maximum output power 10 W) in antiphase, so that the detection path only opened after the laser switched off and any short-lived background decayed to negligible. The chopper used here (C99S, Terahertz Technologies) had a blade consisting of 30 slots with a duty cycle of 1:1. When operating at maximum frequency of 5 kHz (with an accuracy of 0.001 Hz), it gave a rotational speed of ~167 rev/s. A 1 mm diameter pinhole aperture was attached very close to the chopper blade at a radius of 4.2 cm, so that an ON/OFF switching time of 23  $\mu$ s was achieved for the signal light and any stray light was removed. The chopper output a TTL signal, generated from the slotted optical switch built in the chopper head, to trigger a homemade pulse synchronizer. The latter delivered pulses of 70  $\mu$ s duration to the laser controller/driver to switch on the 980 nm laser when the detection path was blocked by the chopper blade, so that the EMCCD camera became effectively time-gated. Delay times of 5  $\mu$ s and 25  $\mu$ s were applied before and after the laser pulses, respectively, for optimizing the time-gating performance in practice.

***In Vivo* Animal Imaging.** Hydrophilic NaLuF<sub>4</sub>:Yb,Tm UCNP were injected hypodermically in the abdomen of Kunming mice (refer to Supporting Information S1 for details). Under the imaging system, they were illuminated with the pulsed 980 nm laser beam output from the fiber without collimation, at an average intensity of 3.18 W/cm<sup>2</sup>. The luminescence signal from the UCNP was collected by the camera lens, purified by the time-gating unit, and recorded by the EMCCD camera. For comparison, the same mice were also imaged using the conventional filter-based approach under continuous-wave 980 nm excitation at the identical intensity, and the upconversion luminescence was collected with one or two pieces of band-pass filters (FF01-800/12, Semrock) inserted in the detection path while the optical chopper was switched off. Bright-field imaging was also conducted simultaneously alongside the time-gated imaging, using a compact light-emitting diode (LED) to illuminate the mice.

**Thermal Effect Evaluation.** Thermal images and temperature elevation curves of mice under continuous-wave and time-gated 980 nm laser were recorded by an infrared thermal camera (FLIR E40). As a typical procedure, mice were anesthetized first through intraperitoneal injection of ketamine/xylazine solution (75 mg kg<sup>-1</sup> ketamine and 15 mg kg<sup>-1</sup> xylazine) and then placed under the *in vivo* imaging system. The thermal camera recorded the temperature changes of mice when the 980 nm laser was switched on and irradiated the mice for half a minute. After the recording, the laser was switched off and the mice were placed on warming pad to avoid an excessive body temperature decrease. Temperature elevation curves were produced using the maximum temperature value in the irradiated region versus irradiation time.

## RESULTS AND DISCUSSION

We compared the imaging contrast obtained by our time-gating approach with that using the conventional filter-based, nontime-gating approach. Although the band-pass filter used here should have eliminated residual excitation at 980 nm as well as other optical background, so that the camera only collected NIR emission within the range of 800  $\pm$  6 nm (Figure 2a), in reality strong signal was also observed from the surroundings of the injection site (Figure 2b). Along a line drawn across the injection area on the 16-bit grayscale image, the maximum intensity recorded was 59 470; nevertheless, the

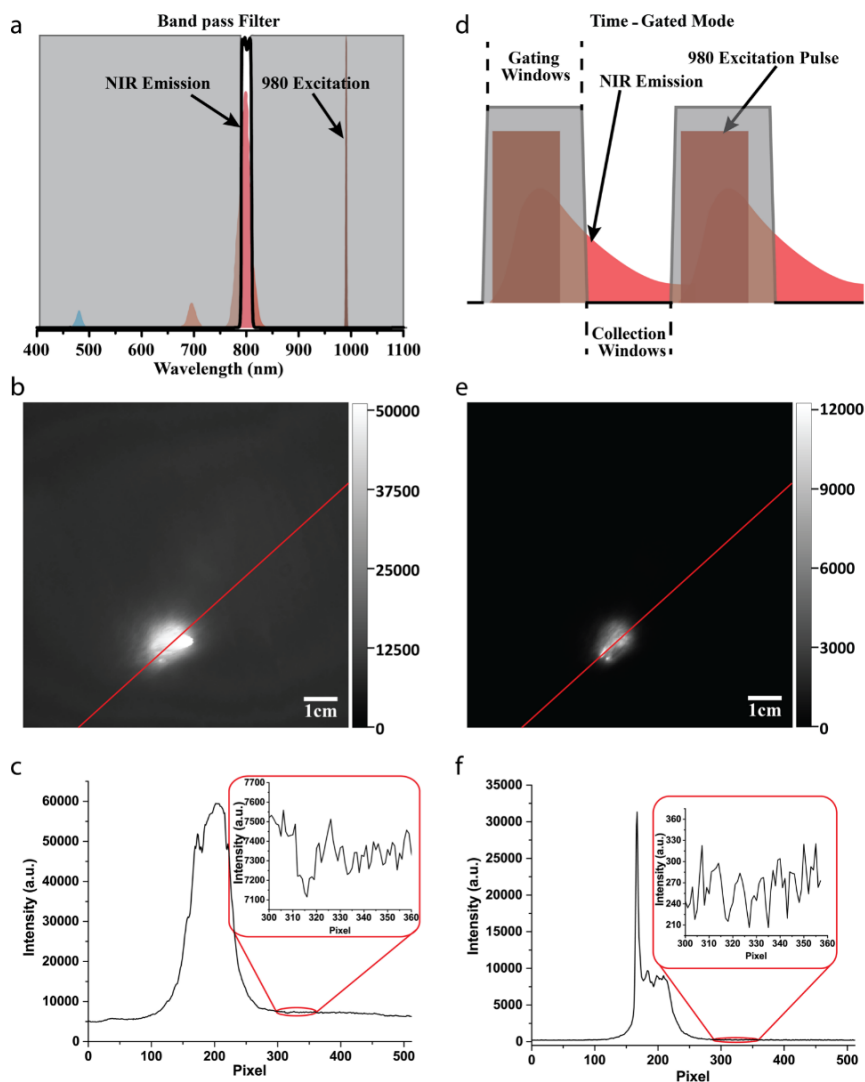


**Figure 2.** Comparison of *in vivo* imaging contrast between the filter-based approach and the time-gating approach. (a) Spectra of the excitation source, the UCNPs luminescence, and the transmission of the band-pass filter. (b) The luminescence image of a Kunming mouse with subcutaneous injection of hydrophilic NaLuF<sub>4</sub>:Yb,Tm UCNPs (200  $\mu$ L, 1 mg/mL), obtained by the filter-based approach under CW 980 nm excitation. (c) The intensity profile along the line across the 16-bit grayscale image in part b. (d) The temporal configuration for time-gated imaging. (e) The time-gated image of the same Kunming mouse. (f) The intensity profile along the line across the 16-bit grayscale image in part e. The highest peak corresponds to the actual injection position. The images in parts b and e were captured by the EMCCD camera with an exposure time of 0.4 s and gain of 10, under an average 980 nm excitation intensity of 3.18 W/cm<sup>2</sup> measured on the object mouse. Note that the EMCCD camera was not saturated during the image acquisition.

average intensity in the background area also reached 7309 yielding a signal-to-noise ratio of merely 8.13 (Figure 3c). By contrast, the time-gating approach employed pulsed excitation of identical peak intensity but 35% duration and gated detection of 50% duty ratio with the same camera settings (Figure 2d). The image, shown as Figure 2e, was taken immediately after Figure 2b was captured to ensure fair comparison, and a well-defined injection site was revealed against the background area. Along the same line drawn across, although the average intensity in the injection site decreased to 8160 (the outstanding peak intensity, 31 314, corresponds to

the actual injection position) due to the effectively reduced excitation and detection time, that of the background area was suppressed more substantially down to 263, so that an enhanced signal-to-noise ratio of 31 was achieved (Figure 2f). Further analysis over the entire images showed the overall signal-to-noise ratio was improved by 12.4-fold using the time-gating approach over the nontime-gated approach (see Supporting Information S2 and Supporting Table 1).

The high optical background here associated with the conventional approach arose from the strong scattering of the excitation light from the animal that one optical filter failed to

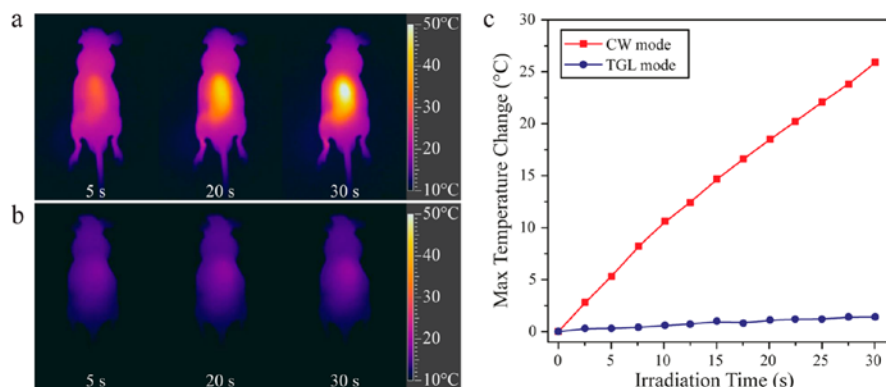


**Figure 3.** Comparison of the thermal effect between the CW mode and the TGL mode. (a) The thermal images of a Kunming mouse under CW 980 nm laser illumination for 5, 20, and 30 s. (b) The thermal images of a Kunming mouse under pulsed 980 nm laser illumination employed in the TGL mode for 5, 20, and 30 s. (c) The maximum temperature elevation over the irradiated area as a function of irradiation time under the CW and TGL modes.

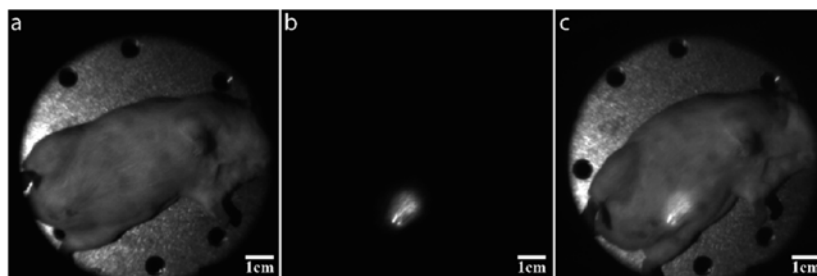


**Figure 4.** Dual-modal *in vivo* animal imaging. (a) A bright-field image of a Kunming mouse with subcutaneous injection of hydrophilic NaLuF<sub>4</sub>:Yb,Tm UCNP (200  $\mu$ L, 1 mg/mL) under a white LED illumination. (b, c) The time-gated luminescence image of the same Kunming mouse in (a) under 980 nm excitation in the absence (b) and presence (c) of the bright-field LED illumination. All images were taken by the EMCCD camera with exposure time of 0.4 s and gain of 10. The average 980 nm excitation intensity was 3.18 W/cm<sup>2</sup> measured on the object mouse.

block. It could be improved by adding more filters, but the effect was still inferior to the time-gating approach (see Supporting Information S3). One possible reason for that was the scattering light had a variety of incident angles, which may also change depending on the position of the animal, making it difficult for the interference-type filters to suppress completely due to their angle-dependent transmission/reflection spectra. Substitution for absorption-type (color-glass) filters is also not possible, as no suitable candidate is currently available to separate 808 nm emission from 980 nm excitation for the UCNP used here. Moreover, in the conventional approach the background may increase further for animals with colored skin and/or fur that introduce pigmentation-related NIR autofluorescence.<sup>41</sup> Nevertheless, the time-gating approach effectively removed residual scattering of the excitation light as well as autofluorescence regardless of its spectrum or incident angle, so that the background was limited close to the electronic noise level of the camera. On the other hand, while the excitation intensity remained identical, the exposure duration to the excitation light was reduced to 35% (70  $\mu$ s ON-time in every 200  $\mu$ s period) under the time-gated mode. This reduced the thermal effect to the animals very effectively. As shown in Figure 3, the maximum temperature increased over 25 °C on the mouse in only 30 s under the CW laser irradiation (same conditions as used in the luminescence imaging), while the

temperature change remained negligible for the time-gated mode.

The high signal-to-noise ratio without spectral filtering further allows the time-gating approach to be implemented alongside bright-field visualization, which was demonstrated using the same mice model. As shown in Figure 4, after adjusting the relative brightness of the white LED light with reference to the 980 nm laser excitation to ensure similar levels of intensity were obtained for the respective bright-field and time-gated luminescence images (Figure 4a,b), the time-gated imaging was directly performed in the presence of the LED light to visualize both the entire animal and the UCNP injection site in real time (Figure 4c). This capability, which is not suitable using the conventional approach (see Supporting Information S4), offers significant potential for practical applications, such as luminescence image-guided surgery.

## CONCLUSIONS

We have realized time-gated luminescence imaging of upconversion nanoparticles upon live small animals. In contrast to the conventional filter-based approach that suffers from the strong scattering of the excitation light, the time-gating approach is capable of efficient elimination of such background, allowing us to achieve a 12-fold enhancement in the signal-to-noise ratio using Kunming mice injected with UCNP as the *in*

*vivo* animal model. The overall exposure was reduced to 35%, alleviating overheating as well as other side effects associated with the NIR excitation light. Apart from the Yb/Tm codoped UCNPs, the technique is applicable to other long-lived luminescent probes with lifetimes in the microsecond-to-millisecond region.<sup>46</sup> For example, the Nd-sensitized UCNPs that are excitable at 800 nm<sup>47–49</sup> can be used to further improve the temperature control as well as tissue penetration depth. Furthermore, the time-gated luminescence imaging can be conducted directly under bright-field visualization. These advancements alongside the low cost of our well-engineered instrumentation address the key issues to implement upconversion nanoparticles for deep-tissue NIR imaging in practice, paving the way for their use in biomedical diagnostics as well as multifunctional applications.

## ■ ASSOCIATED CONTENT

### 📄 Supporting Information

The Supporting Information is available free of charge on the ACS Publications website at DOI: 10.1021/acs.analchem.5b04626.

Sample preparation, TEM image of oleate NaLuF<sub>4</sub>:Yb,Tm UCNPs, upconversion spectrum of NaLuF<sub>4</sub>:Yb,Tm UCNPs, evaluation of signal-to-noise ratio; effect on image contrast using multiple filters, and non-time-gated imaging under the both 980 nm excitation and bright-field illumination (PDF)

## ■ AUTHOR INFORMATION

### Corresponding Authors

\*E-mail: dayong.jin@uts.edu.au.

\*E-mail: fyli@fudan.edu.cn.

### Notes

The authors declare no competing financial interest.

## ■ ACKNOWLEDGMENTS

The authors acknowledge the financial support from the Australian Research Council (Centre of Excellence for Nanoscale BioPhotonics, Future Fellowship of D.J. Grant FT130100517) and Macquarie University (Postgraduate Scholarship of X.Z., Research Fellowship of Y.L.) and assistance in manufacturing the components for the animal imaging system provided by Macquarie Engineering & Technical Services (METS).

## ■ REFERENCES

- (1) Leblond, F.; Davis, S. C.; Valdés, P. A.; Pogue, B. W. *J. Photochem. Photobiol. B* **2010**, *98*, 77–94.
- (2) Quek, C.-H.; Leong, K. W. *Nanomaterials* **2012**, *2*, 92–112.
- (3) Frangioni, J. V. *Curr. Opin. Chem. Biol.* **2003**, *7*, 626–634.
- (4) Cerussi, A. E.; Berger, A. J.; Bevilacqua, F.; Shah, N.; Jakubowski, D.; Butler, J.; Holcombe, R. F.; Tromberg, B. J. *Academic radiology* **2001**, *8*, 211–218.
- (5) Pansare, V. J.; Hejazi, S.; Faenza, W. J.; Prud'homme, R. K. *Chem. Mater.* **2012**, *24*, 812–827.
- (6) Wagnieres, G. A.; Star, W. M.; Wilson, B. C. *Photochem. Photobiol.* **1998**, *68*, 603–632.
- (7) Adams, K. E.; Ke, S.; Kwon, S.; Liang, F.; Fan, Z.; Lu, Y.; Hirschi, K.; Mawad, M. E.; Barry, M. A.; Sevick-Muraca, E. M. *J. Biomed. Opt.* **2007**, *12*, 024017–024019.
- (8) Kosaka, N.; Ogawa, M.; Choyke, P. L.; Kobayashi, H. *Future Oncol.* **2009**, *5*, 1501–1511.
- (9) Hawrysz, D. J.; Sevick-Muraca, E. M. *Neoplasia* **2000**, *2*, 388–417.
- (10) Gurfinkel, M.; Ke, S.; Wen, X.; Li, C.; Sevick-Muraca, E. M. *Dis. Markers* **2004**, *19*, 107–121.
- (11) Du, Y.; An, S.; Liu, L.; Li, L.; Zhou, X. J.; Mason, R. P.; Mohan, C. *PLoS One* **2012**, *7*, e43941.
- (12) Reich, G. *Adv. Drug Delivery Rev.* **2005**, *57*, 1109–1143.
- (13) Roggo, Y.; Jent, N.; Edmond, A.; Chalus, P.; Ulmschneider, M. *Eur. J. Pharm. Biopharm.* **2005**, *61*, 100–110.
- (14) Dai, Y.; Xiao, H.; Liu, J.; Yuan, Q.; Ma, P. a.; Yang, D.; Li, C.; Cheng, Z.; Hou, Z.; Yang, P.; Lin, J. *J. Am. Chem. Soc.* **2013**, *135*, 18920–18929.
- (15) De Grand, A. M.; Frangioni, J. V. *Technol. Cancer Res. Treat.* **2003**, *2*, 553–562.
- (16) Gioux, S.; Choi, H. S.; Frangioni, J. V. *Mol. Imag.* **2010**, *9*, 237.
- (17) Hutteman, M.; Mieog, J.; Van der Vorst, J.; Dijkstra, J.; Kuppen, P.; van der Laan, A.; Tanke, H.; Kaijzel, E.; Que, I.; van de Velde, C.; Lowik, C. W. G. M.; Vahrmeijer, A. L. *Eur. J. Surg. Oncol. (EJSO)* **2011**, *37*, 252–257.
- (18) Michalet, X.; Pinaud, F.; Bentolila, L.; Tsay, J.; Doose, S.; Li, J.; Sundaresan, G.; Wu, A.; Gambhir, S.; Weiss, S. *Science* **2005**, *307*, 538–544.
- (19) Caltagirone, C.; Bettoschi, A.; Garau, A.; Montis, R. *Chem. Soc. Rev.* **2015**, *44*, 4645–4671.
- (20) Zhu, Y.; Hong, H.; Xu, Z. P.; Li, Z.; Cai, W. *Curr. Mol. Med.* **2013**, *13*, 1549–1567.
- (21) He, X.; Gao, J.; Gambhir, S. S.; Cheng, Z. *Trends Mol. Med.* **2010**, *16*, 574–583.
- (22) Kim, S.; Lim, Y. T.; Soltész, E. G.; De Grand, A. M.; Lee, J.; Nakayama, A.; Parker, J. A.; Mihaljevic, T.; Laurence, R. G.; Dor, D. M. *Nat. Biotechnol.* **2004**, *22*, 93–97.
- (23) Wang, F.; Liu, X. *Chem. Soc. Rev.* **2009**, *38*, 976–989.
- (24) Zhao, J.; Jin, D.; Schartner, E. P.; Lu, Y.; Liu, Y.; Zvyagin, A. V.; Zhang, L.; Dawes, J. M.; Xi, P.; Piper, J. A. *Nat. Nanotechnol.* **2013**, *8*, 729–734.
- (25) Lu, Y.; Zhao, J.; Zhang, R.; Liu, Y.; Liu, D.; Goldys, E. M.; Yang, X.; Xi, P.; Sunna, A.; Lu, J. *Nat. Photonics* **2014**, *8*, 32–36.
- (26) Lu, J.; Chen, Y.; Liu, D.; Ren, W.; Lu, Y.; Shi, Y.; Piper, J. A.; Paulsen, I. T.; Jin, D. *Anal. Chem.* **2015**, *87*, 10406.
- (27) Min, Y.; Li, J.; Liu, F.; Padmanabhan, P.; Yeow, E. K.; Xing, B. *Nanomaterials* **2014**, *4*, 129–154.
- (28) Zhou, J.; Sun, Y.; Du, X.; Xiong, L.; Hu, H.; Li, F. *Biomaterials* **2010**, *31*, 3287–3295.
- (29) Liu, Q.; Feng, W.; Yang, T.; Yi, T.; Li, F. *Nat. Protoc.* **2013**, *8*, 2033–2044.
- (30) Wang, F.; Banerjee, D.; Liu, Y.; Chen, X.; Liu, X. *Analyst* **2010**, *135*, 1839–1854.
- (31) Zhou, J.; Liu, Q.; Feng, W.; Sun, Y.; Li, F. *Chem. Rev.* **2015**, *115*, 395–465.
- (32) Nyk, M.; Kumar, R.; Ohulchanskyy, T. Y.; Bergey, E. J.; Prasad, P. N. *Nano Lett.* **2008**, *8*, 3834–3838.
- (33) Chen, G.; Shen, J.; Ohulchanskyy, T. Y.; Patel, N. J.; Kutikov, A.; Li, Z.; Song, J.; Pandey, R. K.; Ågren, H.; Prasad, P. N.; Han, G. *ACS Nano* **2012**, *6*, 8280–8287.
- (34) Dong, N.-N.; Pedroni, M.; Piccinelli, F.; Conti, G.; Sbarbati, A.; Ramírez-Hernández, J. E.; Maestro, L. M.; Iglesias-de la Cruz, M. C.; Sanz-Rodríguez, F.; Juarranz, A. *ACS Nano* **2011**, *5*, 8665–8671.
- (35) Zheng, W.; Tu, D.; Huang, P.; Zhou, S.; Chen, Z.; Chen, X. *Chem. Commun.* **2015**, *SI*, 4129–4143.
- (36) Bünzli, J.-C. G. *Chem. Rev.* **2010**, *110*, 2729–2755.
- (37) Yang, D.; Li, C.; Lin, J. *Nanomedicine* **2015**, *10*, 2573–2591.
- (38) Naccache, R.; Rodríguez, E. M.; Bogdan, N.; Sanz-Rodríguez, F.; Cruz, M. d. C. I. d. l.; Fuente, Á. J. d. l.; Vetrone, F.; Jaque, D.; Solé, J. G.; Capobianco, J. A. *Cancers* **2012**, *4*, 1067–1105.
- (39) Liu, Q.; Sun, Y.; Yang, T.; Feng, W.; Li, C.; Li, F. *J. Am. Chem. Soc.* **2011**, *133*, 17122–17125.
- (40) Cheong, W.-F.; Prahl, S. A.; Welch, A. J. *IEEE J. Quantum Electron.* **1990**, *26*, 2166–2185.

- (41) del Rosal, B.; Villa, I.; Jaque, D.; Sanz-Rodríguez, F. *J. Biophotonics* **2015**, DOI: 10.1002/jbio.201500271.
- (42) Khan, M. H.; Sink, R. K.; Manstein, D.; Eimerl, D.; Anderson, R. *Lasers Surg. Med.* **2005**, *36*, 270–280.
- (43) Zhang, L.; Zheng, X.; Deng, W.; Lu, Y.; Lechevallier, S.; Ye, Z.; Goldys, E. M.; Dawes, J. M.; Piper, J. A.; Yuan, J. *Sci. Rep.* **2014**, *4*, 6597.
- (44) Jin, D.; Piper, J. A. *Anal. Chem.* **2011**, *83*, 2294–2300.
- (45) Song, B.; Ye, Z.; Yang, Y.; Ma, H.; Zheng, X.; Jin, D.; Yuan, J. *Sci. Rep.* **2015**, *5*, 14194.
- (46) Pu, C.; Ma, J.; Qin, H.; Yan, M.; Fu, T.; Niu, Y.; Yang, X.; Huang, Y.; Zhao, F.; Peng, X. *ACS Cent. Sci.* **2016**, *2*, 32.
- (47) Xie, X.; Gao, N.; Deng, R.; Sun, Q.; Xu, Q.-H.; Liu, X. *J. Am. Chem. Soc.* **2013**, *135*, 12608–12611.
- (48) Shen, J.; Chen, G.; Vu, A. M.; Fan, W.; Bilsel, O. S.; Chang, C. C.; Han, G. *Adv. Opt. Mater.* **2013**, *1*, 644–650.
- (49) Wang, Y.-F.; Liu, G.-Y.; Sun, L.-D.; Xiao, J.-W.; Zhou, J.-C.; Yan, C.-H. *ACS Nano* **2013**, *7*, 7200–7206.

## Supporting Information

### High-contrast visualization of upconversion luminescence in mice using time-gating approach

Xianlin Zheng<sup>1</sup>, Xingjun Zhu<sup>2</sup>, Yiqing Lu<sup>1</sup>, Jiangbo Zhao<sup>1,3</sup>, Wei Feng<sup>2</sup>, Guohua Jia<sup>4,5</sup>, Fan Wang<sup>1,5</sup>, Fuyou Li<sup>2,\*</sup> and Dayong Jin<sup>1,5,\*</sup>

<sup>1</sup>*Advanced Cytometry Laboratories, ARC Centre of Excellence for Nanoscale BioPhotonics (CNBP), Macquarie University, NSW 2109, Australia*

<sup>2</sup>*Department of Chemistry & Institutes of Biomedical Sciences & State Key Laboratory of Molecular Engineering of Polymers, Fudan University, Shanghai, 200433, PR China*

<sup>3</sup>*Institute for Photonics and Advanced Sensing and School of Physical Sciences, University of Adelaide, Adelaide, SA 5005, Australia*

<sup>4</sup>*Nanochemistry Research Institute, Department of Chemistry, Curtin University, Perth, Western Australia 6102, Australia*

<sup>5</sup>*Institute for Biomedical Materials and Devices, Faculty of Science, University of Technology Sydney, NSW 2007, Australia*  
Email: [dayong.jin@uts.edu.au](mailto:dayong.jin@uts.edu.au) or [fyli@fudan.edu.cn](mailto:fyli@fudan.edu.cn)

## Supporting Information

Contents	Pages
S1 Sample preparation -----	S-2
Figure S1 The TEM image of oleate NaLuF4:Yb,Tm UCNPs -----	S-3
Figure S2 The upconversion spectrum of NaLuF4:Yb,Tm UCNPs-----	S-4
S2 Evaluation of signal-to-noise ratio -----	S-4
S3 Effect on image contrast using multiple filters -----	S-7
S4 Non-time-gated imaging under the both 980 nm excitation and bright-field illumination -----	S-8

### S1 Sample preparation

**Materials for synthesis.**  $\text{Lu}_2\text{O}_3$  (99.999%),  $\text{Yb}_2\text{O}_3$  (99.999%), and  $\text{Tm}_2\text{O}_3$  (99.999%) were purchased from Shanghai Yuelong New Materials Co. Ltd. Oleic acid (OA) (>90%) was purchased from Alfa Aesar Co. Ltd. 1-octadecene (ODE) (>90%) was purchased from Aladdin Reagent Co. Ltd. NaOH,  $\text{NH}_4\text{F}$ , HCl, and cyclohexane were purchased from Sinopharm Chemical Reagent Co. Ltd.  $\text{LnCl}_3$  (Ln: Lu, Yb, and Tm) was prepared by dissolving the rare earth oxides in 10% HCl solution at elevated temperature with the literature method [*ACS Nano* 2013; 7 (12): 11290–11300]. All chemicals were of analytical grade and used as received. Deionized water was used throughout the experiments.

**Synthesis of OA-capped  $\text{NaLuF}_4\text{:Yb,Tm}$  UCNPs.**  $\text{NaLuF}_4\text{:Yb,Tm}$  UCNPs were synthesized according to the reported protocol [*ACS Nano* 2013; 7 (12): 11290–11300]. In a typical synthesis, 1 mmol as-prepared  $\text{LnCl}_3$  (molar ratio Lu: Yb: Tm 79:20:1) was mixed with 6 mL OA and 15 mL ODE in a round-bottom flask. The mixture was stirred for 40 min at 140 °C to yield a clear solution and then cooled down to 80 °C in ambient atmosphere. After that, 4 mmol  $\text{NH}_4\text{F}$  and 2.5 mmol NaOH dissolved in methanol were added. The resulting mixture was degassed at 120 °C for 30 min under stirring, followed by heating to 300 °C with a rate of about 40 °C/min in argon atmosphere. The mixture was maintained at 300 °C for 1 h to allow the growth of UCNPs. After cooling down to room temperature, the as-synthesized UCNPs were precipitated by using the mixed solution of 20 mL ethanol and 10 mL cyclohexane and collected by centrifugation at 14000 rpm. With washing for several times,  $\text{NaLuF}_4\text{:Yb,Tm}$  UCNPs were redispersed in cyclohexane for use.

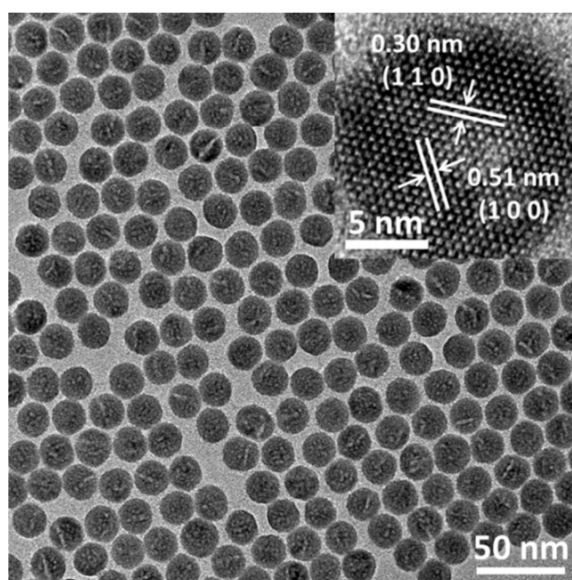
**Preparation of hydrophilic  $\text{NaLuF}_4\text{:Yb,Tm}$  UCNPs.** The oleate capped  $\text{NaLuF}_4\text{:Yb,Tm}$  underwent a ligand exchange process to make them water-soluble according to a reported method (Nano Lett. 2011; 11, 835-840.). Briefly, 100 mg oleate capped  $\text{NaLuF}_4\text{:Yb,Tm}$  were dispersed in 10 mL aqueous solution (pH = 4) by adding 0.1 mol  $\text{L}^{-1}$  HCl and stirring for 2 h. Diethyl ether was used to extract oleic acid yielded from the protonated oleate ligand. After extraction was carried out 3 times, the products in the water layer were collected by centrifugation and washed 3 times with deionized water. The resulting ligand-free  $\text{NaLuF}_4\text{:Yb,Tm}$  nanoparticles were dispersed in 0.9% NaCl aqueous solution.

**General characterizations.** A JEOL JEM-2010 transmission electron microscope (TEM) operated at 200 kV was used to image UCNPs with low and high resolution shown in Supporting Fig. S1. The upconversion spectrum shown in Supporting Fig. S2 was recorded on Edinburgh LFS-920 instrument in conjunction with

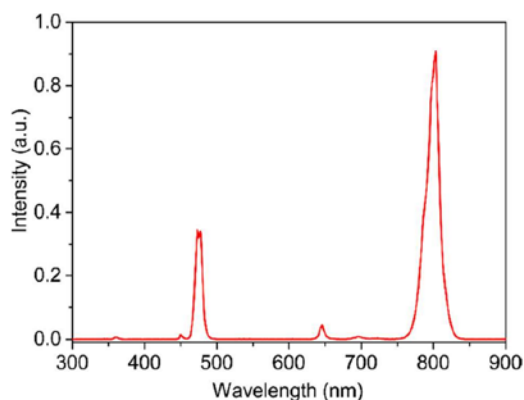
an external 980 nm CW as excitation source (Beijing Hi-Tech Optoelectronic Co. Ltd.). The 980 nm laser was coupled into a fibre and directed on the sample holder.

**Preparation of animal model.** Kunming mice, 6 weeks old and weighing 25-30 g, were purchased from Shanghai SLAC Laboratory Animal and maintained in specific pathogen-free facilities at room temperature ( $22 \pm 2$  °C). Animal protocols were approved by the Institutional and National Animal Care and Use Committee.

Citrate modified NaLuF<sub>4</sub>:Yb, Tm UCNPs in 200 μL saline with the concentration of 1 mg/mL were subcutaneously injected into the mice. The mouse to be studied was first anesthetized with ketamine/xylazine solution (75 mg/kg ketamine and 15 mg/kg xylazine). It was then placed on the stage of the upright system and imaged under different detection modes. During the entire study, the mice was treated with compliance of standards established in the Guide for the Care and Use of Laboratory Animals.



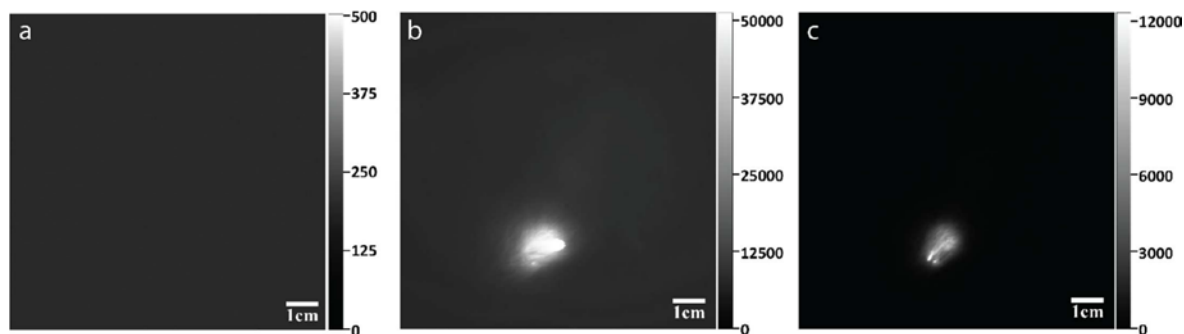
**Supporting Fig. 1.** The low resolution TEM image of oleate NaLuF<sub>4</sub>:Yb,Tm UCNPs illustrates the spherical shape with an average size of  $19.2 \pm 1.1$  nm. The inset high-resolution TEM image at top right shows its high crystalline nature with lattice fringe *d*-spacing of 0.30 nm and 0.51 nm, well matched to the lattice distance in the (110) and (100) plane of hexagonal-phase NaLuF<sub>4</sub>.



**Supporting Fig. 2.** The upconversion spectrum of oleate NaLuF<sub>4</sub>:Yb,Tm UCNPs dispersed in cyclohexane under CW 980 nm laser excitation.

## S2 Evaluation of signal-to-noise ratio

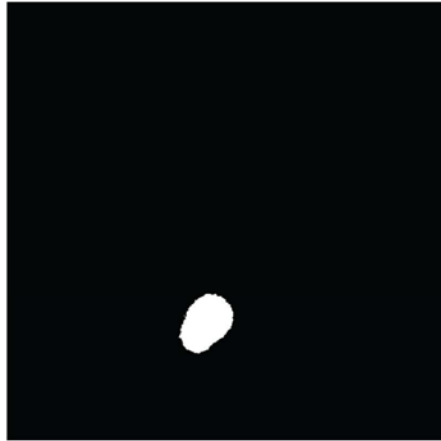
We first assessed the noise baseline of the EMCCD. Supporting Fig. 3a gives the 16-bit grayscale image captured without any illumination using the same camera setting (0.4 s exposure time, 10 gain). The average noise level was subtracted from the original images taken under the non-time-gated and time-gated mode (Fig. 2b and 2e) before the effective signal-to-noise ratios were calculated.



**Supporting Fig. 3.** (a) A 16-bit grayscale image captured by the EMCCD camera without any illumination light, showing an average noise level of 201. (b, c) The 16-bit grayscale images obtained by subtracting the average noise level from Fig. 2b and 2e, respectively.

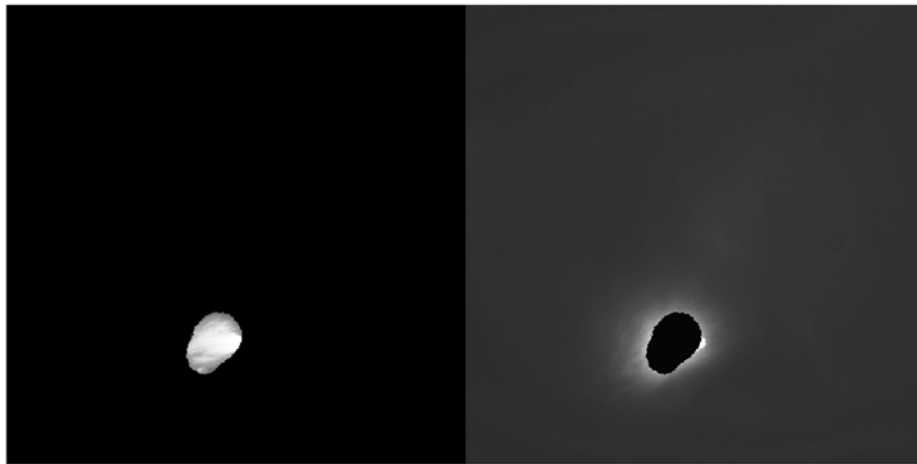
To calculate the signal-to-noise ratio, the target area needs to be defined first. We applied the Otsu

threshold method [Automatica 1975; 11: 23-27] to the time-gated image in Supporting Fig. 3c using MATLAB to create a binary mask image, as shown in Supporting Fig. 4. This allowed the signal area and the background area to be divided to calculate their respective values.

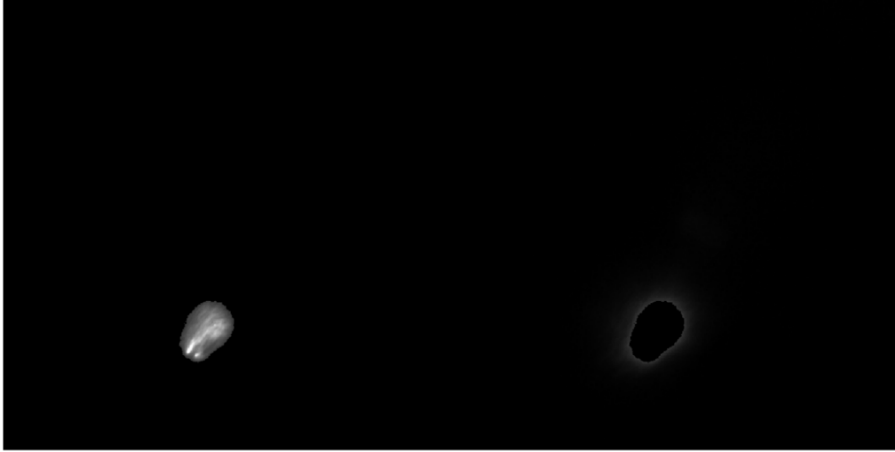


**Supporting Fig. 4.** The mask image generated from Supporting Fig. 3c using the Otsu threshold method. The white patch corresponds to the signal area with binary value of 1, while the black part is the background area with binary value of 0.

The mask image was then applied to the non-time-gated and time-gated images in Supporting Fig. 3b and 3c, segmenting each to the signal part and the background part (Supporting Fig. 5 and 6). The signal-to-noise ratio measurement is summarised in Supporting Table 1.



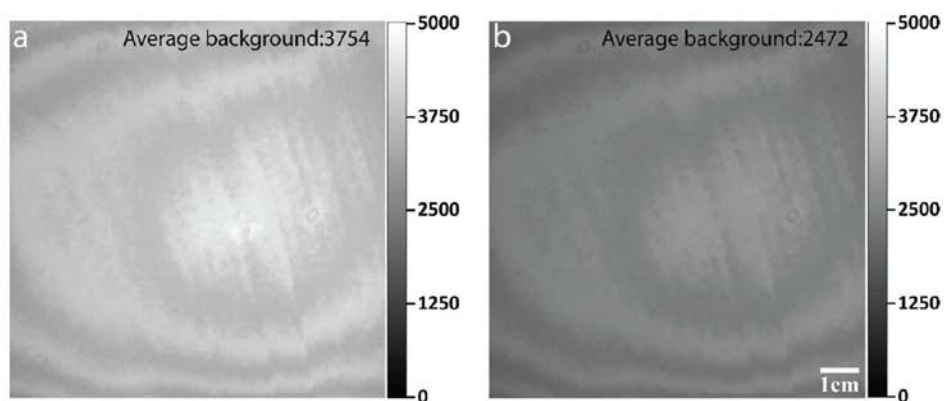
**Supporting Fig. 5.** Segmented signal (left) and background (right) area from the non-time-gated image in Supporting Fig. 3b, using the mask image in Supporting Fig. 4. The maximum, minimum and average values for signal and noise were then obtained from the two images, respectively.



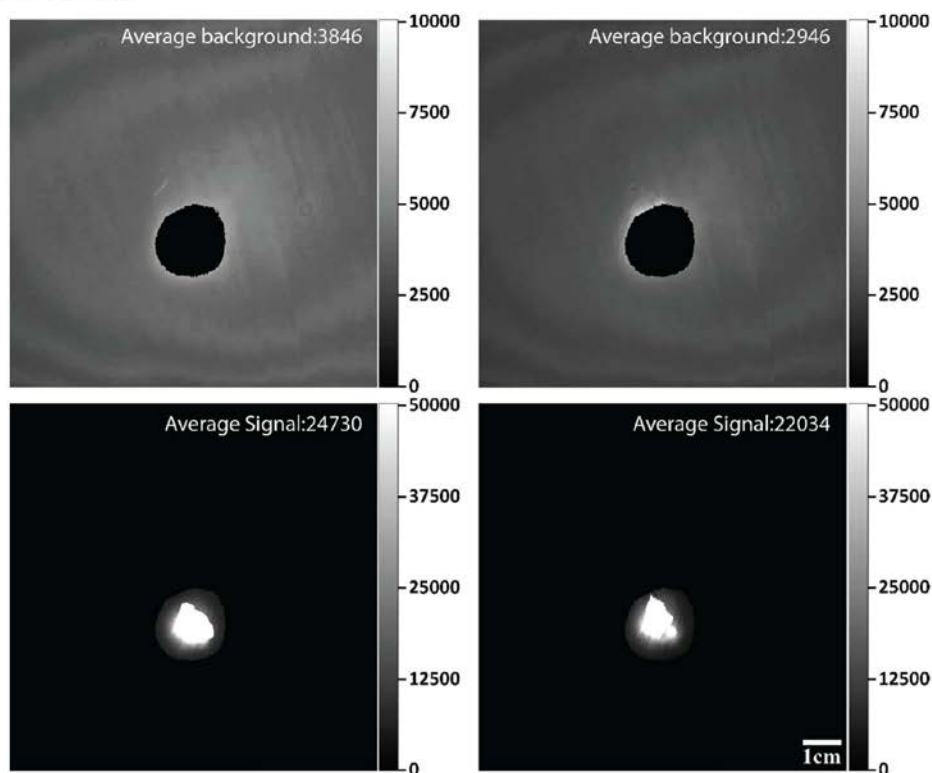
**Supporting Fig. 6.** Segmented signal (left) and background (right) area from the time-gated image in Supporting Fig. 3c, using the mask image in Supporting Fig. 4. The maximum, minimum and average values for signal and noise were then obtained from the two images, respectively.

**Supporting Table 1.** Summary of the signal and noise values measured from Supporting Fig. 5 and 6.

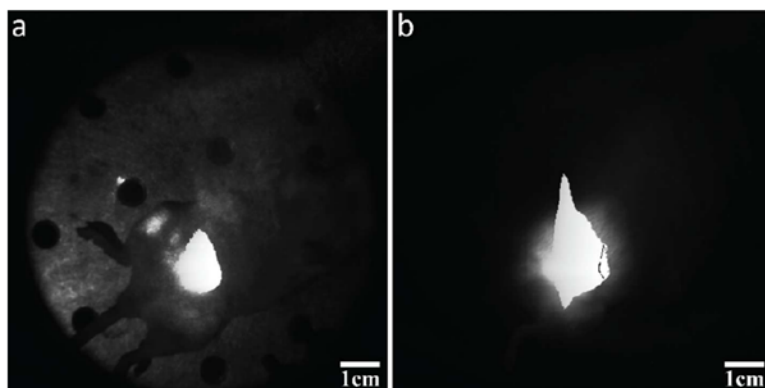
	Signal Maximum	Signal Minimum	Signal Average	Noise Maximum	Noise Minimum	Noise Average	Average signal-to-noise ratio
Non-time-gated mode	62026	23228	47321	62389	4840	6353	7.45
Time-gated mode	32757	2571	5339	2568	0	58	92.1

**S3 Effect on image contrast using multiple filters**

**Supporting Fig. 7.** Background images taken from a mouse without UCNP injection under the non-time-gated mode using one (a) and two (b) identical band-pass filters ( $800 \pm 6$  nm). The average values are given in the images.



**Supporting Fig. 8.** Comparison of signal-to-noise ratios measured from a mouse with UCNP injection under the non-time-gated mode using one (a, b) and two (c, d) identical band-pass filters ( $800 \pm 6$  nm). The images were segmented into signal and background parts following the method described in S2, and the values are shown in the images.

**S4 Non-time-gated imaging under the both 980 nm excitation and bright-field illumination.**

**Supporting Fig. 9.** (a) The non-time-gated image captured without the band-pass filter by the EMCCD camera (exposure time of 0.1 s; gain of 10; 980 nm laser intensity of  $63.6 \text{ mW/cm}^2$ ). (b) The non-time-gated image captured with the band-pass filter ( $800 \pm 6 \text{ nm}$ ) by the EMCCD camera (exposure time of 0.4 s; gain of 10; 980 nm laser intensity of  $3.18 \text{ W/cm}^2$ ).

### 3.5 Remarks

Development of the time-gated *in-vivo* imaging system in this chapter complements the existing time-gated microscopes to enable high-contrast imaging on the macroscopic scale free of autofluorescence and scattering background. Capable of imaging subcutaneous biological tissues with lowered thermal effect, this system offers new opportunities for non-invasive diagnostics and image-guided treatment. Nevertheless, the current optical design leads to low light collection efficiency, which needs to be overcome in the next step to increase the detection sensitivity.



## Chapter 4: Encoder-Assisted Scanning Microscopy

This chapter reports development of the orthogonal scanning automated microscope (OSAM) concept described in 1.4.4 by introducing XY-axes linear encoders and a Z-axis autofocus unit, to achieve high precision location of individual luminescent target in 3-dimensions at high sample throughput. Location precision of the new referenced-OSAM (R-OSAM) system was evaluated using polymer beads incorporating lanthanide probes. The R-OSAM was then used to quantify the luminescence properties of a variety of samples, demonstrating its applications in material characterisation and bioassay. This work is reported in the form of a published journal paper.

### 4.1 Localization method

Precise luminescence quantification requires that all the targets should be measured under identical condition in terms of excitation and luminescence collection. While it is theoretically possible to engineer a top-hat excitation profile, in practice standard delivery optics lead to reduced illumination intensity, particularly for UV wavelengths. Further, the emission collection efficiency is never perfectly uniform in the entire FOV. The OSAM concept provides an alternative approach to uniform measurement by placing every single target at the centre of the FOV; however the variation in located positions and focal lengths associated with the previous prototype, as illustrated in [Figure 1-16](#), needs to be overcome.

The previous-generation OSAM did not measure the real-time position of the stage during rapid scanning. Rather, it calculated the position from the time according to the kinematics of the stage movement. Nevertheless, the actual kinematics from one scan to another can be slightly different, affecting the positional accuracy. This is difficult to correct even using a commercially available encoded motorised stage, which can report the precise position of the stage on demand, but not in real time. This resulted in locational accuracy of  $\pm 30 \mu\text{m}$ , which is large compared with the size of objects of interest, typically  $< 15 \mu\text{m}$  diameter.

In order to improve location accuracy, I attached two miniature optical linear encoders to the X and Y plate of the motorised stage, respectively, which allows access to the raw signals from the encoders that are not provided by encoded motorised stages. One optical linear

encoder comprises a reader head and a pitch scale. As illustrated in Figure 4-1, when they move relative to each other, the reader head generates two outputs of pulses corresponding to the pitches on the scale with a phase difference of  $90^\circ$  (i.e. quadrature output). The displacement is then obtained by counting the number of pulses multiplying the period of the pitch, and the direction of the movement indicated by the advance/delay of the phase. Collect the quadrature signals using a data acquisition card enables real-time monitoring for the stage displacement in parallel to the luminescence signal, so that the luminescent targets can be pinpointed at high precision.

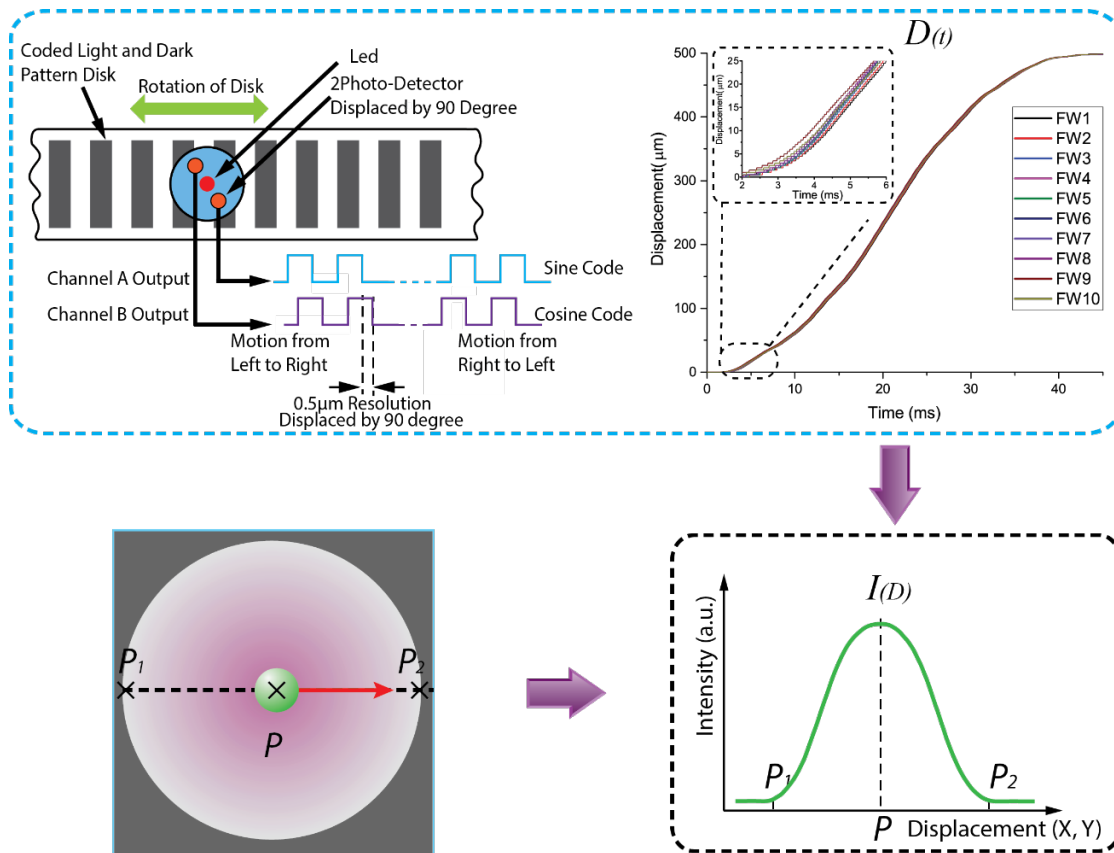


**FIGURE 4-1** Determining the target location along the scanning axis from the signal profile.

I further implemented an autofocus unit to offset any tilt of sample substrate in real time. As shown in Figure 4-2(a), the autofocus unit employs an off-axis LED beam to monitor the distance from the sample substrate to the objective, which influences the position of the reflected beam on the split photodiode. When the sample plane is at focus, the reflected beam reaches the middle of the split photodiode and the output is nearly zero, while focus shift of the sample plane  $\delta$  will generate a displacement  $\theta$  on the split photodiode, resulting in negative feedback that drives the focus to cancel the shift. Figure 4-2(b) plots the output of

the split photodiode in relation to the focal length, in which the green shadow indicates the in-focus area.

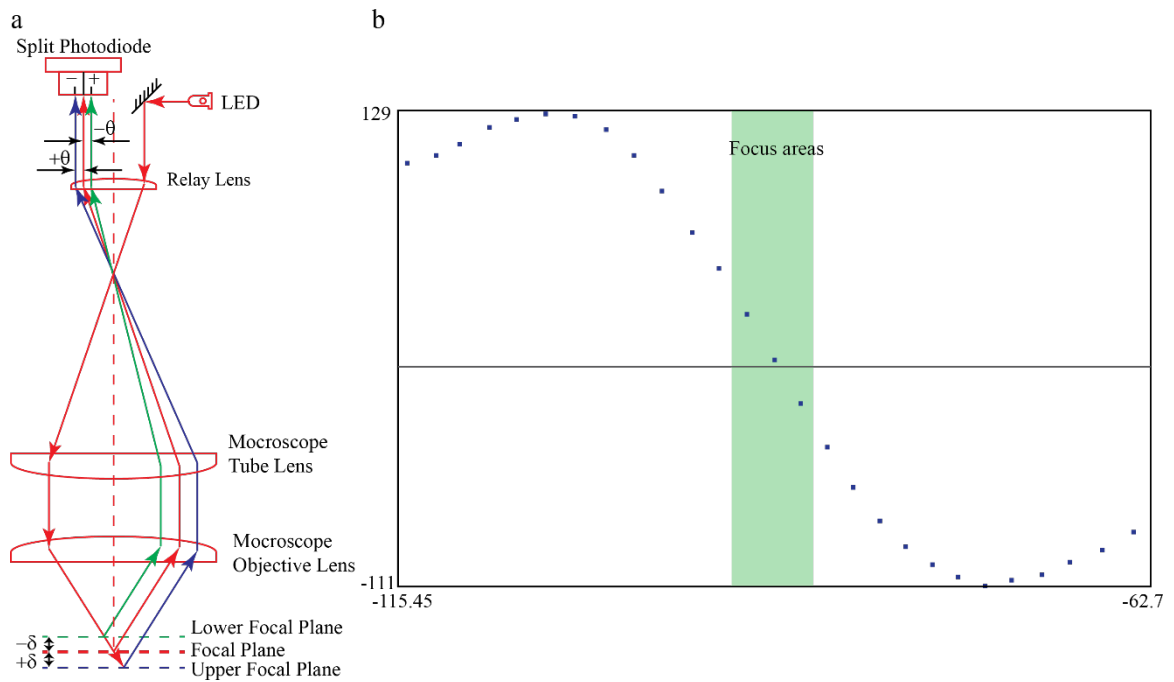


**FIGURE 4-2** (a) Principle of autofocus unit. (b) The performance curve of autofocus unit.

## 4.2 Paper 4

**Xianlin Zheng**, Yiqing Lu, Jiangbo Zhao, Yuhai Zhang, Wei Ren, Deming Liu, Jie Lu, James A. Piper, Robert C. Leif, Xiaogang Liu and Dayong Jin, "High-Precision Pinpointing of Luminescent Targets in Encoder Assisted Scanning Microscopy Allowing High-Speed Quantitative Analysis " *Analytical Chemistry*, 2016, DOI: 10.1021/acs.analchem.5b03767.

On the basis of the original OSAM developed by my supervisors, I introduced the linear encoders and the autofocus unit to the system, and integrated their functions into the LabVIEW program that controls the scanning, time-gated detection and in-line data processing. I coordinated sample preparation with Macquarie colleagues and international collaborators, and collected all data by myself. I analysed the data, prepared the figures and the manuscript under the guidance of my supervisors. Author contributions to this paper are summarised in [Table 4-1](#).

**TABLE 4-1** Summary of author contribution to paper 4 following the order of authors.

	X. Z	Y. L	J. Z	Y. Z	W. R	D. L	J. L	J. P	R. L	X. L	D. J
Experiment Design	•	•									•
System Setup	•										
Sample Preparation	•		•	•	•	•	•	•	•	•	
Data Collection	•										
Analysis	•	•									
Figures	•	•									
Manuscript	•	•	•					•			•

## High-Precision Pinpointing of Luminescent Targets in Encoder-Assisted Scanning Microscopy Allowing High-Speed Quantitative Analysis

Xianlin Zheng,<sup>†</sup> Yiqing Lu,<sup>\*,†</sup> Jiangbo Zhao,<sup>†</sup> Yuhai Zhang,<sup>§</sup> Wei Ren,<sup>‡</sup> Deming Liu,<sup>†</sup> Jie Lu,<sup>†</sup> James A. Piper,<sup>†</sup> Robert C. Leif,<sup>||</sup> Xiaogang Liu,<sup>§,⊥</sup> and Dayong Jin<sup>†,‡</sup>

<sup>†</sup>Advanced Cytometry Laboratories, ARC Centre of Excellence for Nanoscale BioPhotonics (CNBP), Macquarie University, Sydney, New South Wales 2109, Australia

<sup>‡</sup>Institute for Biomedical Materials and Devices, Faculty of Science, University of Technology Sydney, Sydney, New South Wales 2007, Australia

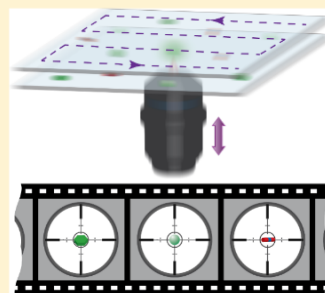
<sup>§</sup>Department of Chemistry, National University of Singapore, 3 Science Drive 3, Singapore 117543, Singapore

<sup>||</sup>Newport Instruments, 3345 Hopi Place, San Diego, California 92117-3516, United States

<sup>⊥</sup>Institute of Materials Research and Engineering, A\*STAR (Agency for Science, Technology and Research), 3 Research Link, Singapore 117602, Singapore

### Supporting Information

**ABSTRACT:** Compared with routine microscopy imaging of a few analytes at a time, rapid scanning through the whole sample area of a microscope slide to locate every single target object offers many advantages in terms of simplicity, speed, throughput, and potential for robust quantitative analysis. Existing techniques that accommodate solid-phase samples incorporating individual micrometer-sized targets generally rely on digital microscopy and image analysis, with intrinsically low throughput and reliability. Here, we report an advanced on-the-fly stage scanning method to achieve high-precision target location across the whole slide. By integrating X- and Y-axis linear encoders to a motorized stage as the virtual "grids" that provide real-time positional references, we demonstrate an orthogonal scanning automated microscopy (OSAM) technique which can search a coverslip area of  $50 \times 24 \text{ mm}^2$  in just 5.3 min and locate individual  $15 \mu\text{m}$  lanthanide luminescent microspheres with standard deviations of 1.38 and  $1.75 \mu\text{m}$  in X and Y directions. Alongside implementation of an autofocus unit that compensates the tilt of a slide in the Z-axis in real time, we increase the luminescence detection efficiency by 35% with an improved coefficient of variation. We demonstrate the capability of advanced OSAM for robust quantification of luminescence intensities and lifetimes for a variety of micrometer-scale luminescent targets, specifically single down-shifting and upconversion microspheres, crystalline microplates, and color-barcoded microrods, as well as quantitative suspension array assays of biotinylated-DNA functionalized upconversion nanoparticles.



Quantitative luminescence measurements of biomolecules, single cells, and tissue specimens in solid phase are particularly valuable for identification and unambiguous confirmation of rare cell types,<sup>1–3</sup> time-lapse study of live cells,<sup>4–6</sup> profiling of subcellular components and biomolecular expressions,<sup>7–9</sup> and a broad range of other diagnostics applications.<sup>10–12</sup> The existing techniques based on digital microscopy,<sup>13–16</sup> however, are time-consuming and resource-demanding, as images are typically captured for the entire sample area, or even through three-dimensional space,<sup>17–20</sup> followed by stitching and processing to identify and quantitate targets of interest. Their quantification is also less accurate, because different types of noise and background emission interfere in the measurement of absolute intensities, and targets that are randomly located at the periphery of the field-of-view (FOV) have large variation in excitation and detection efficiencies.<sup>21–23</sup> The key to realizing a simplified accessible

technique for quantitative luminescence measurements lies in the improvements in both the signal-to-background contrast and the pinpointing precision with which each target is brought to the center of the FOV.

One solution to this problem includes the use of lanthanide luminescent materials exhibiting long lifetimes and/or photon upconversion properties, which are highly useful as either high-contrast molecular probes for direct labeling<sup>24–30</sup> or microsphere-based suspension arrays for high throughput assays.<sup>31–33</sup> Improved sensitivity by orders of magnitude has been demonstrated compared to the conventional fluorescence methods, taking advantage of either time-gated detection or

Received: October 6, 2015

Accepted: December 15, 2015

Published: December 15, 2015

near-infrared (NIR) excitation to remove the autofluorescence background.<sup>34–36</sup> We have also shown recently that luminescence lifetimes of lanthanide-based upconversion materials can be fine-tuned across the microsecond to millisecond range, allowing for creation of temporally multiplexed codes for luminescence detection.<sup>33,37</sup> In parallel, we have developed a controlled synthesis approach for bottom-up production of a library of color-barcoded heterogeneous microrods at low cost.<sup>38</sup> These advances open new opportunities for data storage, document security, and multiplexing assays which allow a large number of labeled biomolecular species to be interrogated simultaneously.

The advantages offered by lanthanide luminescence have further enabled us to develop a novel two-step orthogonal scanning automated microscopy (OSAM) technique<sup>33,39,40</sup> to quickly locate target analytes in a microscope slide-mounted sample with minimum requirements in data acquisition, storage, and processing. Briefly, the initial scan entails continuous sample movement along the *X*-axis, with a single-element photodetector to rapidly identify any randomly distributed luminescent targets on a slide. By doing this, a sunrise–sunset profile of luminescence signal can be collected when a target passes the microscopy FOV, which gives the *X*-coordinate for each target. These coordinates guide orthogonal scans along the *Y*-axis to traverse each target at the center of the FOV, allowing luminescence intensity and lifetime for each target to be measured at maximum detected signal.

In spite of the advances made in both materials and instrumentation, the precision with which targets can be located within the comparatively large area of a microscope slide has been limited (typically to  $\pm 30\ \mu\text{m}$ , large compared with target size) by electronic jitter and mechanical lag of the scanning stage, as well as optical defocusing on the often tilted slide. Truly quantitative luminescence measurement for micrometer-scale targets lies in interrogation of every individual target under identical illumination and detection conditions with a precision in location which is small compared to the target size. Here, we report a major advance in OSAM performance achieved using linear encoders to provide virtual grids of spatial reference in the *XY* plane and addition of an autofocus capability which enables us to offset slide tilt in real time. This new referenced-OSAM (or R-OSAM) achieves order-of-magnitude improvements in the precision of target location and subsequent quantification of luminescence intensity of individual micrometer-scale targets in real-time during rapid scanning. The performance of the R-OSAM is systematically validated by statistical analysis of luminescent microspheres, microplates, and color-barcoded microrods, as well as suspension array assays of biotinylated-DNA functionalized upconversion nanoparticles (UCNPs).

## ■ EXPERIMENTAL SECTION

**Optical Configuration.** Shown in Supporting Figure S1, the R-OSAM is built on an inverted microscope (IX71, Olympus) equipped with a motorized stage (H117, Prior Scientific; typical translation speed 25 mm/s). Two light sources in addition to the original mercury lamp are integrated: a fiber-coupled near-infrared (NIR) diode laser with peak wavelength at 980 nm (Beijing Viasho Technology; maximum CW laser power 1.3 W) and an ultraviolet light-emitting diode (UV LED) with peak wavelength at 365 nm (NCSU033A, Nichia; bandwidth 9 nm fwhm, maximum CW output 250 mW). A doublet collimator (F810SMA-780, Thorlabs;  $f = 36$

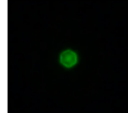
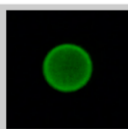
mm) and a fused silica lens ( $f = 30$  mm) are coupled to the additional sources, respectively, to engineer uniformity in illumination. The excitation beam is reflected by a dichroic before illuminating the field-of-view (FOV) through an objective lens (NT38-340, Edmund Optics;  $60\times$ , NA = 0.75). The luminescence is directed to either an electronically gateable photomultiplier tube (PMT, H10304-20-NF, Hamamatsu;  $10^6$  gain at 0.9 V control voltage) or a digital color camera (DP72, Olympus), switched by a movable mirror placed at  $45^\circ$ . In front of the PMT, a convex lens ( $f = 40$  mm) is used to converge the emission onto the photocathode window. Band-pass filters mounted on a filter wheel can be inserted to select target emission bands.

The following dichroic mirrors and filters were used in this work: FF511-Di01 as well as FF750-SDi02 (Semrock) for NIR excitation; 400DCLP (Chroma) for UV excitation; FF01-540/50 and FF01-655/40 (Semrock) for the green and red upconversion emission from  $\text{Er}^{3+}$ ; FF02-475/50 (Semrock) for the blue upconversion emission from  $\text{Tm}^{3+}$ ; 9514-B (New Focus) for the red emission of  $\text{Eu}^{3+}$  complexes; and FF01-842/SP (Semrock) for blockage of excitation wavelengths when taking luminescence images.

**Linear Encoders.** Though the position of the motorized stage can be read out on demand, the in-built serial communication does not provide the capability of real-time reading during continuous motion. We therefore added to the *X* and *Y* axes of the stage, two miniature linear encoders (MercuryII 1600, MicroE Systems) as well as laser tape scales (Supporting Figure S2; the tape scales are attached to the scanning plates, while the encoders are mounted on the immobile frame). Each encoder has a 850 nm infrared laser diode to illuminate the tape scale engraved with  $20\ \mu\text{m}$  grating pitches and a displacement sensor employing  $\times 40$  interpolation to deliver two quadrature square-wave outputs with  $0.5\ \mu\text{m}$  resolution per count when reading the tape scale that moves with the stage. A computer equipped with a multifunction data acquisition card (PCIe-6363, National Instruments) is used to synchronously record the optical signal from the PMT (transduced by a preamplifier at  $10^5\ \text{V/A}$ ; DLPCA-200, FEMTO) and the displacement output from the encoders, enabling correlation in the form of a luminescence vs position curve.

**Autofocus System.** To provide the scanning precision along the *Z* axis (focal length), an autofocus system consisting of a *Z*-drive and a focus feedback unit (CRISP, Applied Scientific Instrumentation) is integrated into the R-OSAM (Supporting Figure S3). It is designed to compensate the difference in *Z* positions across the entire sample area, so that individual targets can be interrogated at identical focal length. The *Z*-drive, incorporating a DC motor and a rotary encoder, is mounted onto the fine focus shaft of the microscope. The focus feedback unit, basically an extra reflective detection module with a LED source (720 nm), a filter cube, and a split photodiode, is inserted in the detection path after the original dichroic. The LED is off the optical axis, so that any focus change of the slide results in the lateral displacement of the reflected light, which is detected by the split photodiode (see Supporting Figure S4).<sup>41</sup> Its signal is conditioned by an in-built log amplifier to provide closed-loop control for the *Z*-drive. To ensure robust operation, the LED intensity, the log amplifier offset, and the photodiode lateral position are carefully adjusted, so that the signal sensitivity in response to focus shift is maximized. In addition, the relative focus height (*Z*

Table 1. Descriptions of the Evaluation Samples as well as Experiments in Which They Are Used

Sample	Description	Use in Experiments	Luminescent Image
1	15- $\mu\text{m}$ polystyrene beads incorporating 40-nm $\text{NaYF}_4\text{:Yb,Er}$ UCNPs with 20 mol % $\text{Yb}^{3+}$ and 4 mol % $\text{Er}^{3+}$	target pinpointing; focus height analysis; R-OSAM vs image analysis; material characterisation	
2	5- $\mu\text{m}$ polystyrene beads containing $\text{Eu}^{3+}$ complexes (i.e. FireRed beads)	quantification enhancement	
3	barcoded upconversion microrods (width 1–1.5 $\mu\text{m}$ ) with $\text{NaYb}_{0.995}\text{F}_4\text{:Tm}_{0.005}$ in the middle (length $\sim 1 \mu\text{m}$ ) and $\text{NaYb}_{0.999}\text{F}_4\text{:Er}_{0.001}$ at the ends (length $\sim 3 \mu\text{m}$ each side)	material characterisation	
4	upconversion microplates of $\text{NaYb}_{0.96}\text{F}_4\text{:Er}_{0.04}$ (size $\sim 4 \mu\text{m}$ , thickness $\sim 0.5 \mu\text{m}$ )	R-OSAM vs image analysis	
5	streptavidin-modified 15- $\mu\text{m}$ polystyrene beads reacted with biotinylated-DNA functionalised UCNPs	suspension array assays	

coordinate), monitored by the rotary encoder of the Z-drive, is displayed on the controller of the autofocus system.

**Evaluation Samples.** Five kinds of lanthanide luminescent samples, as summarized in Table 1, were prepared for comprehensive validation of the new R-OSAM in precise pinpointing of micrometer-sized targets and quantitative luminescence measurements.

Polystyrene microspheres were used as carriers to embed both upconversion and down-shifting luminescent materials via swelling methods. The  $\text{NaYF}_4\text{:Yb,Er}$  upconversion nanoparticles (UCNPs; doped with 20%  $\text{Yb}^{3+}$  and 4%  $\text{Er}^{3+}$ , size  $\sim 40$  nm; see Supporting Figure S5 for the transmission electron microscopy image) were synthesized with their oleic acid surfactants removed and incorporated into 15  $\mu\text{m}$  polystyrene beads (PC07N/8783, Bangs Laboratories) according to existing protocols.<sup>32,37</sup> The Eu-complex-containing FireRed beads (5  $\mu\text{m}$  in diameter, Newport Instruments) were prepared according to the protocol reported previously.<sup>42</sup>

Hydrothermal synthesis was employed for the controlled growth of micrometer-sized upconversion crystals. The upconversion microrods (middle section  $\text{NaYbF}_4\text{:Tm}$  with 99.5%  $\text{Yb}^{3+}$  and 0.5%  $\text{Tm}^{3+}$ ; end sections  $\text{NaYbF}_4\text{:Er}$  with 99.9%  $\text{Yb}^{3+}$  and 0.1%  $\text{Er}^{3+}$ ; length  $\sim 7 \mu\text{m}$ , width 1–1.5  $\mu\text{m}$ ) were synthesized using our reported protocol.<sup>38</sup> A similar method was used to synthesize the microplates ( $\text{NaYbF}_4\text{:Er}$ , with 96%  $\text{Yb}^{3+}$  and 4%  $\text{Er}^{3+}$ ; size  $\sim 4 \mu\text{m}$ , thickness  $\sim 0.5 \mu\text{m}$ ).

To demonstrate the quantitative suspension array assays, first, we functionalized streptavidin (SA) onto the polystyrene beads as the capture substrate (suspension arrays). 50  $\mu\text{L}$  of the 15  $\mu\text{m}$  polystyrene beads was first washed twice by water and then added into 400  $\mu\text{L}$  of 2-(*N*-morpholino)ethanesulfonic acid (MES) buffer containing 20  $\mu\text{L}$  of 2.5 mg/mL SA and 5

mg of 1-ethyl-3-(3-(dimethylamino)propyl)carbodiimide (EDC). The mixture was incubated at 1000 rpm for 2 h. The SA-beads were harvested by centrifugation and washing and finally stored in 200  $\mu\text{L}$  of water. Second, the biotinylated-DNA functionalized UCNPs, as the reporter analytes, were prepared on the basis of a previously reported method.<sup>43</sup> Twenty  $\mu\text{L}$  of 10 mg/mL UCNPs was suspended in 400  $\mu\text{L}$  of chloroform and then mixed with 300  $\mu\text{L}$  of 50 mM MES buffer containing 6.5  $\mu\text{M}$  biotinylated DNA (sequence: 5'-GAA ACC CTA TGT ATG CTC TTT TTT TTT T-biotin-3', Integrated DNA Technologies). The mixture was incubated at 600 rpm for 2 h to perform ligand exchange on the surface of UCNPs from the original oleic acid to the biotinylated DNA. As a result, the UCNPs were transferred from the chloroform to the MES buffer. The latter was collected and centrifuged at 14 600 rpm for 5 min. After removing the supernatant containing unbound biotinylated DNA, the functionalized UCNPs were redispersed into 100  $\mu\text{L}$  of deionized water. The concentration was 2 mg/mL (corresponding to 15.6 nM)<sup>35</sup> assuming no loss in the preparation steps above. Finally, the assay was conducted by mixing 10  $\mu\text{L}$  of the as-prepared biotinylated-DNA functionalized UCNPs (10  $\mu\text{L} \times 15.6 \text{ nM} = 156 \text{ fmol}$ ) or its dilution (10, 50, and 200 times) with 5  $\mu\text{L}$  of the SA-beads. The reaction was allowed for 3 h at room temperature, and the unbound UCNPs were washed away before luminescence measurement.

To prepare the samples for scan, each 20  $\mu\text{L}$  suspension of microspheres, microplates, or microrods ( $\sim 2 \times 10^4$  particle/mL after dilution with ethanol) was spread on one coverslip of 50 mm  $\times$  24 mm, which was preheated to 60  $^\circ\text{C}$  to facilitate evaporation of the liquid. The coverslip was then sealed with a microscopic slide. Flip of the sample was avoided to ensure that

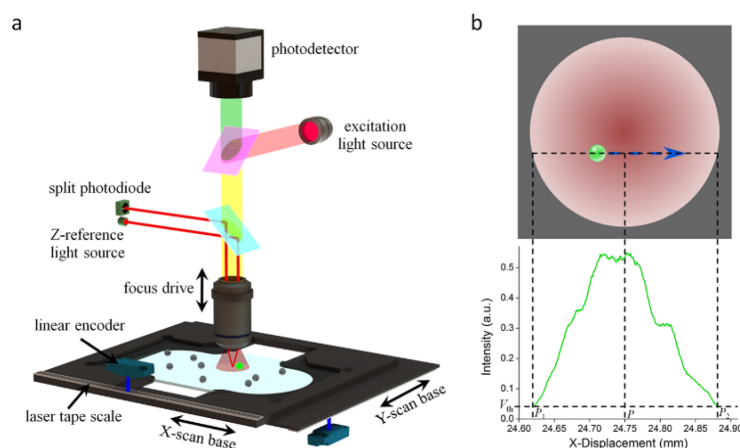


**Figure 1.** (a) Schematic illustrating the concept of R-OSAM, which exploits linear encoders and autofocus to pinpoint targets during rapid scanning of the sample slide. For each of the scan directions ( $X$  and  $Y$ ), a laser tape scale is attached to the stage, and a linear encoder is mounted (fixed to the microscope frame) above the scale to read the displacement when the stage moves. The output is correlated to the luminescence signal recorded by the photodetector to determine the precise location of the target along the scan direction. To enable the autofocus function of the sample slide, a  $Z$ -reference light source delivers its beam in the margin of the optical path, so that any change in the focal length will lead to the shift of the reflected beam. This is detected by a split photodiode, which feedback controls the focus drive to maintain the focal length. (b) The sunrise–sunset luminescence signal profile with respect to the scan displacement of one typical target passing across the field of view (FOV), from which the location of the target along the scan direction is obtained.

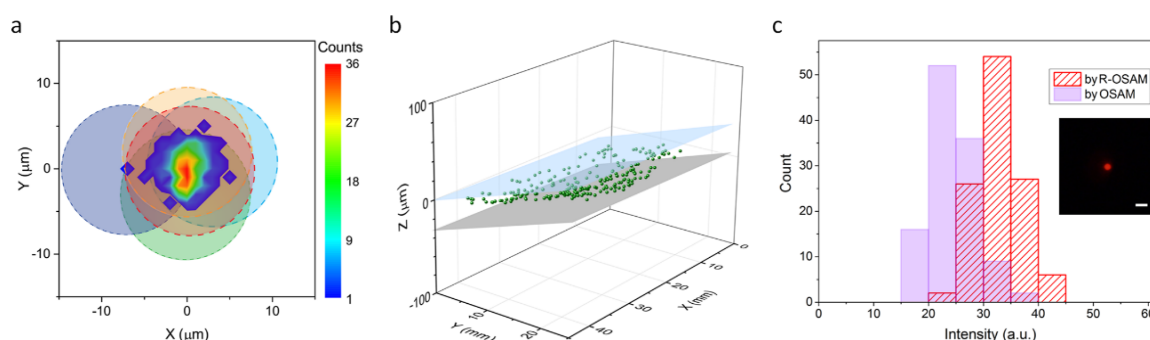


**Figure 2.** (a) A heat plot summarizing the location errors of the UCNP-impregnated calibration beads obtained by the R-OSAM with respect to the center of the FOV for a typical sample slide, with the shadowed circles indicating the size of the beads ( $15\ \mu\text{m}$ ). (b) The spatial distribution of UCNP-impregnated beads spread between a microscopic slide and a coverslip, measured by the R-OSAM. The standard deviations for the  $Z$ -coordinate of the bead and for the distance from each bead to the substrate plane are  $16.2$  and  $6.7\ \mu\text{m}$  respectively, suggesting that the tilt of the slide is usually the major cause of the variance in focus. (c) Comparison of luminescence intensity profiles for  $5\ \mu\text{m}$  Eu-calibration beads on the same sample slide, measured by the R-OSAM (red bars) and the OSAM with both encoders and autofocus disabled (purple bars). Exposure time:  $100\ \text{ms}$ . Scale bar:  $15\ \mu\text{m}$ .

particles stuck to only one surface. Alternatively, adherent surface treatment or spin coating can be applied.

## RESULTS AND DISCUSSION

**High-Speed Scanning by R-OSAM.** The concept of the referenced-OSAM (R-OSAM) employing the linear encoders and the autofocus unit is illustrated in Figure 1a. It rapidly scans sample slides containing luminescent targets by taking advantage of the negligible autofluorescence and scattering background obtained via either time-gated detection or NIR illumination for the upconversion materials, while both the spatial referencing and the autofocus are carried out in real time without affecting the scan speed. For every slide, its entire area is first examined in a serpentine pattern consisting of continuous movement along one ( $X$ ) axis and stepwise

movement along the other ( $Y$ ) axis. As shown in Figure 1b, when a target is scanned continuously across the FOV, its luminescence signal exceeds a preselected threshold ( $V_{\text{th}}$ ), so that the entrance ( $P_1$ ) and exit ( $P_2$ ) positions are registered. The target coordinate along the scanning direction ( $X$ ) is calculated out (as  $P = (P_1 + P_2)/2$ ) regardless of variation in the scanning speed. The other coordinate is obtained by a series of orthogonal scans along the  $Y$  axis across each target particle, during which the luminescence intensity is captured when the target is exactly at the center of the FOV. Scanning a coverslip area of  $50 \times 24\ \text{mm}^2$  typically takes  $5.3\ \text{min}$ , corresponding to an analytical speed of  $225\ \text{mm}^2/\text{min}$ . R-OSAM can be operated in either the continuous-wave mode or the time-gating mode, as described below.

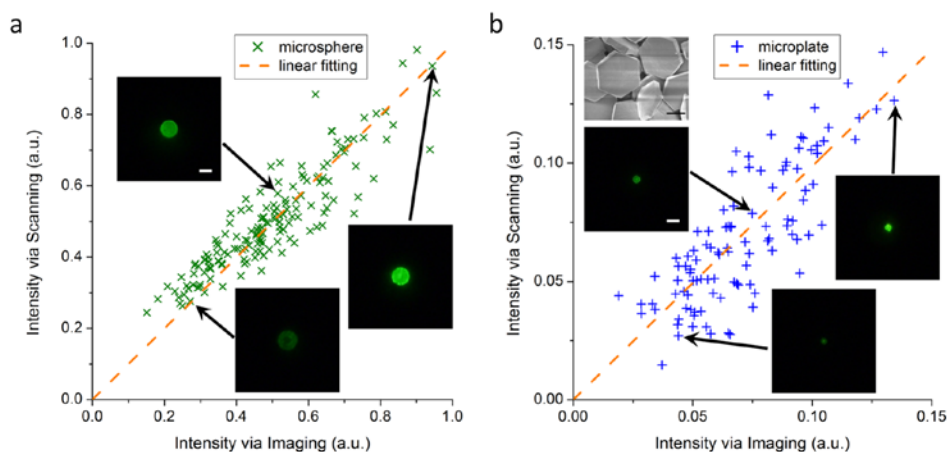


**Figure 3.** Correlation between the luminescence intensity captured by the R-OSAM and that measured from the image taken after target retrieval, for (a) 15  $\mu\text{m}$  UCNP-impregnated microspheres and (b) upconversion microplates (scanning electron microscopy image on the top left corner), over a large dynamic range. Each of the luminescence images show an individual microsphere or microplate that generates the data point, with exposure times of 50 ms for the microspheres and 150 ms for the microplates, respectively. Scale bars represent 15  $\mu\text{m}$  in the luminescence image and 2  $\mu\text{m}$  in the SEM image.

**Precise Target Pinpointing Assisted by Encoders.** To evaluate the enhanced precision of target location achieved by the linear encoders, for each target, its  $XY$  coordinates obtained via orthogonal scanning were retrieved. The motorized stage was then moved to place the target onto the exact center of the FOV, and the movements in  $X$  and  $Y$  were recorded as the error associated with target pinpointing. Figure 2a shows data from one typical slide containing 571 UCNP-impregnated beads (15  $\mu\text{m}$  in diameter) pinpointed during rapid scanning under continuous-wave NIR (980 nm) excitation and PMT detection. The standard deviations of the distances for individual beads moving to the center of the FOV in  $X$  and  $Y$  directions were 1.38 and 1.75  $\mu\text{m}$ , respectively. Similar location precision was achieved upon the smaller microplates and microrods samples, as shown in Supporting Figure S6. These demonstrate that the R-OSAM is capable of target location with precision substantially smaller than the diameter of most targets of practical interest.

To determine the improved precision of R-OSAM in locating down-shifting luminescent targets, the time-gating mode consisting of periodic pulsed UV excitation and delayed detection was employed. With 200  $\mu\text{s}$  time-gating cycles consisting of 90  $\mu\text{s}$  excitation, 10  $\mu\text{s}$  time delay, and 100  $\mu\text{s}$  detection window, standard deviations of 4.01 and 3.74  $\mu\text{m}$  were achieved in  $X$  and  $Y$  directions, respectively, which are about 1 order of magnitude better than the OSAM scanning result without the assistance of the linear encoders (33.0 and 35.6  $\mu\text{m}$ ), as shown in Supporting Figure S7. Because in the time-gating mode a proportion of the targets pass the center of the FOV during the excitation phases when the detector is disabled, the location of them is virtually rounded into the adjacent detection phases, leading to slightly decreased precision compared to the continuous-wave mode.

**Offsetting Z-Axis Variance by Autofocus.** In addition to high-precision  $XY$  target location, accurate luminescence measurement also requires one to bring all the targets to focus in the  $Z$  axis. Figure 2b shows the variance in focus height over a typical slide measured by the autofocus system (with feedback control disabled) upon each target after retrieval as

well as the edges of the slide and the coverslip, which displays both the random positions of each targets between the slide and the coverslip and the tilt of slide itself. It is seen that the latter is usually the major cause of the variance in focus height ( $\sim 70 \mu\text{m}$ ; in contrast, the space between the slide and the coverslip is  $\sim 20 \mu\text{m}$ ) during the whole slide scanning,<sup>44</sup> while the former can be further alleviated with careful sample preparation. By implementing the autofocus system, the focal length is locked with respect to one reflective surface, which essentially compensates the tilt of the sample in real time. The enhanced target location and autofocus of the R-OSAM is demonstrated in Supporting Movie S1.

**Improved Luminescence Quantification by R-OSAM.** The precision of R-OSAM in pinpointing the targets in three dimensions further enhances luminescence quantification with maximized excitation and collection efficiencies. As a result, the average intensity measured from single 5  $\mu\text{m}$  Eu-containing FireRed beads increased by 35% compared with the OSAM with both the encoders and the autofocus unit disabled, as shown in Figure 2c. Moreover, the recorded intensity histogram shows better symmetry with coefficient of variation (CV) improved from 17.0% to 12.7%.

**Comparison of Quantitative Results Obtained by R-OSAM vs Image Analysis.** The intensity captured by the single-element PMT detector during the R-OSAM on-the-fly scanning mode was validated by analyzing the images of each target taken at the retrieval step. Figure 3a shows a good correlation ( $R^2$  of 0.98 for the linear curve fitting) over a large dynamic range by comparing the two approaches in quantifying the intensities of UCNP-impregnated beads. This consistency extends to the upconversion microplates with size of 4  $\mu\text{m}$  or less (Figure 3b;  $R^2$  of 0.95 for the linear curve fitting), suggesting that the R-OSAM gives results comparable to the best conventional image analysis while significantly reducing the processing time.

**High-Throughput Material Characterization by R-OSAM.** Fluorescence microscopy has been conventionally used to assess the quality and dispersity of lanthanide luminescent materials, but the limited number of images by

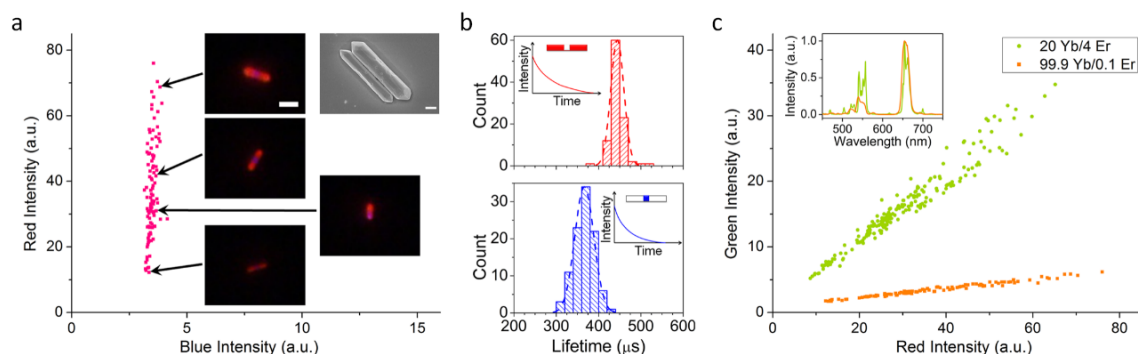


**Figure 4.** (a) A scatter plot showing the luminescence intensities measured by the R-OSAM in the red (ends) and the blue channels (middle) from individual upconversion microrods (SEM image on the top right corner), alongside representative luminescence images taken after target retrieval. Exposure time is 150 ms. Scale bars represent  $5 \mu\text{m}$  in the luminescence image and  $1 \mu\text{m}$  in the SEM image. (b) Histograms of the luminescence lifetimes for the ends (red channel) and the middle (blue channel) of the microrods. (c) The intensity ratios of green to red luminescence with respect to the Yb/Er codoping concentrations. The inset shows normalized emission spectra.

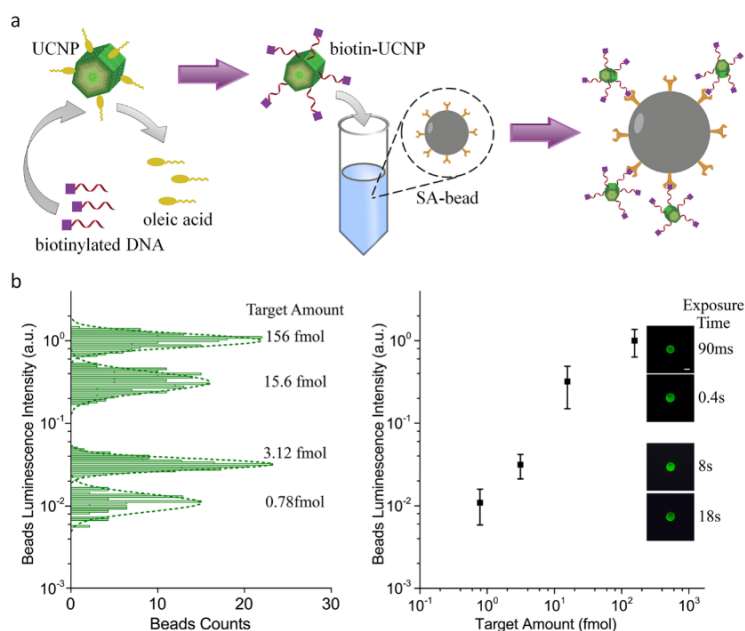


**Figure 5.** (a) The scheme of the demonstration assay using biotinylated-DNA functionalized UCNPs as the target and SA conjugated polystyrene beads as the substrate. (b) The relation between the amount of the biotin-UCNPs and the luminescence intensity of individual beads, concluded statistically from the intensity histograms of the beads populations. The error bars represent twice the standard deviation (95% confidence). The inset images show typical beads from each population, captured with different exposure times. Scale bar:  $10 \mu\text{m}$ .

low-throughput image acquisition and analysis are insufficient to give statistical results. We have developed an analytical application of the R-OSAM scanning microscopy method for statistical characterization of a new type of luminescence material: the epitaxial-grown barcoded upconversion microrods. Figure 4a shows that the as-prepared crystalline microrods have a high-quality consistent core section ( $\text{NaYbF}_4:\text{Tm}$ ) with a narrow CV in the blue luminescence intensity of only 4.93%, but the high CV in the red luminescence intensity of 39.5% reveals substantial variation in growth of the end sections ( $\text{NaYbF}_4:\text{Er}$ ). These results were confirmed by target retrieval showing that the individual variation is attributed to the inconsistency during epitaxial growth in terms of different

lengths and crystalline quality. In fact, a small but significant proportion of the microrods have single ends (see Figure 4a).

In general, the concentrations of sensitizers (Yb) and activators (Tm or Er) in upconversion materials primarily determine the luminescence lifetimes.<sup>37</sup> To further assess the doping uniformity during the crystal growth, we collected the luminescence lifetimes of each individual barcoded microrod. Figure 4b displays the statistics of the luminescence lifetimes for both the blue (Tm) and the red (Er) emissions, yielding CVs of 6.16% and 3.52% (as well as average values of 366 and 444  $\mu\text{s}$ ), respectively. This indicates that dopant concentration of end sections has relatively small variation across the

population of microrods; thus, the large CV for intensity is attributed to variation in the size of the Er-doped end sections.

Moreover, the ratiometric scattering plots by R-OSAM, as shown in Figure 4c, suggest a statistical approach to robust decoding and classification of individual microspheres for multiplexing, in a similar manner to standard flow cytometry assays. Doping UCNPs by 20 mol % Yb and 4 mol % Er yields a consistent green-to-red ratio of 0.526, while doping 99.9 mol % Yb and 0.1 mol % Er yields a consistent green-to-red ratio of 0.0894, with  $R^2$  over 0.99 when linear curve fitting is applied. The intrinsic ratios reflect the specific types of the UCNPs used, independent of the exact number of UCNPs embedded in each microsphere.

**Quantitative Suspension Array Assays.** Suspension array assays provide a high-throughput analytical approach to screening and quantification of multiple biomolecules in a single test.<sup>45,46</sup> These are based on ensembles of spectrally coded microspheres, most commonly using varying combinations of fluorescent dyes.<sup>47–49</sup> While they have major advantages including rapid reaction kinetics, high throughput, and statistical accuracy, their potential for quantitative assays is often compromised, because color-coded microspheres will also generate spectral-channel interference in the fluorescence detection of the reporter dyes. To remove such interference for accurate quantification, we use lanthanide materials as the reporter probes that can be completely distinguished in the time domain. Such an assay was demonstrated here by using the UCNPs as the reporter probes and the R-OSAM in the time-gating mode for quantitative background-free luminescent measurement. Figure 5a illustrates our experiment by mixing the as-prepared biotinylated-DNA functionalized UCNPs with the SA-modified polystyrene beads, with different amounts of the UCNPs used to evaluate the quantification accuracy. As shown in Figure 5b, the time-gated luminescence signal drops largely linearly as the dilution of the UCNPs, with the intensity CV around 20% for each sample. Similar results can be obtained via retrieval of every target followed by conventional image analysis (see Supporting Figure S8); however, this is at the cost of a very long data collection process. This demonstration not only reinforces the practical value of R-OSAM scanning at high speed for precise quantification of target luminescence but also demonstrates the advantage of using UCNPs as reporter probes to remove the optical background for quantitative suspension array assays.

## CONCLUSIONS

By integrating the XY-axes linear encoders and the Z-axis autofocus system into a motorized-stage-based scanning microscopy, precise pinpointing of luminescent targets at an analytical speed of 225 mm<sup>2</sup>/min is realized in this work. Its precision, measured as the distances from the pinpointed targets to the center of the field of view, is 1.38 and 1.75  $\mu\text{m}$  in X and Y directions, respectively, demonstrating that the R-OSAM is capable of target location with precision substantially smaller than typical cells and microorganisms. The use of the autofocus system to lock the optical focus to one reflective surface has essentially compensated the tilt of the sample slide in real time. These new advances deliver the best precision in target pinpointing in three dimensions during rapid scanning over a whole microscopic slide, enabling accurate quantification of the luminescence intensities as well as derivative properties such as ratios and lifetimes upon individual targets.

Our R-OSAM approach benefits from the low-background nature of lanthanide luminescence that is immune to the autofluorescence and scattering background via time-gated detection and/or NIR illumination for upconversion materials. It offers a robust and high-throughput solution beyond conventional image analysis for statistical characterization of luminescence materials. Compared to measurements from collective samples using common spectroscopy and microscopy approaches, the statistical results obtained by R-OSAM provide an array of in-depth information on population variations from one target to another. Such measurement was previously not possible in the routine materials syntheses and characterizations but will enable new understanding and development of advanced materials for quantitative applications that exploit combinations of colors, intensities, lifetimes, and spatial barcodes for high-throughput analysis. Moreover, we demonstrate the upconversion nanoparticles as background-free reporter probes suitable for quantitative biomolecular assays based on the suspension arrays, opening new opportunities in high-throughput multiplexed screening for analytical chemistry, micro- and molecular biology, pharmaceutical discoveries, and clinical diagnostics.

## ASSOCIATED CONTENT

### Supporting Information

The Supporting Information is available free of charge on the ACS Publications website at DOI: 10.1021/acs.analchem.5b03767.

Optical configuration of the R-OSAM; photos of the linear encoders and the autofocus system employed in the R-OSAM; diagram of autofocusing principle employed; TEM image of nanoparticles; additional heat plots of location errors; luminescence intensity plots obtained by image analysis (PDF)

Movie showing the retrieval of individual 15  $\mu\text{m}$  UNCP-impregnated beads after the R-OSAM scanning (MPG)

## AUTHOR INFORMATION

### Corresponding Author

\*E-mail: yiqing.lu@mq.edu.au.

### Notes

The authors declare no competing financial interest.

## ACKNOWLEDGMENTS

This project is financially supported by the Australian Research Council (Linkage Infrastructure, Equipment and Facilities LE150100177, Linkage Project LP140100462, Centre of Excellence for Nanoscale BioPhotonics, and Future Fellowship of D.J. FT130100517), Macquarie University Research Fellowship (Y.L.), and Macquarie University Research Excellence Scholarships. Y.L. acknowledges the ISAC Scholar program of the International Society for Advancement of Cytometry.

## REFERENCES

- (1) Chan, L. L.-Y.; Shen, D.; Wilkinson, A. R.; Patton, W.; Lai, N.; Chan, E.; Kuksin, D.; Lin, B.; Qiu, J. *Autophagy* **2012**, *8*, 1371–1382.
- (2) Chan, L.-Y.; Cohen, D.; Kuksin, D.; Paradis, B.; Qiu, J. *J. Fluoresc.* **2014**, *24*, 983–989.
- (3) Chen, F.; Lu, J.-r.; Binder, B. J.; Liu, Y.-c.; Hodson, R. E. *Appl. Environ. Microbiol.* **2001**, *67*, 539–545.
- (4) Krylov, S. N.; Zhang, Z.; Chan, N. W. C.; Arriaga, E.; Palcic, M. M.; Dovichi, N. J. *Cytometry* **1999**, *37*, 14–20.

- (5) Han, H.-S.; Niemeyer, E.; Huang, Y.; Kamoun, W. S.; Martin, J. D.; Bhaumik, J.; Chen, Y.; Roberge, S.; Cui, J.; Martin, M. R.; Fukumura, D.; Jain, R. K.; Bawendi, M. G.; Duda, D. G. *Proc. Natl. Acad. Sci. U. S. A.* **2015**, *112*, 1350–1355.
- (6) Ball, D. A.; Lux, M. W.; Adames, N. R.; Peccoud, J. *PLoS One* **2014**, *9*, e107087.
- (7) Erenpreisa, J.; Erenpreiss, J.; Freivalds, T.; Slaidina, M.; Krampe, R.; Butikova, J.; Ivanov, A.; Pjanova, D. *Cytometry* **2003**, *52A*, 19–27.
- (8) Fowler, T. L.; Bailey, A. M.; Bednarz, B. P.; Kimple, R. J. *Biotechniques* **2015**, *58*, 37–39.
- (9) Hu, S.; Zhang, L.; Krylov, S.; Dovichi, N. J. *Anal. Chem.* **2003**, *75*, 3495–3501.
- (10) Ymeti, A.; Li, X.; Lunter, B.; Breukers, C.; Tibbe, A. G. J.; Terstappen, L. W. M. M.; Greve, J. *Cytometry, Part A* **2007**, *71A*, 132–142.
- (11) Rossnerova, A.; Spatova, M.; Schunck, C.; Sram, R. J. *Mutagenesis* **2011**, *26*, 169–175.
- (12) Ito, H.; Oga, A.; Ikemoto, K.; Furuya, T.; Maeda, N.; Yamamoto, S.; Kawachi, S.; Itoh, H.; Oka, M.; Sasaki, K. *Cytometry, Part A* **2014**, *85*, 809–816.
- (13) Galbraith, W.; Wagner, M. C. E.; Chao, J.; Abaza, M.; Ernst, L. A.; Nederlof, M. A.; Hartsock, R. J.; Taylor, D. L.; Waggoner, A. S. *Cytometry* **1991**, *12*, 579–596.
- (14) Allalou, A.; Wählby, C. *Computer Methods and Programs in Biomedicine* **2009**, *94*, 58–65.
- (15) Szalóki, N.; Doan-Xuan, Q. M.; Szöllösi, J.; Tóth, K.; Vámosi, G.; Bacsó, Z. *Cytometry, Part A* **2013**, *83*, 818–829.
- (16) Furia, L.; Pelicci, P. G.; Faretta, M. *Cytometry, Part A* **2013**, *83A*, 333–343.
- (17) Rigaut, J. P.; Vassy, J.; Herlin, P.; Duigou, F.; Masson, E.; Briane, D.; Foucrier, J.; Carvajal-Gonzalez, S.; Downs, A. M.; Mandard, A.-M. *Cytometry* **1991**, *12*, 511–524.
- (18) Beliën, J. A. M.; van Ginkel, H. A. H. M.; Tekola, P.; Ploeger, L. S.; Poulin, N. M.; Baak, J. P. A.; van Diest, P. J. *Cytometry* **2002**, *49*, 12–21.
- (19) Ragan, T.; Sylvan, J. D.; Kim, K. H.; Huang, H.; Bahlmann, K.; Lee, R. T.; So, P. T. C. *J. Biomed. Opt.* **2007**, *12*, 014015.
- (20) Choi, H.; Wadduwage, D. N.; Tu, T. Y.; Matsudaira, P.; So, P. T. C. *Cytometry, Part A* **2015**, *87*, 49–60.
- (21) Chieco, P.; Jonker, A.; Melchiorri, C.; Vanni, G.; Van Noorden, C. F. *Histochem. J.* **1994**, *26*, 1–19.
- (22) Rodenacker, K.; Bengtsson, E. *Anal. Cell. Pathol.* **2003**, *25*, 1–36.
- (23) De Vos, W. H.; Van Neste, L.; Dieriks, B.; Joss, G. H.; Van Oostveldt, P. *Cytometry, Part A* **2010**, *77A*, 64–75.
- (24) Beverloo, H. B.; van Schadewijk, A.; van Gelderen-Boele, S.; Tanke, H. J. *Cytometry* **1990**, *11*, 784–792.
- (25) Yuan, J.; Wang, G. *TrAC, Trends Anal. Chem.* **2006**, *25*, 490–500.
- (26) Rajapakse, H. E.; Gahlaut, N.; Mohandessi, S.; Yu, D.; Turner, J. R.; Miller, L. W. *Proc. Natl. Acad. Sci. U. S. A.* **2010**, *107*, 13582–13587.
- (27) Lu, Y.; Jin, D.; Leif, R. C.; Deng, W.; Piper, J. A.; Yuan, J.; Duan, Y.; Huo, Y. *Cytometry, Part A* **2011**, *79A*, 349–355.
- (28) Li, L.-L.; Zhang, R.; Yin, L.; Zheng, K.; Qin, W.; Selvin, P. R.; Lu, Y. *Angew. Chem., Int. Ed.* **2012**, *51*, 6121–6125.
- (29) Liu, Y.; Tu, D.; Zhu, H.; Ma, E.; Chen, X. *Nanoscale* **2013**, *5*, 1369–1384.
- (30) Zhou, L.; Wang, R.; Yao, C.; Li, X.; Wang, C.; Zhang, X.; Xu, C.; Zeng, A.; Zhao, D.; Zhang, F. *Nat. Commun.* **2015**, *6*, 6938.
- (31) Zhang, F.; Shi, Q.; Zhang, Y.; Shi, Y.; Ding, K.; Zhao, D.; Stucky, G. D. *Adv. Mater.* **2011**, *23*, 3775–3779.
- (32) Wang, F.; Deng, R.; Wang, J.; Wang, Q.; Han, Y.; Zhu, H.; Chen, X.; Liu, X. *Nat. Mater.* **2011**, *10*, 968–973.
- (33) Lu, Y.; Lu, J.; Zhao, J.; Cusido, J.; Raymo, F. M.; Yuan, J.; Yang, S.; Leif, R. C.; Huo, Y.; Piper, J. A.; Paul Robinson, J.; Goldys, E. M.; Jin, D. *Nat. Commun.* **2014**, *5*, 3741.
- (34) van de Rijke, F.; Zijlmans, H.; Li, S.; Vail, T.; Raap, A. K.; Niedbala, R. S.; Tanke, H. J. *Nat. Biotechnol.* **2001**, *19*, 273–276.
- (35) Zhao, J.; Jin, D.; Schartner, E. P.; Lu, Y.; Liu, Y.; Zvyagin, A. V.; Zhang, L.; Dawes, J. M.; Xi, P.; Piper, J. A.; Goldys, E. M.; Monro, T. M. *Nat. Nanotechnol.* **2013**, *8*, 729–734.
- (36) Zhang, L.; Zheng, X.; Deng, W.; Lu, Y.; Lechevallier, S.; Ye, Z.; Goldys, E. M.; Dawes, J. M.; Piper, J. A.; Yuan, J.; Verelst, M.; Jin, D. *Sci. Rep.* **2014**, *4*, 6597.
- (37) Lu, Y.; Zhao, J.; Zhang, R.; Liu, Y.; Liu, D.; Goldys, E. M.; Yang, X.; Xi, P.; Sunna, A.; Lu, J.; Shi, Y.; Leif, R. C.; Huo, Y.; Shen, J.; Piper, J. A.; Robinson, J. P.; Jin, D. *Nat. Photonics* **2014**, *8*, 32–36.
- (38) Zhang, Y.; Zhang, L.; Deng, R.; Tian, J.; Zong, Y.; Jin, D.; Liu, X. *J. Am. Chem. Soc.* **2014**, *136*, 4893–4896.
- (39) Lu, Y.; Xi, P.; Piper, J. A.; Huo, Y.; Jin, D. *Sci. Rep.* **2012**, *2*, 837.
- (40) Lu, J.; Martin, J.; Lu, Y.; Zhao, J.; Yuan, J.; Ostrowski, M.; Paulsen, I.; Piper, J. A.; Jin, D. *Anal. Chem.* **2012**, *84*, 9674–9678.
- (41) Li, Q.; Bai, L.; Xue, S.; Chen, L. *Opt. Eng.* **2002**, *41*, 1289–1294.
- (42) Leif, R. C.; Yang, S.; Jin, D.; Piper, J.; Vallarino, L. M.; Williams, J. W.; Zucker, R. M. *J. Biomed. Opt.* **2009**, *14*, 024022.
- (43) Lu, J.; Chen, Y.; Liu, D.; Ren, W.; Lu, Y.; Shi, Y.; Piper, J.; Paulsen, I.; Jin, D. *Anal. Chem.* **2015**, *87*, 10406–10413.
- (44) Bravo-Zanoguera, M.; v. Massenbach, B.; Kellner, A. L.; Price, J. H. *Rev. Sci. Instrum.* **1998**, *69*, 3966–3977.
- (45) Braeckmans, K.; De Smedt, S. C.; Leblans, M.; Pauwels, R.; Demeester, J. *Nat. Rev. Drug Discov* **2002**, *1*, 447–456.
- (46) Wilson, R.; Cossins, A. R.; Spiller, D. G. *Angew. Chem., Int. Ed.* **2006**, *45*, 6104–6117.
- (47) Fulton, R. J.; McDade, R. L.; Smith, P. L.; Kienker, L. J.; Kettman, J. R. *Clin. Chem.* **1997**, *43*, 1749–1756.
- (48) Han, M.; Gao, X.; Su, J. Z.; Nie, S. *Nat. Biotechnol.* **2001**, *19*, 631–635.
- (49) Li, Y.; Cu, Y. T. H.; Luo, D. *Nat. Biotechnol.* **2005**, *23*, 885–889.

## Supporting Information

### High-Precision Pinpointing of Luminescent Targets in Encoder-Assisted Scanning Microscopy Allowing High-Speed Quantitative Analysis

Xianlin Zheng,<sup>†</sup> Yiqing Lu,<sup>\*,†</sup> Jiangbo Zhao,<sup>†</sup> Yuhai Zhang,<sup>§</sup> Wei Ren,<sup>‡</sup> Deming Liu,<sup>†</sup> Jie Lu,<sup>†</sup>  
James A. Piper,<sup>†</sup> Robert C. Leif,<sup>||</sup> Xiaogang Liu,<sup>§,⊥</sup> and Dayong Jin<sup>†,‡</sup>

<sup>†</sup>Advanced Cytometry Laboratories, ARC Centre of Excellence for Nanoscale BioPhotonics (CNBP), Macquarie University, Sydney, New South Wales 2109, Australia

<sup>‡</sup>Institute for Biomedical Materials and Devices, Faculty of Science, University of Technology Sydney, Sydney, New South Wales 2007, Australia

<sup>§</sup>Department of Chemistry, National University of Singapore, 3 Science Drive 3, Singapore 117543, Singapore

<sup>||</sup>Newport Instruments, 3345 Hopi Place, San Diego, California 92117-3516, United States

<sup>⊥</sup>Institute of Materials Research and Engineering, A\*STAR (Agency for Science, Technology and Research), 3 Research Link, Singapore 117602, Singapore

\* Corresponding to Y.L. [yiqing.lu@mq.edu.au](mailto:yiqing.lu@mq.edu.au)

### Contents

Figure S1 .....	S-2
Figure S2 .....	S-3
Figure S3 .....	S-3
Figure S4 .....	S-4
Figure S5 .....	S-5
Figure S6 .....	S-6
Figure S7 .....	S-6
Figure S8 .....	S-7
Movie S1 Description .....	S-7

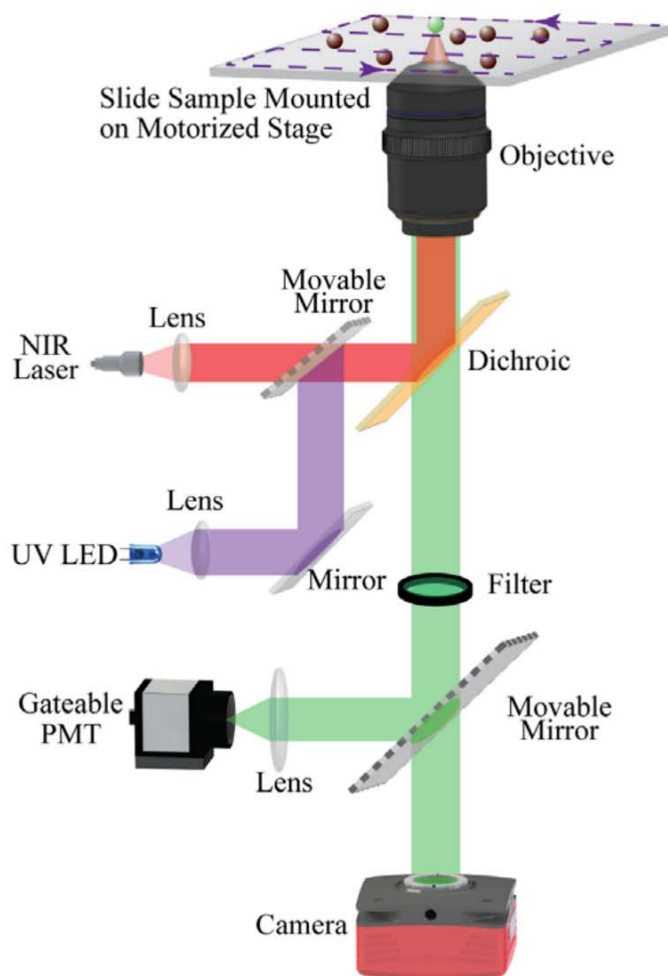


**Figure S1.** Optical configuration of the R-OSAM.



**Figure S2.** The linear encoders (circled in red) attached to the motorized stage.



**Figure S3.** The autofocus system attached to the microscope. Red circle – feedback unit; green circle – Z-drive; blue circle – controller.

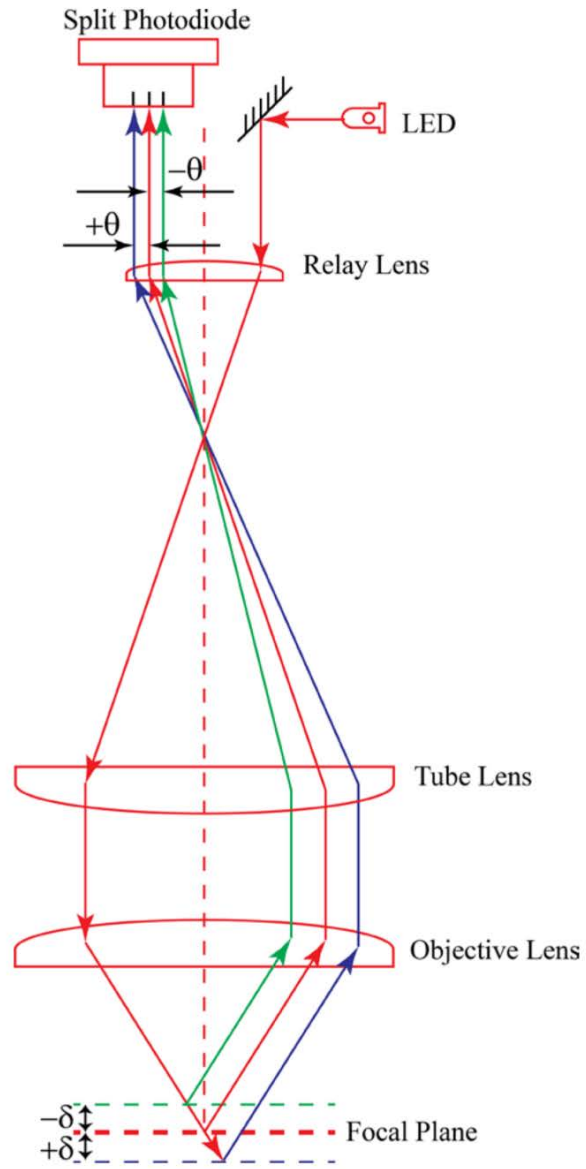


**Figure S4.** Principle of the autofocusing employed in this work.

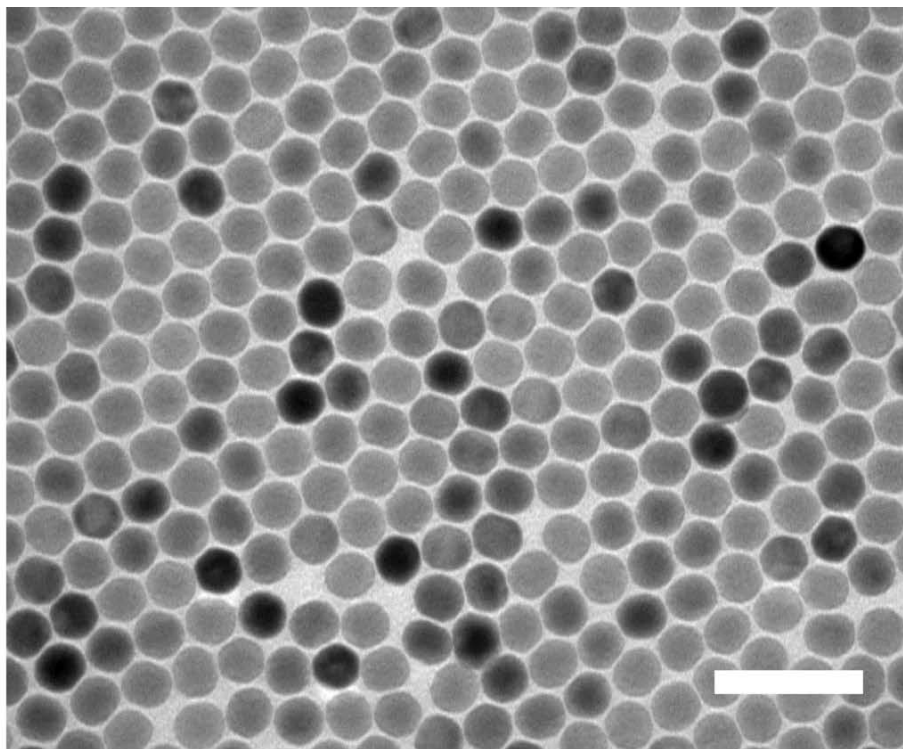


**Figure S5.** TEM image of the upconversion nanoparticles. Scale bar: 100 nm.

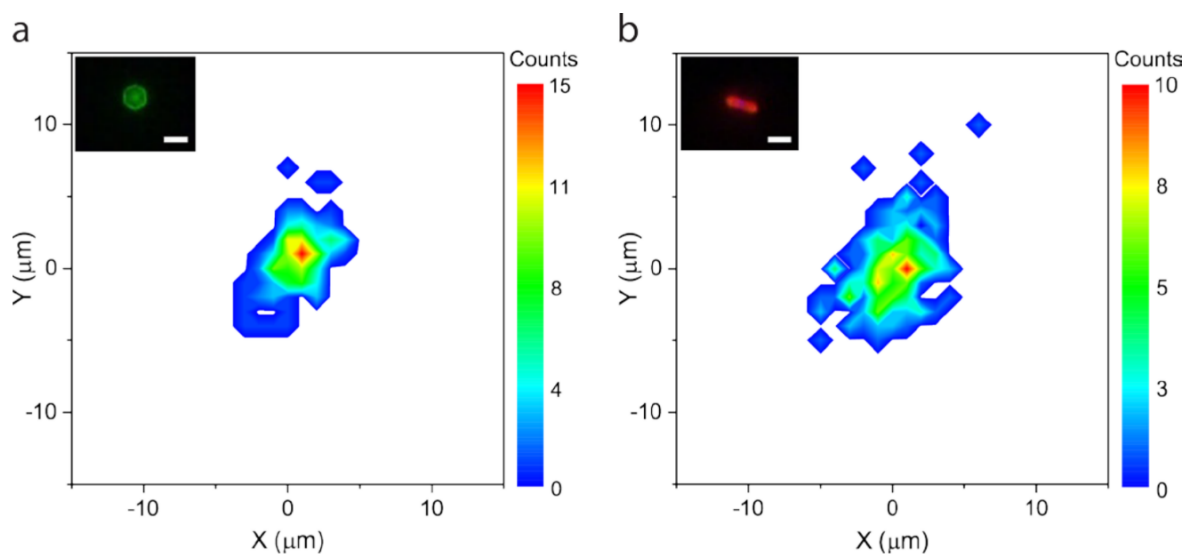


**Figure S6.** The heat plots illustrating the location precision for (a) the microplates and (b) the microrods samples. Scale bars in the luminescence images represent 5  $\mu\text{m}$ .

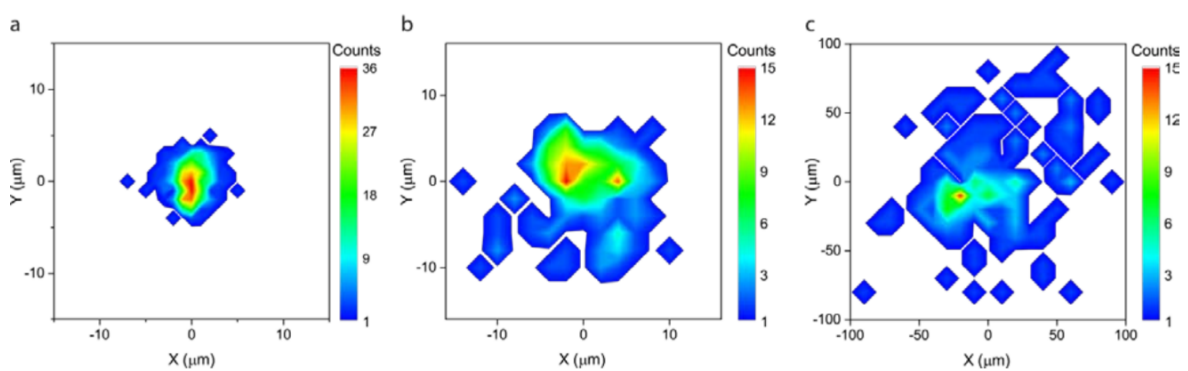


**Figure S7.** The heat plots illustrating the precision of target pinpointing by (a) R-OSAM in the continuous-wave mode, (b) R-OSAM in the time-gated mode, and (c) OSAM with encoders disabled.

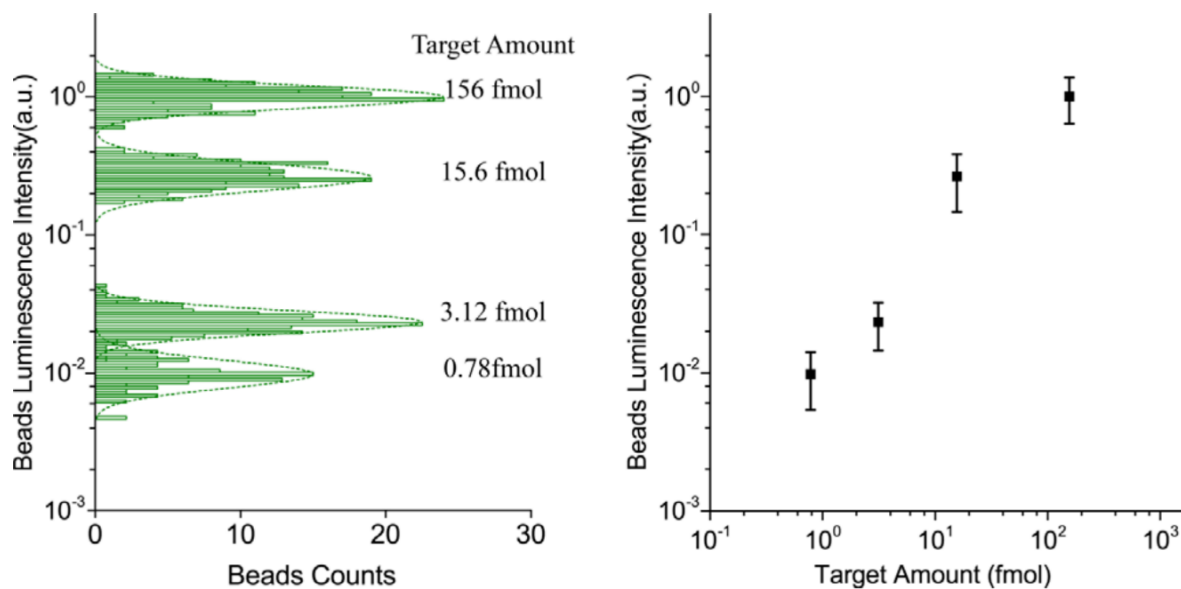


**Figure S8.** The luminescence intensity of beads in relation to the amount of the biotin-UCNPs, quantified via image analysis, in comparison to the results measured by R-OSAM in Figure 5b. The error bars represent twice the standard deviation (95% confidence).

### Movie S1 Description

This supporting movie shows the retrieval of individual 15- $\mu\text{m}$  UNCP-impregnated beads after the R-OSAM scanning. The first half was taken under the bright-field mode and the second half under the luminescence mode. Note that autofocusing was active.

### The hyperlink to the movie

[http://pubs.acs.org/doi/suppl/10.1021/acs.analchem.5b03767/suppl\\_file/ac5b03767\\_si\\_002.mpg](http://pubs.acs.org/doi/suppl/10.1021/acs.analchem.5b03767/suppl_file/ac5b03767_si_002.mpg)

## 4.3 Remarks

The location accuracy of new R-OSAM has been enhanced by 10-folds compared to previous OSAM, enabling quantification of luminescent-labelled targets with precision comparable to conventional image analysis but at a small fraction of processing time. It is particularly suitable for high-throughput detection of rare-event targets in complex samples, such as diagnosis of prostate cancer cells in urine, which is being investigated by my colleagues at the moment.

On the other hand, although this system is capable of recognising and quantifying small aggregated targets, it cannot distinguish multiple targets appearing in the FOV at the same time, due to the use of single-element detector. Currently this is addressed by cautious sample preparation to ensure targets are well dispersed. Future work is planned to introduce array detectors and/or advanced signal analysis to relieve this requirement.

## Chapter 5: Conclusions and Perspectives

### 5.1 Summary

Time-gated techniques in conjunction with long-lived luminescent probes hold great potential to realise ultra-sensitive biosensing and high-contrast imaging at background-free condition; however, only after suitable excitation source, detector, optics and control electronics have been properly designed and implemented.

To achieve such potential, my research has applied advanced engineering concepts to successfully build three prototype instruments, and validate them by applications: i) The multi-colour time-gated microscopy employs a high power and high repetition rate Xenon flash lamp (60 W; 1 kHz) to allow simultaneous observation of multiple microorganisms labelled by different lanthanide probes; ii) The near-infrared time-gated *in vivo* imaging system enables high-contrast visualisation of upconversion nanoparticles distributed in a live small animal, with substantially lowered thermal effect; iii) The referenced orthogonal scanning automated microscopy (R-OSAM) takes advantage of linear encoders and an autofocus unit to achieve high-precision target pinpointing in 3-dimensions during rapid scanning, facilitating accurate quantification of target luminescence characteristics at high sample throughput.

Modular design has been pursued throughout my project, so that the demonstrated illumination, detection and control modules are readily to be installed onto any commercial instruments, with minimum modification and alignment to provide highly-efficient and robust time-gated detection at low instrumentation cost. The demonstrated modules and instruments can be easily adopted by analytical biochemistry labs that do not possess a high level of instrumentation expertise, provide access to advanced time-gated detection techniques for characterization of long-lifetime luminescent materials and applications. Opportunities include:

- 1) A range of luminescent materials that have long lifetimes. During the period of my PhD research, great progress has been made based on the luminescent materials summarised in 1.3, leading to new materials spanning organic compounds and complexes [1-5],

genetically engineered fluorescent proteins [6], semiconductor quantum dots [7-9], gold nanoparticles [9-11], silica or polymer nanoparticles [12-15], and rare earth doped nanocrystals [16-20]. All the time-gated instruments developed here have sufficient flexibility to be configured with suitable spectral selection and temporal control to study these materials.

2) Sensing and imaging using active probes capable of targeting specific biomolecules. For example, I have replicated the multi-colour time-gated microscope at Dalian University of Technology in China, enabling our collaborators to characterize a series of new responsive lanthanide probes, and subsequently to image the distributions of a range of small molecules of biological significance *in vivo*. In addition to the co-authored paper included in this thesis, another two papers have been published by this group subsequently (in *Materials Views* and *Chemical Science*, respectively).

3) The small-animal imaging capability offers significant potential for practical applications ranging from non-invasive biomedical diagnostics to luminescence image-guided surgery. The excitation and emission wavelengths of upconversion nanoparticles can be tuned, e.g. using Nd<sup>3+</sup> sensitizers, to further lower the tissue absorption and increase the penetration depth [21-23]. Moreover, other medical imaging modalities, such as CT, MRI and SPECT, as well as localised therapy, can be integrated for precise medicine, when multi-modality contrast agent based on upconversion nanocrystals are used [21,24-26].

4) Beyond simple images, the statistical analysis of luminescence intensities and lifetimes for individual targets offered by the R-OSAM is highly valuable for material characterisation and quantitative bioassays. The population variations from one target to another, previously often ignored in laboratory research, can be investigated at high sample throughput, which will enable new understandings and guide the development towards real-world applications.

## 5.2 Future Work

The methods and prototype systems developed in this thesis can be further enhanced in terms of mechanics, optics, electronics and software, to better enable translation into commercial products. From the user perspective, the major issues that need to be addressed include:

1) The high-speed optical chopper produces acoustic noise, which is unpleasant for users especially if they work for a lengthy period of time. This noise comes from air friction when chopper blades are rapidly rotating. Currently a plastic enclosure is mounted on the detection module of the prototype system, however its effect in reducing the noise is very limited. I propose design of a new mechanical structure to completely seal the chopper unit while allowing convenient optical alignment. The sealed unit might be evacuated, which will significantly reduce the acoustic noise further.

Once this is done, I will build two more time-gated microscopes for our collaborators: one for Prof. Nicki Packer's group at Macquarie University, and the other for Prof. Brant Gibson's group at RMIT University. Meanwhile, we are endeavouring to commercialize our time-gated detection modules with Olympus, who has shown significant interest in this technology.

2) The current imaging optics of the *in vivo* time-gated system has low efficiency for light collection, due to the introduction of a pinhole that is otherwise necessary for efficient time gating. I propose to redesign the imaging optics using optical simulation software such as (e.g. Zemax), aiming to overcome this dilemma by compact lens design while preserving good imaging quality.

3) The R-OSAM method is good at analysing samples containing well-dispersed targets. While it is capable of recognising and measuring small aggregated targets, it cannot handle large clusters of targets, since the position of individual target cannot be obtained using a single-element detector. This may be solved using an array detector of photomultipliers or avalanche photodiodes together with enhanced data collection and processing. Alternatively, sample preparation standards need to be developed to ensure good distribution of individual targets on the substrate.

In addition to these issues, further advances can be made in the engineering of time-gated luminescence instruments to achieve lifetime measurement. In particular, lifetime-tunable luminescent probes have emerged recently, representing a unique opportunity to achieve highly multiplexed optical detection beyond fluorescence colours [27]. Lifetime measurement has been realised on the original OSAM, and this function can be extended to the new R-OSAM and demonstrated for material characterisation. In the next step, the time-gated luminescence microscope and the time-gated animal imaging system will be further developed to integrate luminescence lifetime imaging, to enable simultaneous visualisation of multiple analytes surpassing the number that can be differentiated by colours alone.

A simple scheme previously demonstrated by Marriott et al. can be implemented [28], which captures gated images of the same area with incremental delay time to calculate the lifetime for each pixel, as illustrated in [Figure 5-1 \(a\)](#). That system used two choppers to gate the excitation (10-20% duty cycle) and emission (50% open duty cycle), synchronised by a phase-locked loop (PLL). However, a major limitation lies in its effective delay range (up to 68  $\mu\text{s}$ , which is 40% of the 170  $\mu\text{s}$  period), which will lead to inaccurate lifetime measurement for luminescent probes with lifetime longer than  $\sim 10 \mu\text{s}$  [29]. On the other hand, the chopper we use has two sections near its edge with different numbers of blades ([Figure 5-1 \(b\)](#)), so that the delay range can be increased by slightly moving the pinhole from the inner section to the outer section to achieve a large dynamic range for lifetime imaging.

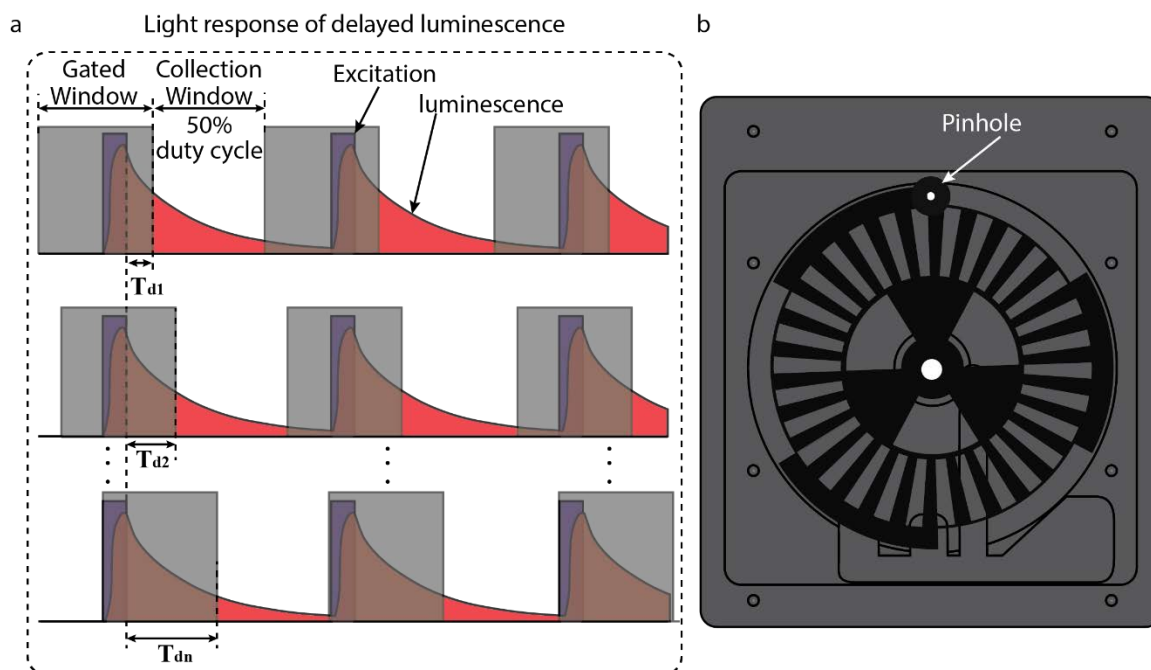


**FIGURE 5-1.** (a) Time sequence of two chopper and the luminescence lifetime imaging collection [28]. (b) Mechanical design of chopper unit.

Implementing the advanced time-gated technique to flow cytometry represents another opportunity for high-speed and high-throughput analytical biotechnology. A few time-gated flow cytometers have been reported previously [30-33], but none can measure the luminescence lifetimes (although measurement of short-lived fluorescence lifetime has been realized). I have designed a spatial-displacement time-gated flow cytometry offering sensitive detection of the target events while effectively measuring the luminescent decay curve. Illustrated in [Figure 5-2 \(a\)](#), time-gated detection is achieved by displacing the detection region at the downstream of the interrogation spot, so that only the slow-decaying luminescence signal is captured. [Figure 5-2\(b\)](#) shows the preliminary data of luminescent decay curves captured from the  $5\mu\text{m}$  beads containing europium complexes. The key issue to be addressed is when two targets are too close and both reside in the collection window, leading to overlap of their decay curves, as shown in [Figure 5-2\(c\)](#). I propose to optimise the spatial-temporal configuration and develop data processing algorithms to decode such overlapped targets and measure their respective lifetimes in the next step. A lifetime decoding method recently demonstrated on laser scanning confocal microscopy, which is based on variable scanning velocity[34], may be adopted for measurement of luminescence lifetimes in the flow.

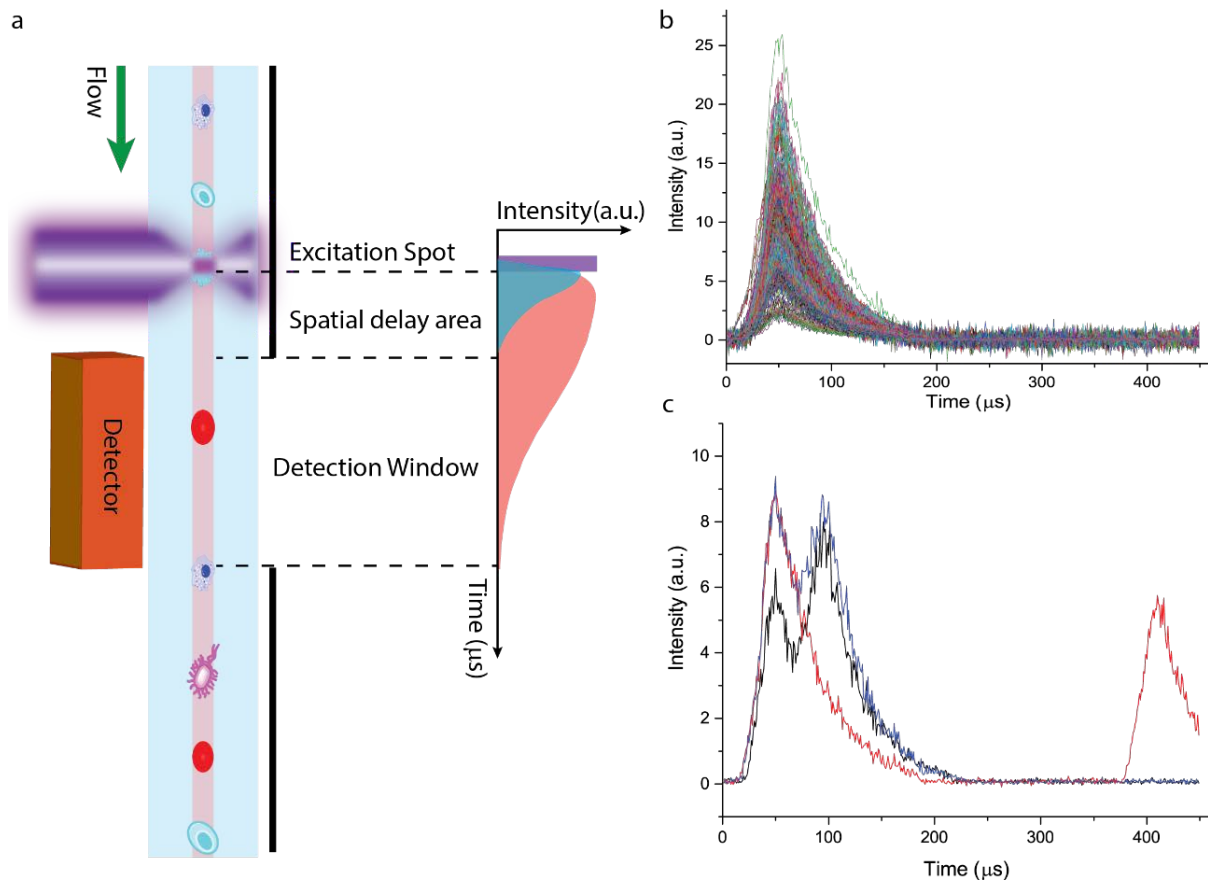


**FIGURE 5-2.** (a) Schematics of spatial-delay time-resolved flow cytometry. (b) The luminescent decay curve is collected by the spatial-delay time-resolved flow cytometry. (c) The overlap of the luminescent decay curve between two targets.

### 5.3 Reference

- [1] Yuan, J., Matsumoto, K. & Kimura, H. A new tetradentate  $\beta$ -diketonate-europium chelate that can be covalently bound to proteins for time-resolved fluoroimmunoassay. *Analytical Chemistry* **70**, 596-601 (1998).
- [2] Guo, X.-Q., Castellano, F. N., Li, L. & Lakowicz, J. R. Use of a long-lifetime Re (I) complex in fluorescence polarization immunoassays of high-molecular-weight analytes. *Analytical Chemistry* **70**, 632-637 (1998).
- [3] Yuan, J., Wang, G., Majima, K. & Matsumoto, K. Synthesis of a terbium fluorescent chelate and its application to time-resolved fluoroimmunoassay. *Analytical Chemistry* **73**, 1869-1876 (2001).
- [4] Zhang, L., Wang, Y., Ye, Z., Jin, D. & Yuan, J. New class of tetradentate  $\beta$ -diketonate-europium complexes that can be covalently bound to proteins for time-gated fluorometric application. *Bioconjugate Chemistry* **23**, 1244-1251 (2012).
- [5] Sayyadi, N., Connally, R. E. & Try, A. A novel biocompatible europium ligand for sensitive time-gated immunodetection. *Chemical Communications* **52**, 1154-1157 (2016).
- [6] Enkvist, E., Vaasa, A., Kasari, M., Kriisa, M., Ivan, T., Ligi, K., Raidaru, G. & Uri, A. Protein-induced long lifetime luminescence of nonmetal probes. *ACS Chemical Biology* **6**, 1052-1062 (2011).
- [7] Pu, C., Ma, J., Qin, H., Yan, M., Fu, T., Niu, Y., Yang, X., Huang, Y., Zhao, F. & Peng, X. Doped Semiconductor-Nanocrystal Emitters with Optimal Photoluminescence Decay Dynamics in Microsecond to Millisecond Range: Synthesis and Applications. *ACS Central Science* (2015).
- [8] Nirmal, M., Murray, C. & Bawendi, M. Fluorescence-line narrowing in CdSe quantum dots: Surface localization of the photogenerated exciton. *Physical Review B* **50**, 2293 (1994).
- [9] Huang, D., Niu, C., Ruan, M., Wang, X., Zeng, G. & Deng, C. Highly sensitive strategy for Hg<sup>2+</sup> detection in environmental water samples using long lifetime fluorescence quantum dots and gold nanoparticles. *Environmental Science & Technology* **47**, 4392-4398 (2013).
- [10] Chhabra, R., Sharma, J., Wang, H., Zou, S., Lin, S., Yan, H., Lindsay, S. & Liu, Y. Distance-dependent interactions between gold nanoparticles and fluorescent molecules with DNA as tunable spacers. *Nanotechnology* **20**, 485201 (2009).

- [11] Wu, Z. & Jin, R. On the ligand's role in the fluorescence of gold nanoclusters. *Nano Letters* **10**, 2568-2573 (2010).
- [12] Saar, A. Photoluminescence from silicon nanostructures: the mutual role of quantum confinement and surface chemistry. *Journal of Nanophotonics* **3**, 032501-032501-032542 (2009).
- [13] Joo, J., Liu, X., Kotamraju, V. R., Ruoslahti, E., Nam, Y. & Sailor, M. J. Gated Luminescence Imaging of Silicon Nanoparticles. *ACS Nano* **9**, 6233-6241 (2015).
- [14] Ow, H., Larson, D. R., Srivastava, M., Baird, B. A., Webb, W. W. & Wiesner, U. Bright and stable core-shell fluorescent silica nanoparticles. *Nano letters* **5**, 113-117 (2005).
- [15] Sun, W., Yu, J., Deng, R., Rong, Y., Fujimoto, B., Wu, C., Zhang, H. & Chiu, D. T. Semiconducting Polymer Dots Doped with Europium Complexes Showing Ultranarrow Emission and Long Luminescence Lifetime for Time - Gated Cellular Imaging. *Angewandte Chemie International Edition* **52**, 11294-11297 (2013).
- [16] Zhao, J., Lu, Z., Yin, Y., McRae, C., Piper, J. A., Dawes, J. M., Jin, D. & Goldys, E. M. Upconversion luminescence with tunable lifetime in NaYF<sub>4</sub>: Yb, Er nanocrystals: role of nanocrystal size. *Nanoscale* **5**, 944-952 (2013).
- [17] Bünzli, J.-C. G. Lanthanide luminescence for biomedical analyses and imaging. *Chemical Reviews* **110**, 2729-2755 (2010).
- [18] Wang, F., Banerjee, D., Liu, Y., Chen, X. & Liu, X. Upconversion nanoparticles in biological labeling, imaging, and therapy. *Analyst* **135**, 1839-1854 (2010).
- [19] Zhou, J., Sun, Y., Du, X., Xiong, L., Hu, H. & Li, F. Dual-modality in vivo imaging using rare-earth nanocrystals with near-infrared to near-infrared (NIR-to-NIR) upconversion luminescence and magnetic resonance properties. *Biomaterials* **31**, 3287-3295 (2010).
- [20] Liu, H., Xu, C. T., Lindgren, D., Xie, H., Thomas, D., Gundlach, C. & Andersson-Engels, S. Balancing power density based quantum yield characterization of upconverting nanoparticles for arbitrary excitation intensities. *Nanoscale* **5**, 4770-4775 (2013).
- [21] Wang, Y.-F., Liu, G.-Y., Sun, L.-D., Xiao, J.-W., Zhou, J.-C. & Yan, C.-H. Nd<sup>3+</sup>-sensitized upconversion nanophosphors: efficient in vivo bioimaging probes with minimized heating effect. *ACS Nano* **7**, 7200-7206 (2013).
- [22] Shen, J., Chen, G., Vu, A. M., Fan, W., Bilsel, O. S., Chang, C. C. & Han, G. Engineering the Upconversion Nanoparticle Excitation Wavelength: Cascade Sensitization of Tri - doped Upconversion Colloidal Nanoparticles at 800 nm. *Advanced Optical Materials* **1**, 644-650 (2013).

- [23] Xie, X., Gao, N., Deng, R., Sun, Q., Xu, Q.-H. & Liu, X. Mechanistic investigation of photon upconversion in Nd<sup>3+</sup>-sensitized core-shell nanoparticles. *Journal of the American Chemical Society* **135**, 12608-12611 (2013).
- [24] Sun, Y., Zhu, X., Peng, J. & Li, F. Core-shell lanthanide upconversion nanophosphors as four-modal probes for tumor angiogenesis imaging. *ACS nano* **7**, 11290-11300 (2013).
- [25] Yang, D., Li, C. & Lin, J. Multimodal cancer imaging using lanthanide-based upconversion nanoparticles. *Nanomedicine* **10**, 2573-2591 (2015).
- [26] Liu, C., Gao, Z., Zeng, J., Hou, Y., Fang, F., Li, Y., Qiao, R., Shen, L., Lei, H. & Yang, W. Magnetic/upconversion fluorescent NaGdF<sub>4</sub>: Yb, Er nanoparticle-based dual-modal molecular probes for imaging tiny tumors in vivo. *ACS Nano* **7**, 7227-7240 (2013).
- [27] Lu, Y., Zhao, J., Zhang, R., Liu, Y., Liu, D., Goldys, E. M., Yang, X., Xi, P., Sunna, A. & Lu, J. Tunable lifetime multiplexing using luminescent nanocrystals. *Nature Photonics* **8**, 32-36 (2014).
- [28] Marriott, G., Clegg, R. M., Arndt-Jovin, D. J. & Jovin, T. M. Time resolved imaging microscopy. Phosphorescence and delayed fluorescence imaging. *Biophysical Journal* **60**, 1374 (1991).
- [29] Lu, Y., Lu, J., Zhao, J., Cusido, J., Raymo, F. M., Yuan, J., Yang, S., Leif, R. C., Huo, Y. & Piper, J. A. On-the-fly decoding luminescence lifetimes in the microsecond region for lanthanide-encoded suspension arrays. *Nature Communications* **5** (2014).
- [30] Condrau, M. A., Schwendener, R. A., Niederer, P. & Anliker, M. Time - resolved flow cytometry for the measurement of lanthanide chelate fluorescence: I. Concept and theoretical evaluation. *Cytometry* **16**, 187-194 (1994).
- [31] Condrau, M. A., Schwendener, R. A., Zimmermann, M., Muser, M. H., Graf, U., Niederer, P. & Anliker, M. Time - resolved flow cytometry for the measurement of lanthanide chelate fluorescence: II. Instrument design and experimental results. *Cytometry* **16**, 195-205 (1994).
- [32] Jin, D., Connally, R. & Piper, J. Practical time - gated luminescence flow cytometry. II: Experimental evaluation using UV LED excitation. *Cytometry Part A* **71**, 797-808 (2007).
- [33] Jin, D., Connally, R. & Piper, J. Practical time - gated luminescence flow cytometry. I: Concepts. *Cytometry Part A* **71**, 783-796 (2007).

[34] Petrasek, Z., Bolivar, J. M. & Nidetzky, B. Confocal luminescence lifetime imaging with variable scan velocity and its application to oxygen sensing. *Analytical Chemistry* **88**, 10736-10743 (2016).